Cranfield University

Patrick Verdin

An Automatic Multi-Stepping Approach for Aircraft Ice Prediction

School of Engineering

PhD Thesis

Cranfield University
School of Engineering
Applied Mathematics and Computing Group

PhD Thesis

Academic Year 2007 - 2008

Patrick Verdin

An Automatic Multi-Stepping Approach for Aircraft Ice Prediction

Supervisors: Dr J.P.F Charpin, Prof C.P. Thompson

October 2007

This thesis is submitted in partial fulfilment of the requirements for the Degree of Doctor of Philosophy

Abstract

Flying an aircraft in icing conditions may seriously degrade its aerodynamical performance and threaten the flight safety. Over the years, new technologies and improved procedures have limited the potential risks caused by aircraft icing. Experimental studies being very expensive, numerous computer codes have been developed to simulate ice shapes and tackle the problem. Typically in these codes, a flow solution and key icing parameters are evaluated around a clean un-iced geometry and their values remain constant during the entire simulation. This approach may be acceptable for short exposure times or when the ice shape only slightly deforms the initial geometry. However, in other cases, the values of the icing parameters may vary and the simulation will loose its accuracy: for large shapes, the presence of the ice influences the surrounding airflow significantly, altering the value of icing parameters and ultimately the ice accretion. Calculating more accurate ice shapes therefore requires to periodically recompute the flow field around the body during the simulation and determine updated values for icing parameters. This procedure, known as multi-stepping, is investigated in this thesis and adapted to the new three-dimensional icing code ICECREMO2. Several multi-step algorithms are presented and tested on cylinders and airfoils. When possible, the ice shapes simulated are compared with experimental results.

The first multi-step calculations were generally performed manually. The user had to perform a rather tedious work and inappropriate instructions could lead to severe inaccuracies in the simulations. To avoid these difficulties, a fully automated procedure will be developed including all stages of a multi-step computation. This significantly reduces user interaction and the overall computing time.

The present research work forms part of the ICECREMO2 project. ICECREMO2 is a three-dimensional ice accretion and water flow code developed collaboratively by Airbus UK, BAe Systems, Dunlop Aerospace, Rolls-Royce, GKN Westland Helicopters, QinetiQ and Cranfield University under the auspices of the UK Department of Trade and Industry.

ACKNOWLEDGEMENTS

There are lots of people I would like to thank for a huge variety of reasons. First, I would like to thank my supervisors: Dr Jean Charpin and Prof Chris Thompson for the guidance and encouragement from the start to the completion of this work. I wish to express my immense gratitude to Jean for being such a great supervisor and mentor for my PhD, and also a great friend. His ideas, friendship and tremendous support had a major influence on this thesis. He kept on supervising me and spent a huge amount of time helping me despite being away from Cranfield University. Without his knowledge and perceptiveness, things would have been even more difficult. I would also like to thank Chris for giving me the opportunity to carry out research in icing, for allowing me to start and complete my PhD and for his support all over these years.

Thanks must go to Dr Ouahid Harireche who took time out of his busy schedules for reading parts of this thesis and offering suggestions and support for this work.

I would also like to thank all the people involved in the ICECREMO2 project for their help, advices and professionalism. Special thanks must go to Nick Dart from Airbus UK and Dr David Hammond from Cranfield University for kindly providing the experimental data used in this thesis.

Many thanks to Prof Abdellatif Ouahsine from the University of Technology of Compiegne (UTC, France), Prof Isam Shahrour from the University of Science and Technology of Lille (USTL, France) and Dr Lahcen Hanich who gave me the opportunity to join Cranfield University.

Thanks also go to my past and present colleagues and friends in the Applied Mathematics and Computing Group: Alexandre, Bo, Christian, Dulcéneia, George, Hans-Dieter, Homa, James, Judith, Julian, Kath, Karl, Mustapha, Peter, Stuart, Timos, Tom and more recently, Dinesh. A special thank you to Rachael for her friendship and countless help during all these years.

On a very different note, I want to thank Christine, who had and still has a special place in my life and in my heart. This PhD would have been much more difficult without her being around. More thanks go to Mylène, Pauline, Yves (and "Souris") for the great moments spent together around "*good food and good drinks*". A deep

thought goes to Jéjé who tragically disappeared a few months ago... I also want to thank all my other friends who have made life much more enjoyable during this long journey. They are mainly and in no particular order Fatiha, Giorgio, Ahmed, Monica, Dan, Aaron and Zabo.

This makes lots of thanks, but I can not stop now. I have to say a huge "thank-you" to my Mum for her kindness and for providing me financial support in the hard months. I also have a deep thought to my Dad who will never know I was going to start and complete a PhD. Finally, I can not forget Anne and Philippe and more especially my little niece Clémence and my little nephew Paul, who are just... wonderful. I hope I will have a bit more time to spend with them in the near future.

Cranfield University, *Patrick Verdin*
October 30, 2007

TABLE OF CONTENTS

NOMENCLATURE

Symbols	**Definition**	**Unit**
b	Ice layer thickness	[m]
c	Chord or Diameter length	[m]
c_i	Specific heat in the ice	[J.kg^{-1}.K^{-1}]
c_w	Specific heat in the water	[J.kg^{-1}.K^{-1}]
d_d	Droplet diameter	[m]
ds	Distance between droplets on the surface	[m]
dy_o	Distance between droplets in the free stream	[m]
e	Water vapor pressure	[Pa.K^{-1}]
F	Freezing fraction	–
h_c	Convective heat transfer coefficient	[W.m^{-2}.K^{-1}]
h	Water layer thickness	[m]
k_a	Thermal conductivity of air	[W.m^{-1}.K^{-1}]
L_f	Latent heat of fusion	[J.kg^{-1}]
LWC	Liquid water content	[kg.m^{-3}]
$\dot{m}$	Mass flux term	[kg.m.$^{-2}$.s^{-1}]
M	Mach number	–
n	Normal to the surface	–
P	Pressure	[Pa]
Pr	Prandtl number	–
Q	Heat flux	[W.m^{-2}]
Re	Reynolds number	–
r	Recovery factor	–
T	Temperature	[K]
t	Time	[s]
V	Velocity	[m.s^{-1}]

Greek symbols

α	Angle of attack	[°]
β	Collection efficiency	–
ϵ	Aspect ratio	–
κ	Thermal conductivity	[W.m^{-1}.K^{-1}]
μ	Dynamic viscosity	[kg.m^{-1}.s^{-1}]
ρ	Density	[kg.m^{-3}]
σ	Surface tension	[N.m^{-1}]
τ	Shear Stress	[Pa]
θ	Water temperature	[K]

Subscripts

a	Air
c	Conduction or Corrector
h	Convection
d	Droplet
e	Evaporation
exp	Exposure
f	Freezing
g	Glaze
i	Ice or Interpolated
imp	Impinging
k	Kinetic
L	Local
p	Predictor
r	Recovery or Rime
rad	Radiation
s	Surface
sl	Sensible and latent
$step$	Step
T	Total
w	Wall or Water
∞	Airstream

List of Tables

List of Figures

LIST OF FIGURES

ACRONYMS

ATCA	Air Traffic Control Association
CIRA	Centro Italiano Ricerche Aerospaziali
DERA	Defense Evaluation and Research Agency
NACA	National Advisory Committee for Aeronautics
NASA	National Air and Space Administration
NATO	North Atlantic Treaty Organization
NTSB	National Transportation Safety Board
ONERA	Office National d'Etudes et de Recherches Aérospatiales
RTO	Research and Technology Organization

CHAPTER 1

INTRODUCTION

1.1 Motivation for Studying Icing

"Federal crash investigations have made repeated calls for tougher rules and more research on flying in icing conditions because 135 planes have fallen out of the sky since 1993 because of ice." This sentence, extracted from the Air Traffic Control Association (ATCA) web page [1] points out that nowadays, the aircraft icing problem is still a major concern for aircraft industries and manufacturers. From 1989 to 1997, the National Transportation Safety Board [2] indicated that in-flight icing was a contributing or causal factor in approximately 11 per cent of all weather-related accidents among general aviation aircraft [3], 12% during the period 1990 to 2000 according to the Air Safety Foundation [4]. For instance, the 1994 crash of an ATR-72 near Roselawn, Indiana which caused 68 fatalities [5] and the 1997 crash of a Comair commuter plane near Detroit that killed all 29 people on board, both took place during icing conditions. More recently and despite ice protection systems on the plane, a fatal crash occurred just after take off at Birmingham International Airport (UK) in January 2002 [6]. Ice accretion does not only affect commercial airliners: it particularly penalises small aircrafts and helicopters:

- Icing adds some unwanted weight. This may be neglected on larger aircrafts but could get a more significant influence for smaller ones.
- These aircrafts tend to fly at lower altitude and are therefore more likely to face icing conditions [7].

Ice may form in a moist environment at temperatures below freezing. It grows on any forward facing part of the aircraft body. The accretion must be watched particularly on the leading edge of a wing or air intakes for an aircraft and on the rotor blades of an helicopter. The ice growth can cause very important aerodynamic degradations [8, 9, 10, 11, 12] or propulsion problems when ice builds up on air intakes and is ingested. As the accumulated ice changes the effective shape of the wings, the surrounding air-flow is modified. Icing, therefore, causes an increase in drag and a decrease in lift, see for instance [9, 13, 14, 15, 16, 17, 18]. The increased drag forces the engine to work harder than normal to maintain the aircraft's cruise speed. In addition, the ice accretion may lead to a stall or loss of lift, due to the turbulent airflow generated around the wing.

Over the years, two types of ice protection devices have been developed by the aeronautical industry to reduce the risk of incidents and accidents due to ice accumulations on critical parts of an aircraft, namely anti-icing and de-icing devices [11, 19]. Anti-icing systems try to prevent ice from accreting at all, working continuously from the start of ice growth [20]. This may be achieved with a chemical or thermal approach.

- *Chemical devices*

  Chemical methods consist generally in applying anti-freezing fluids on critical surfaces. These fluids mix with the impinging water droplets and lower the water freezing point [21]. These devices are mainly used on the ground before take-off, they are blown away by shear stress at the very start of the flight. Later on, thermal systems are preferred.

- *Thermal devices*

  Typically, hot air provided by the engine is circulated in the wings. Alternatively, electrical pads are installed in the metal skin. Thermal devices are located in the leading edge area, where water droplets impinge. They are designed to keep the water running back over the surface above 0^oC, or to evaporate a large part of it.

As thermal anti-icing methods are energy-consuming and energy is limited during the flight, an alternative solution is to use de-icing devices. The objective of a de-icing system is to remove the ice accretion periodically [20]. In this situation, a small layer of ice is allowed to form before removal. Three methods are commonly used [21]: mechanical, electro-impulse, or thermal. Mechanical systems are often a pneumatic boot, which is inflated periodically, breaking the link between the accreted ice layer and the boot. This system is not used on light airfoils as the inflated boots increase the drag. The second method is based on electromechanical impulses that deform the airfoil surface and break the bond between the surface and the accreted ice. Finally, thermal, or more precisely electro-thermal systems, use electrical heaters elements placed on the airfoil to destroy the ice adhesion, so that aerodynamic forces can remove the ice from the surface. Electro-thermal systems are currently the preferred and the most effective methods to deice helicopter blades for example [21].

Despite all these devices, flight safety is still threatened by ice accretion. Other methods to reduce accidents caused by aircraft icing are:

1. To avoid clouds likely to cause icing,
2. To develop a better design that allows an aircraft to fly in an ice tolerant manner.

For commercial flights, the latter is the preferred method as revenue and schedules must be maintained [10]. Today, research is being pursued in both numerical and experimental fields for a better understanding of atmospheric icing, its effects on aircraft performance and the ways to prevent it. Because in-flight tests are rather expensive and potentially dangerous, and the conditions required for icing are often difficult to obtain in wind tunnel experiments, numerical tools have been developed in the last decades.

Computer codes are used to aid design and certification work in the aircraft industry. Aircraft icing analysis methods were initially performed by the NASA Lewis Center in the United States and the Royal Aerospace Establishment (RAE), renamed Defense Evaluation and Research Agency (DERA), now QinetiQ, in the United Kingdom. The French organism, the Office National d'Etudes et de Recherches Aérospatiales (ONERA), joined icing analysis a bit later, in the early 1980s [16]. The ice accretion prediction codes were named LEWICE, TRAJICE and the ONERA Icing code [22, 23, 24]. Other codes appeared later, for instance, codes developed at the Centro Italiano Ricerche Aerospaziali (CIRA) in Italy [25], at the Ecole Polytechnique de Montreal (CANICE) in Canada [26] and at the Concordia University of Montreal with FENSAP [27]. These codes are mainly based on the Messinger model [28]. However, Messinger's derivation has well-known limitations [29]. For instance, the water film is not accounted for accurately although there is clear experimental evidence that water films influence icing significantly [30, 31]. New codes are being developed that aim to produce a better description of the ice accretion than those based on Messinger's approach. A typical example is the ice accretion and water film code ICECREMO [16, 32], born of the collaboration between the leading aeronautical companies in the United Kingdom. The model implemented in ICECREMO is based on a Stefan phase change condition [33] at the ice-water interface. The ice growth model, developed by Myers [34] and improved by Charpin [35] for the water film, has been used for the predictions of the ice growth presented in this thesis.

In most current icing codes, physical parameters influencing ice accretions are evaluated on the clean un-iced body at the beginning of the simulation; they remain constant during the whole calculation. This procedure is known as a single-step algorithm. The values calculated on an ice-clean body become less accurate when the ice layer thickens and exposure time to icing increases: for large shapes, the presence of ice influences the airflow, leading to significant changes in key icing parameters. In order to obtain more accurate results, the flow field around the body should be recomputed periodically during the simulation and the values of important icing parameters should be updated. This procedure, known as multi-stepping, is used in several Messinger-based codes and the objective of this thesis is to apply it to Stefan-based algorithms. When the first multi-step algorithms were developed, the process was performed manually [23, 36] and prone to human error. A fully automated procedure reduces the overall computing time significantly and limits user intervention to a minimum. Algorithms should be developed with these objectives in mind.

The present work describes the first attempt to generate three-dimensional ice shapes using a fully automated multi-step procedure implemented in a Stefan-based code. This work will underline:

1. The importance and necessity of multi-step calculations,
2. The improved accuracy obtained with a multi-step method.

1.2 Structure of the Thesis

The present work is organised as follows:

- Chapter 2 introduces the concepts necessary to develop a multi-step icing code. The different types of icing are presented and the structure of an icing code is analysed. A review of icing models is carried out and the physical parameters varying during ice accretion are pointed out. Finally, existing multi-step algorithms are presented and analysed.
- Chapter 3 presents the fully automatic multi-step approach developed and implemented using the ICECREMO1 and ICECREMO2 codes. The structure of the algorithm is detailed. The differences between the two icing codes and the consequences on the multi-step procedure are highlighted.
- Chapter 4 presents the basic implementation of a multi-step algorithm using the step-by-step method and the ICECREMO1 icing code. The evolution of icing parameters are studied during a multi-step calculation under typical icing situations and the simulated ice shapes are compared with experimental results. Limitations of this initial procedure are pointed out.

- In Chapter 5, a systematic study of the step-by-step method is conducted. Criteria governing the multi-step algorithm are analysed, investigated and tested on typical flight scenarios under icing conditions. Results are calculated using the ICECREMO2 icing code. When possible, the simulated ice shapes are compared with experiments.

- In Chapter 6 and 7, alternatives to the step-by-step algorithm are studied. The predictor-corrector method and a method combining step-by-step and predictor-corrector are introduced. Both methods are studied and their characteristics are pointed out. The two algorithms are again tested on typical icing configurations and the numerical results are then compared with experimental measurements when available.

- Finally, Chapter 8 presents the conclusions drawn from the work presented in this thesis and offers some recommendations for future studies and developments of the multi-stepping methodology applied to aircraft ice prediction.

CHAPTER 2

LITERATURE REVIEW

2.1 Introduction

Aircraft icing may occur at any stage of an aircraft journey: on the ground or during the flight, and particularly the take off and landing phases. Different types of ice can start accreting on the unprotected surfaces of an aircraft and each situation can lead to aerodynamic penalties which can become irreversible. The different icing configurations are presented in Section 2.2, with particular emphasis given to in-flight situations. The different methods used to model the icing phenomenon will then be investigated. The structure of a traditional one-step icing algorithm will be detailed in Section 2.3. The key stage of this algorithm is the ice calculation procedure. The different methods developed over the years will be reviewed in Section 2.4 to determine which of the icing parameters are likely to vary during the calculation, affect the accuracy of the simulation and should be included in multi-step procedures. This review concludes with a description of existing multi-step algorithms in Section 2.5.

2.2 Icing Hazard

Icing occurs in cold and wet situations on the ground or during a flight. The characteristics of the phenomenon will now be presented in both ground and in-flight situations.

2.2.1 Ground Icing Problem

Icing occurring on the ground does not constitute an immediate threat for an immobilised aircraft but there might be a high price to pay afterwards. Situations leading to ground icing include the following [20]:

- Ice may grow when the plane is on the ground in cold and wet conditions or during freezing rain,
- Aircraft moving in slush along taxiways or runways can also encounter a surface contamination, even if precipitation has stopped [3],
- When an airplane has been flying in cold conditions for a while, the fuel stored in the wings can be at temperatures below freezing. In this case, ice may form on the wings while the aircraft is on the ground, even if the ambient temperature is above 0^oC [18, 37].

The consequences of ground icing become quite clear when the aircrafts start moving:

- Engine inlets, propeller blades and instrument orifices can be covered with ice. Airspeed, pressure and altitude measurement instrumentation may be affected and problems can subsequently lead to the loss of control or navigation errors.
- Ice builds up on the wing or tail areas of an aircraft. If this layer is not removed before take off, the accreted ice modifies the aerodynamics and the aircraft may not be able to climb up to cruise altitude and unwanted descent, pitch, or roll can be encountered shortly after take off.

To overcome the difficulties due to ground icing and limit the associated risks, anti-icing fluids may be applied. This kind of treatment is common [11] but only effective for a limited period, known as the holdover time [38]. Regulation therefore requires a visual inspection five minutes prior to take off, even when the aircraft has been treated with such fluids.

Ground icing situations are easier to deal with than in-flight icing problems where a visual inspection is not always an easy task to perform and direct removal is impossible. This problem will now be discussed.

2.2.2 In-flight Icing Problem

When an aircraft flies through clouds at a temperature below freezing, ice contamination is likely to develop on unprotected surfaces, particularly on the wings and engine inlets. Ice can also appear when the ambient temperature is above freezing. In this case, as already mentioned, icing is due to the very cold temperature of the fuel stored in the wings [37]. Any impinging droplet is then likely to freeze when hitting the wing surface. This accretion will affect the control, stability and aerodynamic performances of the aircraft [16, 20, 39, 40]. Airflow disruption will reduce the maximum lift coefficient and will increase the drag, which can therefore seriously jeopardize the flight safety.

When an aircraft flies through clouds, three key parameters govern the ice growth: the liquid water content (LWC), the exposure time and the size of the droplets. The liquid water content is defined as the mass of water in a given unit volume of cloud. The greater the liquid water content in a cloud, the higher the water flux impinging on the surface and the greater the rate of ice accretion [8]. The ice growth obviously depends on the exposure time. The duration of the encounter with icing conditions varies with the extent of the cloud, aircraft airspeed and pilot awareness. Short exposure times clearly reduce the ice growth.

Stratiform and cumuliform clouds can lead to icing conditions. Stratiform clouds have an horizontal extent up to 300 km, located at altitudes close to 1.5 km and have a liquid water content ranging from 0.1 g/m^3 to 0.8 g/m^3. Cumuliform clouds cause intermittent icing conditions and may be found at altitudes below two kilometers. They extend vertically for up to 17 km, horizontally for up to 10 km and the liquid water content usually ranges between 0.1 g/m^3 to 3 g/m^3 [41]. The size of the droplets inside the cloud influences the ice accretion significantly. Large droplets are more likely to hit the aircraft than smaller ones that may be easily carried away by the air flow [16]. Droplet diameters usually vary from 10 to 50 μm in both stratiform and cumuliform clouds.

Icing is then likely to be more serious in cumuliform clouds where the liquid water content is high and the hazard can occur in a short time. However, due to their great horizontal extent, stratiform clouds can also generate serious icing situations.

In order to classify in-flight icing conditions, four icing severity levels have been defined [11, 12]:

- ***trace***: Ice becomes visible but there is no immediate need to activate deicing or anti-icing devices. However, ice protection systems may be necessary when accumulation is encountered for more than one hour.
- ***light***: The rate of accumulation may create a problem if the flight is prolonged in this environment over one hour. The occasional use of deicing/anti-icing equipment to remove/prevent accumulation may be necessary. Relatively minor performance degradation may become noticeable as the ice accretion continues.
- ***moderate***: The rate of accumulation is such that even a short encounter becomes potentially hazardous and the use of deicing and anti-icing equipment or diversion is necessary. Performance degradation becomes noticeable with

the ice growth. The exposure time should not exceed 45 minutes for aircraft with ice protection systems.

- ***severe or heavy***: The rate of accumulation is such that deicing and anti-icing equipment fails to reduce or control the hazard. An immediate flight diversion is necessary. Severe icing results in an aircraft that is not controllable and can lead to structural damage from shed ice.

Severity of icing is a combination of the state of the icing environment, the aircraft's response and the pilot assessment of the response. To deal with icing situations, the pilot must constantly monitor current weather conditions along his intended path of flight and must be alert to any conditions that could lead to icing. Light icing is the most frequent severity, responsible of 60-70% of the icing reports and severe icing is reported in only a few cases.

When droplets impinge on a surface during the flight, they may produce different types of ice. This is highly dependent on the atmospheric conditions as will now be detailed.

2.2.3 Ice Accretion Types

When the temperature is below freezing, $T < 0^oC$, the droplets composing a cloud may still be liquid. When an aircraft flies through such a cloud, the resulting ice accretion depends on the size of the droplets as shown in Figure 2.1. These droplets, known as supercooled droplets, have a temperature typically between -30^oC and 0^oC. They are in an unstable state and freeze totally or partially when they hit the surface. The ice layer is significantly more extended and thicker for larger droplets.

Supercooled droplets are typically small with an average mean diameter usually between 10 and 20 μm and up to 50 μm [18]. As the droplets size increases, the droplet inertia increases and droplet impingement moves further back on the airfoil surface [18, 43]. When they become large, droplets present the most hazards to the aircraft as they can flow and freeze in areas where no ice protection system is present. The supercooled large droplets with a diameters greater than 50 μm occur during freezing drizzle (less than 0.5 mm in diameter) and freezing rain (greater than 0.5 mm in diameter) [44].

Depending on the operating conditions, supercooled droplets will turn either into rime or glaze ice which are the most common types encountered by an aircraft.

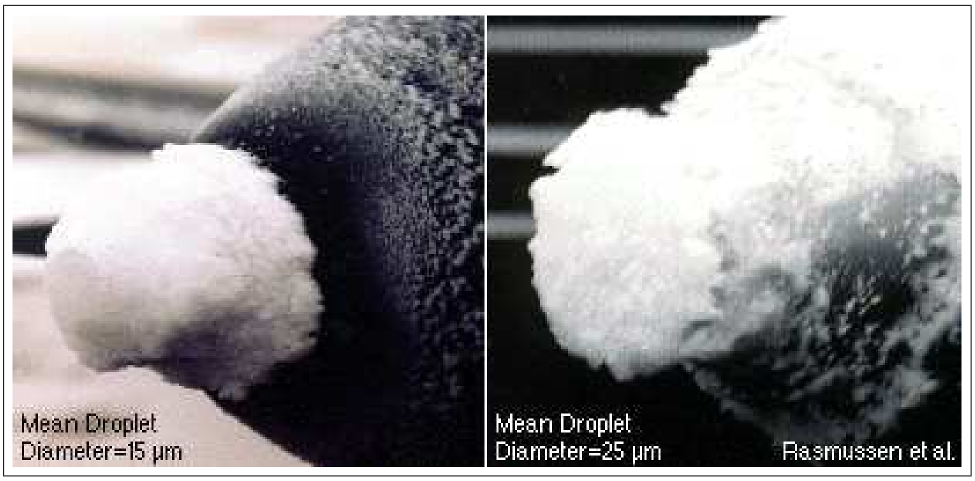

Figure 2.1: *Influence of the droplet size on the ice accretion. Picture from Rasmussen et al. [42]*

Rime Ice

Rime ice usually occurs in stratiform clouds at temperatures ranging from -30^oC to -15^oC. This type of ice forms when tiny supercooled droplets impinge on the surface. In these conditions, all supercooled droplets hitting the plane surface freeze due to the convective heat transfer [45]. Airspeed and liquid water content are relatively low [20] and the density associated with rime ice is typically equal to $\rho = 880\ kg/m^3$. Rime ice is opaque, associated with small surface roughness [46] and is the most common type of ice. As the freezing process is very fast, the ice build-up contains air pockets trapped inside. The irregular texture reduces the aerodynamic efficiency of the aircraft. Rime ice is considered the least hazardous type of accretion and represents 75% of icing reports [47]. This situation is quite different with glaze ice.

Glaze Ice

Glaze ice, also known as clear ice, occurs in cumuliform clouds for temperatures ranging from -10^oC to 0^oC and in freezing rain, at temperatures lower than 0^oC. It is associated with large supercooled water droplets that hit the wing surface, generally at high velocity and high liquid water content. In glaze ice type conditions, the heat transfer is insufficient to freeze all of the impinging water. The supercooled droplets only freeze partially when they hit the aircraft and a substantial fraction may remain liquid and run back over the wing surface [22]. In the end, the resulting water freezes in downstream regions. The water film formed by these droplets influences the ice shape [48, 49] due to its effect of redistributing the impinging water mass. In the vicinity of the stagnation point, the flow tends to be a thin film, whereas the water separates into streams or rivulets near the impingement limits [49, 50]. The density for glaze ice is typically equal to $\rho = 917\ kg/m^3$ [20], which is higher than the rime ice density. It is associated with large surface roughness, mainly influenced by the airflow temperature [14]. It takes a clear, dense or solid appearance and can be more cohesive and harder to break than rime ice. Due to the slow formation process, no air bubbles are entrapped during the accretion and because of its texture and color, glaze ice can be hard to see from inside the cockpit of the aircraft. A pilot may be unaware of the ice build-up, leading to a situation that can induce a serious threat to the flight safety. Glaze ice is more hazardous than rime icing as its shape and structure can perturb the surrounding airflow, significantly. A typical double horn ice shape can grow around the stagnation line as shown in Figure 2.2. This can cause severe aerodynamic penalties, more important than for rime icing. Glaze ice is responsible for about 10% of icing reports [47].

Figure 2.2: *Glaze ice accretion. Typical double horn ice shape. Picture from Purvis et al. [51].*

Mixed Ice

An aircraft may also encounter a mixture of both rime and glaze ice at the same time, this is known as mixed ice or cloudy ice [8]. This type of ice forms due to variations of temperature, liquid water content and droplet size. Glaze ice forms next to the stagnation point where the airflow is laminar while rime ice builds up further downstream, where the flow is turbulent [22, 45], and forms feather-like shaped patterns known as rime feathers, see Figure 2.3. Mixed ice is the most serious type of icing: it has the weight of rime ice and disturbs the flow like glaze ice. Mixed ice represents about 15% of the icing reports [47].

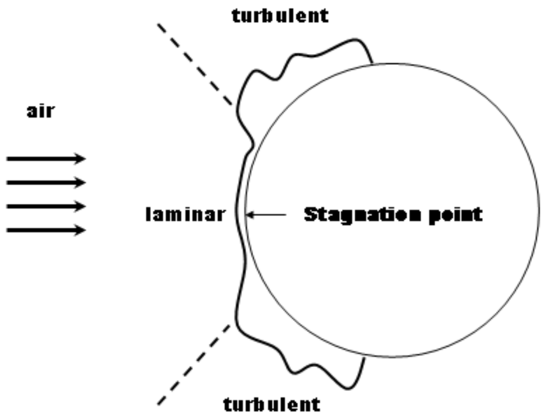

Figure 2.3: *Mixed ice type accretion on a cylinder. Glaze ice is present near the stagnation point where the flow is laminar and rime ice further downstream, where the flow is turbulent.*

Conclusion

Rime, glaze and mixed ice will be the only ice types considered in the present study since they are the most commonly encountered. All three can cause severe aerodynamic penalties and are mainly influenced by the airflow temperature.

Rime ice is nowadays reasonably well understood and can be reproduced almost accurately. However, some of the important physical phenomena associated with glaze ice type accretions are still not clearly understood [52]. Many factors will influence the accretion and will therefore have to be accounted for in the predictions. They will have to be included in the icing algorithms that will now be studied.

2.3 Structure of an Ice Prediction Code

Computer based software are the most adequate and cost effective tools to study icing. They have the capacity to simulate complex geometry, reproduce in-flight conditions and can be run as many times as required. A number of codes have been developed to simulate icing. Their structure and the models they use will now be analysed.

2.3.1 Icing Codes

Over the years, numerous computer codes have been created. They are nowadays widely used to aid design and certification work in the aircraft industry. Aircraft icing analysis methods were initially developed by the NASA Lewis Center in the United States [22, 53], the Defence Evaluation and Research Agency (DERA), now QinetiQ [23] in the United Kingdom and the Office National d'Etudes et de Recherches Aérospatiales (ONERA) [24, 54] in France. The ice accretion prediction codes were named LEWICE, TRAJICE and ONERA Icing code, respectively. Other codes appeared later, for instance, from the Centro Italiano Ricerche Aerospaziali (CIRA [25] in Italy), from the Ecole Polytechnique de Montreal (CANICE [26] in Canada), from Newmerical Technologies International [55] (FENSAP [27, 56] in Montreal) and from Boeing and the University of Washington [57] in the United States. These codes are based on the icing model developed by Messinger [28]. New codes are being developed, based on alternative icing models. A example is the ICECREMO ice accretion/runback water code [32], born from the collaboration between the leading aeronautical companies in the United Kingdom.

Icing codes are generally split into four parts [52, 53]. The flow around the body is determined in the first place, using computational fluid dynamics techniques. Supercooled droplets trajectories are then evaluated to obtain the quantity of water that impinges on the substrate. This parameter is known as the collection efficiency, also named catch efficiency. During the third stage, the collection efficiency and the heat transfer coefficient (HTC) are calculated. Finally, a thermal analysis of the air-water-body system is performed to determine the ice growth. The structure of a typical ice prediction code may be summarized as:

1. Solve for the air-flow around the body,
2. Study the droplet trajectories to evaluate the catch,
3. Calculate physical parameters influencing the ice accretion,
4. Perform a thermal analysis to determine the ice accretion.

This algorithm is the base of what is known as a single-step method: the physical parameters are calculated at the start of the simulation on the clean un-iced airfoil and they remain constant during the entire calculation. The different stages of this icing algorithm will now be analysed briefly.

2.3.2 Airflow Calculation and Droplet Trajectories

Solving for the flow around the considered geometry is the first step in any icing code. This first stage using grid-based CFD methods may be divided in two major tasks:

- Generate a mesh on which the flow solution will be calculated,
- Solve the equations governing the flow.

Once this has been done, the droplet trajectories may be simulated.

Mesh Generation

Prior to the flow calculation, a solution grid has to be defined, generally via a mesh generator. This stage is rather important as it will influence the accuracy of the flow solution and consequently quality of the ice prediction. Mesh generation tools may be stand-alone applications or part of a larger pre-processing suite. In the aeronautical industry, mesh generators are often created "in-house" to allow an easier development and control than with commercial mesh generators. In the present work, the mesh is generated from a commercial package, the well-established industry standard GAMBIT, part of the FLUENT suite [58, 59].

Two types of mesh can be generated: *structured* and *unstructured*. A structured mesh can be recognized by all interior nodes of the mesh having an equal number of adjacent elements. The mesh generated by a structured grid generator is typically made of quadrilateral or hexahedral cells. Unstructured mesh generation, on the other hand, allows any number of elements to meet at a single node. Triangular and tetrahedral meshes are most common when referring to unstructured meshing. The predominant advantage of an unstructured grid is its flexibility for complex geometric domains [60]. However, unstructured meshes require much more computational memory in comparison to structured grids. This may be problematic on slow computers or when generating complex 3-D shapes. For the present studies, both structured and unstructured meshes are generated and used in the simulations to determine the flow past the ice covered bodies.

Aerodynamic Flow

The aerodynamic flow around the body is required to determine some of the parameters required for icing calculations or the trajectories of the supercooled droplets and the impingement limits. Typically, two methods are used in the current ice accretion codes to solve for the flow: the inviscid panel (incompressible potential) approach and a method based on a spatial grid around the body such as a Navier-Stokes approach.

The inviscid panel method is used in both the American and British codes, LEWICE and TRAJICE. In this case, viscosity is neglected. Accuracy may be lost when calculating the flow field around the considered surface and this may lead to large errors due to flow separation [18, 24, 61, 62].

Solving the Navier-Stokes equations may be time consuming but it leads to more accurate results around the iced geometry. Attempts have been performed to replace a compressible Navier-Stokes solver by an incompressible solver for low Mach number flows. Incompressible flow solvers considerably reduce the computing time. However, when comparing the output obtained with compressible and incompressible flow solution, the method only shows good agreement in rime ice conditions. This approach is not adapted to glaze ice conditions associated with large surface deformations [57]. In the present thesis, the flow around clean and iced bodies is obtained using the flow solver FLUENT and the Navier-Stokes equations are solved with the air modelled as a compressible perfect gas.

Droplet Trajectories

When an aircraft flies through a cloud, the small droplets will be swept around the airframe, following the airflow streamlines [63]. In this case, the impingement limits is rather small, this corresponds to the location on the body beyond which no droplet hits the surface. This situation is typical of a rime ice type regime. On the other hand [18, 19, 63], in a glaze ice regime, larger droplets will tend to reach the surface more easily: the impingement limits will become larger and icing will occur further downstream.

Depending on the atmospheric and icing conditions, the flow around the body will affect physical parameters, which in return will influence the surrounding airflow. These parameters are now described.

2.3.3 Physical Parameters

Once the airflow has been calculated around the surface, key flow dependent parameters for the icing calculation may be evaluated: collection efficiency and heat transfer coefficient. In the one step algorithm, when each algorithm component is performed only once, these parameters are determined on the clean body prior to the ice simulation and remain constant in time throughout the calculation.

Collection Efficiency

The amount of supercooled water droplets hitting the surface is defined as the product of liquid water content (LWC), free stream velocity and the collection or catch efficiency β. For two-dimensional studies, this parameter is defined as the ratio of the mass flux through a surface in the upstream flow and the mass flux of the corresponding surface on the body, as represented on Figure 2.4.

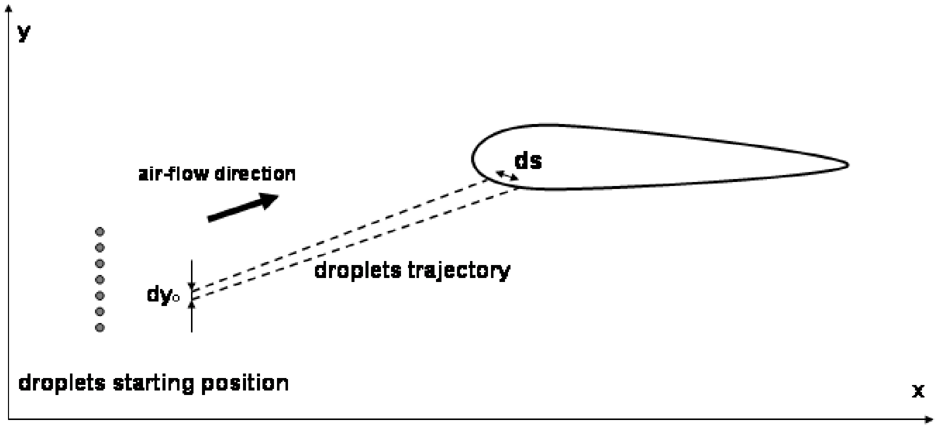

Figure 2.4: *Local collection efficiency.*

For two dimensional studies [52, 64], the local collection efficiency can be written as:

$$\beta = \frac{dy_o}{ds} \ ,$$

where dy_o is the distance between two droplets in the free stream and ds is the distance along the body surface between the impact locations of the same two droplets. For three dimensional geometries, the definition is modified and four trajectories are usually used to define a surface and extend the definition [16, 19].

Numerically, the droplets are launched sufficiently far away upstream from the studied geometry so that initial velocity conditions can correctly be defined. The collection efficiency is then calculated using the initial and final points of trajectories of droplets hitting the considered surface.

Heat Transfer Coefficient

The ice growth rate is determined using an energy balance involving the temperature inside the ice and potential water layers. At the interface with the air, the heat flux is defined as the product of the temperature gap $(T_w - T_\infty)$ and the heat transfer coefficient h_c [65, 66]:

$$Q_h = -k_f \left.\frac{\partial T}{\partial n}\right|_w = h_c(T_w - T_\infty), \tag{2.3.1}$$

where $\partial T/\partial n$ denotes the gradient in the direction normal to the wall, k_f the thermal conductivity of the ice, T_w and T_∞ the temperatures at the wall and in the airflow, respectively.

Differences, sometimes important, between predicted and measured ice shapes are often thought to be due to the inaccuracies in modeling the heat transfer coefficient h_c [67]. This local quantity will depend on the chord length, airspeed, incidence or angle of attack, pressure and temperature [68]. It can only be determined with precision when the CFD grid is sufficiently refined close to the surface to accurately represent the wall temperature gradient. The heat transfer coefficient may be calculated using two different methods:

- Theoretically using an Integral Boundary Layer (IBL) calculation which takes into account the roughness due to ice deposit [69, 70, 71, 72].
- Via empirical correlations, where the local roughness is considered through an equivalent sand grain roughness [73]. In this case, the transition from laminar to turbulent location [16, 74, 75] is usually based on the roughness-based Reynolds number Re_k.

The correlation-based approach has significant advantages in terms of computational facility and usually provides better results than theoretical solutions [23, 75]. As there can be significant variations in surface temperature in the vicinity of the roughness element, turbulence may not immediately occur when the Re_k threshold for transition between laminar and turbulent is reached [76, 77]. In addition, theoretical and empirical methods are not always suitable for glaze ice studies, when a water film is present on the ice layer. In this case, the heat transfer coefficient is difficult to obtain with accuracy as the film influences the heat transfer between the air and the surface [18].

For the results obtained using ICECREMO1, the heat transfer coefficient is provided by the CFD software FLUENT and is based on the standard “wall functions” that use semi-empirical formulas [78]. Correlations will not be used to generate the results calculated with ICECREMO2. The heat transfer coefficient is obtained via a module, based on the integral boundary layer, already implemented in the ice prediction code.

2.3.4 Conclusion

In this section, the structure of an icing code has been presented. The first steps of the algorithms have been detailed and typical procedures were introduced. These different steps will have to be repeated several times during a multi-step algorithm. Flow dependent parameters so far are the collection efficiency and the heat transfer coefficient. The most important part of the icing algorithm is the icing module itself and it will also have to be included in a multi-step loop. Two models are available to evaluate the ice growth rate: the Messinger model and the Stefan model. They are based on a mass and energy balance and will now be detailed.

2.4 Energy and Mass Balances

The thermodynamic and mass balances are the centre of an icing calculation. Most of the codes rely on the Messinger approach [19, 28, 52] to evaluate the heat and mass balance and subsequently the ice growth rate. This model will be described in Section 2.4.1 and its limitations will be pointed out. To tackle the remaining problems, several researchers improved Messinger's derivation [53] or based their approach on the Stefan phase change problem [29, 79]. The Stefan approach will be discussed in Section 2.4.2. In all cases, the flow dependent parameters that should be included in a multi-step algorithm will be pointed out.

2.4.1 Messinger Approach

The model developed by Messinger [28] is the base of numerous icing codes [22, 25, 27, 80, 81]. This approach rely on a heat flow balance on a surface assumed to be at freezing temperature. The typical configuration of the Messinger model is shown in Figure 2.5.

The energy balance is studied on control volumes between the energy losses and gains. The main heat fluxes are the energy losses by evaporation/sublimation Q_e, convection Q_h, the sensible and latent heat Q_{sl}, the kinetic energy gained from the air Q_a, from the impacting water Q_k and the radiative heat flux Q_{rad}. Conduction through the ice Q_c may remove or add heat [48]. Balancing all these terms yields:

$$Q_c + Q_e + Q_h + Q_{sl} - Q_a - Q_k - Q_{rad} = 0 \tag{2.4.1}$$

Three Messinger-based ice prediction codes: LEWICE [22, 82, 83], the ONERA icing code [24, 54, 80] and TRAJICE [16, 23] will be presented. For the sake of clarity, the energy balance implemented in Messinger-based codes such as CANICE

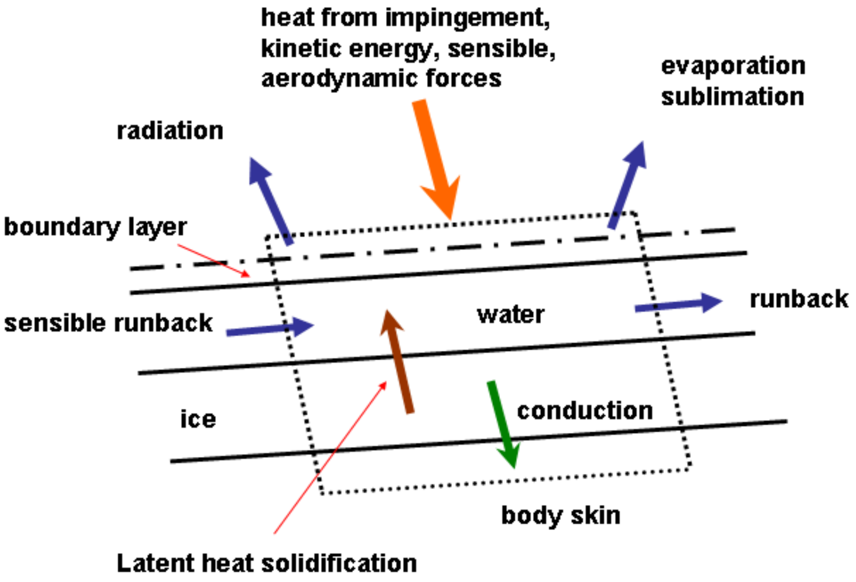

Figure 2.5: *Energy balance in a control volume.*

[84], CIRA Icing Code [25], BUWICE [57] or FENSAP [27] are not detailed in the present document. Each icing code uses its own energy balance. However, they comprise a great number of similar terms, see Table 2.1.

	LEWICE	ONERA	TRAJICE
Q_e	X	X	X
Q_h	X	X	X
Q_c	X		
Q_k	X		X
Q_a	X		X
Q_{sl}	X	X	X
Q_{rad}		X	

Table 2.1: *Energy terms in the main Messinger-based icing codes.*

Most of the terms in LEWICE, TRAJICE and the ONERA icing code are similar. However, as the icing codes are evolving, small differences might be introduced in their formulation.

Convection and air kinetic heating

The heat loss due to convection, also known as Newton's law of cooling, is the product of the temperature difference between the surface and the airflow and the heat transfer coefficient. The airflow temperature is sometimes replaced by the recovery temperature to include the effects of the air compressibility [16, 80]. The kinetic heat gain due to the air is also determined via the recovery and the surface temperature. Convective heat flux and air kinetic heating terms are therefore sometimes combined in one single formulation as in TRAJICE [16]:

$$Q_h - Q_a = h_c(T_s - T_r) \ .$$

The heat transfer coefficient h_c varies significantly with the flow around the surface, in the boundary layer: it should therefore be recalculated during a multi-stepping algorithm.

Evaporation / sublimation

Evaporation appears when the surface is wet whereas sublimation occurs when the surface is “dry ”. Sublimation terms are therefore sometimes accounted for in the energy balance instead of the evaporation term. The heat loss due to the evaporation of the water on the surface is function of the latent heat of evaporation L_v and is proportional to the mass flux of the water that evaporates $\dot{m}_e$:

$$Q_e = \dot{m}_e L_v \ .$$

This mass flux of evaporation is function of the temperatures and pressures on the surface and in the surrounding airflow, written for TRAJICE as [16, 85]:

$$\dot{m}_e = \frac{0.622 h_c}{c_a P_T L_e^{2/3}} \left[e_s \left(\frac{T_T}{T_s} \right) \left(\frac{P_L}{P_T} \right)^{-\frac{1}{\gamma}} - e_\infty \left(\frac{P_T}{P_\infty} \right) \right] \ ,$$

where the notation is defined in the Nomenclature section and the subscripts L and T indicate local and total properties. The subscripts ∞ and s indicate properties in the freestream and on the surface, respectively. The term e stands for the water vapor pressure and Le represents the Lewis number, which is the ratio of thermal diffusivity to mass diffusivity.

The heat transfer coefficient and the pressure are involved in this energy term. The effect of the surface pressure on the ice profile is small and may be neglected in standard icing conditions [23]. However, the heat transfer coefficient should vary in the flow and be recomputed in a multi-stepping procedure.

Kinetic energy from droplets

Due to the impinging water, the system gains energy. The droplets release kinetic energy when they hit the surface as their velocity suddenly drops to zero.

$$Q_k = \frac{1}{2}\beta(LWC)V_\infty^3 = \dot{m}_{imp}\frac{V_\infty^2}{2} \ ,$$

where LWC is the liquid water content and V_∞ indicates the free stream air velocity. This kinetic energy is dependent on impinging water mass flux $\dot{m}_{imp}$, proportional to the collection efficiency β: this parameter must be recalculated in a multi-stepping algorithm.

Conduction

The conduction term is function of the thermal conductivity of the ice and is proportional to the difference between the recovery temperature and the surface temperature. None of the constants involved are flow dependent.

In TRAJICE and the ONERA code, the conduction term is not accounted for, the body surface being considered adiabatic.

Radiative heat

The heat flux due to radiation is proportional to the fourth order temperature difference between the airflow and the surface. As compressibility affects the temperature of the air around the solid surface, the air temperature may be approximated by the recovery temperature in the vicinity of the substrate [34, 35, 85, 86]. According to Hedde [80], the radiative heat flux can be negligible when studying the ice accretion on aircrafts, where the liquid water content is generally much higher than $0.1 g/m^3$. When the liquid water content is less than this value, the radiative heat flux still can be neglected since it represents less than 1% of the heat exchanges. Here again, the constants involved are not flow dependent: none of them should be recalculated in a multi-stepping algorithm.

Sensible and latent heat

Sensible heat is released by the supercooled droplets when they hit the surface and gained by the ice/water layer. This only depends on droplets temperature and surface temperature. Latent heat is the energy released when water turns into ice. Three situations can be encountered when studying the ice accretion phenomenon:

1. All the impinging droplets freeze and rime ice type grows. Sensible heat is lost to the system when the water reaches the freezing temperature and latent heat is gained during the liquid/solid phase change.
2. Only part of the incoming water freezes and glaze ice grows. The latent heat released when the droplets turn into ice is used as sensible heat to warm up the liquid phase at the freezing temperature.
3. The impinging droplets and running back water always remain liquid. There is only sensible released by the impinging droplets when they reach the surface.

In the Messinger model, the sensible and latent heat is usually expressed using the freezing fraction denoted F, which represents the fraction of water that turns into ice. F is calculated using the energy balance (2.4.1), assuming the surface temperature is equal to the freezing temperature $T_s = 0^oC$. The freezing fraction F must be in the range $0 \leq F \leq 1$. In practice it can be estimated outside these limits [29, 35]. The value obtained is then tested to ensure it is physically realistic and when necessary, the surface temperature is recalculated via the energy balance. Three cases are possible [16]:

- The calculation returns a value less than 0: the surface temperature is above freezing. All the incoming droplets remain in a liquid state. The freezing fraction is then held equal to $F = 0$ and the surface temperature is recalculated using the energy balance.
- The freezing fraction obtained is located in the range $0 \leq F \leq 1$: only one part of the incoming fluid freezes while the other part remains liquid. If $F = 1$, rime ice appears and if the freezing fraction is close to $F = 0$, glaze icing occurs. The freezing fraction value is then used in subsequent calculations.
- The calculation returns a freezing fraction greater than 1: the surface temperature is below freezing. Only rime ice will occur. In this case, the freezing fraction is taken equal to 1 and the surface temperature recalculated.

The freezing fraction F is held constant during the calculation and is not time-dependent since none of the terms are in Equation 2.4.1. It should be recalculated at each stage of a multi-step algorithm and would vary as a consequence of the highlighted flow dependent parameters: the collection efficiency and the heat transfer coefficient.

When solving the global energy balance in Messinger-based codes, two unknowns are determined: the surface temperature and the freezing fraction. When their value is evaluated, a mass balance may be written to determine the ice growth ratio.

Mass Balance

When the energy balance is solved, a mass balance may be performed. This determines the mass flux of water leaving the control volume due to freezing and the mass flux of the run-back water, see Figure 2.6.

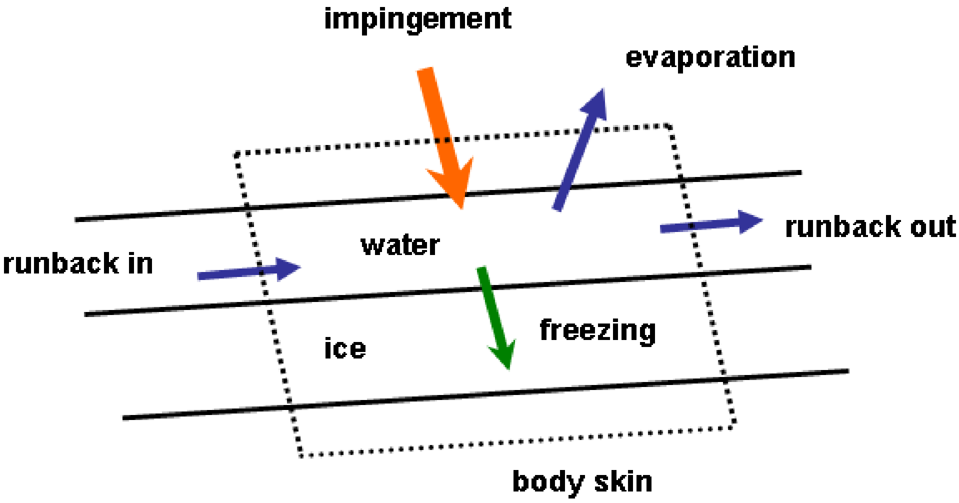

Figure 2.6: Mass balance in a control volume.

A typical mass balance is written as follows [25, 52, 64, 80]:

$$\dot{m}_{imp} + \dot{m}_{r,in} = \dot{m}_{r,out} + \dot{m}_i + \dot{m}_e \ , \tag{2.4.2}$$

where the quantities $\dot{m}_{imp}$, $\dot{m}_{r,in}$, $\dot{m}_{r,out}$, $\dot{m}_i$, $\dot{m}_e$ represent the mass flow rates of incoming water from the impingement of the supercooled droplets which is proportional to the collection efficiency, the run-back water from the upstream to the downstream control volume and the water leaving this control volume due to freezing and evaporation, respectively.

The mass flux of the water that leaves the control volume due to freeze out, can be written as [52, 64]:

$$\dot{m}_i = F(\dot{m}_{imp} + \dot{m}_{r,in}) \ , \tag{2.4.3}$$

or

$$\dot{m}_i = F(\dot{m}_{imp} + \dot{m}_{r,in} - \dot{m}_e) \ , \tag{2.4.4}$$

if the evaporative mass flux is taken into account [87]. Calculations on the upstream control volume will determine $\dot{m}_{r,in}$, first estimated at the surface leading edge, where the water flux is zero and all terms in the mass balance are now determined

When considering the mass balance (2.4.2), all the water which does not freeze in a control volume is supposed to run back in the next control volume [18]. No water layer is therefore allowed to remain in any control volume. This situation is not in agreement with experimental observations. In addition, as stated in [35], the water flow is highly dependent on the size of the control volume, which is a "*choice made in the numerical model and has no physical meaning*". The water flow behaviour can therefore not be modelled accurately in the Messinger model.

Limitations of the Messinger Model

The Messinger model provides a complete model to study the ice growth phenomenon. The constants involved in the governing equations are mostly flow independent apart from the collection efficiency and the heat transfer coefficient. However, physically unrealistic phenomena arise from Messinger's approach [29].

- The conduction term is not accounted for in the energy balance. Ice and water layers are assumed to be isothermal and the substrate insulated. The ice growth is assumed identical on both a clean surface and a surface covered with a thick ice layer. The accretion is therefore not affected by the existing ice shape.
- The transient behaviour of ice accretion is not correctly evaluated since the decrease of the freezing fraction is not continuous at the transition between rime and glaze ice. This freezing fraction may be expressed as function of constant parameters, which are assumed to be constant during the ice calculation. However, these icing parameters are likely to evolve with the accretion.
- The water movement is not described accurately. When modeling, all the water which does not freeze in a control volume is assumed to move to the following control volume. No water is then allowed to remain in this control volume at the end of each iteration.

Codes and models based on Messinger sometimes try to improve the evaluation of the different heat terms [22]. However, these evaluations remain incomplete as the water film layer on top of the ice layer is not accounted for. A new and more realistic model will now be presented. This model, based on a Stefan approach, incorporates the contribution of the water film in the thermodynamics of the problem.

2.4.2 Stefan Approach

Evidence of liquid water on top of the ice surface has been shown through many icing experiments at mild temperatures [30, 31, 45, 88]. The movement of this fluid layer may be modelled using the Navier Stokes equations, simplified using lubrication theory [29, 35, 89, 90, 91, 92]. A key assumption used in the Messinger model is then not valid any more: water may remain in any control volume and consequently the freezing fraction F may not be determined. The energy balance of the Messinger model is therefore replaced by a Stefan condition applied at the moving ice-water boundary to determine the ice growth rate [48, 89, 93]. The model described in this section, developed by Myers et al. [29, 35, 48, 94], is currently implemented in the ice prediction code ICECREMO [32, 95, 96, 97].

Fluid Flow

The governing equation for the fluid flow is derived from the Navier-Stokes equations. As the water film on top of the ice layer is thin, a full resolution of this set of equations is not necessary: the lubrication theory can be applied [35, 48, 94]. The square of

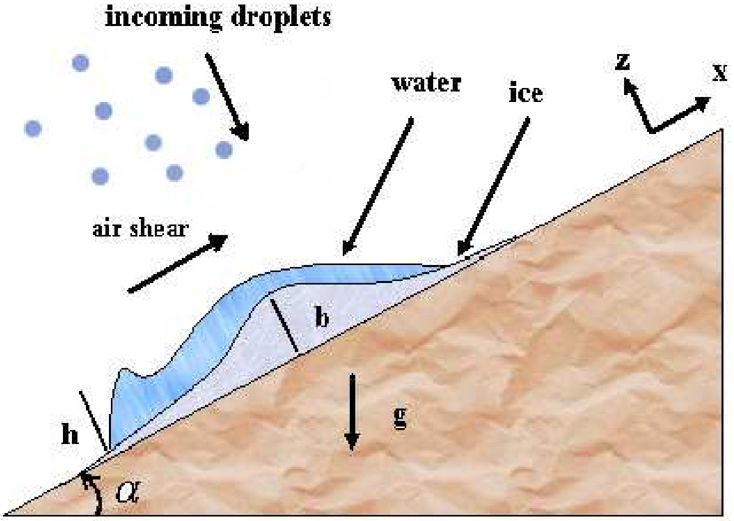

Figure 2.7: Problem configuration.

the aspect ratio of the flow ϵ^2, defined as the ratio of typical height and length, and the reduced Reynolds number $\epsilon^2 Re$ are small and all terms with either order of magnitude may be neglected. The first approximation is valid since the film is thin, $\epsilon^2 \ll 1$. The second approximation is valid when the flow regime is laminar or at least not too turbulent, which leads to $\epsilon^2 Re \ll 1$ [98]. This is true for all cases considered in this work.

As the effect of temperature on the viscosity and density of the fluid is relatively small until the sudden solidification change, viscosity and density are taken as constant for the flow calculation [94].

A Cartesian coordinate system is defined as shown in Figure 2.7, where x and y axis represent the substrate and z the direction normal to this substrate. In the following, b stands for the ice height while h stands for the water height.

Based on the previous assumptions, the Navier-Stokes and continuity equations may be simplified and integrated [98]. They directly lead to the following system:

$$\rho_i \frac{\partial b}{\partial t} + \rho_w \left(\frac{\partial h}{\partial t} + \frac{\partial Q_x}{\partial x} + \frac{\partial Q_y}{\partial y} \right) = \rho_a \beta V_\infty \ , \tag{2.4.5}$$

where ρ_i and ρ_w denote the densities of ice and water respectively, $\rho_a \beta V_\infty$ represents the flux of impinging water droplets expressed as the product of the collection efficiency the liquid water content and the free stream velocity. The movement of water is summarised in the flux divergence. The components can be written as:

$$Q_x = \frac{h^3}{3\mu_w} \left[\sigma \frac{\partial^3 h}{\partial x^3} - G_1 - \frac{\partial P_a}{\partial x} \right] + A_1 \frac{h^2}{2\mu_w} \ , \tag{2.4.6}$$

$$Q_y = \frac{h^3}{3\mu_w} \left[\sigma \frac{\partial^3 h}{\partial y^3} - G_2 - \frac{\partial P_a}{\partial y} \right] + A_2 \frac{h^2}{2\mu_w} \ , \tag{2.4.7}$$

where μ_w is the dynamic viscosity of water, σ denotes surface tension, P_a represents the ambient pressure, $(G_1, G_2) = \rho_w g(\hat{\mathbf{g}} \cdot \hat{\mathbf{x}}, \hat{\mathbf{g}} \cdot \hat{\mathbf{y}})$ and (A_1, A_2) are the gravity and shear stress components projected on the x and y directions respectively. The fluid flux terms show that the fluid is driven by ambient pressure, gravity along the surface, shear stress and surface tension. This equation is characteristic of thin film flows [35, 94, 98]. Of all the involved parameters, only two are strongly flow dependent: the collection efficiency as already pointed out, and also the shear stress. They will need to be studied carefully when considering multi-stepping algorithms.

Ice Accretion Rate

Both Messinger and Stefan models are similar for rime studies as all the impinging droplets freeze upon contact with the surface. Using the current formulations, the rime ice growth is directly provided by the mass balance (2.4.5), with the water thickness h and the fluid flux Q set to zero, yielding to:

$$b = \frac{\rho_a}{\rho_i} \beta V_\infty \, t. \tag{2.4.8}$$

When a water film forms on the surface, Equation (2.4.5) needs to be solved. This equation involves two unknowns: the film height h and the ice height b. The ice accretion rate $\partial b/\partial t$ can be determined by considering the thermal problem. An energy balance is performed at the ice-water interface. Most of the terms of the Messinger model can be retrieved in Stefan's approach. The latent heat released when water freezes, is conducted through the ice and water layers. A Stefan phase change condition can be written as:

$$\rho_i L_f \frac{\partial b}{\partial t} = \kappa_i \frac{\partial T}{\partial z} - \kappa_w \frac{\partial \theta}{\partial z} \ , \tag{2.4.9}$$

where T and θ are the temperatures in the ice and water respectively and L_f is the latent heat of fusion. Unlike the Messinger model which assumes an isothermal temperature in the layers, the Stefan condition requires full information on the temperature gradients in each layer and the model is clearly time dependent. The corresponding thermal equations in both layers are [48]:

$$\frac{\partial T}{\partial t} = \frac{\kappa_i}{\rho_i c_i} \frac{\partial^2 T}{\partial z^2} \ , \tag{2.4.10}$$

$$\frac{\partial \theta}{\partial t} = \frac{\kappa_w}{\rho_w c_w} \frac{\partial^2 \theta}{\partial z^2} \ , \tag{2.4.11}$$

where the coefficients κ, ρ and c are respectively the thermal conductivity, density and specific heat in the ice (subscript i) and in the water (subscript w).

A study of order of magnitudes show that time variations may be neglected. The heat equations (2.4.10) and (2.4.11) then reduced to pseudo-steady forms [94]:

$$\frac{\partial^2 T}{\partial z^2} \simeq \frac{\partial^2 \theta}{\partial z^2} \simeq 0. \tag{2.4.12}$$

The ice accretion rate can be evaluated by solving (2.4.12). Temperatures are imposed on the substrate and at the ice-water interface. At the water surface, the flux is imposed by the same energy terms involved in the Messinger model:

$$\kappa_w \frac{\partial \theta}{\partial z}\bigg|_{z=b+h} = -Q_e - Q_h + Q_a + Q_k + Q_{rad} \ , \tag{2.4.13}$$

and the parameters important for multi-stepping algorithms are similar to those pointed out in Messinger's model.

2.4.3 Conclusion

The mass and energy balances (2.4.5) and (2.4.13) provide a complete model for the icing problem. The water height is accounted for, the evaluation of the conduction term is performed in both ice and water layers and the freezing rate is time-dependent. However, the ice accretion is strongly influenced by flow related parameters:

- Collection efficiency,
- Shear stress,
- Heat transfer coefficient.

These parameters usually determined on the clean body remain constant during the accretion time. This procedure can be acceptable for a short icing exposure time or when the impinging water droplets freeze instantaneously upon contact on the body. However, for longer accretion times, the surrounding airflow and associated parameters may change drastically. Being completely time-dependent, they should be recalculated throughout the icing simulation to ensure a better accuracy in the predictions. This approach, known as multi-stepping will be detailed in the next section.

2.5 Multi-Stepping

In current icing studies, the ice growth rate is usually determined using a single-step procedure. The multi-step approach has first been introduced in the Messinger-based codes to deal with the lack of time-dependence in the model [22]. Such a procedure has never completely been tested and validated in a Stefan-based ice accretion code.

A basic attempt to implement a step-by-step algorithm with a Stefan-based model was performed in [35]. However, it mainly focussed on implementing the icing module of the algorithm. The thermal history was not taken into account and the flow dependent parameters were evaluated with empirical formulas. The multi-stepping parameters were also chosen for numerical convenience. A systematic study of the algorithm will be carried out here.

Flow-field data along with the physical parameters listed in the previous section, must (or should) be updated during the icing process in order to obtain a better and more accurate prediction. Two options are associated with a multi-stepping approach: the *step-by-step* and the *predictor-corrector*.

2.5.1 Step-by-Step

Several current ice prediction codes have a capability for step-by-step calculations. LEWICE [22], TRAJICE [23] or other codes based on the same technology such as BUWICE [57], the Da Silveira et al. code [81] are all based on the Messinger approach.

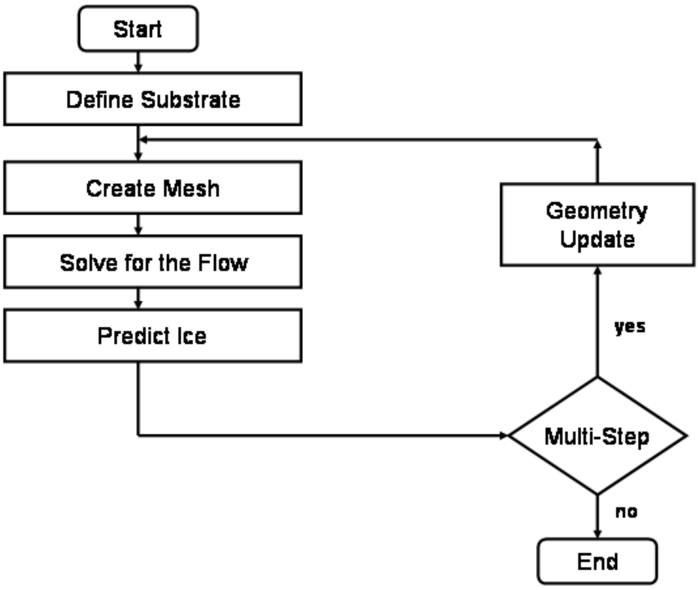

Figure 2.8: *Icing code algorithm.*

In a step-by-step ice calculation, the procedure starts with the flow-field evaluation, droplet impingement and icing parameters determined on the clean un-iced geometry. The ice growth is then calculated by applying the thermodynamic model.

A time increment is specified and an ice growth rate determined for this time increment. The initial geometry is then adjusted to account for the accreted ice and a new flow-field calculation is performed around the iced geometry. This procedure can be repeated again until the specified total icing exposure time is reached. The algorithm relative to this approach is shown on Figure 2.8 . Figure 2.9 represents

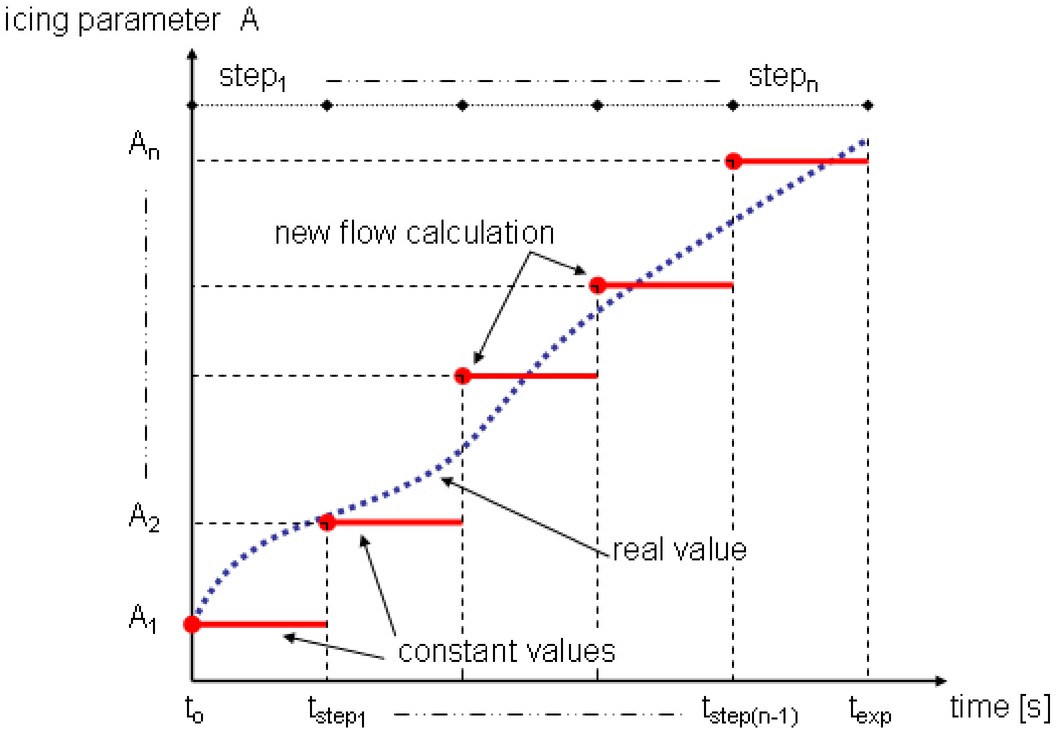

Figure 2.9: *Step-by-step algorithm. The total icing exposure time is divided into a given number of steps. The flow-field and physical parameters are determined at the beginning of each step. An ice prediction is performed with the flow-related parameters held constant during each step.*

the evolution for one of the icing parameter value during the step-by-step procedure. A stands for a physical parameter, for instance the shear stress. The real value, represented by the dashed line is approximated by a succession of steps (short plain segments), where each segment represents the value used during an ice prediction. A_1 stands for the value determined on the clean geometry. A new flow solution is determined after each step, leading to a new calculation of the physical parameters which remain constant during each time increment.

The number of steps required to obtain accurate ice predictions is a key-parameter in a multi-step procedure. According to Gent [23] using a panel method, *"if too few* *steps are used there will be an insufficient allowance for the effect of the ice. However, if too many steps are used, errors due to the limitations in the aerodynamic calculation become significant"*. Eberhardt and Ok [57] have also pointed out the importance of the time-step increment. A very large number of time steps is no guarantee improved results [22]. The whole process could become extremely time consuming and errors committed when estimating flow dependent parameters during each of the steps may pile up and compromise the accuracy gained with the use of a multi-step algorithm [99, 100]. Flow dependent parameters should therefore be calculated with great care.

A trigger criterion for a new flow calculation also needs to be defined with care. The most common one used in the icing codes is based on time. The total icing exposure time is usually divided into a given number of equal time increments.

A step-by-step calculation being potentially rather time-consuming, another approach has been developed which aims to approximate the variations of the physical parameters with a reduced number of flow calculations. This procedure is known as the predictor-corrector method and is now detailed.

2.5.2 Predictor-Corrector

The predictor-corrector approach [25, 35, 75, 100] aims to approximate the variation of the physical parameters with only two airflow calculations. This procedure may be summarized as:

- Determine the flow and icing parameters on the clean body (predictor),
- Perform an ice accretion calculation using the "clean" constant value in a single-step procedure,
- Re-calculate the parameters on the iced body (corrector),
- Perform a new ice calculation using time-dependent values determined via an interpolation between the clean and the iced value.

Figure 2.10 shows the evolution for one of the icing parameter value during the predictor-corrector procedure. The real icing parameter, denoted A is represented by the dashed line, as shown in Figure 2.10. In the first stage of the procedure the value A_p, calculated on the ice clean geometry, remains constant during a single-step procedure. This is referred to as the predictor and represented by the horizontal plain line on Figure 2.10. When the corrected value A_c is determined, the icing model is run again for the total icing exposure time t_{exp} using interpolated values from the clean body A_p to the ice covered body A_c.

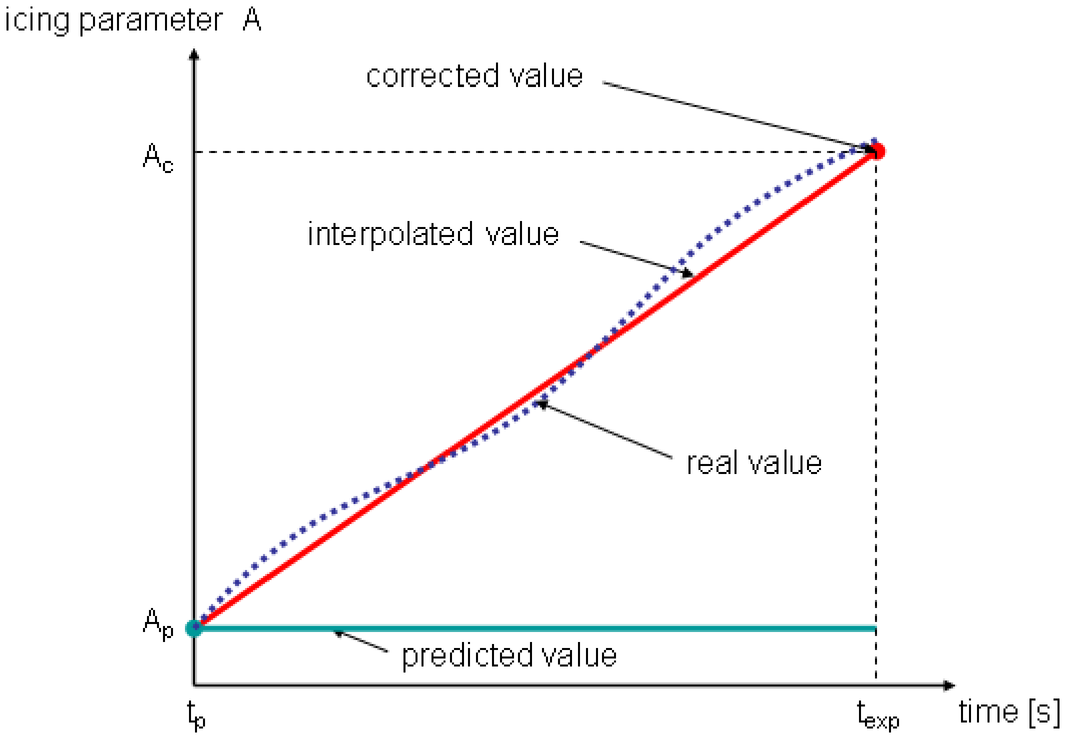

Figure 2.10: *Predictor-Corrector algorithm. Flow data and icing parameters (A_p) are first evaluated on the clean body. An ice calculation is performed using A_p (predictor) constant during a single-step procedure. Flow data and icing parameters are re-evaluated about the iced geometry (A_c), referred to as the corrector. The icing model is run again using interpolated values from the clean to the iced body.*

The advantage of this procedure is to limit the number of new flow field calculations in comparison with the step-by-step approach. In the latter, there are generally more than two flow re-evaluations whereas in a predictor-corrector approach, only two steps are required to obtain the estimated ice shape [100]. This explains that several current ice prediction codes [25, 75, 100] use this approach to evaluate the ice growth rate.

2.6 Conclusion

This chapter has introduced the key-elements necessary for the development of a fully automated multi-stepping procedure. The main ice prediction codes all follow the same pattern:

- Generate a solution grid,
- Solve for the flow and determine the droplet trajectories,
- Determine the physical parameters,
- Study the heat balance and calculate the ice growth ratio.

However, as these codes are most of the time based on the Messinger approach, the accuracy of the final results could be improved. In the present study, a more realistic approach will be adopted, based on a Stefan condition at the water-ice interface.

In order to improve the accuracy in the predictions a multi-step approach has been developed. The idea of the current research work is to study the impact of a fully automated multi-step procedure implemented in a Stefan-based icing code. When applying a multi-step procedure, airflow and physical parameters need to be updated between each step of the procedure. They are:

- Collection efficiency,
- Heat transfer coefficient,
- Shear stress needed for the water film update.

One can also add the surface pressure in the previous list. This parameter is however directly updated with the flow solution.

A multi-stepping approach can be either a step-by-step or a predictor-corrector method. Although both methods are detailed, the present work mainly focuses on the step-by-step procedure. The term multi-stepping therefore usually refers to the step-by-step approach in the following. When confusion is possible, the correct formulation will be specified.

- In the step-by-step approach, the estimation of the number of times the flow-field needs to be re-computed is a key-element and should to be determined with care. A criterion triggering a new flow, either based on time or ice height needs to be investigated. The goal will be to determine which criterion predicts the highest accuracy with a reduced number of flow calculation.
- In a predictor-corrector approach, only two flow calculations are necessary to determine the final estimated ice shape. Icing parameters will be linearly interpolated from their value on the clean body to the ice covered body.

These fully automated procedures will form the first attempt to generate final ice estimations in a Stefan-based ice accretion code with a complete update of flow-related parameters.

The results presented in this thesis are performed with the ice accretion and run-back water code ICECREMO. This Stefan-based ice growth code is presented in Appendix A. The algorithm established for a single step in ICECREMO needs to be adapted to multi-step procedures. This will be detailed in the next chapter.

Chapter 3

Automatic Multi-Stepping Procedure

3.1 Introduction

Nowadays, numerical simulations play a key role in ice accretion predictions. Computational Fluid Dynamics (CFD) systems and codes form tools much less expensive than tunnel and in-flight tests. However despite numerous improvements, their have not reached the required accuracy [101]. Most of the current ice accretion codes are based on a single-step procedure. Key icing parameters are determined on the clean geometry and remain constant during the entire ice calculation. Allowing some time dependence for flow related parameters will increase the accuracy of the ice calculation. This may be achieved through multi-stepping: the parameters are updated several times (or continuously) during the calculation. Basic one-step algorithms may be used to perform multi-step simulations. However this a complex and tedious process, with a lot of room for human error. Therefore, a fully automated procedure is highly desirable.

In this chapter, the practical aspects of an automated algorithm will be considered. As already mentioned, the key steps in an icing calculation are:

- Define the geometry,
- Calculate the flow solution,
- Calculate flow dependent icing parameters,
- Perform the icing calculation

and these four stages may be repeated as many times as necessary when performing a multi-step calculation.

The geometry and CFD aspects of the algorithm are developed using the mesh generator GAMBIT and the corresponding flow solver FLUENT [102]. These softwares are widely used in industry. They also offer a capability to read scripts that will be key in the development of an automated procedure. Any other software presenting similar features would also be eligible for this algorithm development.

The ice calculation will be performed using the aircraft icing code ICECREMO, a complete description of which may be found in Appendix A. Initial tests were carried out using the first version of the code, ICECREMO1, developed on a structured grid. Further tests were conducted using the updated version ICECREMO2 that uses unstructured grids. The automated algorithm is presented for each configuration.

3.2 Creating the Mesh

The accuracy of the icing calculation is strongly related to the accuracy of the flow field around the airfoil. The mesh used to calculate the flow solution should therefore be created very carefully and of course automatically. The characteristics of the mesh are detailed in this section and the automatic procedure will be discussed in the last section of this chapter.

3.2.1 Geometry Description

Aircraft icing codes are mostly tested over cylinders or NACA0012 airfoils. These will be the only shapes considered in this work. A NACA0012 airfoil is shown in Figure 3.1. NACA 4-digit airfoils are defined by a 4-digit code of the form *pmxx* where p and m represent positions reserved for specification of the camber and xx for specification of the thickness-chord ratio as a percentage [103]. For instance, *pm12* designates a 12% thick 4-digit airfoil. This means $t/c = 0.12$ where t denotes the thickness of the airfoil and c is the chord length. A NACA 0012 is therefore a symmetrical airfoil with a thickness-chord ratio equal to $t/c = 12\%$. Ordinates can be determined with the following equation:

$$\frac{y}{c} = a_0\left(\frac{x}{c}\right)^{1/2} + a_1\left(\frac{x}{c}\right) + a_2\left(\frac{x}{c}\right)^2 + a_3\left(\frac{x}{c}\right)^3 + a_4\left(\frac{x}{c}\right)^4 \tag{3.2.1}$$

where

$$a_0 = 0.2969\ ,\ \ a_1 = -0.1260\ ,\ \ a_2 = -0.3516\ ,\ \ a_3 = 0.2843\ ,\ \ a_4 = -0.1015\ .$$

Grid generation around iced aircraft configurations is a crucial problem. Ice shapes can be geometrically complex and the generation of a good global mesh is difficult and time-consuming [104]. A NURBS (Non-Uniform Rational B-Spline) scheme also known as Bézier Spline [105], was applied to generate clean or iced

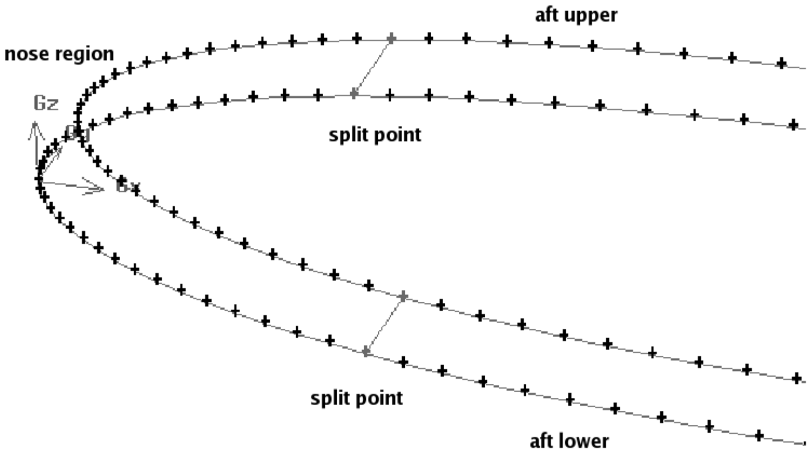

Figure 3.1: *Geometry of the wing (NACA0012 airfoils). The wing surface is split into three parts: the aft upper, aft lower and nose regions defined with a Non-Uniform Rational B-Spline description.*

surface geometries in GAMBIT. The airfoil surface was split into three parts, each surface defined with a NURBS description:

- The aft upper surface,
- The nose region,
- The aft lower surface.

They correspond to the locations on the airfoil described in Figure 3.1. Two split points, function of the airfoil chord length or cylinder diameter, are automatically defined to allow the ice accretion to be contained within the nose region. They are located at about 33% and 66% of the total number of nodes on the geometry, the first point being located at the trailing edge, which is the downstream extremity of the airfoil.

On clean and iced bodies, the surface near the nose region is generated using a higher number of nodes. Typically, in the present study 60 or 80 points were used in this interval, with a concentration increasing progressively towards the leading edge. This automatically adds computer time for the flow solver to obtain a converged solution, but the final flow solution is better described and the ice more accurate. The automated re-meshing must always be successful, even for the jagged surface near the nose. Consequently, the number of nodes needs to be carefully chosen. If too many nodes are used, the automatic re-meshing around the iced body can fail or add consequent computing time without a real benefit on the final ice prediction. On the other hand, if too few nodes are used, the flow solution will be less accurate and the ice shape simulation will be poor.

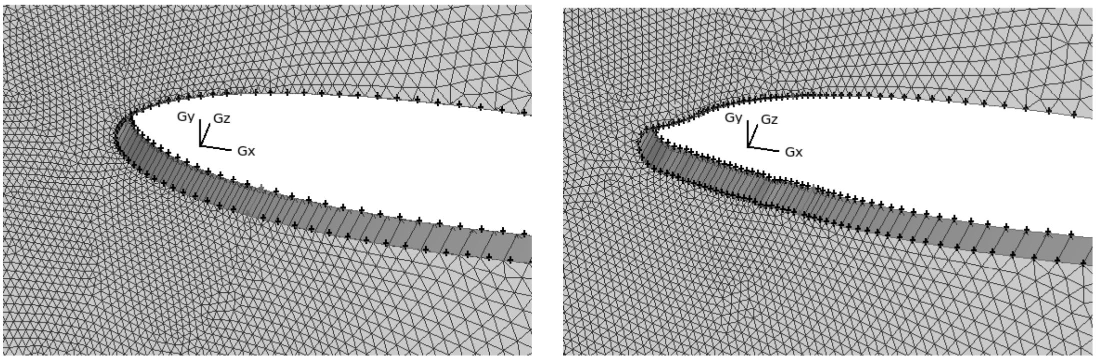

(a) Clean Airfoil (b) Iced Airfoil

Figure 3.2: *Mesh generated around both clean and iced wings (NACA0012 airfoil). The grids, generated for ICECREMO2, are structured on the airfoil surface and hybrid in the external domain volume. The mesh is fine in the vicinity of the leading and coarse away from it.*

Figure 3.2 shows a mesh generated for the current ice accretion code. An identical number of nodes is used on the clean and iced surfaces. The mesh is fine near the leading edge and is progressively coarsened from this region up to the trailing edge. Depending on the icing routine, different types of mesh should be created.

- ICECREMO1 can only cope with a structured grid. A mesh consisting of quadrilateral elements is therefore created, see Figure 3.3. Around the complex geometries obtained during icing calculations, this might be an extremely difficult and time consuming task. The problem becomes really acute for multi-step calculations, as stated by Moser and Gent [106], *"this procedure is not well suited to the requirement for structured grids"*. The problem due to re-meshing was one of the motivations for the development of ICECREMO2, a code that can handle unstructured meshes.

- ICECREMO2 can use either a structured or an unstructured mesh. Although an ideal option would be to generate a complete unstructured grid, limitations due to the automatic re-meshing within the mesh-generator impose a structured grid to be created on the body surface. However, a hybrid mesh is created away from the surface geometry, within the flow domain.

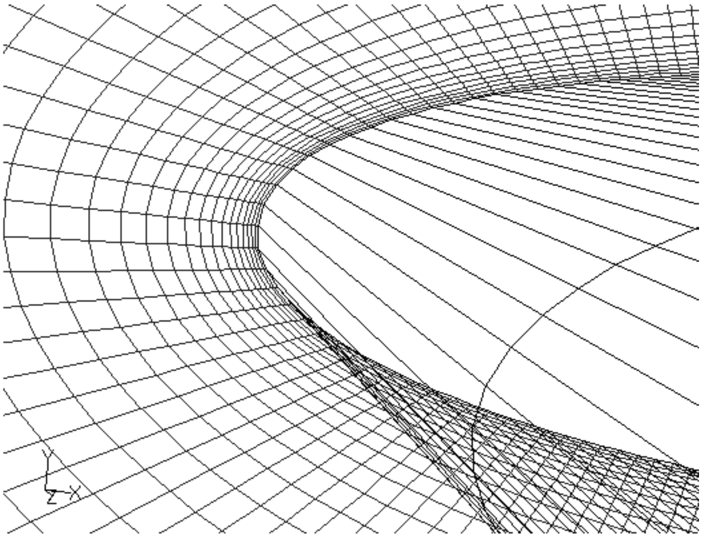

Figure 3.3: *Structured mesh generated in GAMBIT for ICECREMO1. The grid is refined in the vicinity of the leading edge and coarse away from it.*

This type of mesh is well suited for icing studies: they provide accurate enough flow data and flow dependent icing parameters. They also comply with internal requests of the FLUENT software.

3.3 Surrounding Airflow Calculation

The grid generated in the previous section is used to calculate the flow around the wing. Practically, the flow solver uses a finite-volume method to convert the governing Navier-Stokes equations to algebraic equations that can be solved numerically.

First, the boundary conditions and some model specifications must be defined. Here again, this may be performed automatically using the journal feature of FLUENT. The flow is calculated inside a large cylinder with the studied geometry at its center. A typical configuration may be seen on Figure 3.4. The radius of the cylinder is large enough to guarantee that the flow is not perturbed on the outer limit by the presence of the wing or cylinder.

The FLUENT flow solver being highly versatile, the package offers a wide range of turbulence models. It is generally admitted that one and two-equation turbulence models have difficulties to accurately determine the flow field in regions where separation occurs, for instance behind horns [107]. The Spalart-Allmaras [108, 109] was selected. This is a one-equation model designed for aerodynamical applications with wall bounded flows and is well suited for the sort of study performed in this work

[110]. This model is less sensitive to the size of the grid in the boundary layer and is faster than two-equation turbulence models such as $k-\epsilon$ and $k-\omega$. For instance, the $k-\omega$ turbulence model requires grid refinement within the boundary layer [65]. In addition, this model has been shown to reproduce free shear layer and boundary layer behaviour quite accurately [111].

Boundary Conditions

Boundary conditions are required all around the flow domain and wing surface. They are similar for both single and multi-step calculations. A typical configuration is shown in Figure 3.4. Note that this figure is not at the correct scale, the purpose being here to represent the different boundary conditions used in the CFD model.

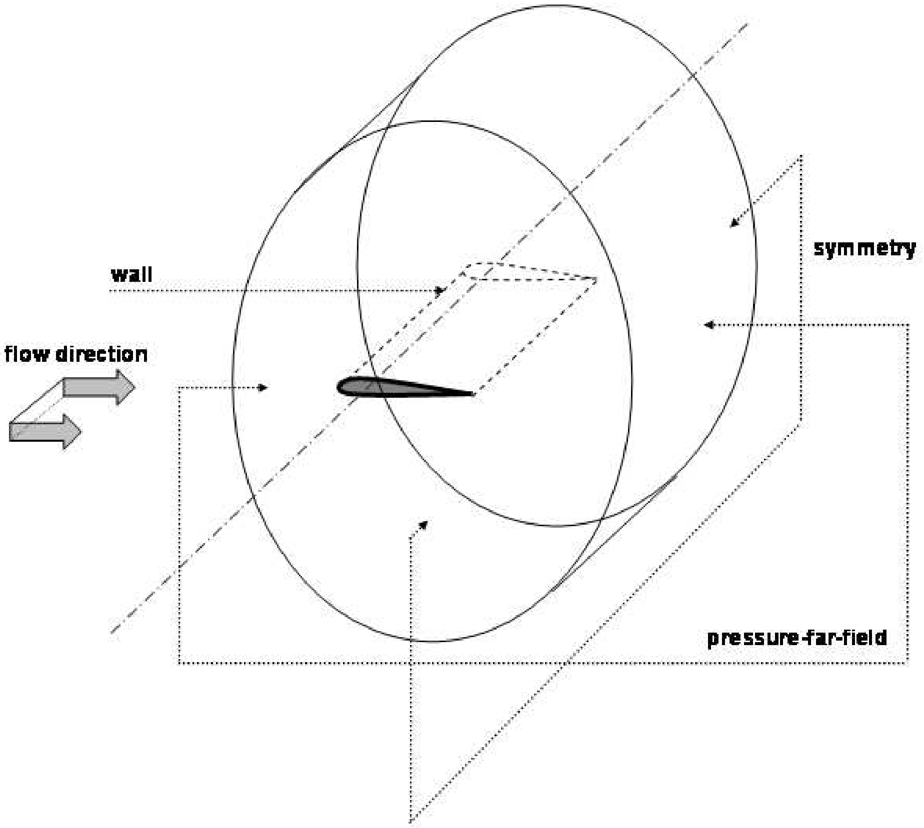

Figure 3.4: *Boundary conditions set-up for the airflow calculation around a wing: "wall" on the airfoil surface, "symmetry" for the faces perpendicular to the span of the wing and "pressure-far-field" far away from the airfoil.*

1. *Pressure-far-field.*

   Pressure-far-field is used to model a free-stream condition at infinity, with free-stream Mach number and static conditions being specified. The far-field condition needs to be applied far enough from the object of interest to guarantee the flow solution is not perturbed by the imposed boundary conditions. This condition is generally used in aerodynamic applications and is therefore adapted to this study. In the present configuration, the pressure-far-field is applied on the outer cylinder domain, 8 chord lengths away from the body.

2. *Symmetry.*
   FLUENT assumes a zero flux of all quantities across a symmetry boundary. There is no convective or diffusive fluxes across a symmetry plane: the normal velocity component and the normal gradients of all flow variables at the symmetry plane are therefore equal to zero. This condition is applied on the outer cross sections, perpendicularly to the span direction.

3. *Wall.*
   Wall boundary conditions are used to bound fluid and solid regions. In viscous flows, a no-slip boundary condition is enforced at walls by default. This option has been chosen for the simulations and the wall temperature specified for the airfoil or cylinder surface.

Flow Solution

The flow past the body can be determined either with the “coupled” or with the “segregated” solver. In a coupled solver, the complete system of governing equations are calculated simultaneously whereas the segregated solver solves the equations updated sequentially. When working with 3D bodies, memory problems are often encountered. The segregated solver, which is the default option, has therefore been adopted in the simulations as it consumes less memory.

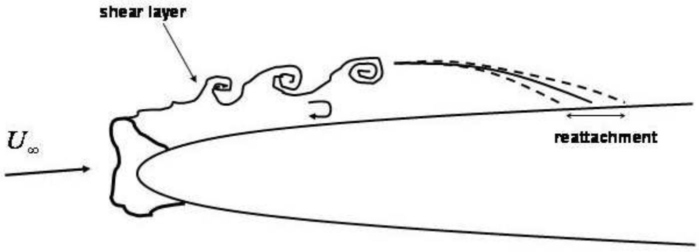

Figure 3.5: *Schematic of the flow separation on the upper surface of an iced airfoil.*

When dealing with high surface deformations such as a double-horn ice structure, typical of glaze icing, a recirculation zone exits behind the horn regions. As the air flows around the upper horn of the ice shape, a severe adverse pressure gradient causes the flow to separate from the surface, see Figure 3.5. Vortices form in the separate shear layer and the flow may reattach to the surface further downstream due to the increase of energy [112]. Flow separation causes a drastic decrease of lift and increase of drag of the aircraft. This phenomenon is known as a “stall”. As the region of interest needs to be studied with caution, a viscous model has been adopted in the simulations.

The CFD flow solver potentially provides all the parameters required for ice predictions: the surrounding airflow solution, including the positions of the nodes and associated velocities, the pressure, the heat transfer coefficient and the shear stress values.

Flow Solution for ICECREMO1

Three-dimensional flow data are required to run the particle tracking routine implemented in ICECREMO1 and determine the trajectories of the droplets that hit the surface. The ice prediction code has a capability to calculate the heat transfer coefficient and the shear stress using an internal process. Nevertheless, for studies performed on the initial code version, these parameters are directly provided by the flow solver.

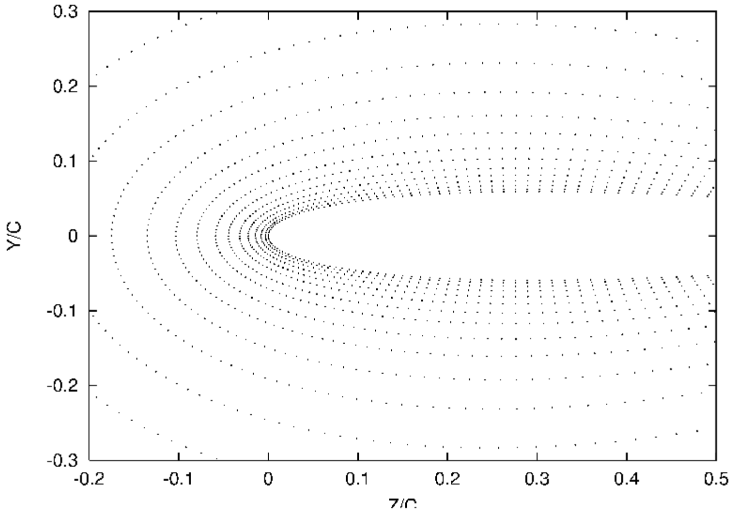

Figure 3.6: *New structured grid accepted by ICECREMO1, created within the interface between the flow solver and the icing code.*

The pre-processing stage is fundamental. If an incorrect format is used for the flow data, the code will crash or only a few number of particles will hit the surface. In addition, the collection efficiency is likely to be wrong, leading to an inaccurate ice growth rate. Due to the structured mesh and specific format required by the ICECREMO1 code, an interface had to be added to transform the CFD package results into a file readable by the icing code. FLUENT unstructured results are interpolated on a structured grid that can be read by the icing module of the algorithm. A typical grid may be seen in Figure 3.6. The mesh is fine close to the wing surface and much coarse away from it. More details about the grid definition can be found in Reference [32]. For the sake of simplicity, the number a nodes remains identical for each step of the multi-step calculation and the chord length remains constant along the span.

This procedure is rather time consuming. The interpolation between the FLUENT unstructured grid and the structured grid used in ICECREMO is long. This considerably slows down the whole algorithm, particularly when fine grids are generated.

Flow Solution for ICECREMO2

When using the updated version of the icing code ICECREMO, the grid used in the FLUENT package may be used straightaway and no interpolation is necessary. The time required to perform single and multi-step ice predictions is largely reduced: the time lost during the flow calculation on a hybrid mesh is therefore compensated by the absence of interface.

Conclusion

The geometry description, mesh generation and flow solution have been detailed. Associated with the icing module, they form the key steps of a single-step icing calculation. The complete multi-step algorithms will now be defined for both versions of the ICECREMO code.

3.4 Multi-Stepping Algorithms

The single-step algorithm will now be adapted to multi-step requirements. Two possible options will now be presented.

3.4.1 Step-by-Step Algorithm

Step-by-step algorithms for both versions of the ICECREMO code are described in Figures 3.7 and 3.8 with all major parts of an ice calculation included. Depending on the ICECREMO version, the substrate geometry is updated after each step with the surface temperature, ice and water heights.

1. In ICECREMO1, the flow is recalculated around the iced geometry, which includes the ice and water heights, as shown in Figure 3.7. To slightly simplify the problem, the water layer being on top of the ice layer is considered as solid in the flow solver. When glaze ice grows, the new grid is therefore created on the water surface, the water height being added to the coordinates of the ice layer. However, the free surface temperature is not updated between the different steps. This could be an immediate limitation in the procedure. Each time the icing model is run, the new accreted ice is estimated as if this free surface temperature was the initial one (i.e. the initial temperature on the clean surface). In addition, the real water height estimated in the previous

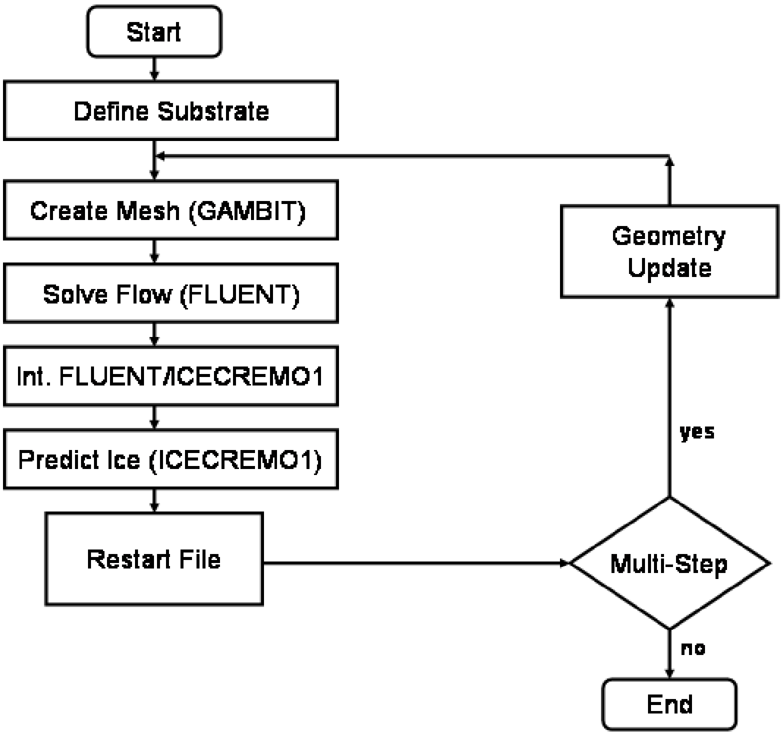

Figure 3.7: *Algorithm ICECREMO1 for single and multi-step calculations. An update of the water and ice heights is performed between each new step. The flow is determined around the iced body (water height added to the ice height).*

step is not considered in the new prediction. This is the approach usually adopted when performing manual multi-step calculations and could lead to a loss of accuracy. This will be detailed in Chapter 4.

2. In the ICECREMO2 code, the new flow solution is calculated solely around the ice layer, i.e. no longer around the system ice plus water heights. The corresponding algorithm is shown in Figure 3.8. Water height and surface temperature are updated each time the icing model is run. A restart procedure has therefore been created. Water height and surface temperature are stored in this file, allowing the surface to be updated before the start of a new ice prediction. With this approach, there is no loss of temperature or water between the different steps. Since the water height is very small compared to the ice height, it does not modify the surrounding airflow significantly and can be neglected in the flow calculation.

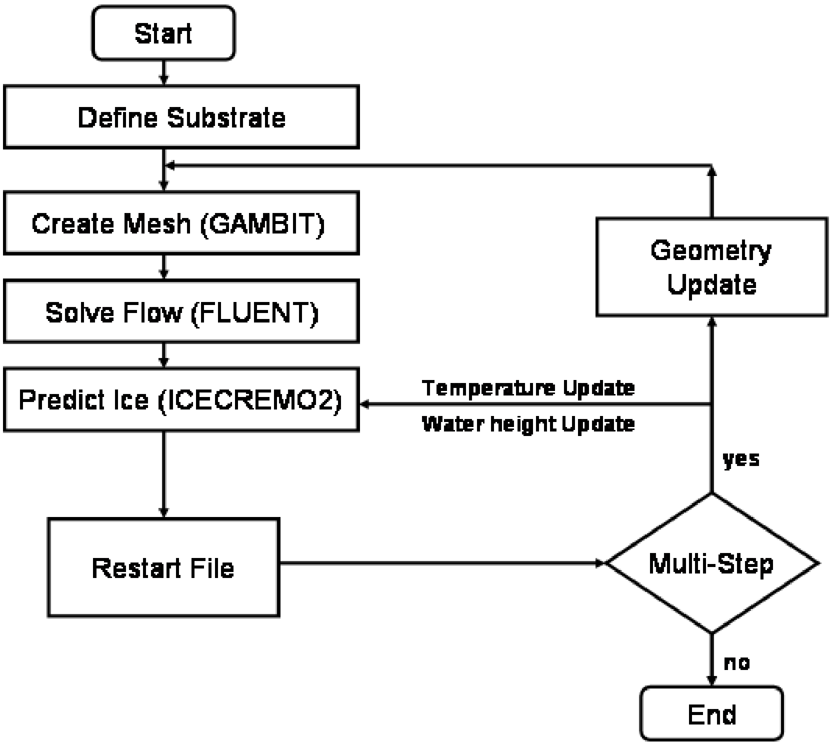

Figure 3.8: *Algorithm ICECREMO2 for single and multi-step calculations. An update of the surface temperature and water height is performed between each new ice prediction. The flow solution is generated around the iced surface (no water height added to the ice height).*

At the end of each step, a new grid is created. The flow past the iced body and the physical parameters are re-evaluated. The procedure can be repeated over again until the total ice accretion time is reached. This approach allows some time variation of flow dependent parameters. However, their evolution is not continuous with this algorithm. An alternative will now be presented that results in fully continuous flow dependent parameters.

3.4.2 Predictor-Corrector Algorithm

A predictor-corrector algorithm is presented in Figure 3.9. The airflow and flow dependent parameters are first determined on the clean geometry and the values are stored for subsequent calculation. The ice accretion is then predicted for the total exposure time. When this single-step procedure is complete, airflow and related

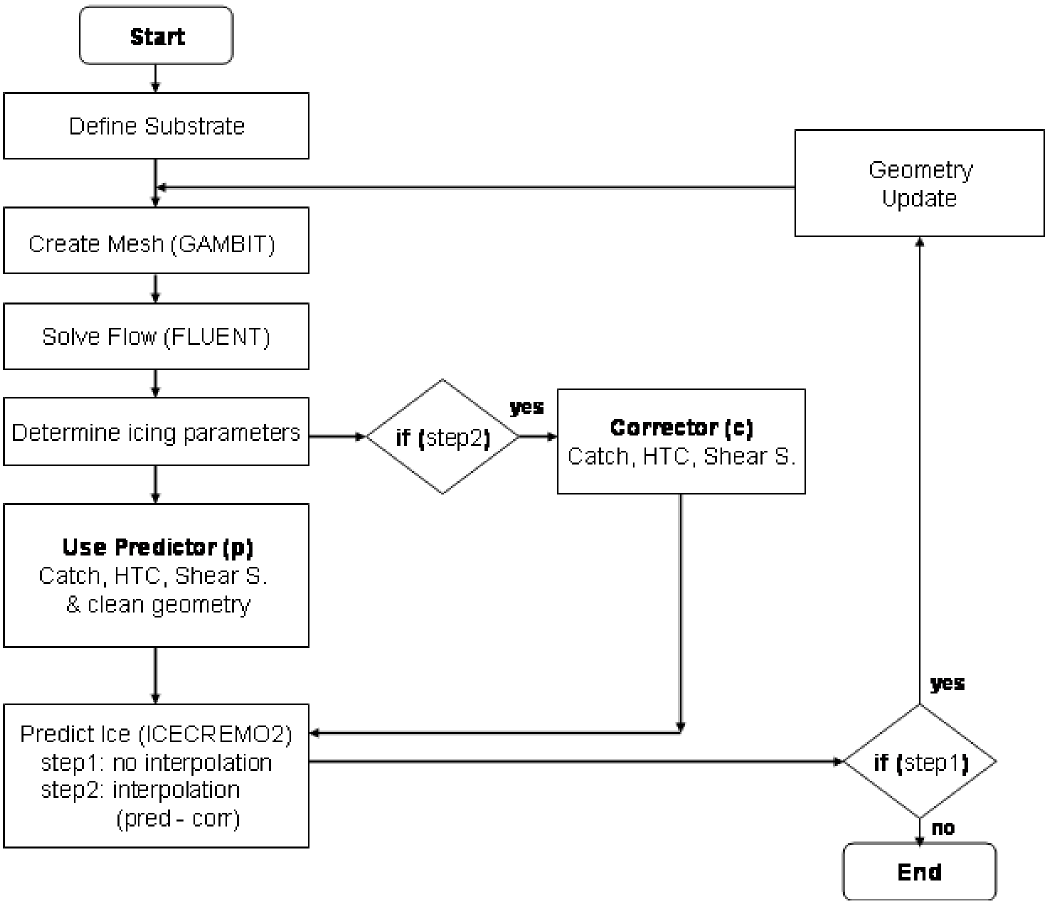

Figure 3.9: Algorithm of the predictor-corrector approach in ICECREMO2.

parameters are re-estimated for the iced geometry. The corrector is formed by the icing parameters determined on this iced geometry. Another ice calculation is finally performed on the clean geometry for the same exposure time, using new flow dependent parameter values obtained via an interpolation between the predictor and the corrector values calculated previously. The interpolation predictor-corrector is accomplished for each time-step increment in the icing model. This allows fully time dependent icing parameters.

3.4.3 Automated Procedure

The automation of the whole procedure is based on scripts also known as "*journal files*" for the CFD suite FLUENT. These files contain all the instructions to be performed by the meshing algorithm and flow solver and may be activated automatically when starting the softwares. They are dependent on the icing, atmospheric conditions and requests of the user.

When running a journal file, the mesh generator and the flow solver automatically execute all of the commands in sequence. Additional scripts have also been created to link the different modules of the icing code, to postprocess, plot the final ice shapes and keep a trace of the results obtained at the end of each step [95, 96, 113, 114].

A basic and simplified example for a step-by-step calculation using the CFD package FLUENT and the ice prediction code ICECREMO2 is written below:

```
while [ ! −r "END.dat" ]
do
    CreateJournalFileGambit.exe
    Execute GAMBIT
    while [ ! −r "Mesh.msh" ]
    do
        IncrementNodesOuterSurface.exe
        CreateJournalFileGambit.exe
        Execute GAMBIT
    done
    CreateJournalFileFluent.exe
    Execute FLUENT
    UpdateScriptsICECREMO2.exe
    Execute ICECREMO2
    CheckIfMultiSteppingFinished.exe
done
```

This script is based on two loops. The outer one, starting line 2 and finishing line 16, defines the number of steps required in a multi-step calculation. The end of this loop is detected by the presence of a file called "*END.dat*", created at the appropriate moment inside the loop. An independent routine, "*CreateJournalFileGambit.exe*", creates the journal file for the mesh generation ("*Execute GAMBIT*") and may also be run when the second loop of the algorithm starts (lines $6-10$). The aim of this loop is to limit difficulties with the automatic re-meshing procedure. If a mesh can not be generated in the first attempt, for instance for a too rough iced surface, a new journal file is written including an increased number of nodes on the domain outer surfaces. The process is repeated until a mesh is successfully generated. When this first stage is complete, the journal file for the flow solver is written ("*CreateJournalFileFluent.exe*") and the flow solution is calculated ("*Execute FLUENT*"). The input files for the ICECREMO code are generated ("*UpdateScriptsICECREMO2.exe*") and the ice shape estimated with "*Execute ICECREMO2*".

A complete step of the procedure is evaluated and when the total number of required steps are successfully completed, the multi-step calculation will stop and the "*END.dat*" file will be created.

A similar approach can be adapted to an ice growth determined with a predictor-corrector procedure. The procedure follows the algorithm described in the previous section. In this case, the calculation will stop when the second step is complete. Information is retained from the first step and used as a predictor the second time the icing model is run.

3.5 Conclusion

In this chapter, the automated multi-step procedure was introduced. The practical aspects of combining a CFD package with ICECREMO were presented along with the automated procedure that links the different stages of the process. Several of the multi-step results obtained on a NACA0012 airfoil will be presented in the next chapter. The experience gained with the first development of the automatic procedure was highly useful to elaborate and adapt an improved procedure for the ICECREMO2 code. Simulation results obtained with this code are presented in Chapter 5.

Chapter 4

Basic Step-by-Step Implementation

4.1 Introduction

The model for a multi-stepping algorithm has been developed in the previous chapter. It consists in repeating the same four or five steps of a one-step algorithm as many times as requested: generate the mesh, solve for the flow, calculate flow dependent icing parameters, perform the icing calculation and eventually use an interface that guarantees the flow data are entered in the correct format in the icing routine. The objective of this section is to investigate how a step-by-step calculation affects the flow dependent parameters and the ice growth.

As already mentioned, the flow dependent parameters necessary for an icing calculation are mainly the collection efficiency, the heat transfer coefficient and the shear stress. Surface pressure is sometimes important particularly when the total temperature is around zero [23], but it will be automatically accounted for as part of the CFD update. These parameters will be calculated first on a clean surface and the corresponding one-step ice and water layers will be estimated. The effect of the step-by-step calculation on these parameters will be studied. The ice and water layers will be recalculated and the differences will be analysed.

This initial study was carried out using ICECREMO1, the structured version of the icing module. They were many constraints on the mesh used for the flow solution and the grid on the wing could not be as refined as requested. Consequently, the parameters studied do not always appear very smooth but this does not affect the results significantly. The unstructured version of the code, ICECREMO2, will only be used from Chapter 5.

4.2 Problem Configuration

Figure 4.1 shows the general configuration of a NACA0012 airfoil subject to an incidence α. The airflow is moving from left to right and droplets are introduced ahead of the airfoil at a distance sufficiently large, ideally seven times the chord length as discussed in the previous chapter: the flow at this location is not perturbed by the presence of the airfoil and droplets move at the free stream velocity. In the following, the incidence angle is $\alpha = 4^o$ and the free stream velocity is $V_\infty = 67m/s$. Flow dependent parameters will be studied for a rime ice situation with the air stream temperature $T_\infty = -26^oC$ and for a glaze ice situation at $T_\infty = -5.6^oC$ with droplets of size $d_d = 20\mu m$ under the specific conditions Shin and Bond used to measure ice shapes on a two-dimensional NACA0012 [17]. These conditions are listed in Table 4.1, where M and P_∞ represent the Mach number and free stream pressure of the airflow, LWC is the liquid water content in the cloud and t_{exp} represents the total icing exposure time.

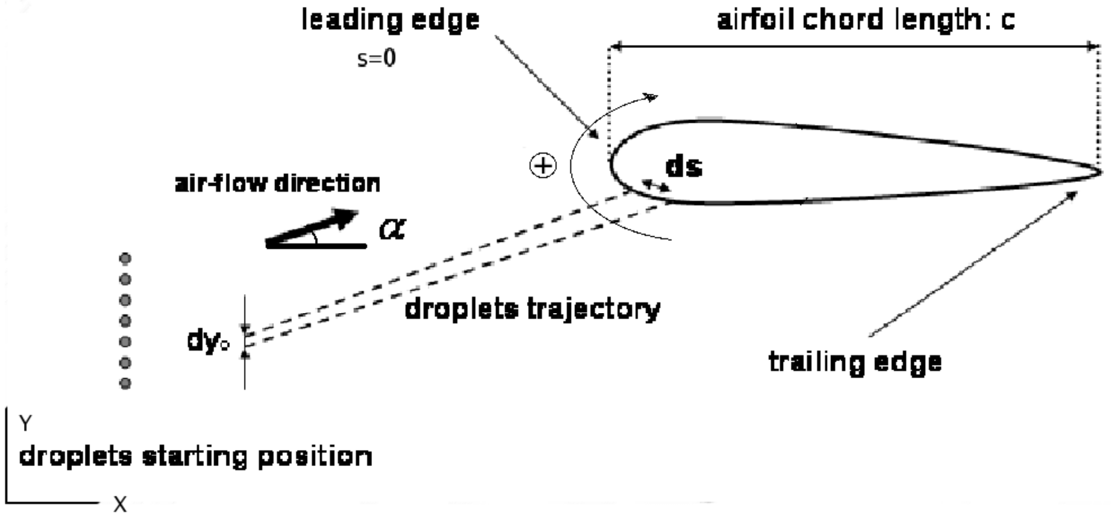

Figure 4.1: *Problem configuration.*

M	V_∞ (m/s)	α $(^o)$	P_∞ (Pa)	LWC (g/m^3)	d_d (μm)	t_{exp} (min)
0.21	67	4	101300	1.00	20.0	6

Table 4.1: *Airflow and icing conditions applied to a NACA0012 wing [17].*

4.3 One-Step Calculation

To start with, the results obtained with a single step calculation are presented. These results will be used as a benchmark to evaluate the effects of a multi-step algorithm.

Collection Efficiency

The trajectories of the injected droplets are calculated in the tracking module of the ICECREMO code and the collection efficiency is determined. As already mentioned, the collection efficiency β represents the proportion of the free stream water droplets that hit the surface. Mathematically, this parameter is defined as:

$$\beta = \frac{dy_0}{ds} \ ,$$

where dy_0 represents the distance between two droplets in the free stream and ds is the distance between the corresponding impacts on the surface.

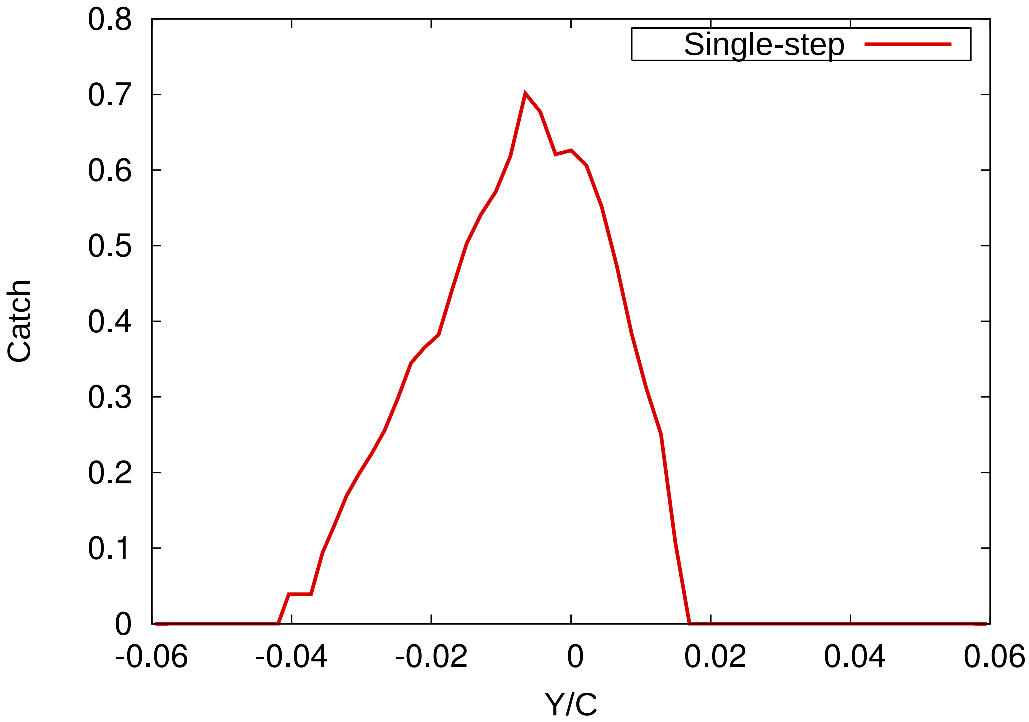

Figure 4.2: *Collection efficiency on a clean unfolded airfoil.* $\alpha = 4^o$, $V_\infty = 67\ m/s$.

Numerical results for a NACA0012 airfoil may be seen on Figure 4.2, where y/c is a non-dimensional number representing the ratio of the position y and of the chord length of the airfoil, c. The lower and upper surfaces correspond to the regions of the wing where $y/c < 0$ and $y/c > 0$, respectively. These results apply to both rime and glaze ice situations: numerically, the temperature does not affect the results, although in reality, temperature dictates the size of the droplets and therefore influences the collection efficiency [63, 115]. In the present case, the droplets are assumed spherical with a diameter of 20 μm. This size is quite standard for icing situations [18]. They tend to follow the air flow and their own inertia has little effect on the trajectory [43].

Generally, the collection efficiency has an approximate parabolic profile, except for a spike around the maximum value, $\beta = 0.70$ that is reached for $y/c = -0.0065$. The collection efficiency decreases sharply on both sides of the peak value, until the impingement limits: $y/c = -0.042$ for the lower surface and $y/c = 0.017$ for the upper surface of the airfoil. As could be expected, the collection is more extended on the lower part. This is due to the angle of attack and also, in a minor proportion, to the effect of gravity [35]. Small discrepancies may be noticed around the peak collection efficiency. This is probably due to two main factors:

1. An insufficient number of droplets is injected in the airflow,
2. The grid is too coarse but this was hard to correct.

Unfortunately, further tests could not be performed because of difficulties with the computer network. These results are however quite acceptable and will be used in the following.

Shear Stress

The shear stress corresponding to the collection efficiency presented in Figure 4.2 is plotted in Figure 4.3. This parameter is defined as:

$$\tau = \mu \frac{\partial u}{\partial n} ,$$

where μ is the dynamic viscosity, a positive quantity, and $\partial u/\partial n$ denotes the velocity gradient in the direction normal to the surface. The shear stress may therefore be either positive or negative depending on the sign of the gradient. Due to the definition and orientation of the curvilinear coordinate s on the surface of the wing, the shear stress is negative over most of the lower surface and positive above the stagnation point located at $y/c = -0.007$. Along the lower surface, the shear stress decreases slowly and reaches its lowest value $\tau = -9.5 Pa$ for $y/c = -0.025$: the incoming air flow is partially shadowed by the airfoil but this effect disappears close to the nose when the incoming air flow hits the surface directly. The shear stress then increases drastically up to $\tau = 44Pa$ for $y/c = 0.0035$. At this stage, the incoming flow starts being shadowed again and the shear stress decreases progressively.

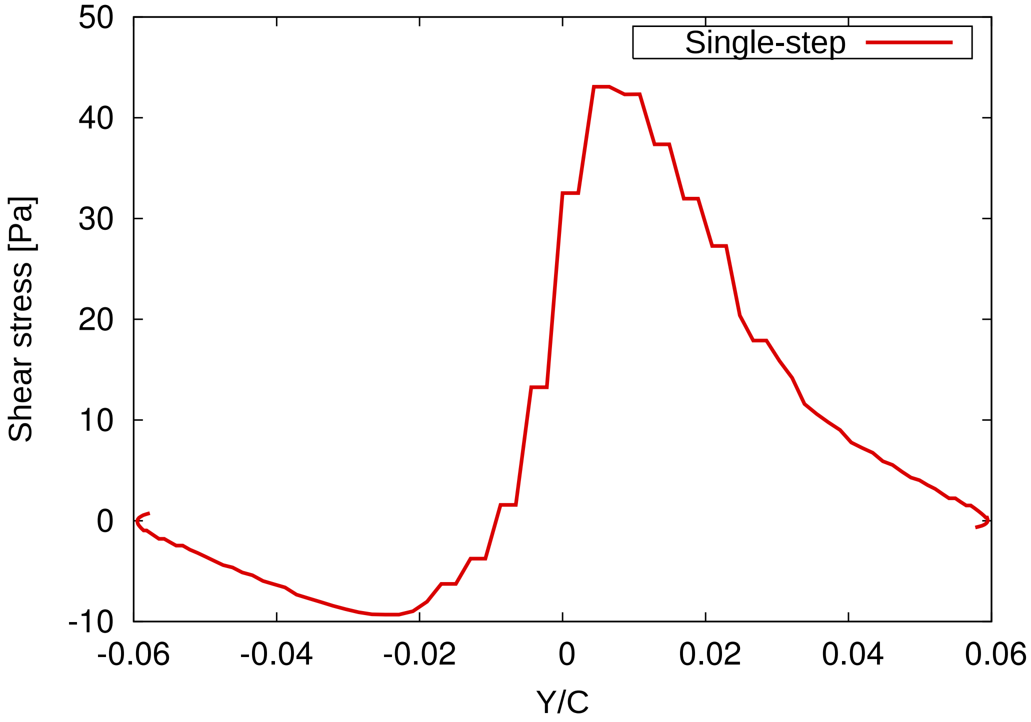

Figure 4.3: *Shear stress on a clean unfolded airfoil.* $V_\infty = 67\ m/s$, $\alpha = 4^o$.

The differences between the maximum and minimum values of shear stress may be explained by the angle of the wing to the horizontal, α. The streamlines passing along the upper surface have to turn sharply around the leading edge and the high curvature accelerates the flow. A similar phenomenon occurs on the lower surface, but with a much lower curvature, the flow is then less accelerated and the shear stress does not reach as high an extremum.

Here again, the parameter is almost independent from the ambient temperature. Only the dynamic viscosity μ varies slightly between the rime and glaze situations because of the temperature variation, but this difference is small and may be neglected. The values of shear stress calculated on the clean airfoil are therefore valid for both rime and glaze ice situations.

Heat Transfer Coefficient

In rime ice studies, the ice height is obtained directly from the mass balance. Therefore, the heat transfer coefficient has no real impact on the ice accretion in rime ice conditions. For glaze icing, the ice growth rate considers both mass and energy balances and takes into account the water film flowing on the surface. In this situation, the heat transfer coefficient influences largely the ice accretion [68]: it relates the ice growth to the variations of the surrounding air flow and surface temperatures. Figure 4.4 shows this parameter plotted on a clean unfolded airfoil, at the airflow temperature $T_\infty = -5.6^oC$.

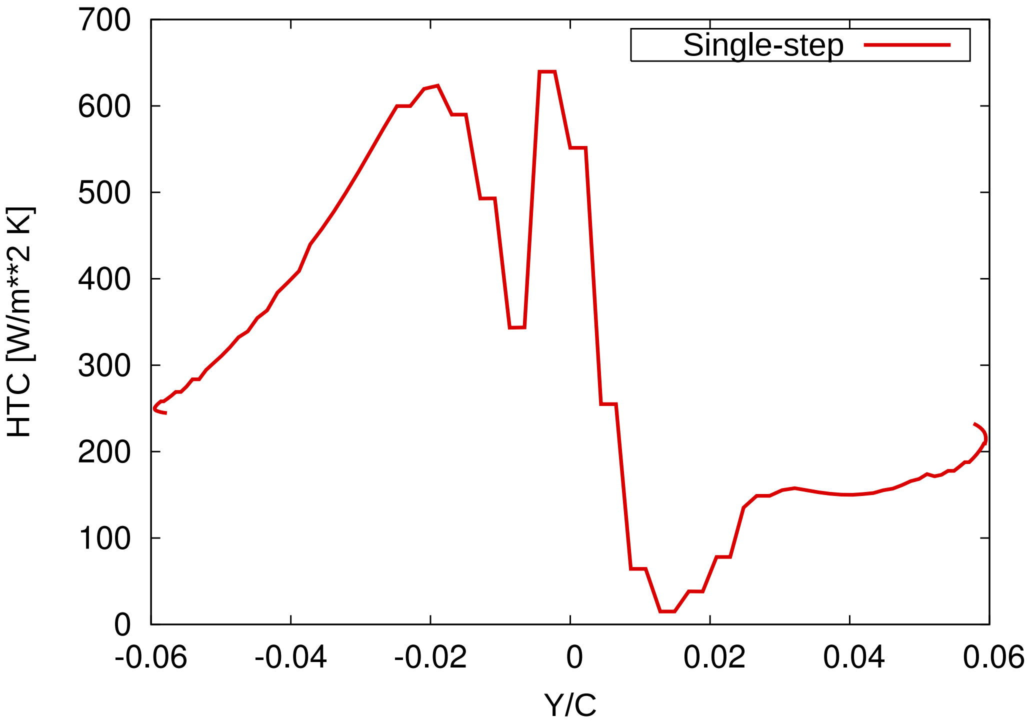

Figure 4.4: *Heat transfer coefficient on a clean unfolded airfoil.* $V_\infty = 67\ m/s$, $\alpha = 4^o$.

The heat transfer coefficient starts with the value $h_c = 245 Wm^{-2}K^{-1}$ on the lower surface. This value increases to reach $h_c = 624 Wm^{-2}K^{-1}$ for $y/c = -0.019$. Past this point, there is a sudden drop and the value reduces to reach $344 Wm^{-2}K^{-1}$ for $y/c = -0.007$ and increases quickly until the maximum value $h_c = 639 Wm^{-2}K^{-1}$. Beyond this point, the heat transfer coefficient value decreases again to reach its minimum value $h_c = 15 Wm^{-2}K^{-1}$ for $y/c = 0.013$. This fast decrease is followed by a smooth increase along the upper surface of the airfoil to reach the value $h_c = 233 Wm^{-2}K^{-1}$.

The two heat transfer coefficient peaks correspond to the region on the airfoil where ice is likely to form and grow in higher quantity. The two-peak structure around the stagnation point, as shown on Figure 4.4, will play an important role in glaze ice growth: this is the location where the typical double-horn ice structure will develop.

The ice and water height will now be calculated in ICECREMO1 using these values of collection efficiency, shear stress and heat transfer coefficient.

Ice height

The ice height is different, depending on the atmospheric conditions and type of accretion. Figure 4.5 shows the resulting ice height for a 6 min exposure time at $T_\infty = -26^oC$. This shape is typical of rime ice conditions and is exactly proportional to the collection efficiency represented in Figure 4.2. The maximum rime ice height value $b = 18.66$ mm is located on the lower surface and corresponds to the maximum value of the collection efficiency. More ice accretes on the lower part of the airfoil, mainly due to the effects of the angle of attack ($\alpha = 4^o$) and gravity on the droplets before they hit the surface. The ice growth is solely present within

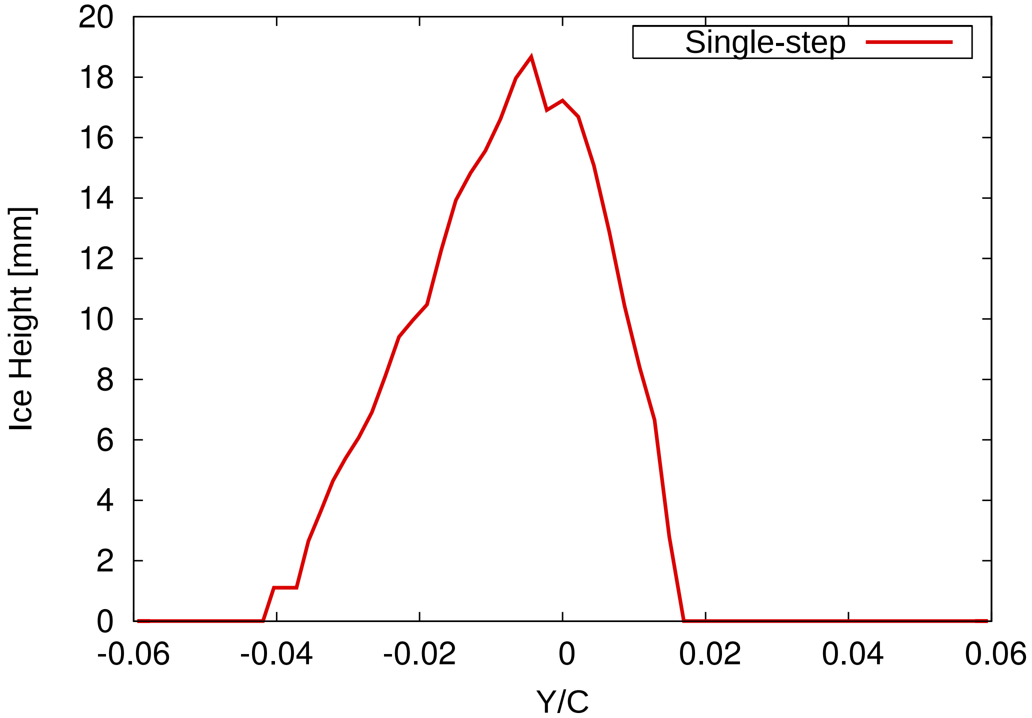

Figure 4.5: *Ice height obtained in a single-step calculation for a 6-minutes exposure time under rime icing, plotted on a clean unfolded NACA0012 airfoil.* $T_\infty = -26^oC$, $V_\infty = 67m/s$, $\alpha = 4^o$.

the range $-0.042 < y/c < 0.017$. These boundary points correspond to the droplet impingement limits, as shown in the collection efficiency curve on Figure 4.2.

In glaze ice conditions, the situation is very different. Both the runback water and the heat transfer coefficient shown on Figure 4.4 have a large influence on the accretion. Figure 4.6 shows the ice accretion predicted in a single-step calculation after a 6 min exposure time at $T_\infty = -5.6^oC$. The shape obtained is typical of glaze ice conditions: the ice profile is wider than in rime conditions and the profile is globally smoother. A small depression is noticeable from either side of the stagnation line. This corresponds to the sharp drop observed in the heat transfer coefficient. The maximum ice height $b = 10.4\ mm$ corresponds to the peak heat transfer coefficient, but is significantly lower than the corresponding rime ice height $b = 18.66\ mm$. The same amount of water has hit the surface but the ice layer has spread considerably, as may be seen on Figure 4.7. Note the curves are plotted as a function of the vertical axis. Consequently, they appear wider around the nose and shrunk further downstream. The mass of ice formed is the same in both rime

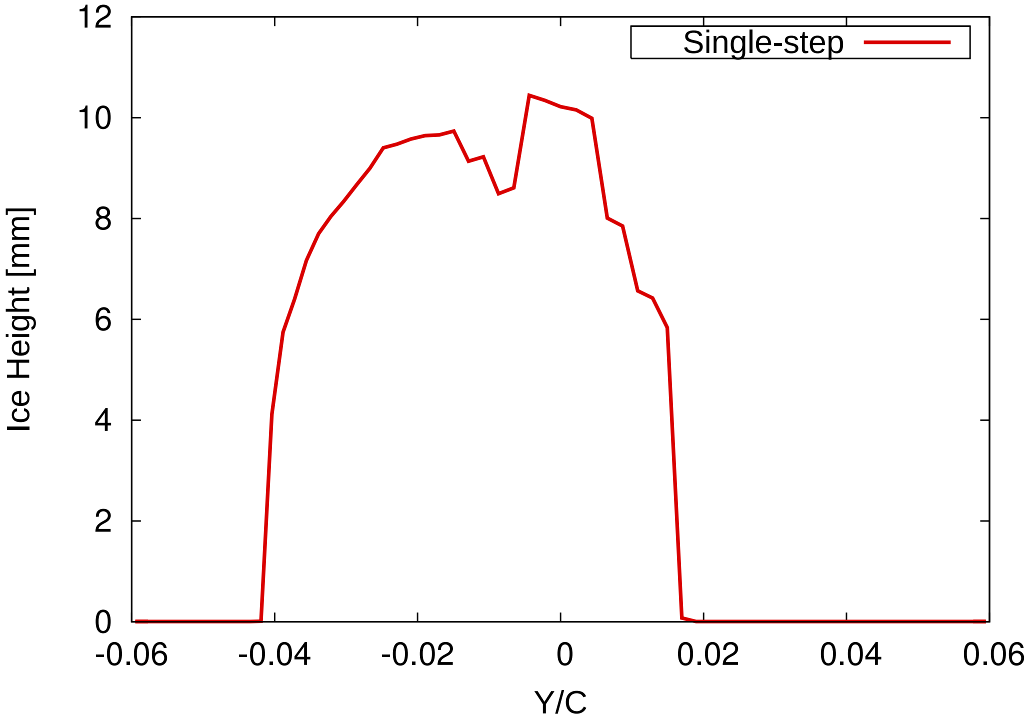

Figure 4.6: *Ice height obtained in a single-step calculation for a 6-minutes exposure time under glaze icing, plotted on a clean unfolded NACA0012 airfoil.* $T_\infty = -5.6^oC$, $V_\infty = 67m/s$, $\alpha = 4^o$.

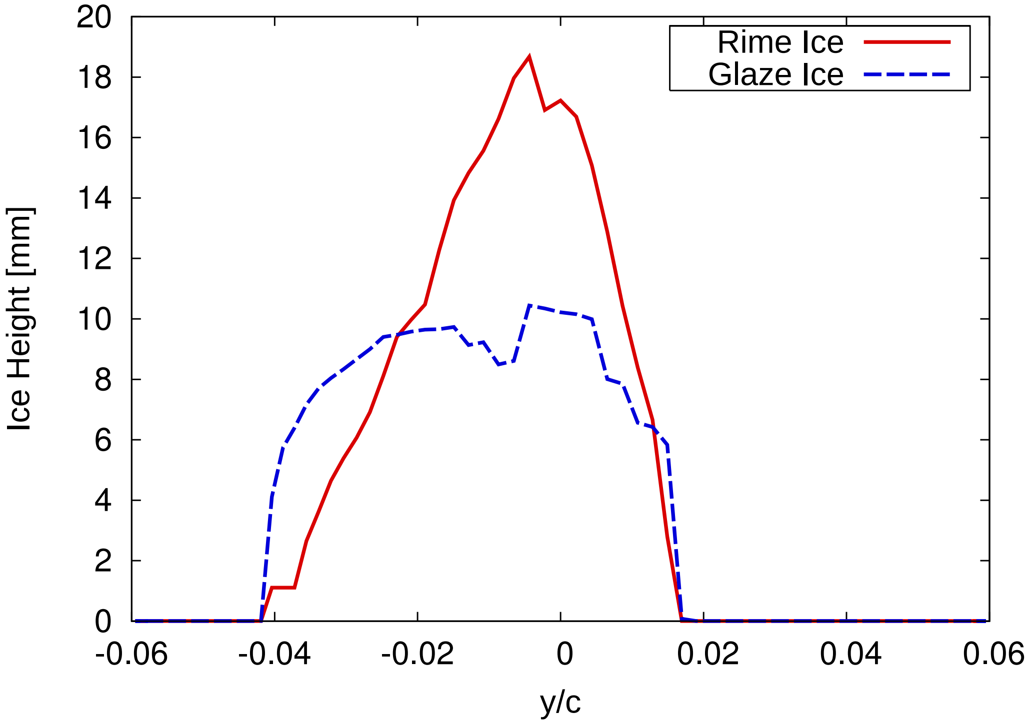

Figure 4.7: *Comparison of the ice height obtained in a single-step calculation for a 6-minutes exposure time under rime and glaze icing, plotted on a clean unfolded NACA0012 airfoil.* $V_\infty = 67m/s$, $\alpha = 4^o$.

and glaze ice cases for these conditions. The differences between the two curves are mainly due to the evolution of the water layer as will now be described.

Water height

In glaze ice conditions, the accretion greatly depends on the liquid layer running back on top of the ice. The water height corresponding to the glaze ice conditions described in Section 4.2 may be seen on Figure 4.8. It extends from $y/c = -0.042$ to $y/c = 0.017$, which is very similar to the extent of the ice layer. This situation is typical for glaze icing: the ice forms further than collection efficiency extends, only thanks to the water layer behaviour. The water forms a peak next to the stagnation point where the forces applied are almost zero. The shear stress is very small and the layer is too thin for the fluid to be moved by gravity. In addition, the heat transfer coefficient is also very small at this location. Most of the incoming droplets that hit the surface in this region will remain liquid, the heat transfer coefficient being too small to allow all these droplets to turn into ice. Away from the low heat transfer

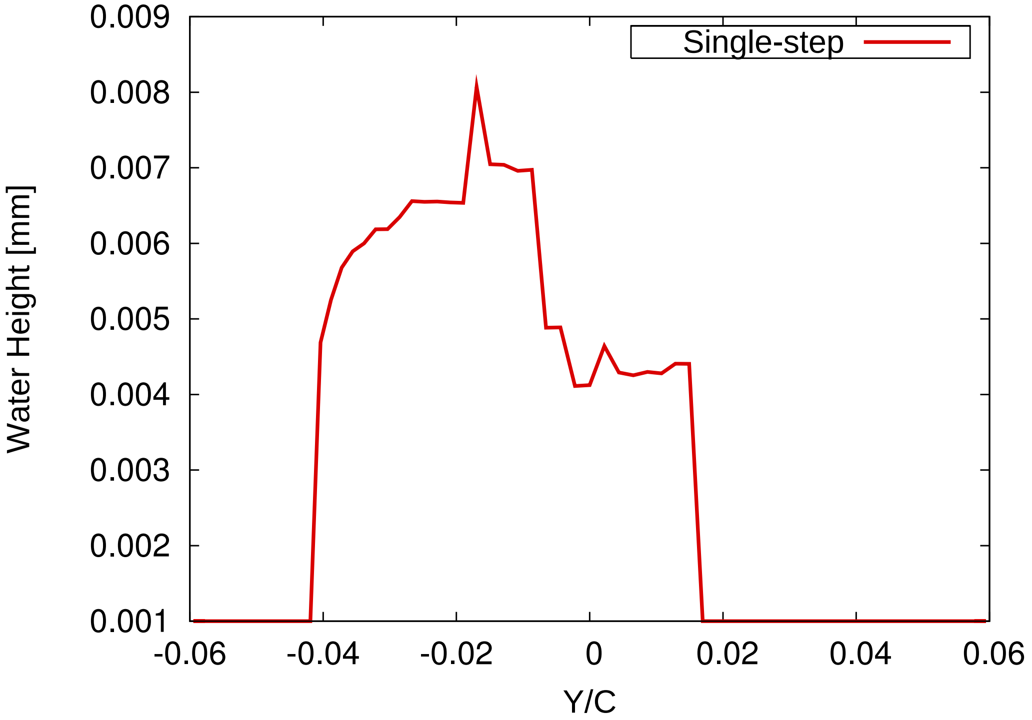

Figure 4.8: *Water height obtained in a single-step calculation for a 6-minutes exposure time under glaze icing, plotted on a clean unfolded NACA0012 airfoil.* $T_\infty = -5.6^o C$, $V_\infty = 67 m/s$, $\alpha = 4^o$.

coefficient region, the layer is quite flat and then suddenly drops to zero at the limits of the wetted area. The layer is much thicker on the lower aft of the wing: this is consistent with the collection efficiency values that are significantly higher on this side of the wing, and with the shear stress that pushes the liquid further down the lower aft. A similar phenomenon occurs on the upper aft, the water layer is almost flat, but there is much less water there hence the lower water height.

This preliminary study underlines the importance of the water layer in the glaze icing process: despite its extreme thinness, the water layer controls the extent of the ice layer and the resulting accretion is more regular an less spiky than in rime ice conditions.

Conclusion

In this section, a single-step icing calculation was considered for both rime and glaze ice conditions. The collection efficiency, shear stress and heat transfer coefficient have been calculated and analysed. Their influence on the resulting water and ice shapes has been clearly highlighted.

The ice accretion will modify the flow around the airfoil and therefore the values of the three flow dependent parameters: collection efficiency, shear stress and heat transfer coefficient. A multi-step icing algorithm allows for some sort of time dependence. This will now be studied for the two examples considered in this chapter.

4.4 Evolution of Flow Dependent Parameters

The ice accretion will now be studied using a step-by-step algorithm. The flow dependent parameters are recalculated periodically after a period called the multi-time-step. The objective of this section is to investigate the differences between single-step and multi-step results.

As explained in the previous chapter, the water layer and thermal profiles are not transmitted from one multi-time-step to the next. The ice and water layers are considered to be part of the wing and the calculation is restarted with this new geometry, as if it was ice free. This is a typical practice in a multi-step algorithm. This considerably simplifies the modifications necessary in the icing module. The consequences of this simplified procedure will be pointed out.

The parameters determined for the first multi-time step are identical to those determined in a single-step procedure. Therefore, the results from the previous section established on the clean airfoil can be used for the first step in the following calculations. The evolution in time of the flow-dependent parameters under rime and glaze ice type accretions will now be detailed.

Collection Efficiency

Figure 4.9 shows the evolution of the collection efficiency for two steps of 3 min each, leading to a 6 min total exposure time in rime ice conditions. An identical number of droplets has been injected in the air flow for both rime and glaze ice simulations.

The two curves have a lot of common points. Their global shapes are quite similar with a maximum value next to the stagnation line and a sharp decrease to zero on either side. Both have a peak value which is not modified significantly: $\beta = 0.66$ for $y/c = -0.0024$ in the second step instead of $\beta = 0.7$ for $y/c = -0.0065$ in the first step. The collection efficiency in the second step is shifted slightly towards the lower surface. This again is a consequence of the inclination angle: the upper aft of the wing is more shadowed from incoming droplets than before, due to the accreted ice layer. In the lower surface region, the collection efficiency corresponding to the second step is more jagged than on the clean airfoil.

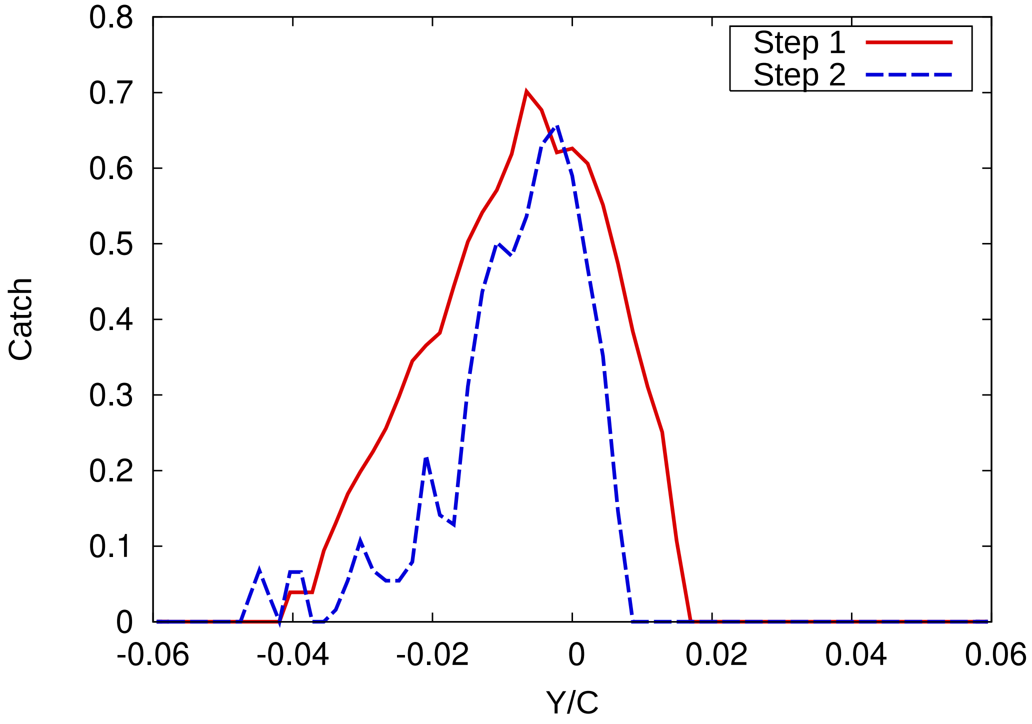

Figure 4.9: *Multi-stepping calculation performed in 2 steps of 3 min each for a 6 min total exposure time. Evolution of the collection efficiency in rime icing.* $T_\infty = -26^oC$, $\alpha = 4^o$.

Two factors may explain this evolution:

1. The presence of the ice layer creates larger turbulence close to the airfoil surface and the impinging droplet trajectories are more erratic in this region.
2. A more refined grid and a larger number of droplets could certainly provide smoother results. This modification was not an option in ICECREMO1 and may not have been practical anyway. A considerably finer grid would have been required to describe the droplets trajectory with a significantly improved accuracy and the flow calculation would have taken much longer time.

All being considered, these results show that rime ice does not affect flow characteristics too badly around the nose, even if some changes may be noticed. However, the accreted rime ice affects the collection efficiency in a greater proportion on the upper and lower surfaces of the airfoil.

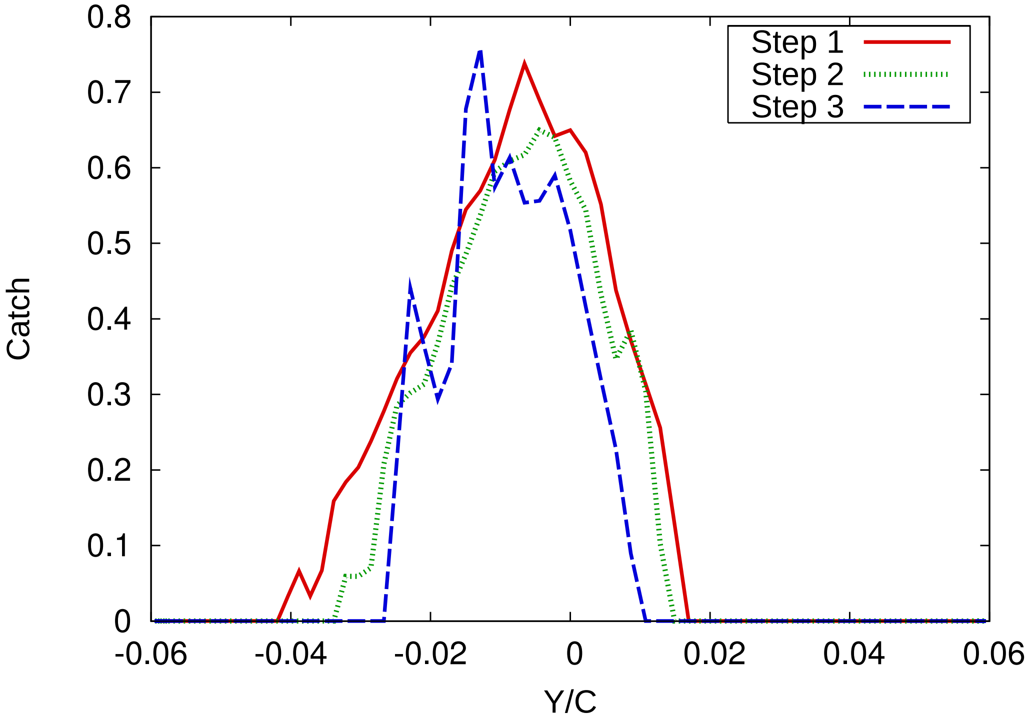

Figure 4.10: *Multi-stepping calculation performed in* 3 *steps of* 2 *min each for a* 6 *min total exposure time. Evolution of the collection efficiency in glaze icing.* $T_\infty = -5.6^oC$, $\alpha = 4^o$.

Figure 4.10 shows the evolution of the collection efficiency on a wing subject to glaze icing. Three steps of 2 *min* each are considered, to reach a 6 *min* icing exposure time. The collection efficiency varies more significantly than in rime ice conditions. This situation could be expected; the ice layer becomes less streamlined and the surface is much more deformed because of the ice accretion. Fewer droplets impinge near $y/c = 0$ and the upper aft, when the exposure time increases. Here again, this region is shadowed by the growing ice layer. The collection efficiency in this region decreases with the number of updates. The same phenomenon appears on the lower surface of the airfoil, far away from the leading edge but at this location, the phenomenon is due to turbulence created by the ice layer. A similar effect may be observed with the shear stress and heat transfer coefficient as will now be discussed.

Shear Stress

The shear stress does not influence the accretion for rime icing: there is therefore no need to study this parameter under these conditions. However, the shear stress evolves with the accretion in glaze ice conditions, as shown in Figure 4.11. Globally, it keeps a similar profile during all three multi-time-steps. It reaches its maximum value around $y/c = 0.0065$ and then decreases on both sides. The maximum value increases with each new calculation ($\tau_y^1 = 43.08Pa$, $\tau_y^2 = 48.7Pa$, $\tau_y^3 = 49Pa$). Along the lower aft, the shear stress decreases gently in all three cases, with a small peak appearing around $y/c \approx -0.04$, which corresponds to the limit of the ice layer. More significant changes may be observed on the upper aft: the ice shape grows in such a way that the flow separates from the surface. Consequently, the shear stress drops very sharply before readjusting to clean airfoil values progressively, far away from the leading edge. This change should clearly affect the evolution of the water layer, but the consequences might be only limited here since the water layer disappears form one multi-time-step to the other.

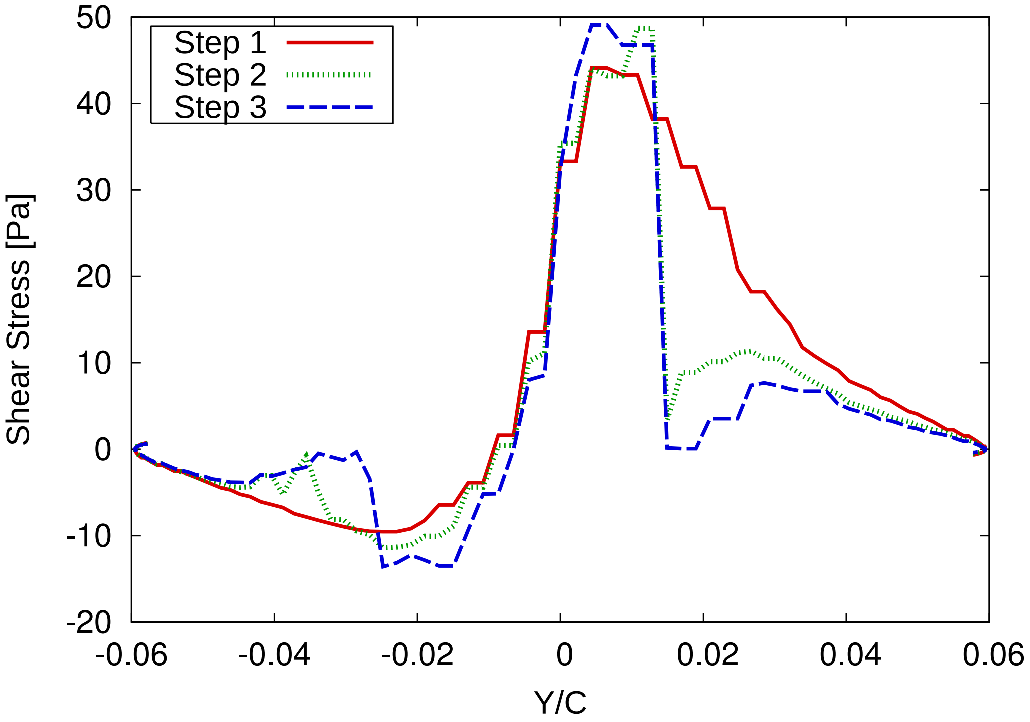

Figure 4.11: *Multi-stepping calculation performed in* 3 *steps of* 2 *min each, for a* 6 *min total exposure time. Evolution of the shear stress in glaze icing.* $T_\infty = -5.6^oC$, $\alpha = 4^o$.

The same sort of changes occur with the heat transfer coefficient.

Heat Transfer Coefficient

The evolution of the heat transfer coefficient for glaze icing is shown in Figure 4.12. The first step, evaluated on the clean airfoil has been described in the previous section. The second and third steps show that this parameter clearly evolves with the accretion. Although a bit more jagged when determined on the ice covered wing, no significant difference is noticeable on the lower surface. However, the heat transfer coefficient is largely different when $y/c > 0$, more precisely past the large decrease at $y/c = 0.01$. A new peak is noticeable on the upper nose surface: this corresponds to the point where the ice layer stops. Consequently, these variations of the heat transfer coefficient will not affect the ice growth. On the clean surface,

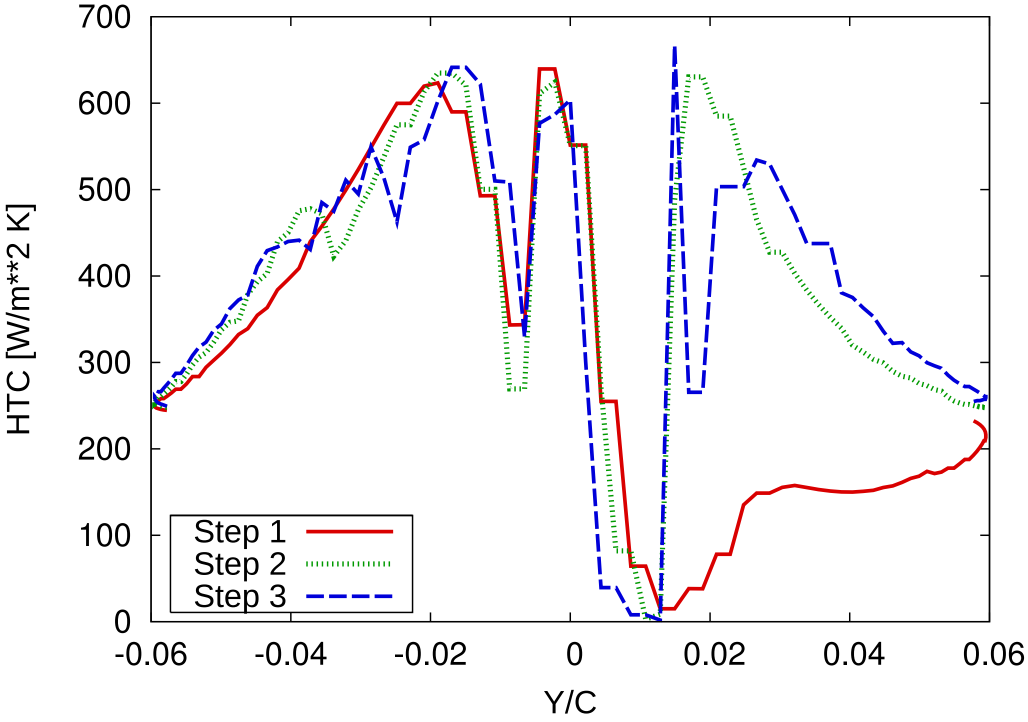

Figure 4.12: *Multi-stepping calculation performed in* 3 *steps of* 2 *min each, for a* 6 *min total exposure time. Evolution of the HTC in glaze icing.* $T_\infty = -5.6^oC$, $\alpha = 4^o$.

this increase is smoother and of weaker intensity: on iced surfaces, this corresponds to the point where flow separation occurs. The high values of the heat transfer coefficient will trigger a rather high ice growth rate in the regions concerned.

However, the quality of the results obtained with the flow solver may be questioned: this solver was not developed to deal with high surface deformations that exist in glaze conditions, as stated in [78]: *"when the near-wall flows are subjected to* *severe pressure gradients, the quality of the predictions is likely to be compromised".* Coupled with a coarse grid, this explains the first thin sharp peak occurring around $y/c \approx 0.015$ during the third step. Despite these defects, in the following, the general trend of the heat transfer is considered acceptable. This parameter will be calculated inside the icing module in the ICECREMO2 code used from the next chapter.

Ice Height

The evolution of the ice growth for a two-step rime ice prediction is shown in Figure 4.13. The ice height obtained in the second step is added to the ice height from the first one. The final ice shape reflects the variations of the collection efficiency. This ice shape becomes thinner and thinner and the single horn structure continues to grow in the vicinity of the nose region. Less ice accretes on the upper surface of the wing in the second step of the calculation. As this part of the surface is shadowed by the existing ice, no droplet impinges in this region. This situation is even accentuated with the inclination of the airfoil, $\alpha = 4^o$. This is consistent with the collection efficiency values but the phenomenon is enhanced by the new surface

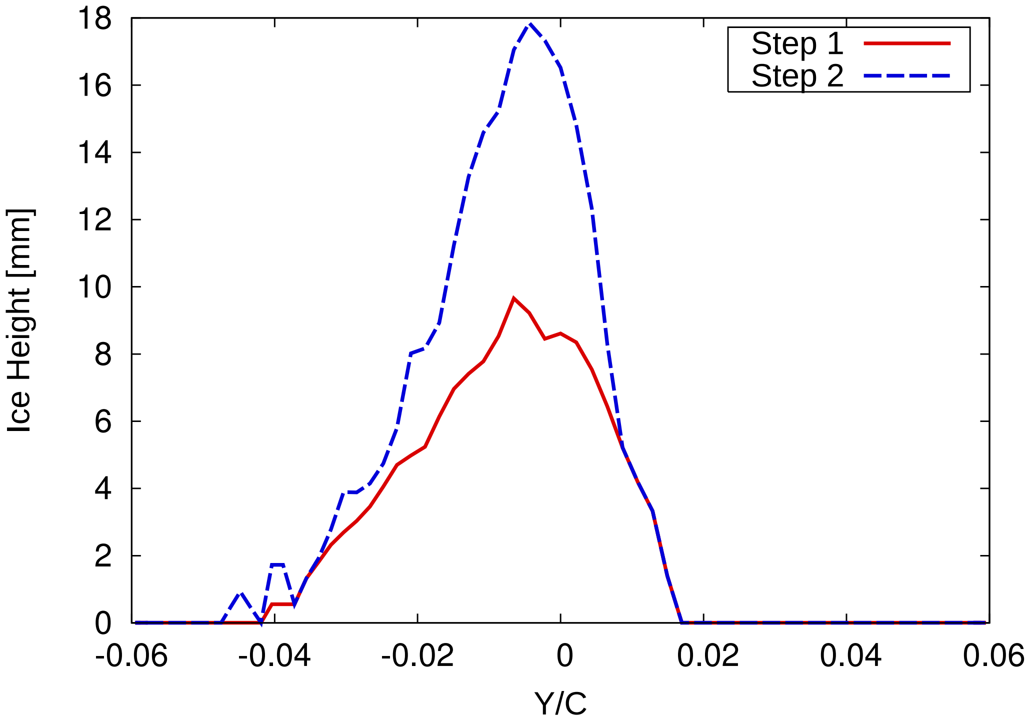

Figure 4.13: *Ice height determined with a multi-stepping calculation performed in* 2 *steps of* 3 *min each, for a* 6 *min total exposure time in rime icing.* $T_\infty = -26^oC$, $\alpha = 4^o$.

geometry. Supercooled droplets still impinge on the lower surface and the ice layer reflects the jagged aspect of the collection efficiency.

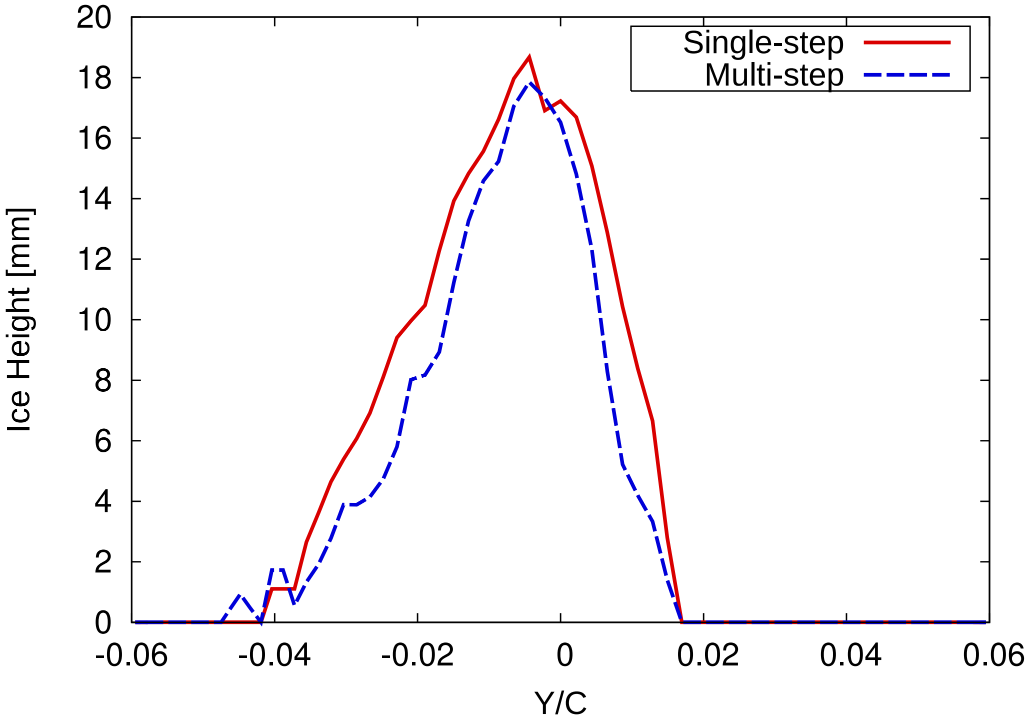

Figure 4.14: *Comparison of ice height for single and multi-step calculations performed in* 2 *steps of* 3 *min each, for a* 6 *min total exposure time in rime icing.* $\alpha = 4^o$, $T_\infty = -26^oC$.

To quantify the effect of a multi-step procedure on the final ice shape, the ice heights from single and multi-step simulations are plotted together in Figure 4.14. The multi-step algorithm does not differ significantly from single-step results. It extends a bit further on the lower part of the wing and the bulk of the multi-step ice shape is slightly thinner. As already mentioned, this reflects the variations of the collection efficiency.

The effect of the multi-step algorithm is far more obvious in glaze ice conditions. Figure 4.15 shows the evolution of glaze ice for three steps of two minutes at the temperature $T_\infty = -5.6^oC$. In this case, the ice accretes mainly in the nose region and on the upper part of the wing. The simulated ice shape around the nose region reflects the evolution of the collection efficiency and shear stress and in a higher proportion, the evolution of the heat transfer coefficient. Two peaks were noticeable in the heat transfer coefficient evolution before the flow separation. These two peaks are also apparent in Figure 4.15 and correspond to the horns that form from part to part of the stagnation region.

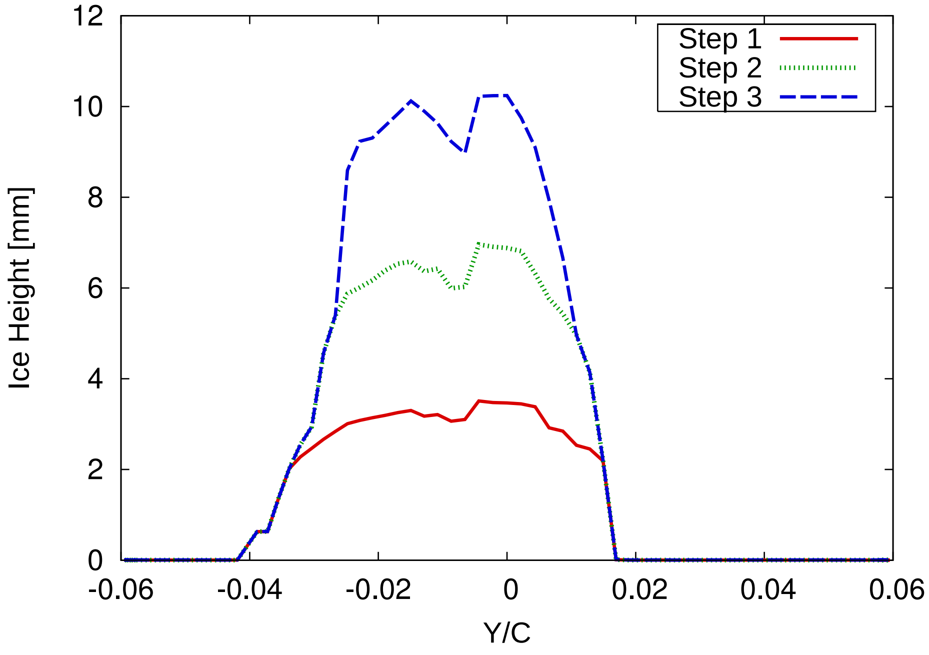

Figure 4.15: *Ice height determined with a multi-stepping calculation performed in* 3 *steps of* 2 *min each, for a* 6 *min total exposure time in glaze icing.* $T_\infty = -5.6^oC$, $\alpha = 4^o$.

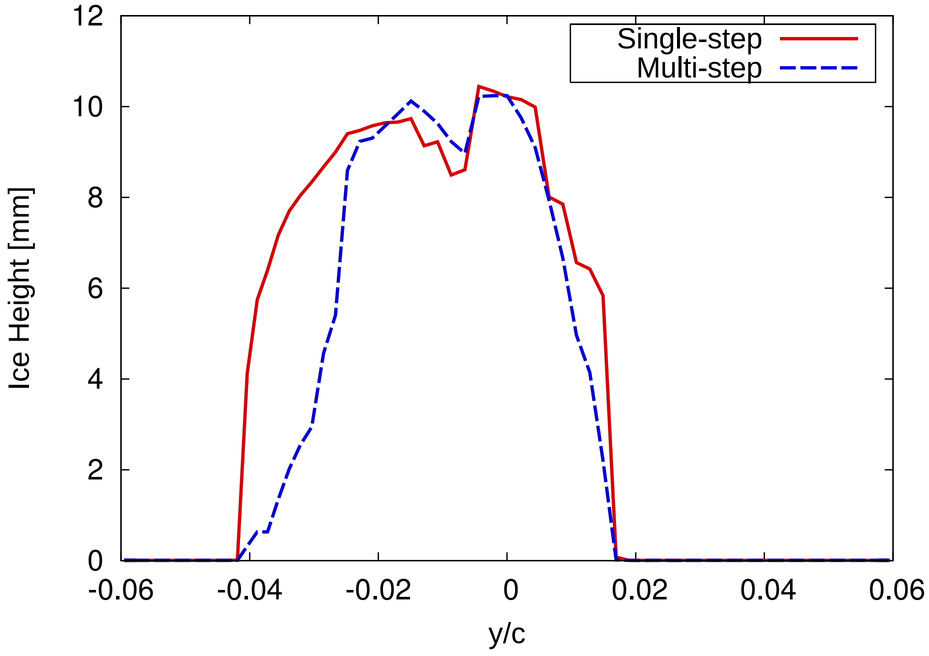

Figure 4.16: *Comparison of ice height for single and multi-step calculations performed in* 3 *steps of* 2 *min each, for a* 6 *min total exposure time in glaze icing.* $\alpha = 4^o$, $T_\infty = -5.6^oC$.

Figure 4.16 shows the comparison between the single and the multi-step predictions in glaze ice conditions. Both calculations estimate almost the same maximum ice height, around $b_{max} \simeq 10.5\ mm$. The multi-step shape is not as wide as the single-step ice shape, this again reflects the evolution of the collection efficiency. This is also a consequence of the water behaviour that will now be discussed.

Water height

The water layer model is simplified in this early version of the code, traditionally used in current multi-step algorithms. The evolution of the water height in glaze ice conditions may be seen on Figure 4.17. In all three cases, the features observed in the one-step calculation appear: the water height has a maximum value at the end of each step around $h \simeq 0.007\ mm$ and on either side, the water is driven downstream by the shear stress and this determines the height of the plateaus that are formed. The small height variations observed are caused by the heat transfer coefficient that governs the ice growth rate and therefore the water height. The extent of the water

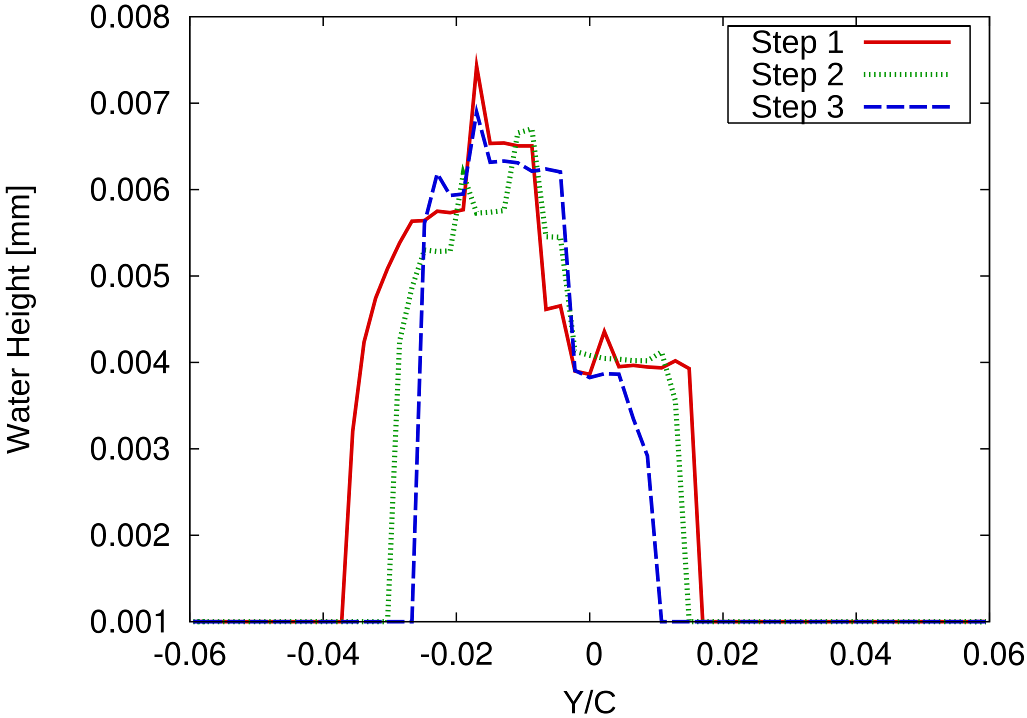

Figure 4.17: *Evolution of the water height obtained with a multi-step calculation performed in 3 steps of 2 min each for a 6 min total exposure time in glaze icing.* $\alpha = 4^o$, $T_\infty = -5.6^oC$.

layer reduces as time goes by and is smallest at the end of the latest multi-time step. This is a direct consequence of the simplified algorithm: at the end of each multi-time-step, the water and ice layers are integrated in the surface geometry and the new multi-time step starts with and ice and water free surface. The extent of the water layer is then limited by primarily the collection efficiency but mainly the chosen duration of the multi-time step. This means that the results depend greatly on a choice made in the numerical model with absolutely no physical meaning. This is clearly not acceptable and the model should be upgraded.

Conclusion

This chapter has shown the evolution of the icing parameters under rime and glaze ice type accretions. The parameters evolved differently when calculated on the clean surface, in the case of a single-step calculation or on the iced surface in the case of multi-step predictions. Limitations due to the lack of water update between the different steps of the calculation have been described. The iced surface temperature should therefore be different and also updated between the steps. These limitations are addressed in the new version, ICECREMO2, and this model will be studied in the next chapter. To conclude the present study, the ice heights obtained in this section for rime and glaze situations are now plotted directly on the airfoil and compared to experimental data.

4.5 Comparison with Experimental Results

Experimental results for aircraft icing are not easily released by aircraft companies. This section is based on data from Shin and Bond [17], corresponding to the conditions described in Section 4.2.

4.5.1 Rime Ice Conditions

The numerical results are first compared with experiments in rime ice conditions, at $T_\infty = -26^oC$, for an exposure time of six minutes. The resulting experimental shape is rather typical of rime ice accretion, as may be seen in Figure 4.18. The accreted ice concentrates at the leading edge of the wing and forms a smooth peak pointing in the upwind direction. The shape decreases smoothly on both sides of the peak and extends rather far down the lower aft of the wing due to the angle of inclination, $\alpha = 4^o$. Three numerical simulations were carried out to approximate

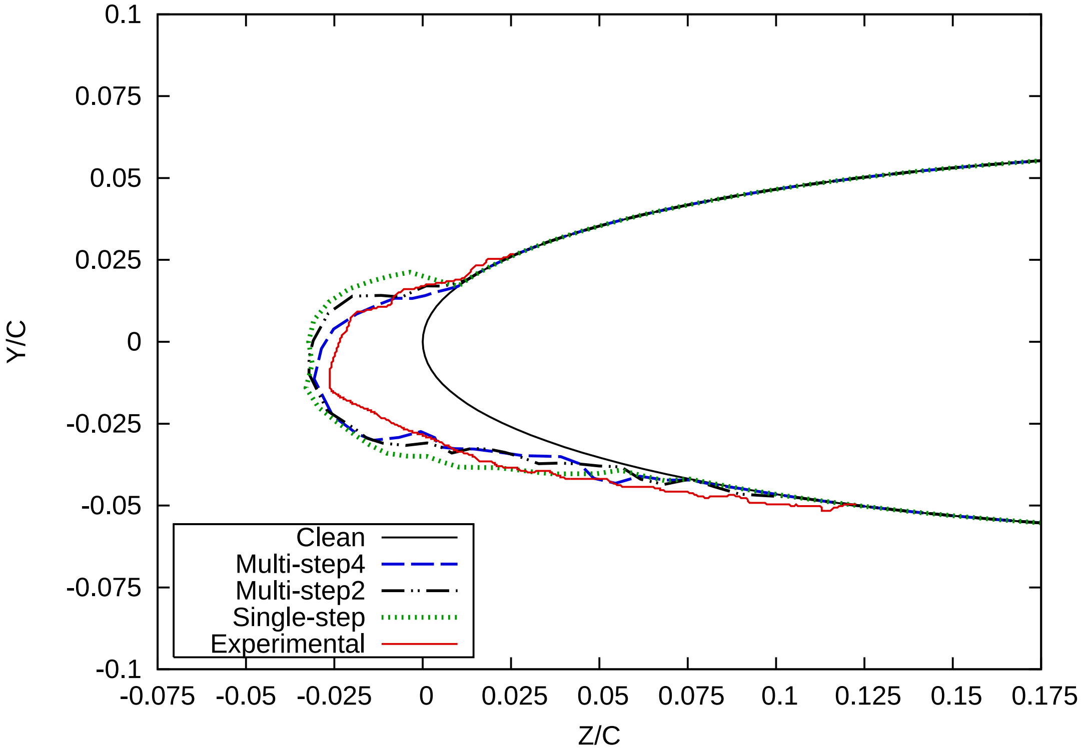

Figure 4.18: *Comparison of ice shapes obtained on a NACA0012 wing with experimental data. Single and multi-step calculations (2 and 4 steps) are performed for a* 6 *min total exposure time under rime icing.* $T_\infty = -26\ ^oC$, $\alpha = 4^o$.

this shape. A single step calculation was performed first. As already mentioned, due to the low temperatures, the ice layer is exactly proportional to the collection efficiency. The simulated ice layer is significantly thicker and wider than what was measured experimentally and reflects the shape observed in Figure 4.2: two very small horns appear at the very front of the ice layer and the global shape is quite far from the experimental results.

Two other calculations were performed using a step-by-step algorithm. In one case, the exposure time was divided into two steps of three minutes each, in the other case, four steps of 90 seconds each were considered. In both situations, the simulated shapes are much closer to experimental observations. First, the excess of ice noticed at the front is clearly smaller and this aspect improves with the number of multi-time steps used: this is consistent with results of Section 4.4 for the collection efficiency. For a similar reason, the extent of the ice layer is better described as the number of multi-time step increases.

The geometry of the shape is also getting closer to experimental results when the multi-step algorithm is used: the two little horns formed during the single-step simulation have disappeared and the smooth peak structure becomes more evident, particularly in the four-step calculation results. The results for a two-step algorithm on the three-dimensional wing structure may be seen on Figure 4.19. The shape remains approximately constant along the cross section. Small discrepancies due to slight variations in the collection efficiency may be noticed, particularly along the stagnation line.

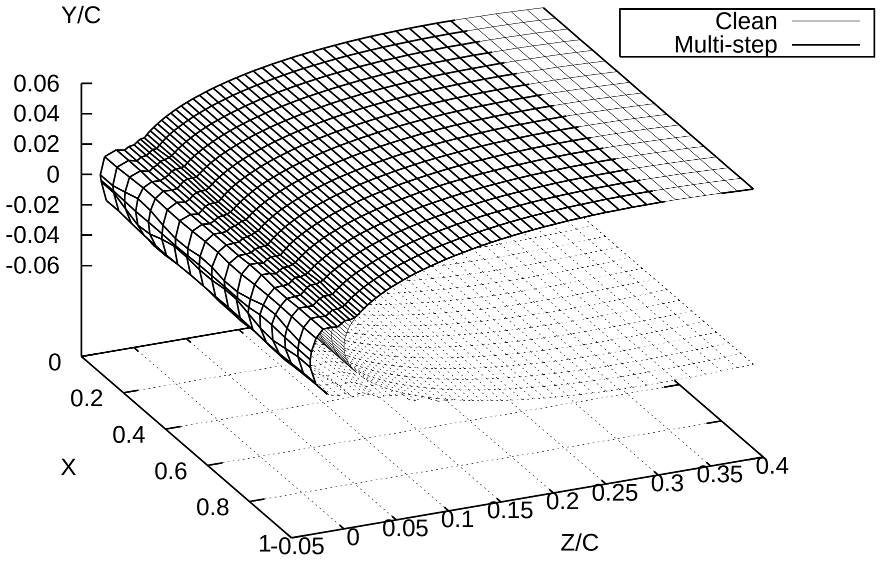

Figure 4.19: *3D ice shape obtained with a multi-stepping calculation performed in* 2 *steps of* 3 *min each for a* 6 *min total exposure time under rime icing,* $T_\infty = -26\ ^oC$, $\alpha = 4^o$.

The multi-step procedure has a globally positive effect in rime ice conditions. Glaze ice conditions will now be studied.

4.5.2 Glaze Ice Conditions

Numerical simulations and experimental results will now be compared in glaze ice conditions, at $T_\infty = -5.6^oC$, here again for an exposure time of six minutes, as may be seen in Figure 4.20.

The experimental shape is now very far from being proportional to the collection efficiency. A peak of ice has formed next to the leading edge. The ice thickness drops very sharply towards the upper aft of the wing, and the region is now totally

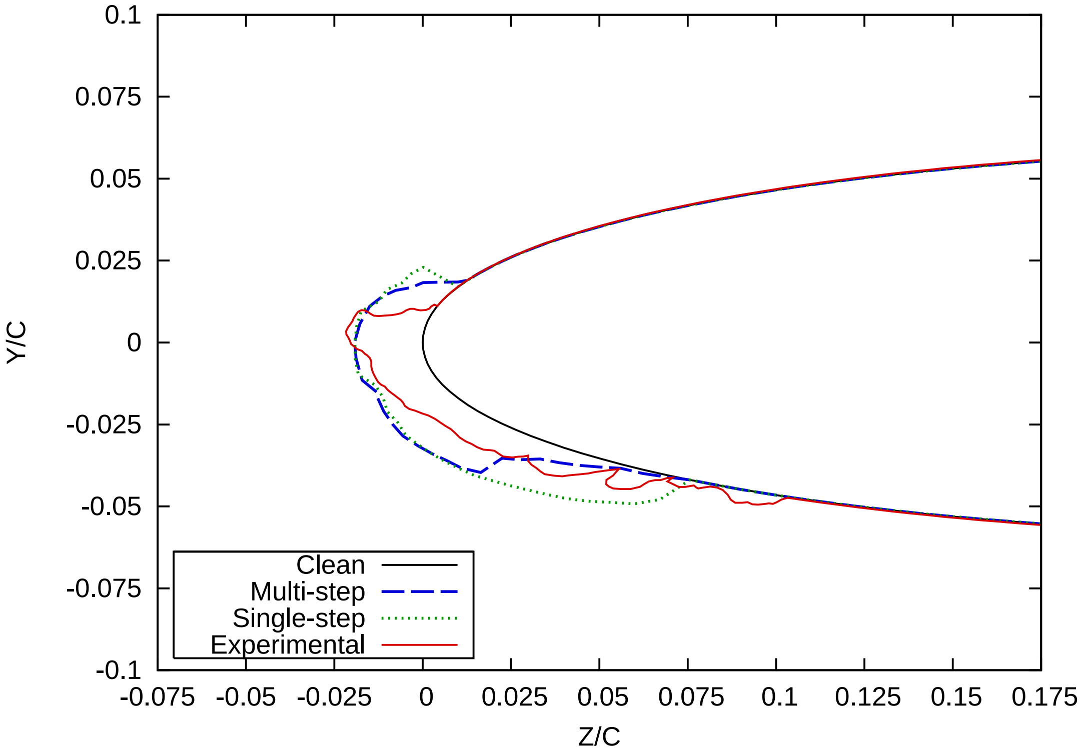

Figure 4.20: *Single/multi-step and experimental shapes obtained on a clean NACA0012 wing for a* 6 *min total exposure time under glaze icing.* 3 *steps of* 2 *min each,* $\alpha = 4^o$*,* $T_\infty = -5.6^oC$*.*

ice free. The ice accretion decreases progressively on the lower aft of the wing and extends very far downstream. Here again, this occurs because of the inclination angle of 4^o.

Two simulations were carried out: a single and a multi-step calculation. The experimental curve is characterised by a peak near the stagnation point. The ice layer decreases very abruptly on the upper aft while the evolution is much smoother on the lower aft and it extends for a rather long distance downstream. These characteristics do not appear very clearly in the one-step result. The peak at the leading edge is totally absent. The simulated ice layer is very smooth in this region and the ice layer extends slightly further downstream and stops even more abruptly than the experimental shape. An extremely smooth layer has accreted on the lower aft with a rather sharp stop. The rather spiky collection efficiency is totally smoothed out by the presence of the water running back over the top of the ice layer. This shape is characteristic of simulation in glaze ice but does not compare very well with experimental data.

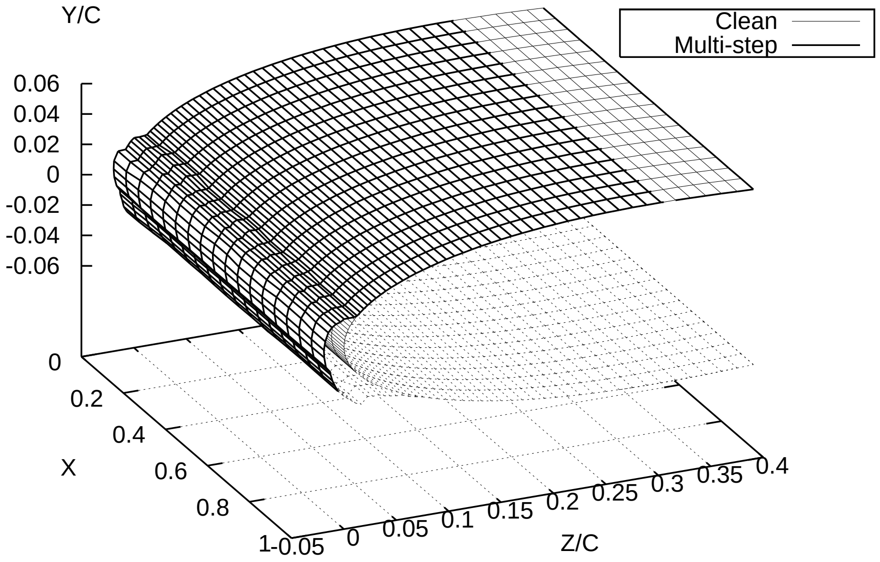

Figure 4.21: *Ice shape obtained with a multi-stepping calculation performed in* 3 *steps of* 2 *min each on a NACA0012 wing, for a* 6 *min total exposure time under glaze icing.* $T_\infty = -5.6^oC$, $\alpha = 4^o$.

The effect of the multi-step algorithm is less obvious than in the rime ice conditions. In this case, three multi-time steps of two minutes were used. The ice layer is identical in the nose region. However, the peak characteristic appears slightly, though without most of its sharpness. The layer on the upper aft readjusts more progressively to zero. On the lower aft, the ice thickness drops suddenly as in the one-step simulation but this occurs at a level that compares much more favourably with experimental results. This aspect would probably be improved without merging the ice and water layers to the wing geometry between each of the multi-steps. In general, the amount of ice formed remains however much larger than the quantity observed experimentally.

Finally, the complete three-dimensional shape corresponding to the multi-step calculation may be seen on Figure 4.21. Here again, the cross section remains more or less constant along the span. Only small variations may be noticed in this direction; they are probably due to small variations of the collection efficiency or heat transfer coefficient.

4.5.3 Effects of Multi-Stepping

The multi-step algorithm clearly changes the simulation results in two ways:

1. The amount of ice forming over the surface decreases with the number of time steps. This is related to the variation observed for the collection efficiency: the flow is more turbulent around the ice layer and droplets are less inclined to hit the wing surface. Despite the reduced amount of ice in the rime ice conditions, the ice layer is too thick at the leading edge and too thin further downstream. In glaze ice conditions, the layer remains too smooth at the leading edge and too thick further downstream.

2. The geometry of the layer is clearly modified when the number of steps is increased: the higher the number of multi-time steps, the closer the ice layer gets to experimental results. The extent of the ice layer remains however quite different from experimental observations. This points out a weakness in the droplet trajectory calculation or heat transfer coefficient evaluation.

4.6 Conclusion

In this chapter the basic implementation of a step-by-step algorithm traditionally used in aircraft icing has been studied using the ice prediction code ICECREMO1. A single-step simulation has been performed as a starting point for comparison and then, the evolutions of the key icing parameters have been detailed. The effects of the multi-step algorithm have been outlined:

1. In rime ice conditions, the use of the multi-step algorithm has clearly improved the accuracy of the prediction: taking into account the time variation of the key collection efficiency parameter has proved very successful.

2. The results are less convincing in the glaze ice case but improvements were still pointed out. Incorporating the ice and water layers to the wing geometry could be part of the difficulty encountered.

Comparison with shapes measured experimentally show that generally too much ice forms during the simulations and the ice layer extent does not correspond to experimental values. However, the use of a multi-step procedure tends to reduce this trend. The implementation of the step-by-step algorithm has therefore proved successful. It has also underlined that the water layer and temperature information should be transmitted from one multi-time step to the other. If this is not performed, the ice layers simulated in glaze ice conditions are dependent on user chosen parameters. These corrections will be performed in the next chapters, when the icing module ICECREMO2 is in use.

Chapter 5

Advanced Step-by-Step Implementation

5.1 Introduction

A preliminary study of multi-stepping has been carried out in the previous chapter using the ICECREMO1 code. When rime ice grows, only the collection efficiency should be recalculated. When glaze ice grows, the ice shape also depends on the heat transfer coefficient and shear stress. So far, all these parameters have been re-evaluated every two or three minutes. The objective of this chapter is to perform a more systematic study of the criteria used to trigger a new flow calculation. The following points will be investigated and adapted to the ICECREMO2 code:

1. Define the sort of criterion to be used,
2. Study the convergence of the methods,
3. Analyse the ice shapes for various configurations,
4. Conclude about the best method to be used.

Limitations were present in the multi-step procedure implemented in the initial icing code ICECREMO1: the update of the water was not performed and the temperature history was not preserved between the different steps of the calculation. These difficulties have been solved in ICECREMO2 and this version of the icing routine is used in this chapter. The simulated results generated in this chapter will be compared to those obtained with standard aircraft icing codes.

5.2 Trigger Criteria for a New Flow Calculation

A criterion triggering the flow calculation will now be defined. The objective is to find the optimum number of multi-time steps, this means the number of times the step-by-step algorithm should be repeated, bearing in mind:

- Each flow calculation is extremely long and their number should be as small as possible to reach an acceptable global simulation time.
- Accuracy is lost when too many steps are used. The re-meshing process is based on a Non Uniform Rational Basis Spline (or Bézier Spline), the deformation of the surface due to icing may not always be described in a satisfactory fashion and errors will pile up.
- If the number of steps is too small, the insufficient update of the flow parameters will not reflect the real evolution of flow parameters and again errors increase with time.

Two methods will be considered in the present work:

1. **Time criterion**

   A multi-stepping procedure based on a multi-time-step calculation is the simplest procedure. The flow is systematically recalculated at the start of each multi-time-step with the duration held constant for the entire calculation and defined at the start of the procedure. This is the most widely used procedure [57, 99, 100, 116]. Two equivalent methods may be used to define the length of the multi-time-steps:

   - The user directly chooses the duration of multi-time steps.
   - An alternative method is based on the chord length: the number of steps is dependent on the geometry studied. According to Wright [117], the maximum amount of ice in any step should not be greater than 1% of the chord. This number of steps n_{step} may be estimated using the following expression [118]:

   $$n_{step} = \frac{1}{Xc}\left[\frac{(LWC)V_\infty t_{exp}}{\rho_i}\right] , \tag{5.2.1}$$

   where LWC is the liquid water content, t_{exp} the exposure time, V_∞, the airstream velocity and c denotes the chord length. The term in the square brackets represents the maximum ice height that could form during the exposure time t_{exp} and X represents the proportion of chord length c considered. The proportion of the chord, $X = 1\%$ for example, should be chosen by the user, although it remains constant in the multi-step procedure implemented in LEWICE [118]. For very small geometries such as cylinders, this may lead to a prohibitive number of multi-time steps [119]. In the current work, this method will not be studied as it appears only as an automated version of the standard step-by-step algorithm.

2. **Ice height criterion**

   A time based criterion may not be the most appropriate method when glaze ice is growing: the preliminary studies in the previous chapter proved that the layer is much wider and may come out much thicker locally. The flow is therefore likely to become really disturbed by the ice layer before the time of a multi-step has elapsed. A criterion based on the ice height may therefore be much more effective: a new flow calculation is started when the ice height growing during the exposure time at any location on the surface reaches a value chosen by the user.

The criteria defined in this section will now be studied on classical geometries such as a cylinder and a NACA0012 wing.

5.3 Ice Predictions on Cylinders

Cylinders are a very convenient geometry to begin an icing study: they limit the difficulties related to surface geometry and the flow around this geometry has been studied extensively. Numerical simulations obtained with a single-step evaluation and experimental tests have been conducted during the NATO/RTO exercise held in December 2000 [120] on the two cylinder configurations studied in this chapter. These test cases were referred to as case $O5$ and case $O6$, they will be called $O1$ and $O2$ in the following as they are the only two cylinder configurations studied in the present work.

In the two cases, a cylinder of diameter $c = 6.35$ cm is flowing at the velocity $V_\infty = 77.2$ m/s. Supercooled droplets at the temperature $T_\infty \simeq -3^oC$ are introduced in the system in glaze ice conditions. The liquid water corresponds to $LWC = 0.44$ g/m^3 in case $O1$ and $LWC = 0.37$ g/m^3 in case $O2$. In the first case, small droplets are studied ($d_d = 18$ μm) whereas in the second case, larger droplets ($d_d = 100$ μm) are launched far away from the body. The latter ones fall in the category of supercooled large droplets (SLD), their diameter being greater than 50 μm. Airflow and icing conditions are listed in Table 5.1. When possible, the experimental data from the NATO/RTO exercise will be used to compare the criteria, as will be seen in the following section.

	c **[mm]**	**V_∞** **[m/s]**	**LWC** **[g/m^3]**	**d_d** **[μm]**	**t_{exp}** **[s]**
case 01	63.5	77.2	0.44	18	330
case 02	63.5	77.2	0.37	100	330

Table 5.1: *Airflow and icing conditions applied to cylinders during the NATO/RTO validation exercise held in December 2000 [120].*

5.3.1 Time Criterion

Single and multi-step calculations are presented in this section for rime and glaze ice conditions applied to the cylinder. The first criterion tested is based on time and simulations are performed with a various number of multi-time steps. The procedure is tested, starting from a 1-step up to a 20 multi-time-step algorithm. The duration per step is manually defined by the user and the ice accretion is studied for a total exposure time $t_{exp} = 330$ seconds. The objective of this section is to determine the ice shape convergence under various icing conditions.

Rime ice conditions

Simulations are carried out when rime ice grows. The cylinder case $O1$, as described in Table 5.1, is first studied. For this analysis, the angle of attack is $\alpha = 0^o$ and the airflow temperature is $T_\infty \simeq -26^oC$. Final ice shapes obtained with single and multi-step calculations are plotted together as may be seen on Figure 5.1. Different multi-time steps have been studied for a total icing exposure time $t_{exp} = 330$ seconds. However, for the sake of clarity, only the relevant ice shapes are presented here, the objective of this study being to analyse their convergence. All simulation results obtained on the case $O1$ in rime ice conditions are presented in Appendix B.

As could be expected, the estimated ice shape in rime ice conditions reflects the collection efficiency. It has a streamlined appearance that points out in the air flow

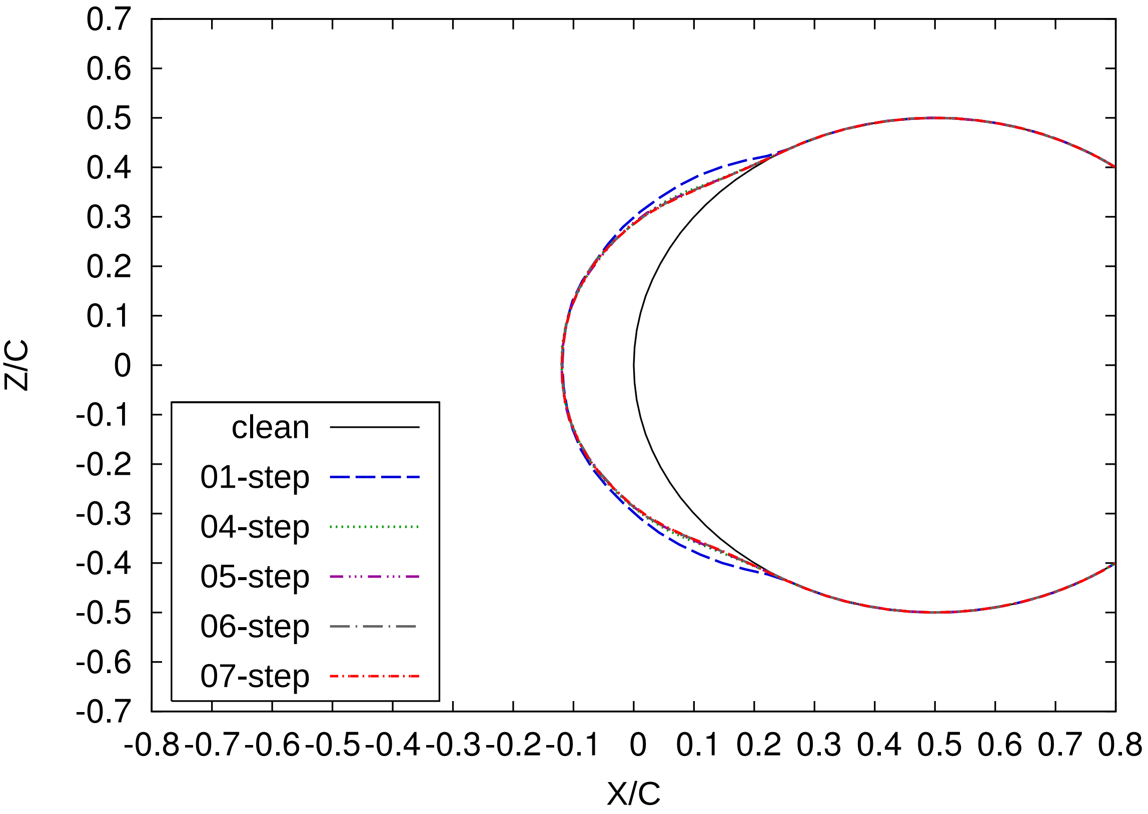

Figure 5.1: *Rime ice shapes obtained on a cylinder with a step-by-step calculation based on the time-criterion. Exposure time: 5min 30s.* $T_\infty \simeq -26^oC$.

direction. The shape is symmetrical, this is consistent with the small diameter of the incoming droplets and the angle of attack $\alpha = 0^o$. On the forward part of the cylinder, the predicted ice shape does not differ significantly when performed either in a single or in a multi-step algorithm: the latter predicts an ice height slightly higher in the stagnation region, although this is not obvious from Figure 5.1. The global ice layer is however slightly thicker for the one-step calculation. This is consistent with the results of the previous chapter. The ice shape mainly varies at the top and bottom boundaries of the cylinder $(x/c = 0.25, z/c = \pm 0.43)$, and the ice layer reduces slightly when the number of time step increases. This may clearly be seen in Figure 5.2. The full convergence is achieved for 6 multi-time steps: no significant ice shape difference may be noticed between the 6-step and the 7-step algorithm. However, the 4-step calculation provides results very close to convergence. This solution should be favoured since it will save a considerable amount of time.

An average value of the ice height per step may be defined as the total ice

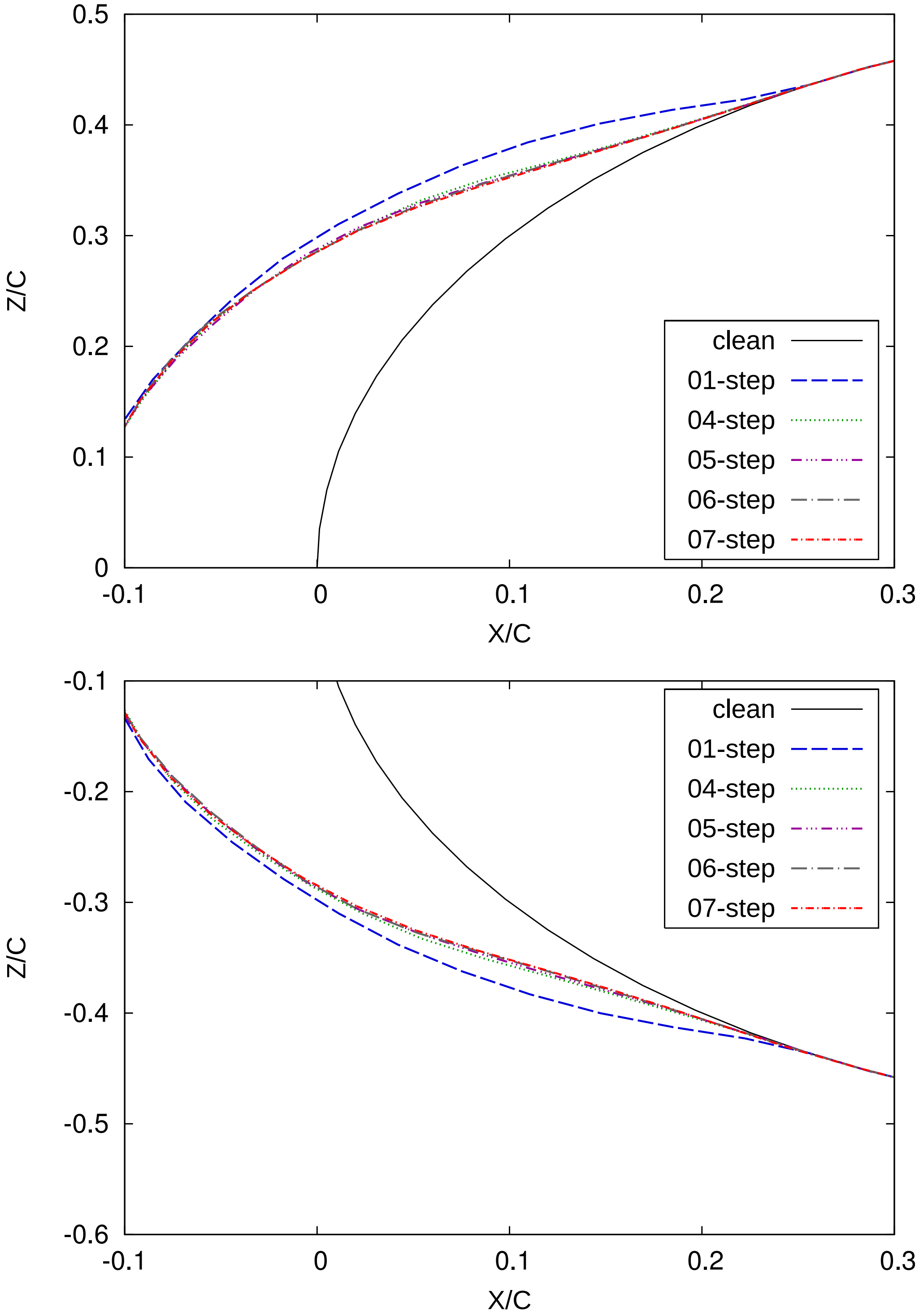

Figure 5.2: *Closer view of the rime ice shapes obtained on a cylinder with a step-by-step calculation based on the time-criterion. Exposure time: 5min 30s.* $T_\infty \simeq -26^oC$.

height divided by the number of steps. For this test case performed in 4 steps, this is equivalent to the proportion of diameter length $X = 3\%$. However, the real proportion of chord should be established for the 6-step algorithm, equal to $X = 2.16\%$. This value is more or less consistent with the theoretical proportion of chord $X = 3.3\%$ determined from Equation 5.2.1 used in LEWICE [118] for a number of steps equal to 6.

The same atmospheric conditions, except for the droplet size and airflow temperature, are applied to this cylinder for glaze ice study. This will now be described.

Glaze ice conditions

Final ice shapes obtained in glaze ice conditions with single and multi-step algorithms are plotted together against the experimental shape as may be seen in Figure 5.3. Different multi-time steps have been studied at the temperature $T_\infty \simeq -3^oC$

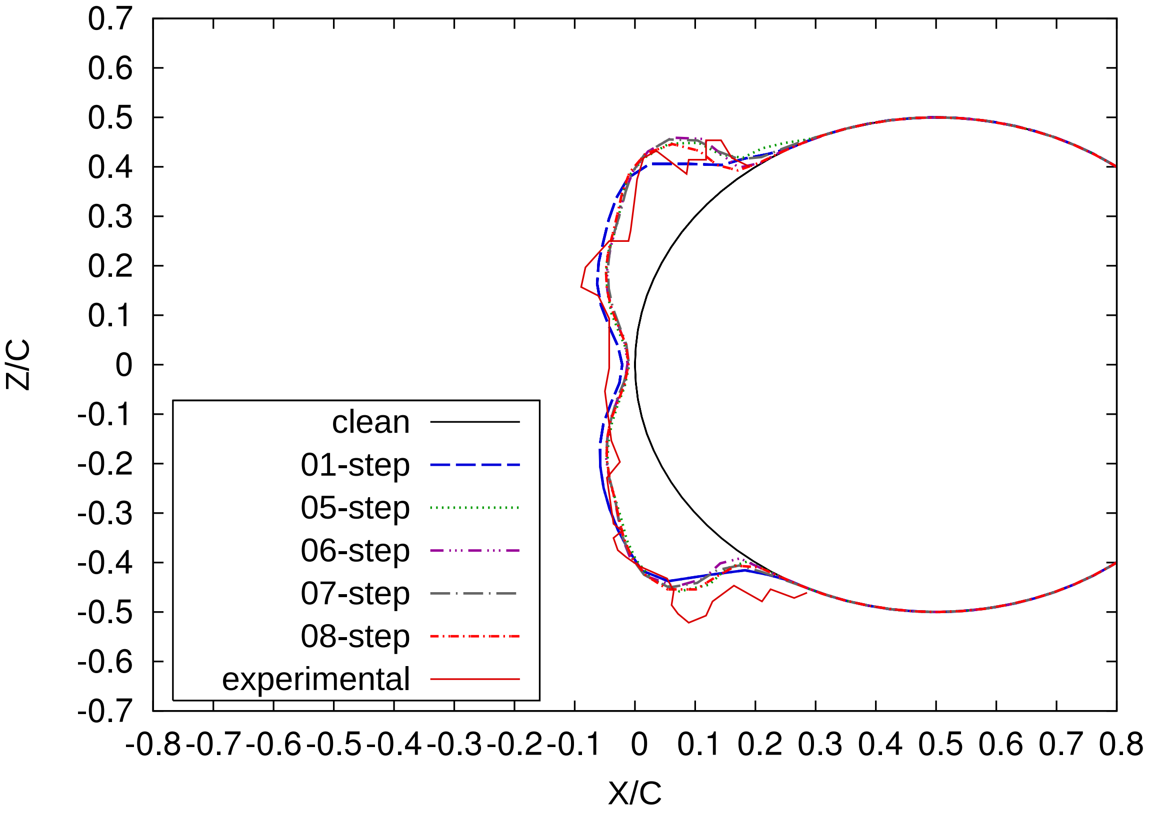

Figure 5.3: *Glaze ice shapes obtained on a cylinder with a step-by-step calculation based on the time-criterion. Small droplets. Exposure time: 5min 30s.* $T_\infty \simeq -3^oC$.

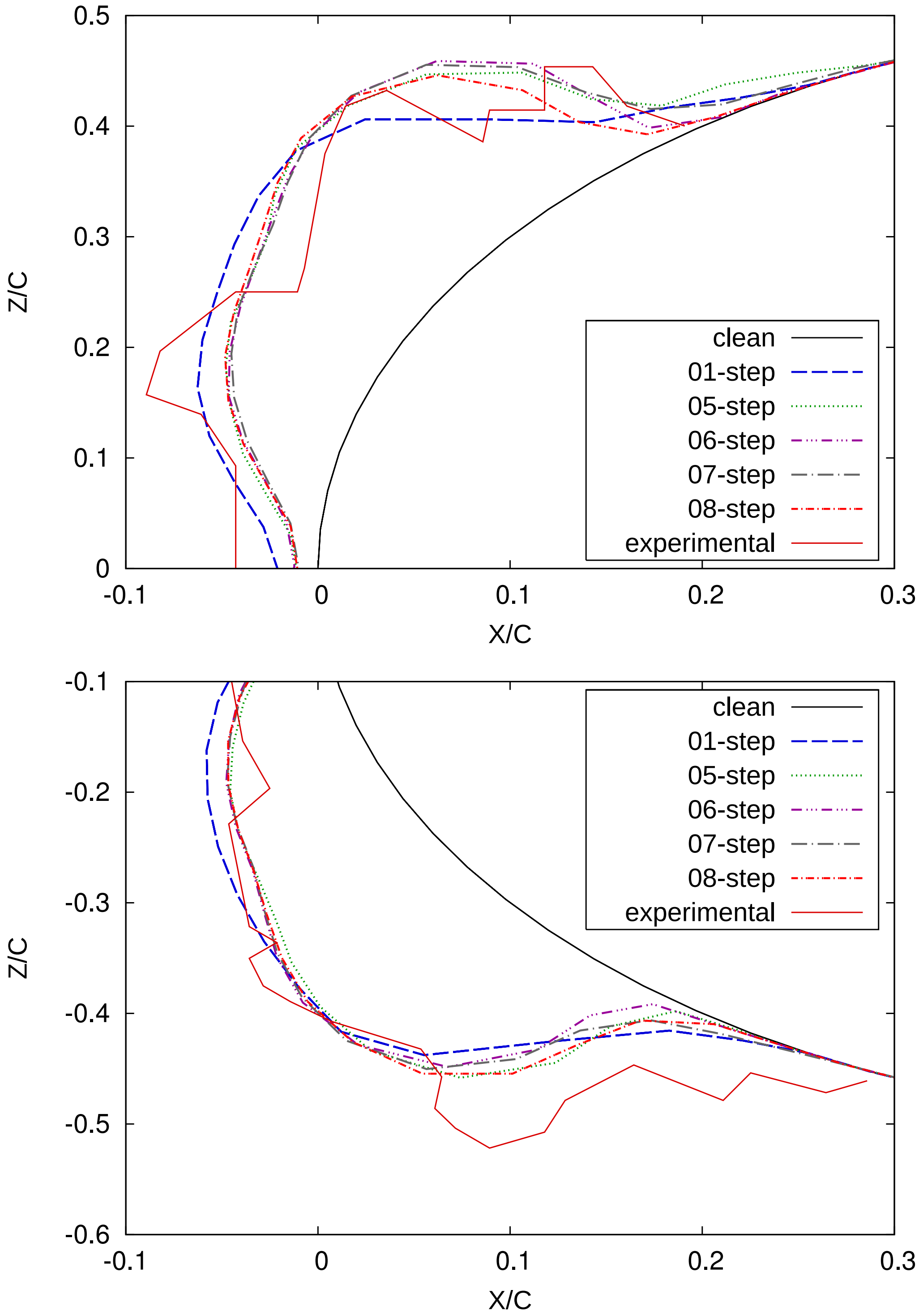

Figure 5.4: *closer view of the glaze ice shapes obtained on a cylinder with a step-by-step calculation based on the time-criterion. Small droplets. Exposure time: 5min 30s.*

for a total icing exposure time $t_{exp} = 330$ seconds. Once again, for the sake of clarity, only the essential ice shapes are described here. Additional simulations results obtained on the case $O1$ are however presented in Appendix C.

The experimental results show two different regions. Around $z/c = 0$, near the stagnation line, the ice layer is constant (and covered by a thin water film). Further away from the stagnation region, the ice layer becomes much thicker and a double horn structure, typical of glaze ice has formed, consequence of heat transfer coefficient variations mainly due to the roughness effect [121].

The estimations are relatively close to experiments and they all depict the different regions of the ice layer. Distinctions between predictions are more apparent on the closer view, see Figure 5.4. As may be seen, the convergence of the ice shape based on the time-criterion is rather difficult to obtain (see Appendix C for more details). The benefits of using a high number of multi-time steps is not obvious: a predicted ice shape with a 10-step or 20-step calculation is not more accurate than a 5-step or 6-step calculation. Convergence seems to be reached for 6 multi-time steps as the final ice predictions obtained in 6 and 7 steps are relatively close in all regions except for the limits on the upper and lower surfaces. When increasing the number of multi-time steps, the benefits seem to be lost due to error accumulation.

All the curves, including the one-step result, have however about the same profile:

- The horn structure is more or less accurately described, with minor differences between top and bottom. The ice extent on the upper surface of the cylinder is the same for all simulations, around $z/c = 0.43$. In all cases, the multi-step evaluation compares better to experiments than the single-step procedure.

- In the vicinity of the stagnation region, the ice layer is not constant: it reaches its lowest point for $z/c = 0$ and the ice height increases progressively on both sides. The estimated ice height in this region is slightly better predicted with the single-step calculation. At the stagnation point, the ice height is around $b \simeq 1.4$ mm for the single-step algorithm whereas the ice estimation is around $b \simeq 0.9$ mm for the multi-step predictions. This predicted ice shape, much thinner than expected in the stagnation zone, is due to the temperature on the substrate: this temperature is maintained constant during the ice accretion. In reality, heat is released inside the cylinder and the temperature of the substrate increases slightly. With the present model, heat is piling up inside the ice layer and this is equivalent to switching a heater on. This is particularly noticeable at this location because the layer is comparatively thinner than most places and supercooled droplets hit this position continuously.

A multi-step algorithm predicts the ice shape more accurately than a single-step procedure. The double horn structure is estimated with more accuracy. While the best simulation in the stagnation region is obtained with the single-step procedure, the multi-step result matches the experimental data better when looking at the overall shape. For the present study, convergence has been achieved with the 6-step algorithm. The average value of the ice height that forms per step may be determined, which is equal to $X = 2.36\%$ of the diameter length c. This value is a bit lower than the theoretical proportion of diameter length $X = 3.2\%$ determined from Equation 5.2.1, which is used in the ice prediction code LEWICE.

As pointed out in the previous chapter, the thin water layer flowing back over the ice layer is a key element of the model. To conclude this first example in glaze ice conditions, the evolution of this layer will be studied briefly.

Influence of the water height update:

The ice shape previously generated with the 6-step algorithm based on the time criterion was performed with a complete update of the water film between the different

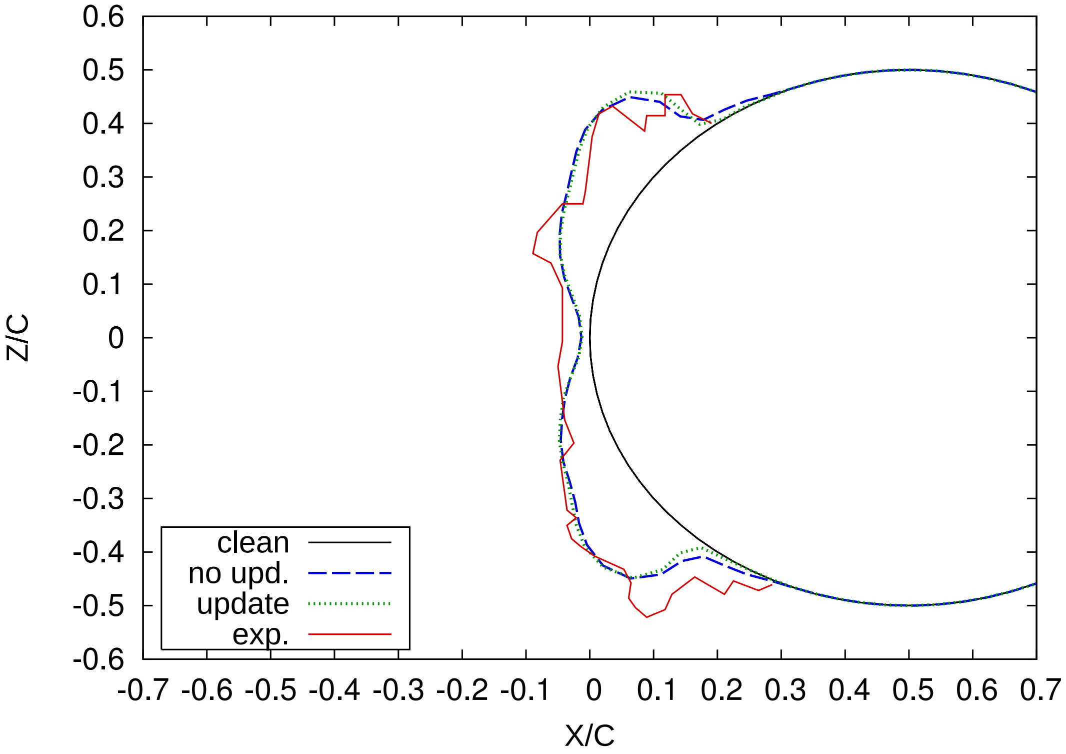

Figure 5.5: Influence of the water height update in a 6-step multi-stepping algorithm based on the time-criterion. Exposure time: 5min 30s. $T_\infty \simeq -3^oC$.

steps of the procedure. This result, shown in Figure 5.5, is compared to a 6-step multi-step calculation performed this time without retaining information on the water height from one multi-step to the next. In the latter case, a special algorithm has been used, very similar to the one developed for ICECREMO1 and detailed in the previous chapter: the ice and water layers are considered to be part of the wing, the thermal history of the existing ice layer is completely ignored and the calculation is restarted with this new geometry as it was ice free.

The estimated ice shapes shown in Figure 5.5 for both multi-step simulations are almost identical in the stagnation region. In reality, although hardly noticeable on this picture, the ice height is slightly higher in this region when the update is not performed. This is consistent with the icing model: at the start of every iteration of the multi-step, a thick enough layer of rime ice must accrete before droplets may remain liquid and glaze ice starts accreting. The main differences are noticeable past the upper and lower horns regions, when the ice height stops and reattaches to the clean surface. The influence of the water film appears small but observable: it allows the ice to accrete in a higher proportion on the upper surface, leading to a final ice estimation closer to experiments. In the lower region, the ice extends less when the update is not performed. Using the update guarantees that the water layer moves with the shear stress right from the start. Consequently, more fluid is pushed upwards and this explains the evolution of the ice layer.

To better analyse the water movement and its influence on the final ice prediction, the water height is plotted on the unfolded cylinder surface at the end of each step of the calculation, respectively after each new multi-time step of $55s$, see Figure 5.6. A quick analysis of the curves plotted in this figure points out the following comments:

- There is no difference between the water heights estimated with or without update at the end of the first step and a very little difference in the second one.

- The water layer is slightly higher when no update is performed. This appears in all steps except the first one. Here again, this is consistent with the model. When a pre-existing water layer is present, fluid can be moved promptly up to the limits of the liquid layer where it freezes. The process is not as easy with no pre-existing water layer: a lower proportion of the incoming fluid may turn into ice and the water layer becomes logically larger.

- The shapes of the water layers depend on the length of the multi-time step. For short values, the water layer with no update would remain very small and the effects of the water layer would be cancelled. For longer times, as it is the case here, the two water layers with and without update should be of the same order of magnitude, but their geometry could be slightly modified by the geometry of the ice layer.

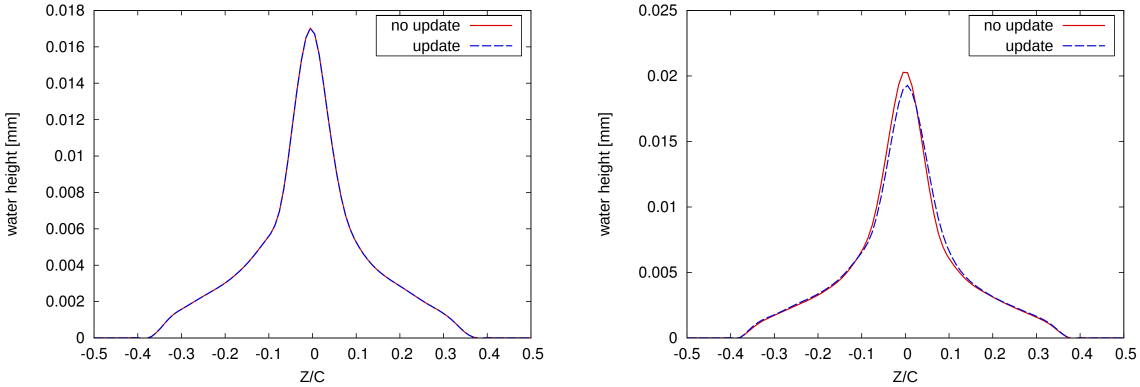

(a) Step 1 (55s) (b) Step 2 (1min 50s)

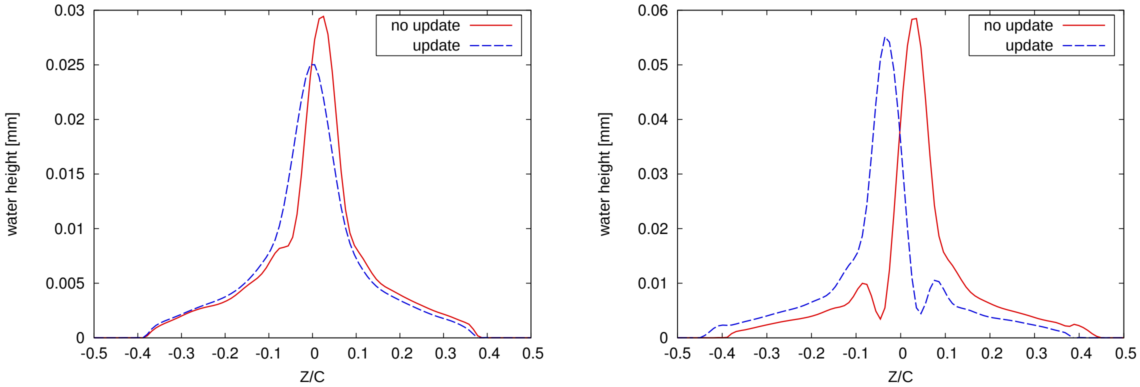

(c) Step 3 (2min 45s) (d) Step 4 (3min 40s)

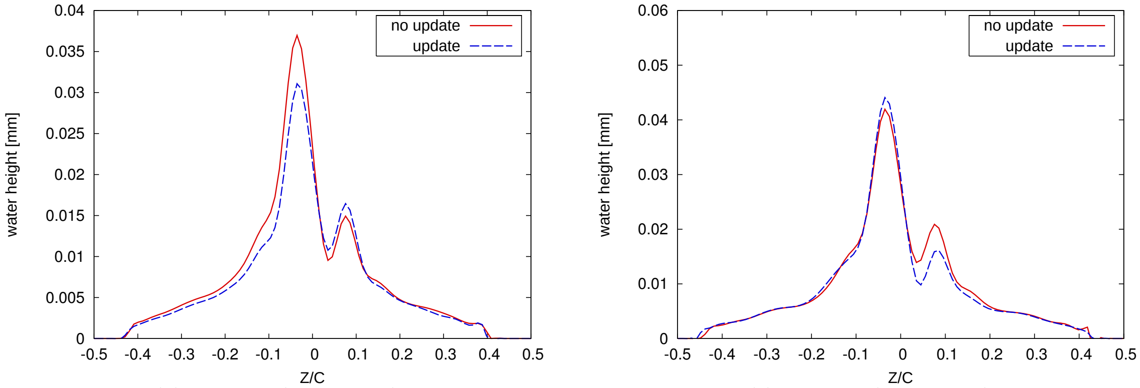

(e) Step 5 (4min 35s) (f) Step 6 (5min 30s)

Figure 5.6: *Influence of the water height update in a 6-step multi-stepping algorithm based on the time-criterion. Exposure time: 5min 30s.* $T_\infty \simeq -3^oC$.

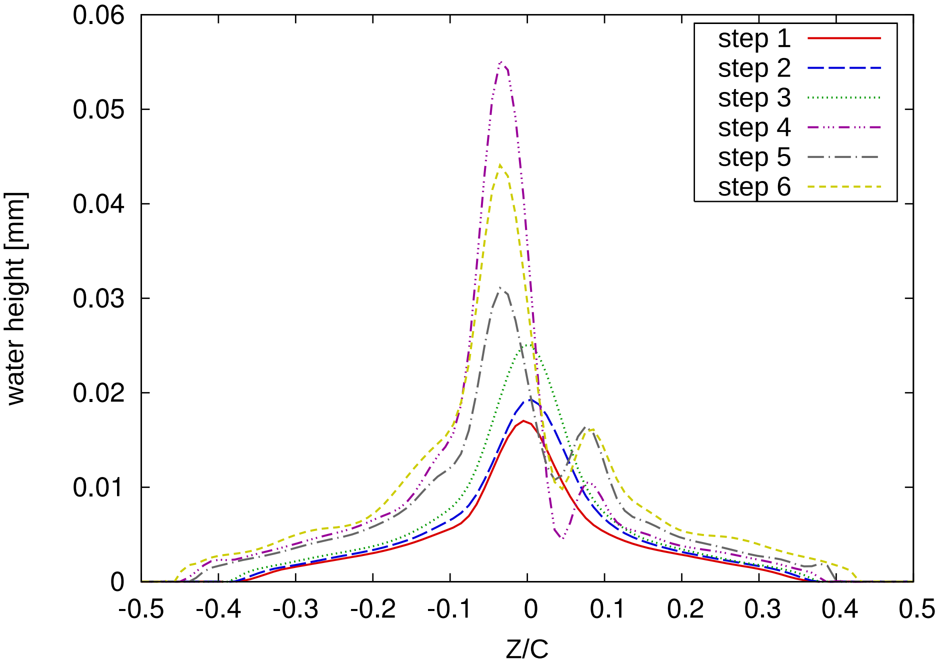

Figure 5.7: *Evolution of the water height during a 6-step multi-stepping algorithm based on the time-criterion (update of the water film). Exposure time: 5min 30s.* $T_\infty \simeq -3^oC$.

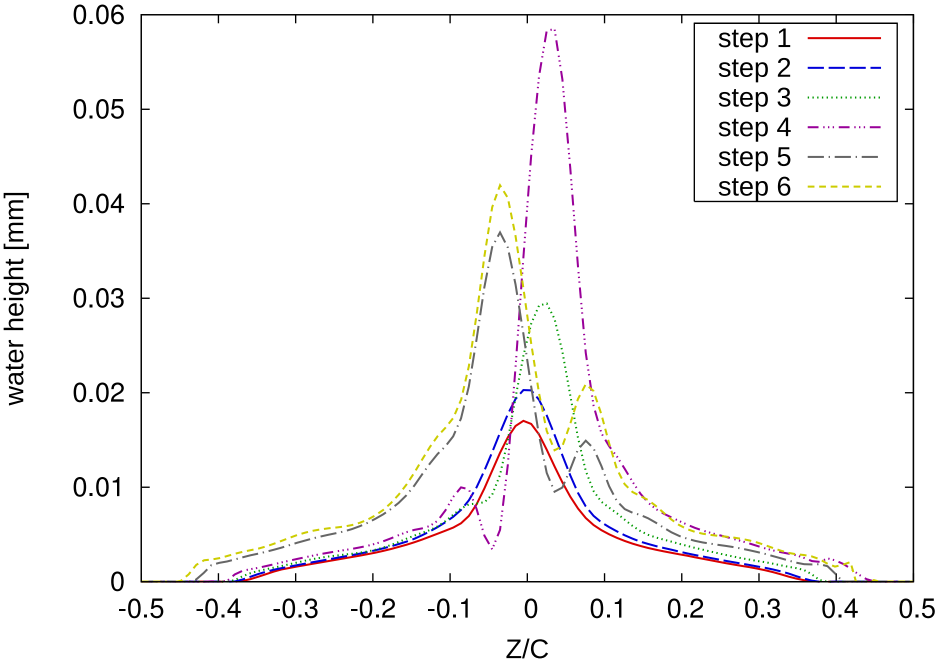

Figure 5.8: *Evolution of the water height during a 6-step multi-stepping algorithm based on the time-criterion (no update of the water film). Exposure time: 5min 30s.* $T_\infty \simeq -3^oC$.

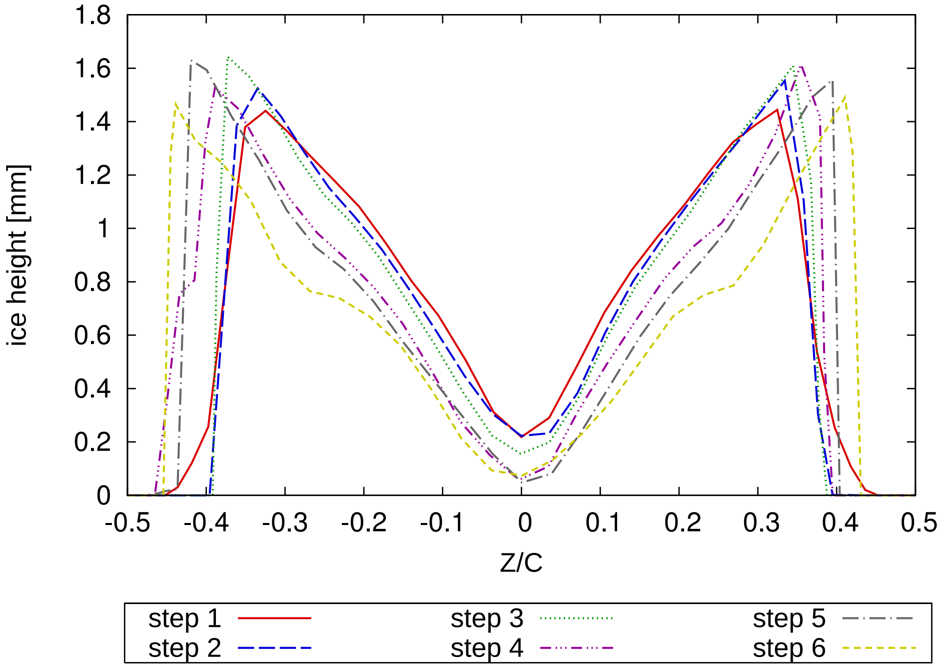

Figure 5.9: *Evolution of the ice height during a 6-step multi-stepping algorithm based on the time-criterion (update of the water film). Exposure time: 5min 30s.* $T_\infty \simeq -3^oC$.

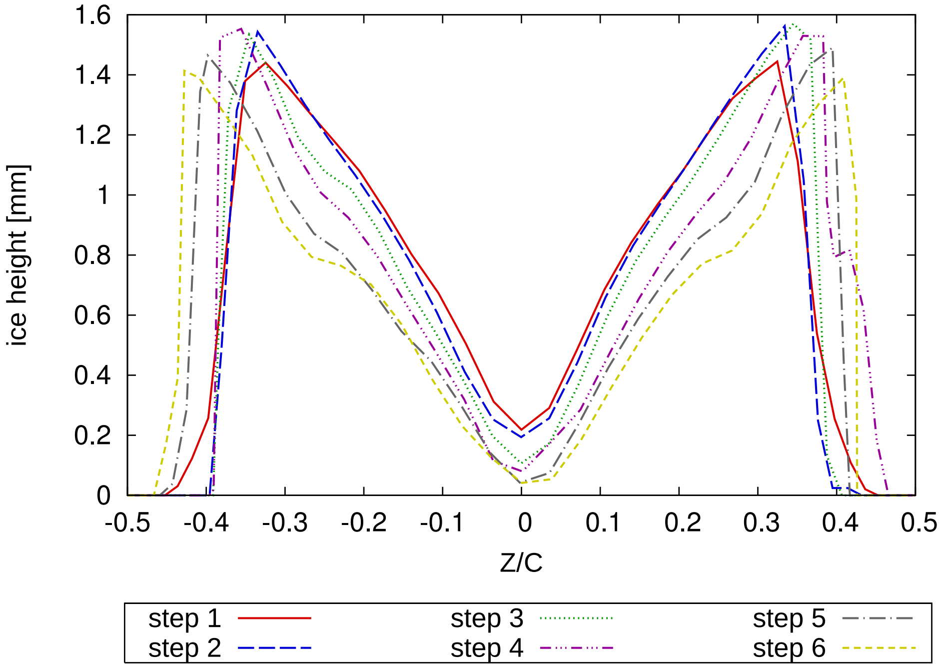

Figure 5.10: *Evolution of the ice height during a 6-step multi-stepping algorithm based on the time-criterion (no update of the water film). Exposure time: 5min 30s.* $T_\infty \simeq -3^oC$.

Under the conditions of the case $O1$, the evolution in time of the water height is shown in Figure 5.7 for the simulation performed without any water update and in Figure 5.8 when the water height history is preserved from one step to the next. As may be seen, there is no significant difference between the two water heights.

The corresponding ice height evolution are represented in Figure 5.9 when the water update is performed and in Figure 5.10 when this update is missing. The type of algorithm used in the multi-step calculation affects the ice height evolutions. This ice height is slightly higher on the upper and lower horns when the update is performed and the ice extends mores in the upper region in the same conditions. This is in agreement with the final ice estimations plotted directly on the cylinder, see Figure 5.5.

The effects of the water layer are visible in this study. This points out the influence of the thermal history and water height update from one step to the next on the final ice shape. Neglecting this history may lead to final ice predictions which are not in agreement with the real evolution of the ice growth.

The method used to model the water layer therefore influences the final estimated ice shape. The size of the impinging droplets is also an important factor in the ice accretion, as will now be discussed.

Influence of the droplets size:

The ice shape that forms on the cylinder is now studied for large supercooled droplets with a diameter $d_d = 100\mu$m. As already mentioned, large droplets reach the surface more easily and produce a large water film extent.

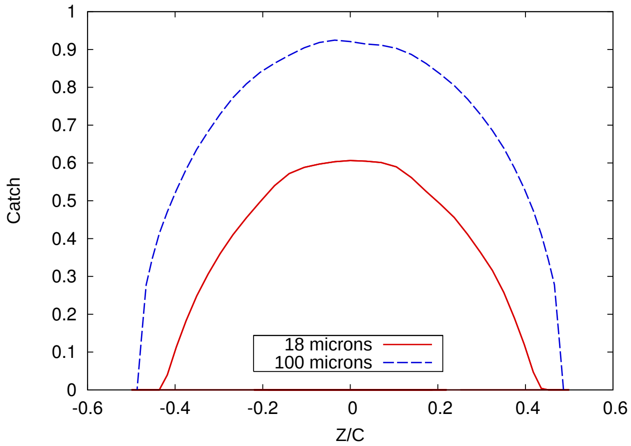

Figure 5.11: *Comparison of the collection efficiency on a cylinder obtained with small and large droplets in glaze ice conditions.*

Figure 5.11 shows the two collection efficiencies obtained in a single-step calculation for small ($d_d = 18\mu$m) and large ($d_d = 100\mu$m) droplets. As could be expected, the collection efficiency is much higher for large droplets $\beta \simeq 0.9$ than for small ones, where $\beta \simeq 0.6$. The impingement limits are also larger for the biggest droplets on both upper and lower sides of the cylinder surfaces. Ice accretion on a cylinder with large droplets will now be considered in glaze ice conditions.

Ice accretion for large droplets:

The experimental ice shape measured under the impingement of the large droplets for case $O2$ is shown in Figure 5.12. The global ice shape obtained in these conditions is smoother and more uniform than for the impingement of small droplets. The ice limits of both the upper and lower surfaces is moved downstream and the double-horn structure is less apparent.

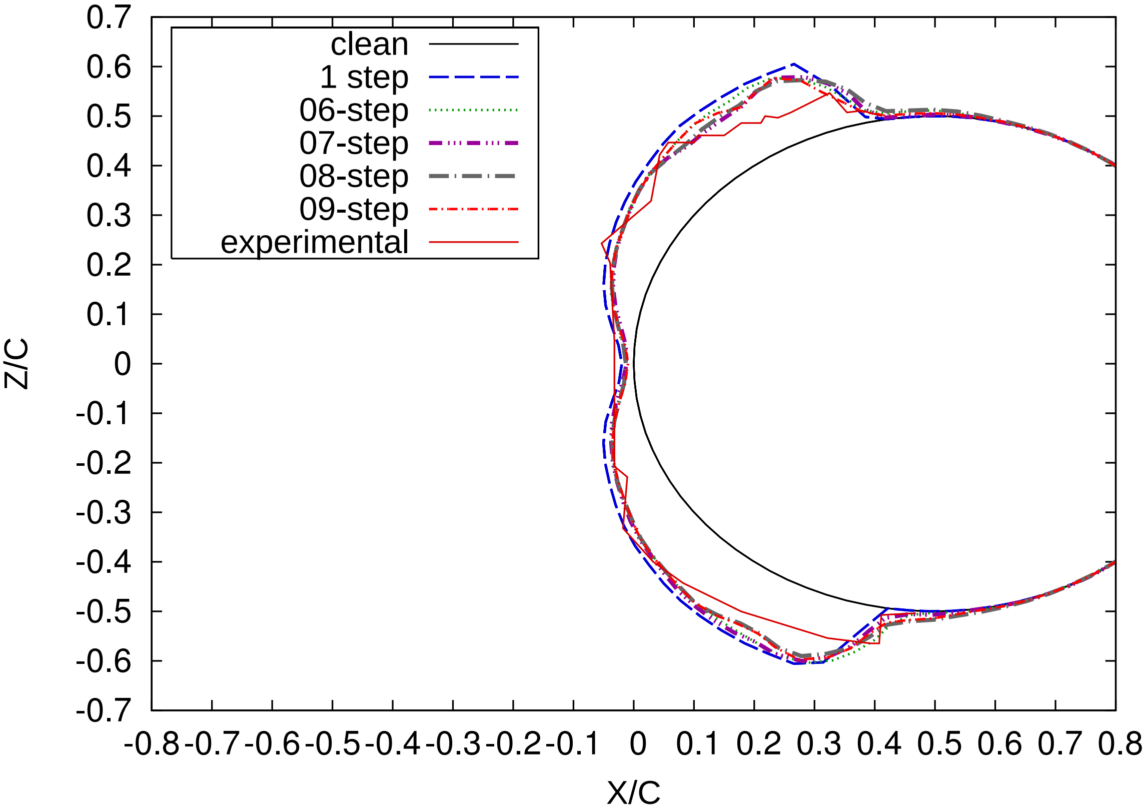

Figure 5.12: *Glaze ice shapes obtained on a cylinder with a step-by-step calculation based on the time-criterion. Large droplets. Exposure time: 5min 30s.* $T_\infty \simeq -3^oC$.

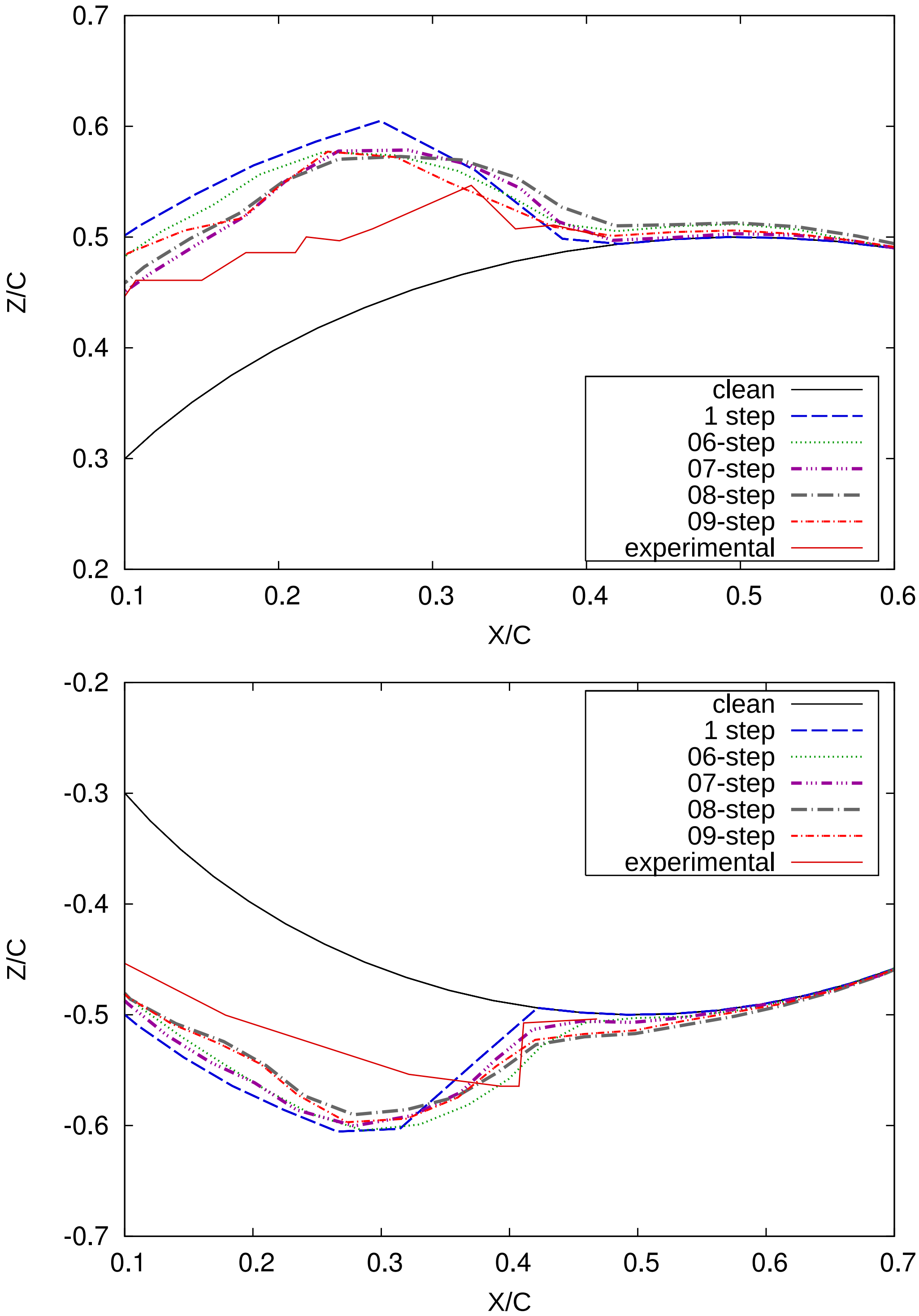

Figure 5.13: *Glaze ice shapes obtained on a cylinder with a step-by-step calculation based on the time-criterion. Large droplets. Exposure time: 5min 30s.* $T_\infty \simeq -3^oC$.

The convergence of the ice shape has been studied through several simulations performed in 1 and up to 20 multi-time steps. The most relevant ice shapes are represented in Figure 5.12. All additional results obtained under these conditions can be found in Appendix D.

As may be seen more precisely from Figure 5.13, the convergence occurs for 7 multi-time steps, this is one more multi-time step than in the previous results. In general, the predicted ice shape is too thick. This is most probably due to over-estimated values of the collection efficiency, the droplets being not introduced far enough from the body. As mentioned previously, droplets should ideally be introduced 7 chord length ahead of the body. This distance was reduced here to 3.5 diameter length, see Appendix H. This strategy was used for time/space saving reasons. It is clear that droplets launched further away in the airstream would require:

- A much larger mesh around the body,
- An increase of droplets number as they would be more likely to miss the body.

Consequently, the overall computing time would be increased considerably when generating meshes and flow solutions and when calculating the droplet trajectories. This cost would very significantly increase with the number of multi-time steps used in the computation.

Furthermore, water droplets splash when they impinge on the surface, particularly when they are large [122, 123, 124]. Gent et al. [125] have reported a percentage of incoming water lost to splash for droplets above 100μm is approximately 20% for a NACA0012 wing and 50% for a cylinder. However, this effect is not taken into account here but could modify the collection efficiency results and therefore the estimated ice shape.

The final ice shapes obtained for the impingement of the small and the large droplets are plotted together in Figure 5.14 in 6 and 7 multi-time steps, respectively. The ice height is identical in the stagnation region. However, large differences in the ice shape may be noticed on the upper and lower regions, this reflects the different values of collection efficiency. The maximum ice height is higher for the impingement of the large droplets, with $b \simeq 9.3$mm against $b \simeq 9$mm for the small ones. As the number of multi-time steps required is almost identical, the time-based criterion may not be the best criterion for studying the convergence of the ice shape. A criterion based on the ice height might be more appropriate.

To conclude, the best accuracy of the ice shape is not necessarily achieved with the greater number of steps, this agrees with the statement from Wright [22], Gent [23], and Eberhardt and Ok [57]. If a too high number of steps is used, the ice shape will no longer converge due to pile up errors. In this study, the 7-step

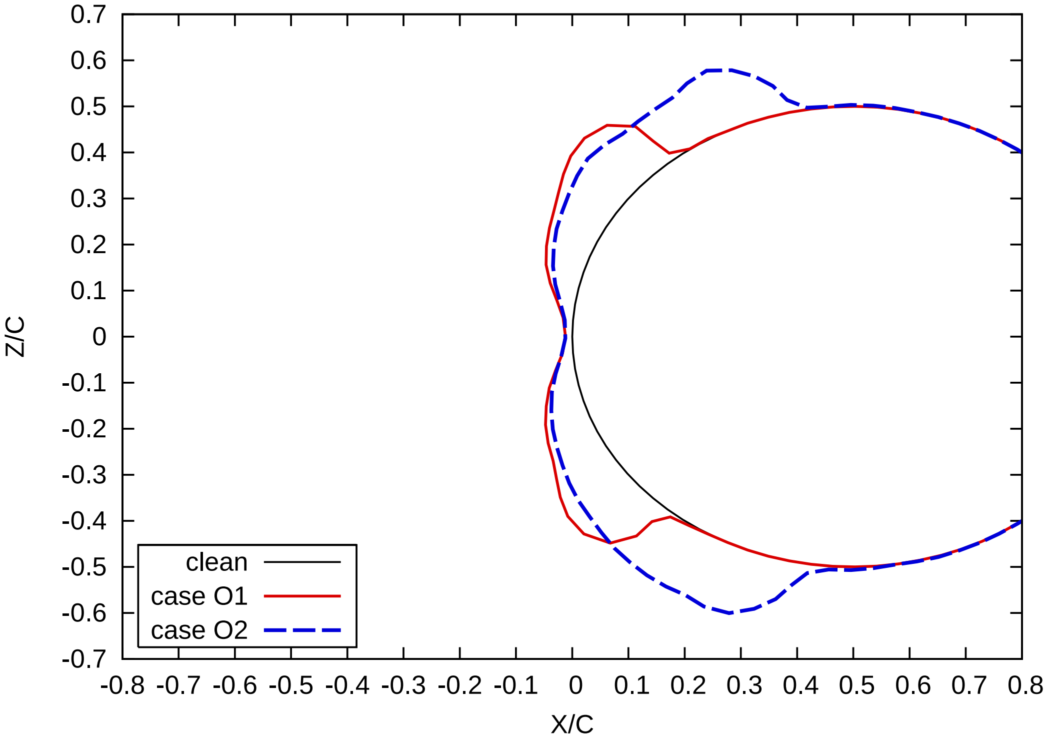

Figure 5.14: *Comparison of glaze ice shapes obtained on a cylinder with a step-by-step calculation based on the time-criterion for small and large droplets. Exposure time: 5min 30s.* $T_\infty \simeq -3^oC$.

algorithm can be retained for further analysis under these specific conditions. A proportion of chord equivalent to 2.08% can be used to determine the number of steps necessary. This value is relatively close to the previous results and the number of multi-time steps required does not seem to vary too much with the size of the droplets. This result is also more or less consistent with the theoretical proportion of diameter length $X = 2.7\%$ determined from Equation 5.2.1 when considering a number of steps equal to seven.

Conclusion

The number of time-steps is a key-parameter in a multi-step algorithm. For the rime ice case investigated, convergence of the algorithm is achieved with 6 multi-time steps. A number of 4 multi-time steps would also produce acceptable results. For the cases investigated in glaze ice conditions, it has been shown that the size of the droplets had only a small influence on the required number of multi-time steps. In these conditions, some convergence is achieved for about $6-7$ multi-time steps. The corresponding averaged ice height per multi-time step may be written in Table 5.2 as the proportion X of the diameter length c. These values may be recommended for further studies under the conditions investigated in this chapter.

	ice type	$\mathbf{n_{step}}$	**X** [%]	**c** [mm]
case O1	rime	6	2.16	63.5
case O1	glaze	6	2.36	63.5
case O2	glaze	7	2.09	63.5

Table 5.2: *Number of multi-time steps and corresponding average ice height per step, written as a percentage of the diameter length.*

The effect of the water film update on the final ice shape has also been outlined briefly in this section. This update increases the thickness of the simulated ice layers in the upper region of the cylinder surface and more ice is predicted in the horn regions.

In all cases investigated, overall results generated with a multi-step algorithm compared better to experiments than the standard single-step algorithm. This conclusion is valid in all regions except the stagnation line.

The validity of the criterion may be questionable in glaze ice conditions. Consequently, a similar study will now be conducted for the same droplet sizes using a multi-step procedure based on the height criterion.

5.3.2 Ice Height Criterion

A step-by-step algorithm based on the ice height criterion automatically recalculates a new air flow solution and any flow-related parameters when the ice growth during each multi-time step becomes higher than a defined maximum ice height value. This ice height criterion, defined by the user as a proportion of cylinder length, is verified when the ice layer at any location on the surface reaches this value. The ice height criterion will be satisfied in the nose region when rime ice type grows and in the upper (or lower) horn region for a glaze ice type accretion. The exposure time in a multi-time step is then likely to be different from one step to the next. Several values of the ice height criterion will be tested under rime and glaze ice conditions. The percentages investigated will vary from 1% up to 5% of the diameter length. Atmospheric and icing conditions remain identical; they are those specified in Table 5.1.

Rime ice conditions

Small droplets are injected in the airflow at the temperature $T_\infty \simeq -26^oC$. The predicted rime ice shape obtained after 5min and 30s may be seen in Figure 5.15. Similarly to the predictions obtained with the time-based multi-step algorithm, this approach determines ice shapes that become slightly thinner with the increase of the number of steps. However, the differences are hardly noticeable. As may be seen more precisely in Figure 5.16, convergence is achieved for an ice height criterion equal to 4% of the diameter, which corresponds to the maximum ice height allowed per step $b_{max} \simeq 2.54$mm. For this step-by-step calculation, three flow calculations have been necessary.

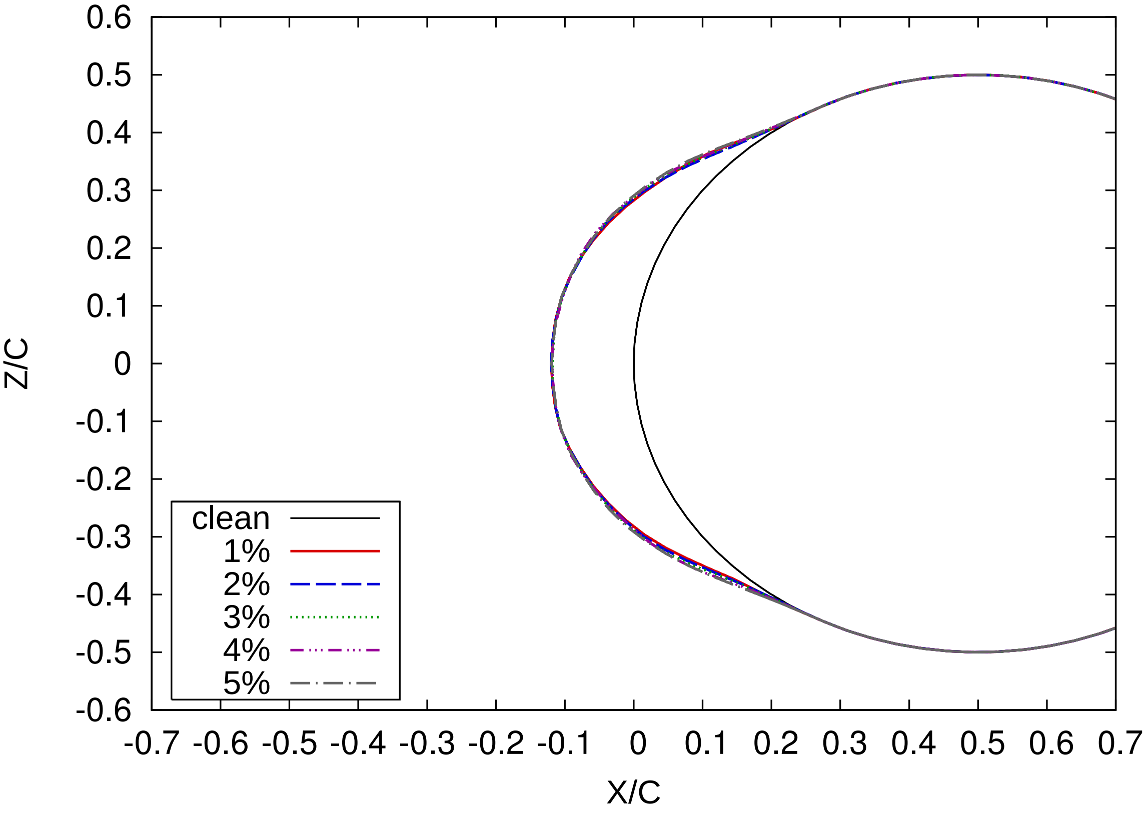

Figure 5.15: *Rime ice shapes obtained on a cylinder with a step-by-step calculation based on the ice height criterion. Small droplets. Exposure time: 5min 30s.* $T_\infty \simeq -26^oC$.

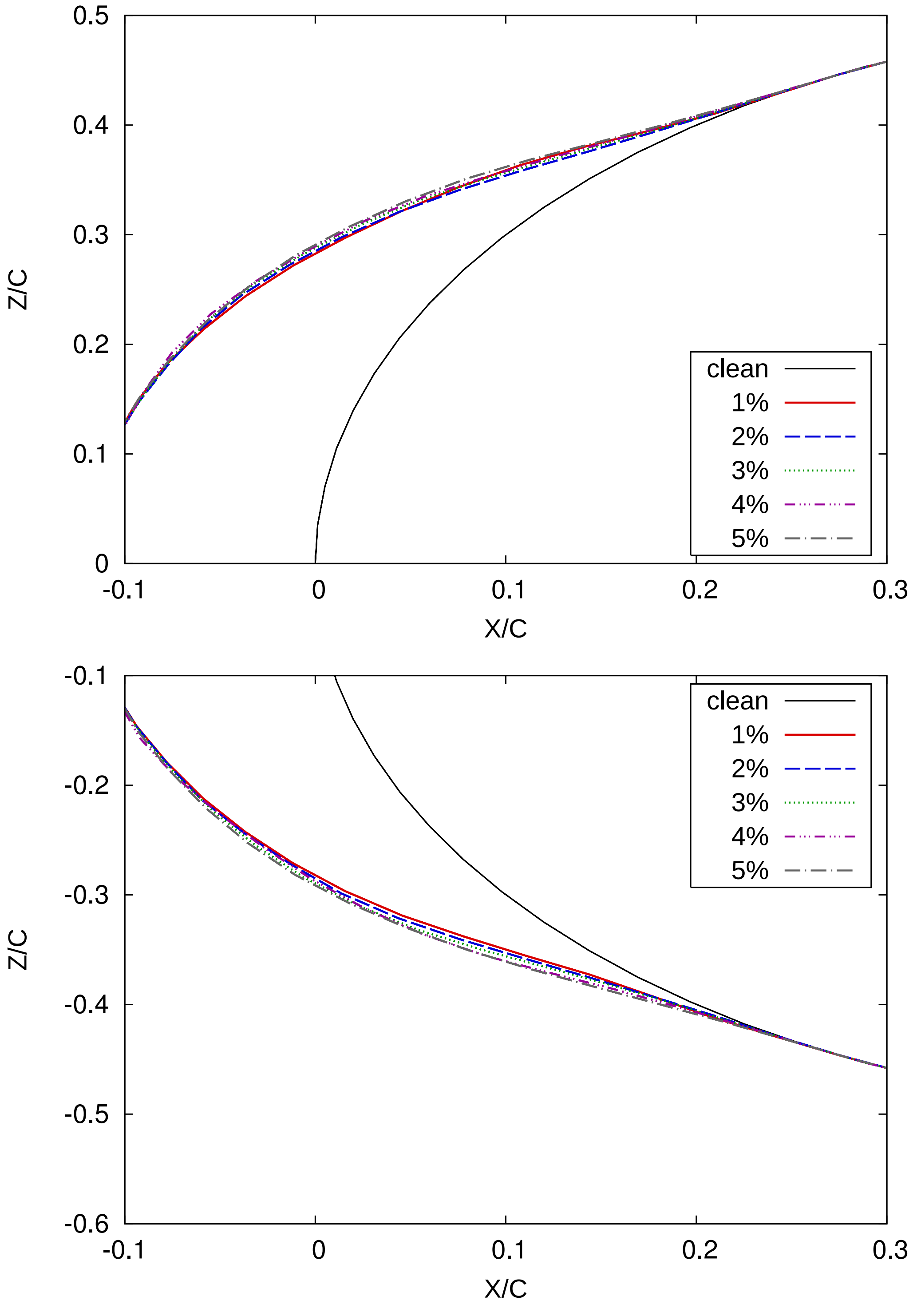

Figure 5.16: *Rime ice shapes obtained on a cylinder with a step-by-step calculation based on the ice height criterion. Exposure time: 5min 30s.*

Figure 5.17 depicts the frequency of the flow updates in each simulation, i.e. the time required in any step for the ice height criterion to be satisfied. The curves on this picture are extended using a linear interpolation for clarity purposes. As may be observed, the time per step in each simulation seems rather similar and constant: as expected for rime ice studies, the ice growth is proportional to the exposure time.

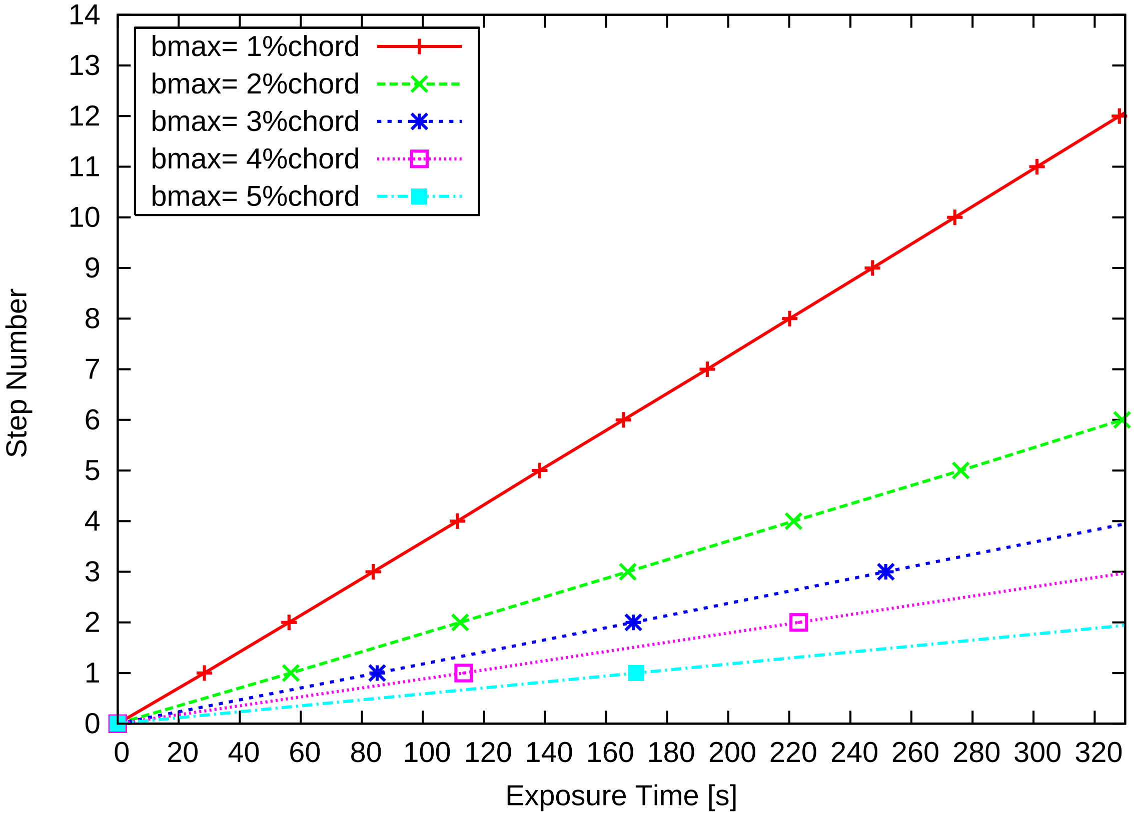

Figure 5.17: *Frequency of flow updates on a cylinder for the ice height criterion. Exposure time: 5min 30s.* $T_\infty \simeq -26^oC$.

Convergence using the time-based criterion has been determined after 6 steps in Section 5.3.1 and the ice height estimated per step around $X = 2.16\%$ of the diameter length. The percentages of chord length are not identical for both criteria, they can not however be compared directly:

- For the time-based criterion, the ice height per step written as a percentage of chord is determined as the total ice height divided by the number of steps. The proportion of chord is therefore an average ice height value, and the real ice accretion may be different from one step to the next. It has been observed that the ice growing in the first step of the rime ice prediction is usually slightly less than in the other steps.

- For the ice-based criterion, the percentage of chord corresponds to the maximum ice height allowed to form in one multi-time step. However, for the very last step of the procedure, the ice criterion is never verified since the simulation is stopped when the total exposure time to icing is reached.
- The two proportions of chord length will therefore always be different since the flow updates occur at more suitable and necessary times when the ice-based criterion is used.

To summarise, what is really important is not necessarily the proportion of chord estimated in each step, this parameter being not comparable directly for the two algorithms. What is a key-element in the process is the number of steps and more precisely the number of flow calculations necessary to achieve convergence: a reduced number of steps will speed-up the whole computation.

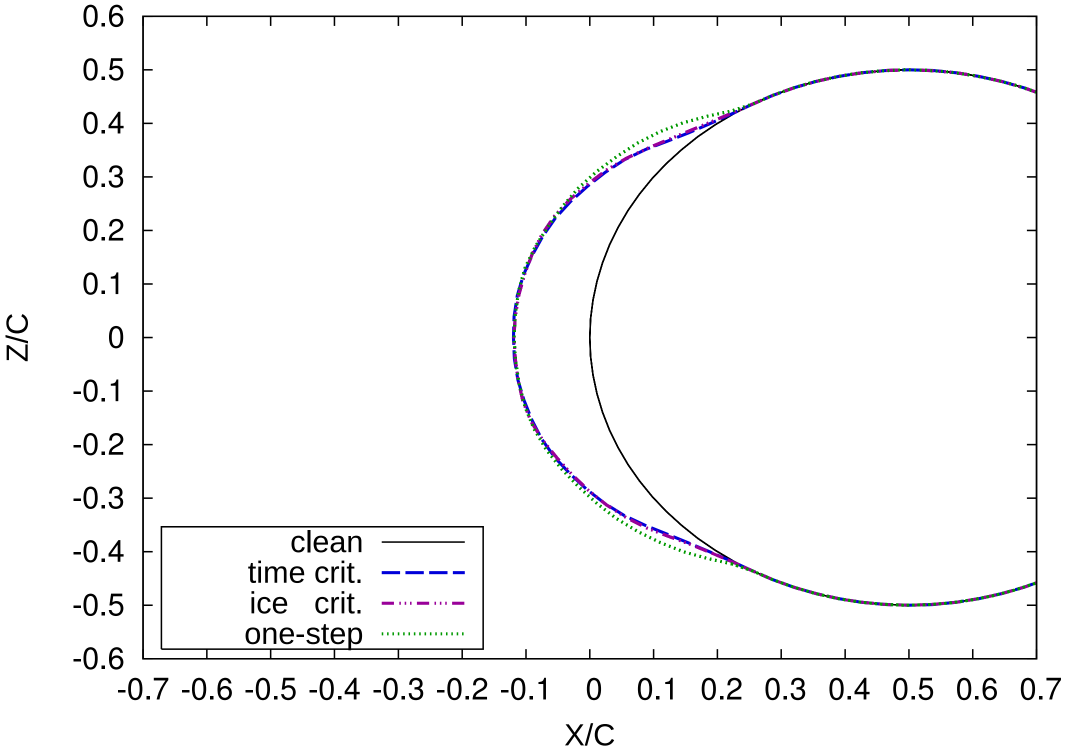

Figure 5.18: *Criteria comparison. Ice shapes obtained on a cylinder in rime ice conditions. Small droplets. Exposure time: 5min 30s.* $T_\infty \simeq -26^oC$.

A comparison of the converged ice shapes obtained with both criteria may be seen in Figure 5.18. The final estimated ice shapes obtained with the two multi-stepping algorithms are strictly identical. This result was expected as the rime ice accretion is fully proportional in time to the collection efficiency. In this situation, the final predicted ice shape is not useful to determine the most accurate criterion. However, the simulation performed with the ice-triggering criterion is faster since three flow solutions only are necessary to reach convergence while six (eventually four, as pointed out in Section 5.3.1) were necessary for the calculation based on the time criterion. This corresponds to an average gain of time of 50%. An ice-height criterion of 4% of the diameter length is therefore recommended for a step-by-step calculation on a cylinder in rime ice conditions.

The ice height criterion will now be studied in glaze ice conditions with the objective to establish the most accurate number of steps required to achieve convergence in the step-by-step algorithm.

Glaze ice conditions

- **Case O1**

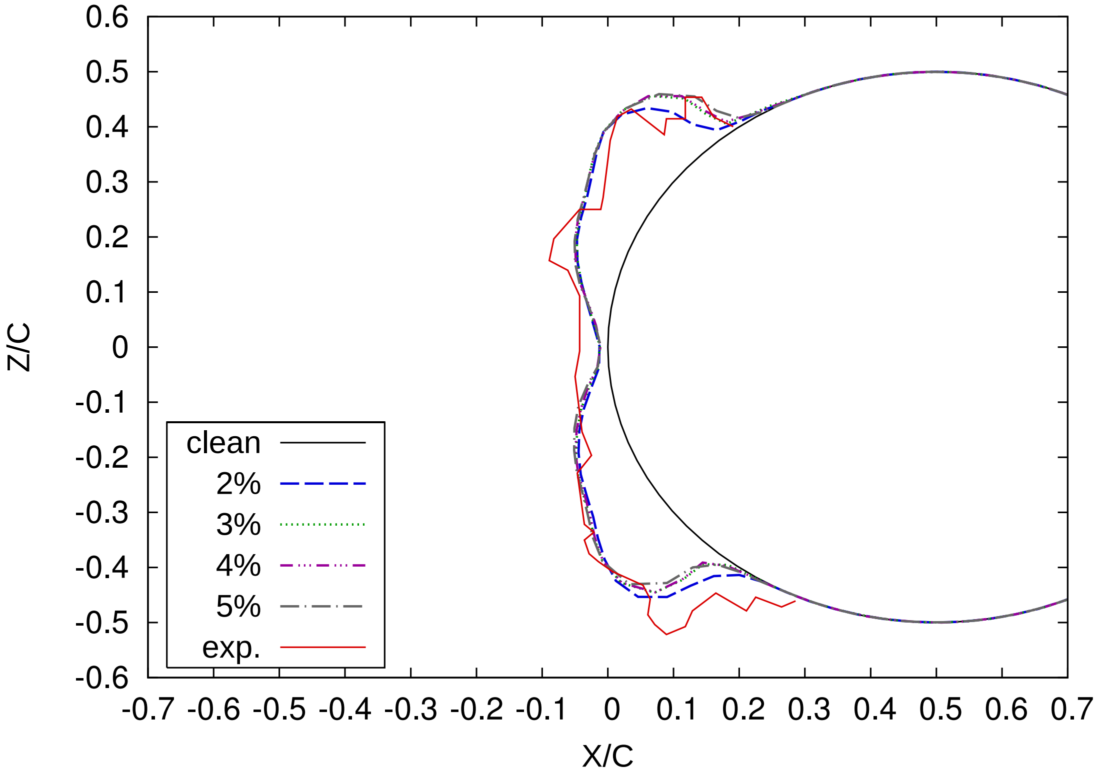

Figure 5.19: *Glaze ice shapes obtained on a cylinder with a step-by-step calculation based on the ice height criterion. Small droplets. Exposure time: 5min 30s.* $T_\infty \simeq -3^oC$.

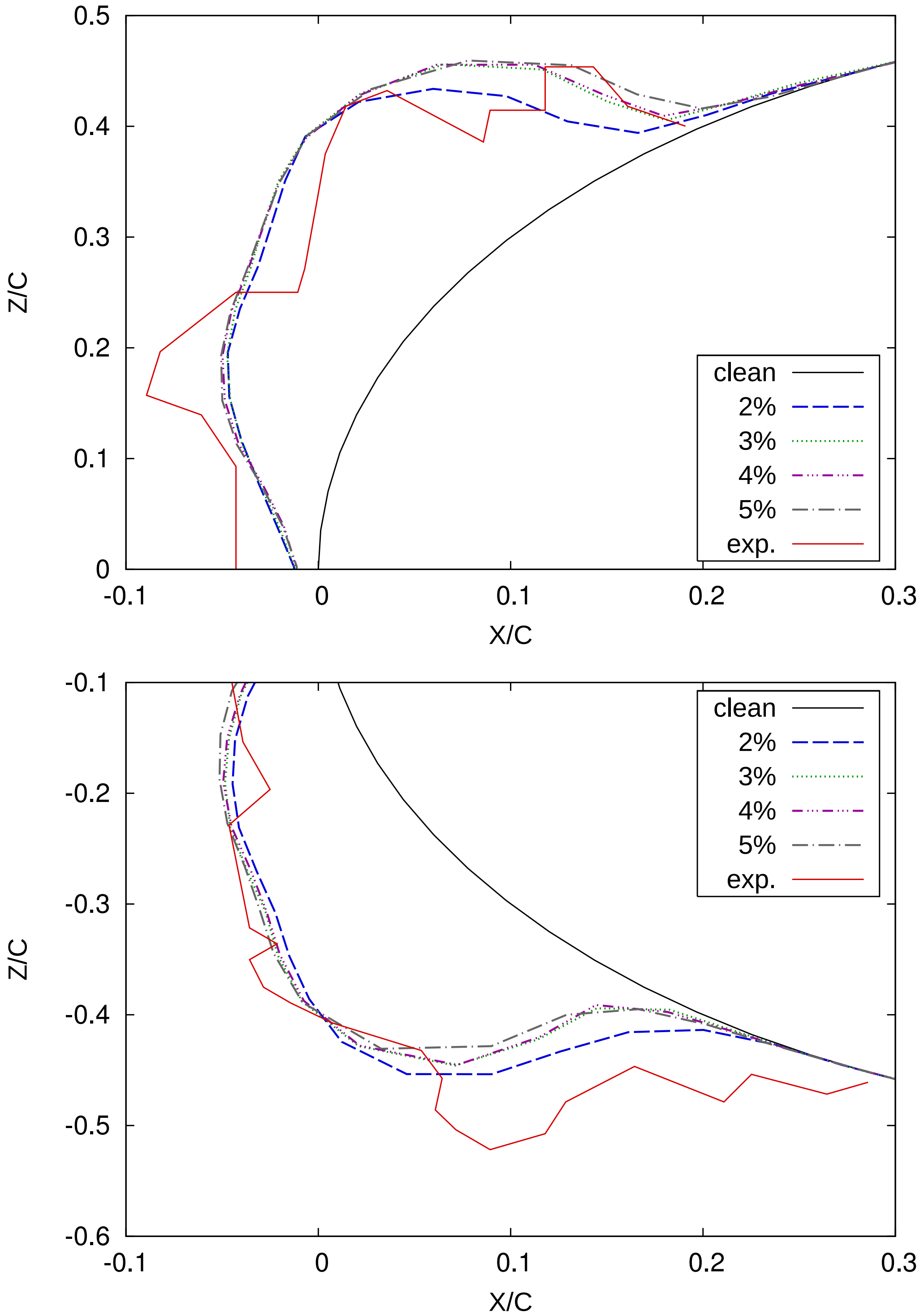

Figure 5.20: *Glaze ice shapes obtained on a cylinder with a step-by-step calculation based on the ice height criterion. Small droplets. Exposure time: 5min 30s.*

Small droplets are released in the airflow at $T_\infty \simeq -3^oC$, which corresponds to the conditions of the case $O1$. The final estimated glaze ice shape after 5min and 30s are represented in Figures 5.19 and 5.20 for simulations performed with different values of the ice height criterion. The maximum ice height values investigated here are also written as a percentage of the diameter length c. All the simulated results show a similar shape and the upper and lower ice extents are identical for all cases. The main differences appear past the upper and lower horns, when the ice reattaches to the clean geometry.

Convergence is reached with an ice height criterion of $b_{max} = 4\%$ of the diameter length equal to $b_{max} = 2.54$mm and 4 flow solutions are necessary. All additional results obtained for different values of the criterion are shown in Appendix C.

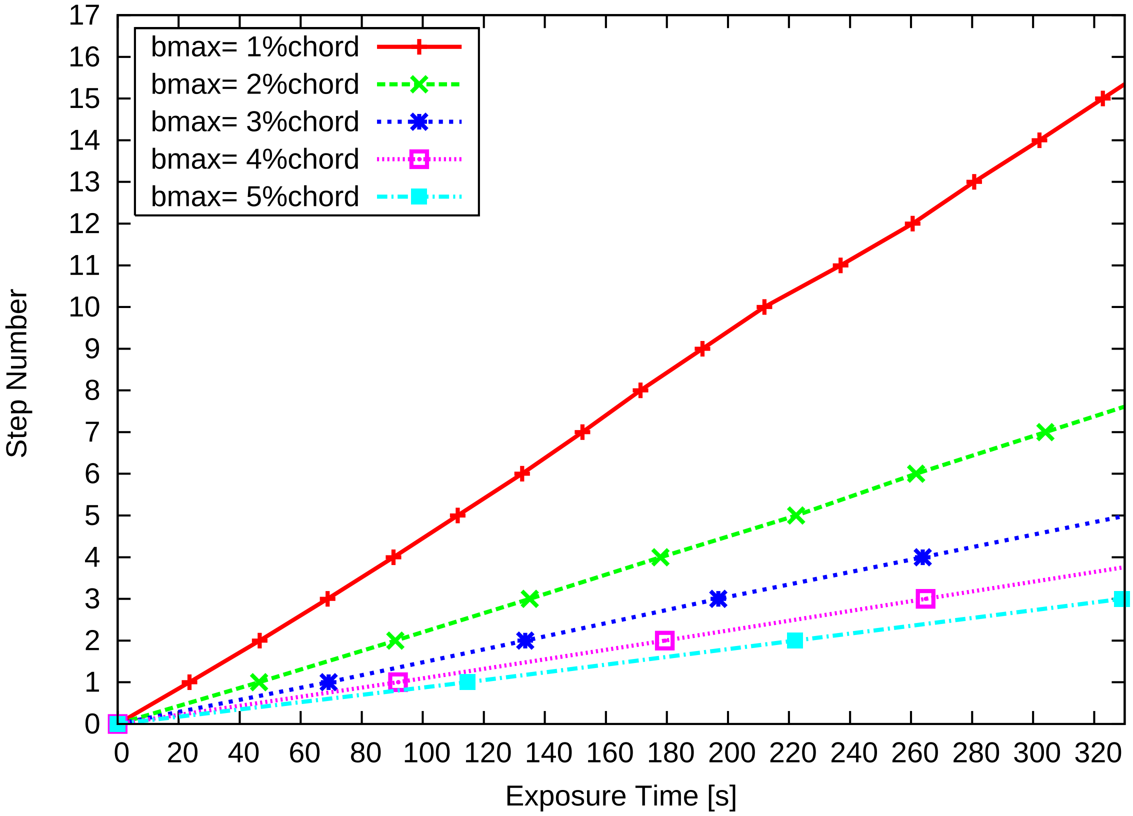

Figure 5.21: *Updates for the computation on a cylinder with the ice height criterion. Small droplets. Exposure time: 5min 30s.* $T_\infty \simeq -3^oC$.

The time necessary in each step for the ice height criterion to be satisfied is plotted in Figure 5.21. The curves displayed in this figure correspond to ice height values ranging from 1 to 5% of the diameter length. As may be seen, the evolution is less linear than for rime ice simulations, this means the glaze ice growth is not proportional to the exposure time.

	1%c	**2%c**	**3%c**	**4%c**	**5%c**
step	$\mathbf{t_{step}}$ [s]	$\mathbf{t_{step}}$ [s]	$\mathbf{t_{step}}$ [s]	$\mathbf{t_{step}}$ [s]	$\mathbf{t_{step}}$ [s]
1	23.53	46.32	69.11	91.91	114.70
2	22.99	44.71	64.44	87.42	107.25
3	22.27	44.01	63.31	85.45	108.05
4	21.6	42.86	66.95	65.22	
5	21.07	44.42	66.19		
6	21.11	39.36			
7	19.76	42.36			
8	18.98	25.96			
9	20.32				
10	20.33				
11	24.95				
12	23.61				
13	20.2				
14	21.38				
15	20.75				
16	7.15				

Table 5.3: *Time-step duration in the multi-step calculation based on the the ice criterion.*

Table 5.3 summarises the different time-step durations required by the ice-based algorithm for values of criterion ranging from 1%c to 5%c. As shown in the previous section, convergence of the time-based algorithm was achieved in 6 steps of 55s each, the first flow update being performed at $t_{exp} = 55$s. The results of the ice-based

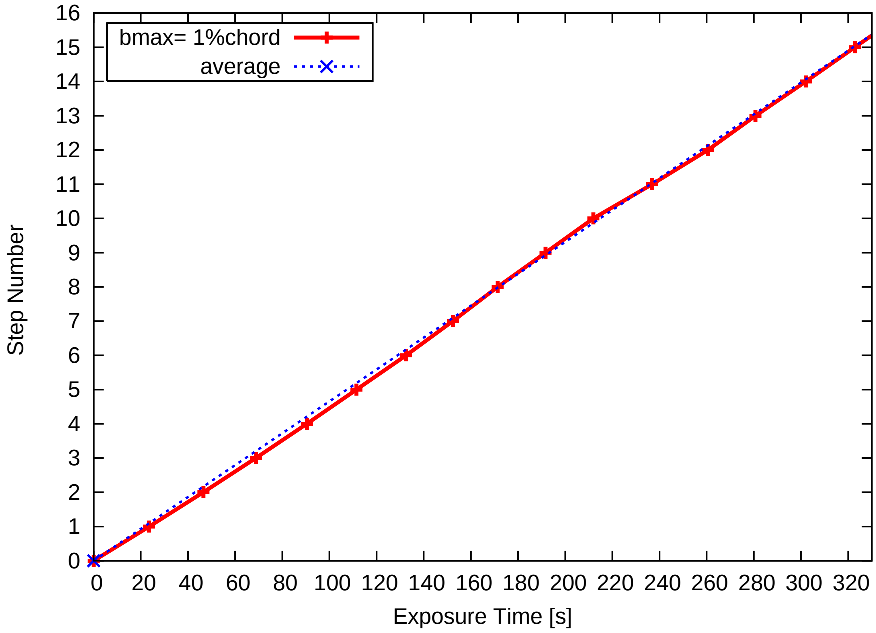

Figure 5.22: *Updates for the computation on a cylinder with the ice height criterion* $b_{max} = 1\% c$. *Small droplets. Exposure time: 5min 30s.* $T_\infty \simeq -3^oC$.

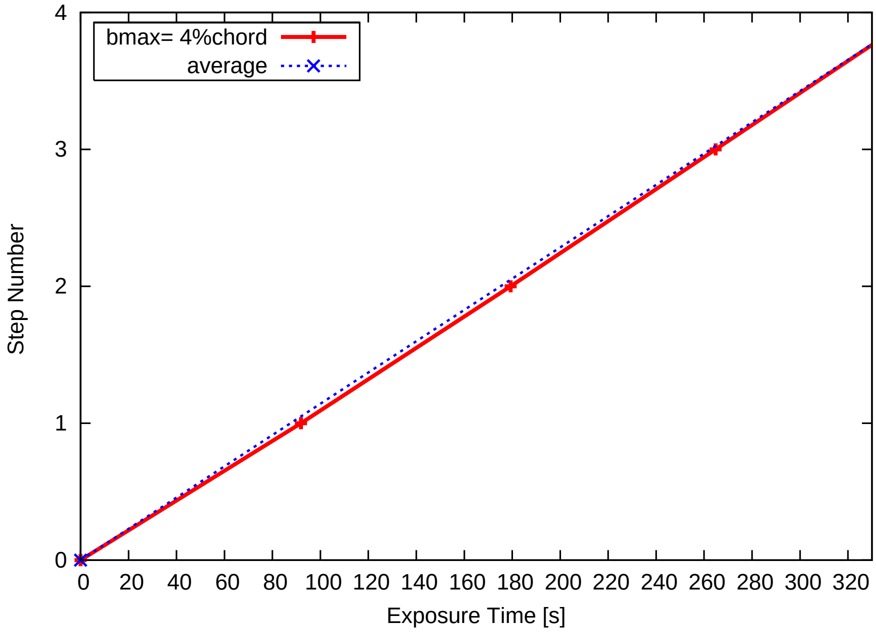

Figure 5.23: *Updates for the computation on a cylinder with the ice height criterion* $b_{max} = 4\% c$. *Small droplets. Exposure time: 5min 30s.* $T_\infty \simeq -3^oC$.

algorithm for 4%c show clearly that the time based criterion may not be the best ice estimator since a new update of the flow solution is not required before $t_{exp} \simeq 92$s. It also confirms that the ice growth is not exactly proportional to the exposure time in glaze ice conditions. The criterion is reached after 92 seconds in the first step, 87 seconds in the second and 85 seconds in the third step. In the rime ice case, the accretion time per step was more constant and the ice growth proportional to this accretion time. It should also be noted that simulations show a different profile. As may be seen in Figures 5.22 and 5.23 for 1%c and 4%c respectively, the duration of the time-step either decreases or increases in the 1%c case while it decreases only for the 4%c case.

The ice-based result using a criterion of 4%c will now be compared to the results obtained with the time criterion.

Comparison with the time-based result:

The converged ice shape is compared to the solution obtained in Section 5.3.1 for the

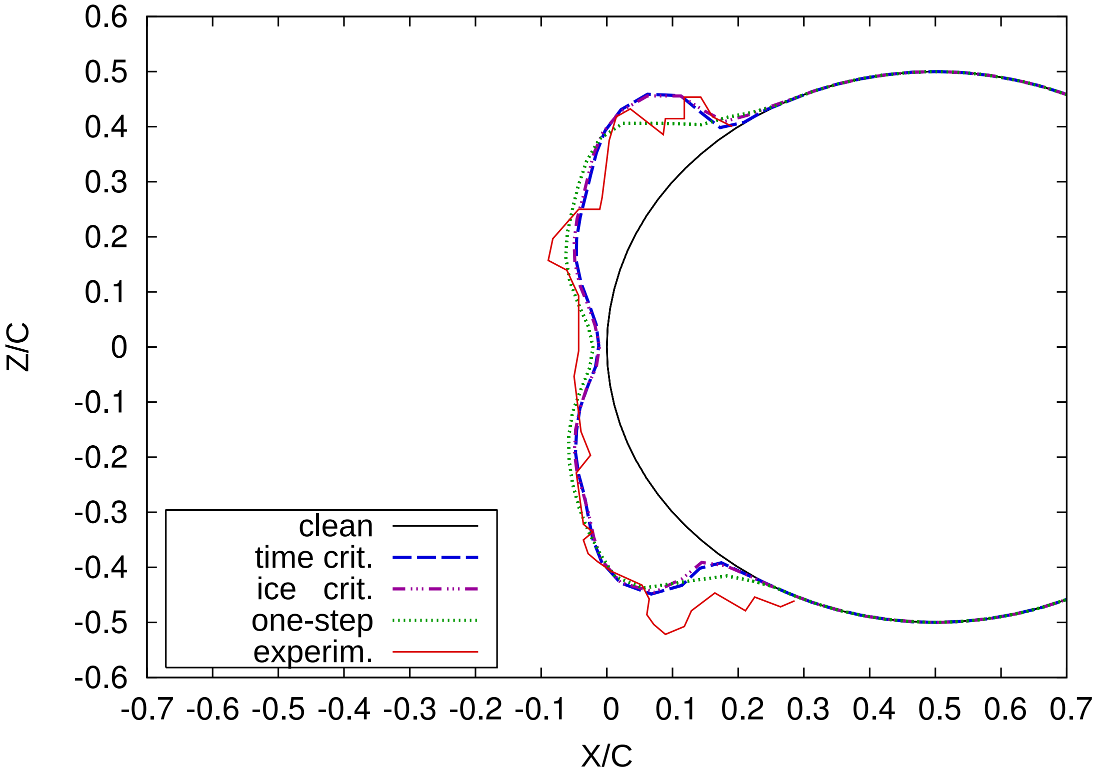

Figure 5.24: *Criteria comparison. Ice shapes obtained on a cylinder in glaze ice conditions. Small droplets. Exposure time: 5min 30s.* $T_\infty \simeq -3^oC$.

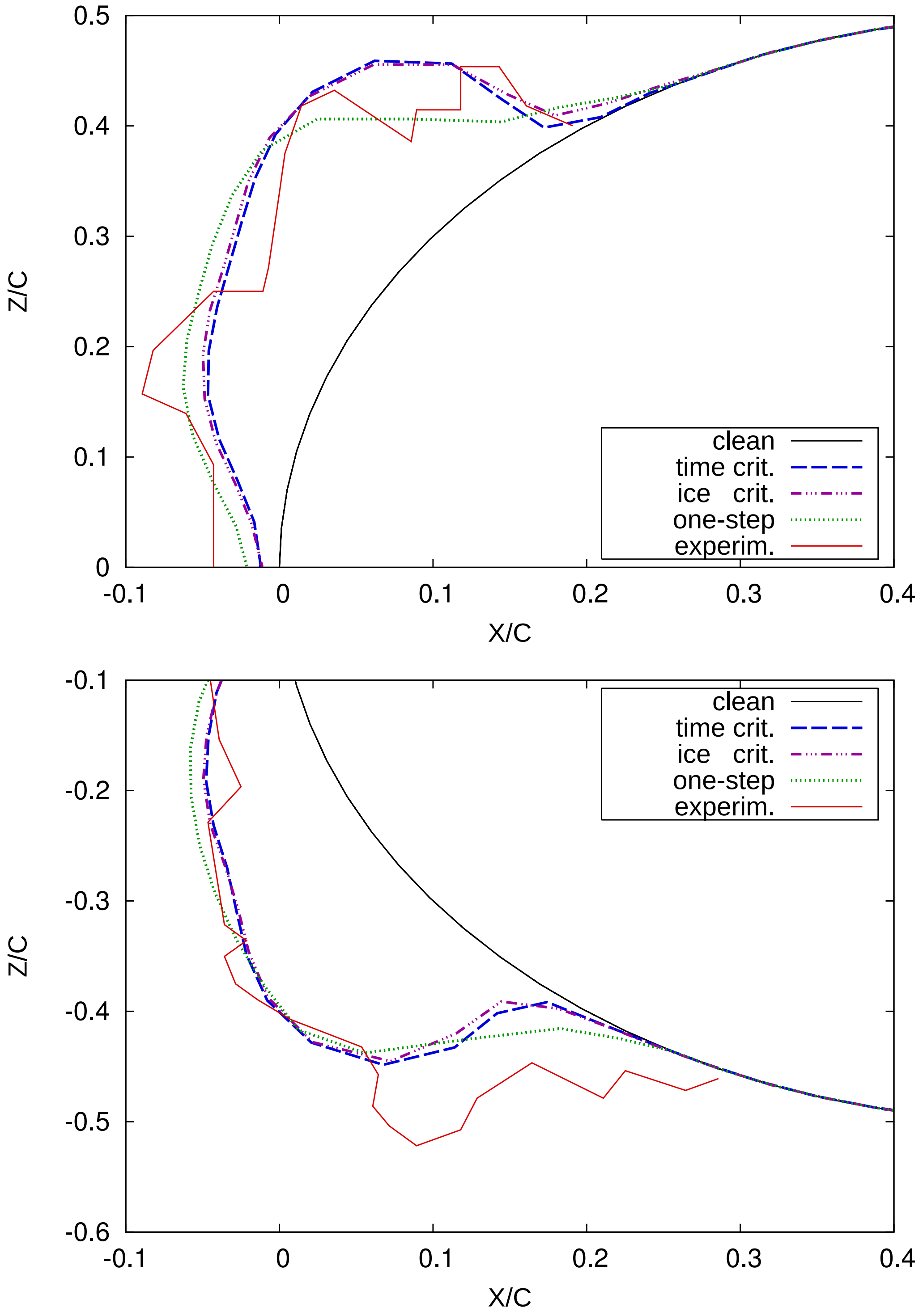

Figure 5.25: *Criteria comparison. Ice shapes obtained on a cylinder in glaze ice conditions. Small droplets. Exposure time: 5min 30s.* $T_\infty \simeq -3^oC$.

time-based criterion, as may be seen in Figure 5.24. A closer view of the simulated ice structure on the upper and lower surfaces of the cylinder is shown in Figure 5.25. An analysis of the different curves generated with the multi-step algorithms outlines the following remarks:

- Both multi-step algorithms are more accurate than the standard ice prediction method performed in a single step procedure.
- The predicted ice heights obtained with the multi-step algorithms are almost identical in the stagnation region and very close in the upper and lower horns regions.
- Slight differences are noticeable past the double horn structure, when the ice starts reattaching to the clean surface. However, these differences being minor, there is no way to determine which ice shape matches better experiments.

Once again, the predicted ice shapes only are not sufficient to determine the best criterion. Both methods are equivalent: slightly more is noticeable on the upper surface when the ice criterion is used and slightly more ice appears on the lower surface for the time based criterion. These differences are minor and they do not modify the whole ice shape significantly. However, the overall computation time using the ice height criterion is reduced with 4 flow calculations against 6 for the time-based criterion, which corresponds to an average gain of time of 33%. This criterion is therefore to be recommended in glaze conditions for ice predictions on a cylinder subject to the impingement of small droplets.

The ice-based algorithm being the most efficient of the two methods, the simulated ice shape using the ice criterion implemented in ICECREMO2 will now be compared with the shapes calculated with the three standard Messinger icing codes: LEWICE, TRAJICE2 and ONERA2000. Since codes evolve constantly and are always being improved, the shapes obtained with Messinger-based icing codes may be different if they were simulated again today. However, for lack of more recent data, the results of the NATO/RTO exercise held in December 2000 [120] will be used as references.

Comparison with standard icing codes:

The simulated results obtained with the ice height criterion implemented in ICECREMO2 may be seen in Figure 5.26, along with those generated by the standard Messinger-based icing codes. As can be noticed, ice prediction codes have difficulties to generate an accurate answer. The estimated ice shape is usually under-predicted

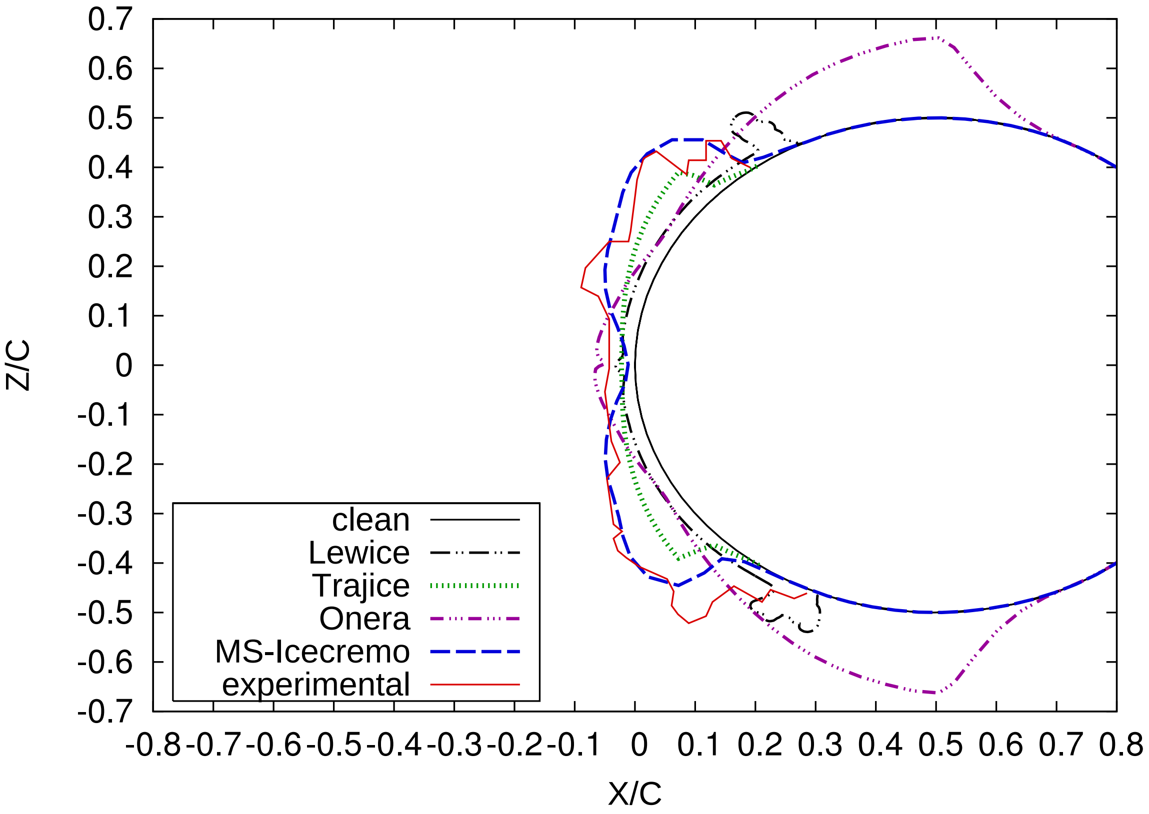

Figure 5.26: *Comparison of the multi-step result with standard icing codes [120] in glaze ice conditions at* $T_\infty = -3^oC$. *Exposure time: 5min 30s.*

for all Messinger-based codes and none of them can match the experimental data. A closer view of the cylinder upper, lower and stagnation regions is shown in Figures 5.27 and 5.28.

The ice extent on the upper and lower aft are different for all simulations, the largest ones being observed for the calculations performed with the ONERA and LEWICE codes. The global ice shape generated by the ONERA code appears very far from experiments while the overall estimated ice shape produced by LEWICE is very strange. When comparing all simulations, the upper and lower horns are undeniably better reproduced with the ICECREMO2 code while standard Messinger-based codes largely under-predict them.

In the vicinity of the stagnation region, none of the ice accretion codes could find a value close to the measured ice height. Results are disparate. For instance LEWICE under-predicts the ice layer, but shows a high peak at the stagnation point and the ONERA code over-predicts the ice layer, but shows

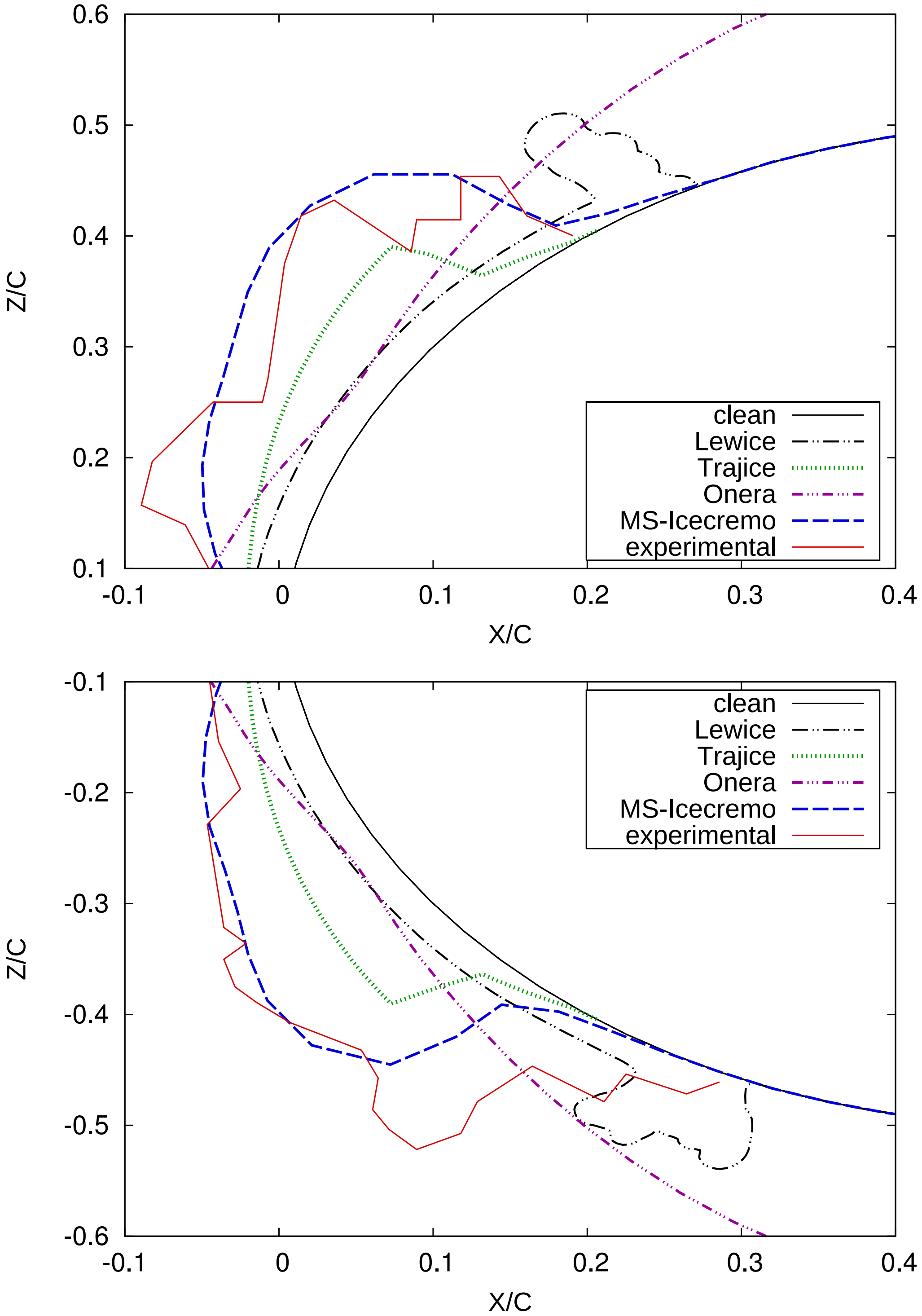

Figure 5.27: *Comparison of the multi-step result with standard icing codes [120] in glaze ice conditions at $T_\infty = -3^oC$. Exposure time: 5min 30s. Upper and lower regions.*

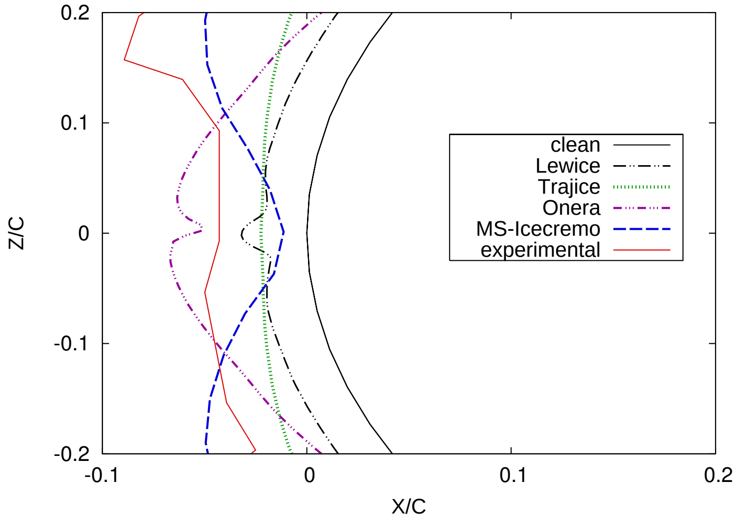

Figure 5.28: *Comparison of the multi-step result with standard icing codes [120] in glaze ice conditions at* $T_\infty = -3^oC$*. Exposure time: 5min 30s. Stagnation region.*

a depression at the stagnation point. In a general manner, all codes except ONERA under-predict the ice height in the vicinity of the stagnation point.

- **Case O2**

For the case $O2$, the size of the impinging droplets is increased. Simulations are run with the same values of ice height criterion as in the case $O1$, leading to different time durations per step. The corresponding final ice estimations may be seen in Figures 5.29 and 5.30 and additional results are presented in Appendix D.

As may be observed, the predicted ice shapes have about the same profile. A study of the results shows that convergence is achieved for $b_{max} = 4\%$c, corresponding to a maximum ice height allowed per step of 2.54mm. For this criterion, four flow calculations were performed at appropriate times during the total icing exposure time. When calculations are performed with an ice height triggering criterion of 5%c, the predicted ice shape is different from results obtained with a lower criterion value. When the criterion is increased, the amount of accreting ice is higher because of the loss of accuracy on the collection efficiency.

The time required for each step of the calculation may be seen in Figure 5.31 and the durations of the time step are summarized in Table 5.4. The time duration appears slightly higher in the first step than in the second one, this means that the ice growth is slower at the beginning of the ice accretion. If the criterion is too high, there will be a lack of accuracy of the flow-related parameters. The opposite happens

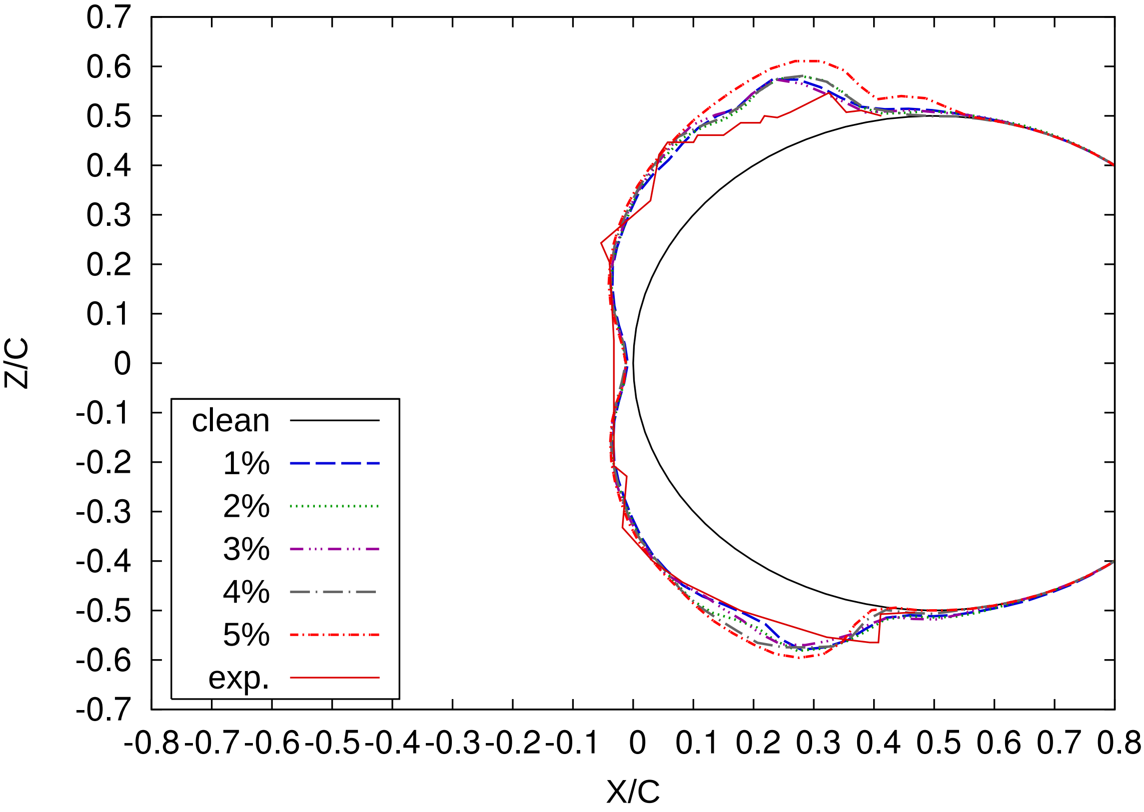

Figure 5.29: *Glaze ice shapes obtained on a cylinder with a step-by-step calculation based on the ice height criterion. Large droplets. Exposure time: 5min 30s.* $T_\infty \simeq -3^oC$.

for a too small criterion value: the profile will show more variations because of pile-up errors associated with a too high number of re-meshing and flow re-calculations. Such a problem is noticeable in Figure 5.31 for $b_{max} = 1\%$c and $b_{max} = 2\%$c.

Figures 5.32 and 5.33 show the profiles obtained for $b_{max} = 1\%$c and $b_{max} = 4\%$c respectively, each one being plotted with the average result that links the initial and the virtual last point of the simulation. As a reminder, this last point is generated via a linear interpolation for clarity purposes. The profile obtained here with the converged solution is in agreement with the results obtained on the cylinder case $O1$. Both curves show the same sort of profile, the simulated one being in each case globally below the average solution, see Figure 5.34. This means that the speed of the ice accretion behaves the same way on the cylinder surface, independently of the size of the droplets. Note that in both cases, the first update of the flow solution occurs at about the same time, around $t_{exp} = 90$s and the profile shows some linearity at the beginning of the computation (up to 30s). This can be explained by the nature of the ICECREMO model: when glaze ice occurs, the icing

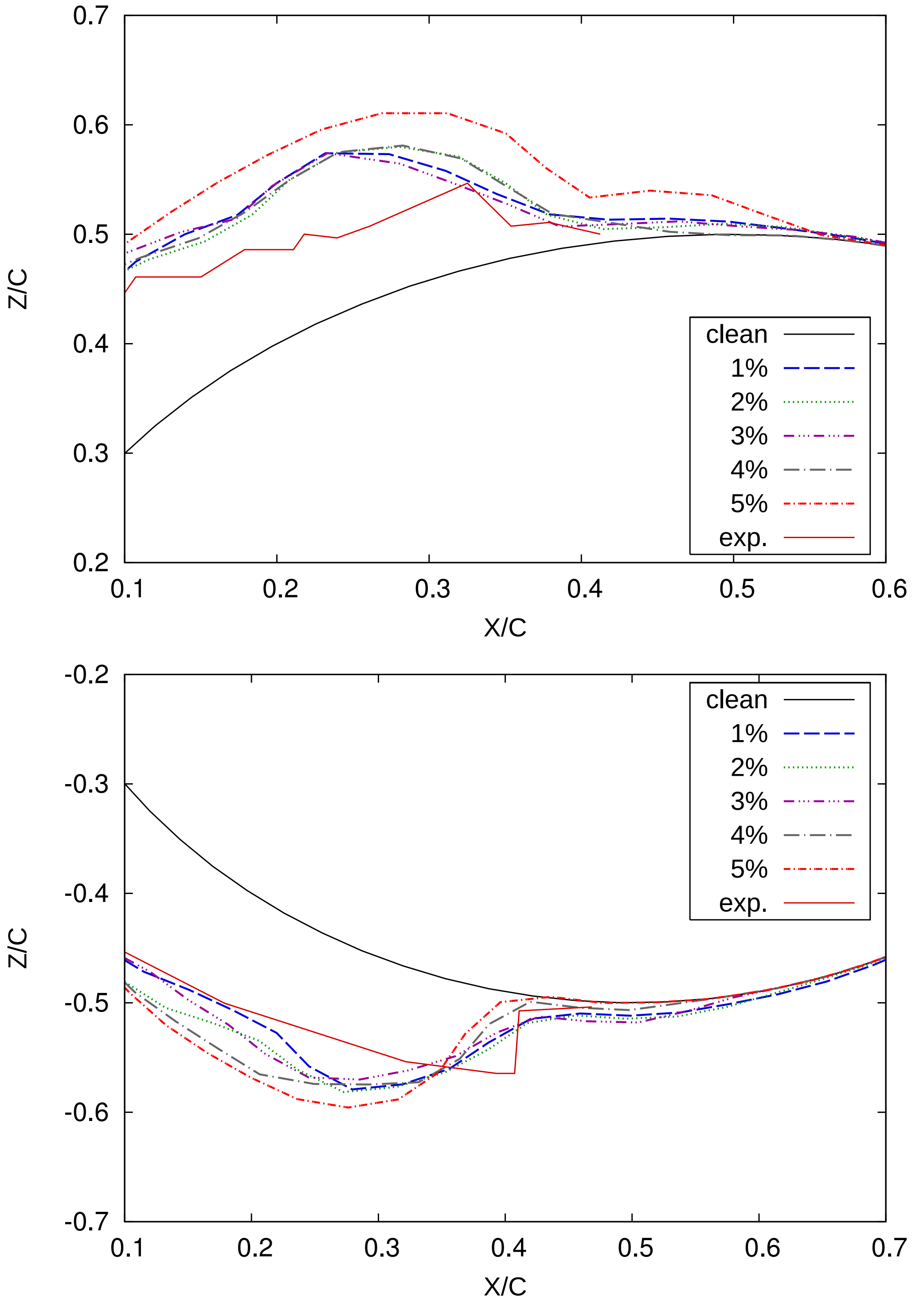

Figure 5.30: *Glaze ice shapes obtained on a cylinder with a step-by-step calculation based on the ice height criterion. Large droplets. Exposure time: 5min 30s.*

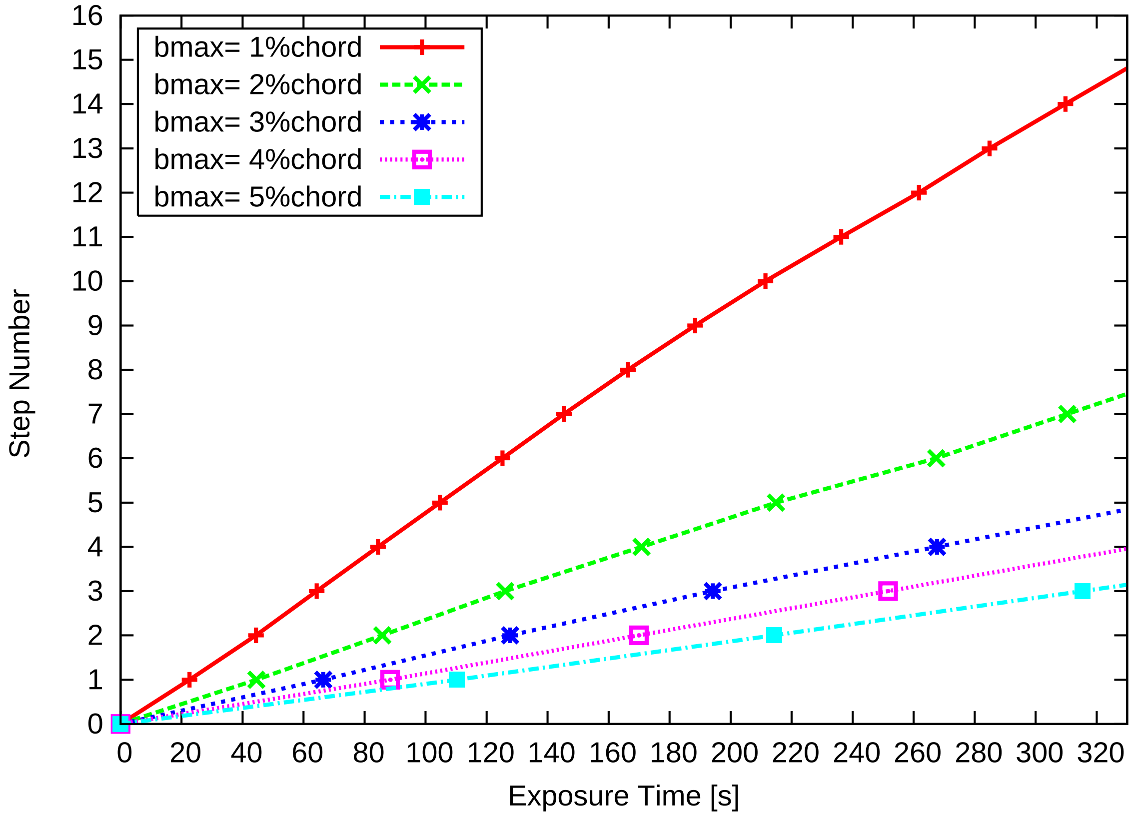

Figure 5.31: *Updates for the computation on a cylinder with the ice height criterion. Large droplets. Exposure time: 5min 30s.* $T_\infty \simeq -3^oC$.

model assumes that rime ice forms in the first place. Right after the first step, the ice accretion rate becomes faster when large droplets impinge on the cylinder surface.

	1%c	**2%c**	**3%c**	**4%c**	**5%c**
step	$t_{\mathbf{step}}$ [s]	$t_{\mathbf{step}}$ [s]	$t_{\mathbf{step}}$ [s]	$t_{\mathbf{step}}$ [s]	$t_{\mathbf{step}}$ [s]
1	22.61	44.53	66.45	88.36	110.29
2	21.75	41.27	61.23	81.57	104.05
3	19.95	40.30	66.45	81.71	101.09
4	20.11	44.73	73.57	78.36	14.57
5	20.24	44.05	62.30		
6	20.54	52.50			
7	20.18	43.02			
8	20.95	19.60			
9	21.98				
10	23.11				
11	24.79				
12	25.50				
13	23.19				
14	24.88				
15	20.22				

Table 5.4: *Time-step duration in the multi-step calculation based on the the ice criterion.*

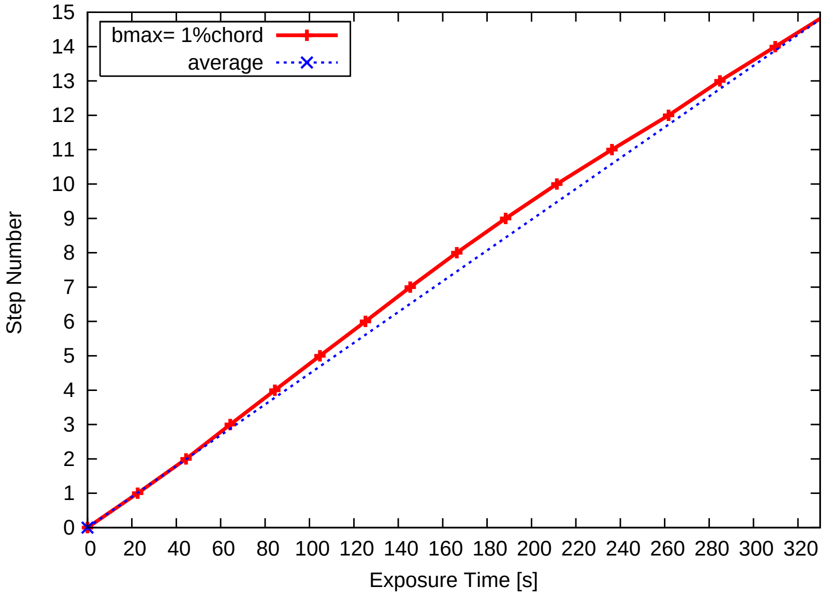

Figure 5.32: *Updates for the computation on a cylinder with the ice height criterion* $b_{max} = 1\%c$. *Large droplets. Exposure time: 5min 30s.* $T_\infty \simeq -3^oC$.

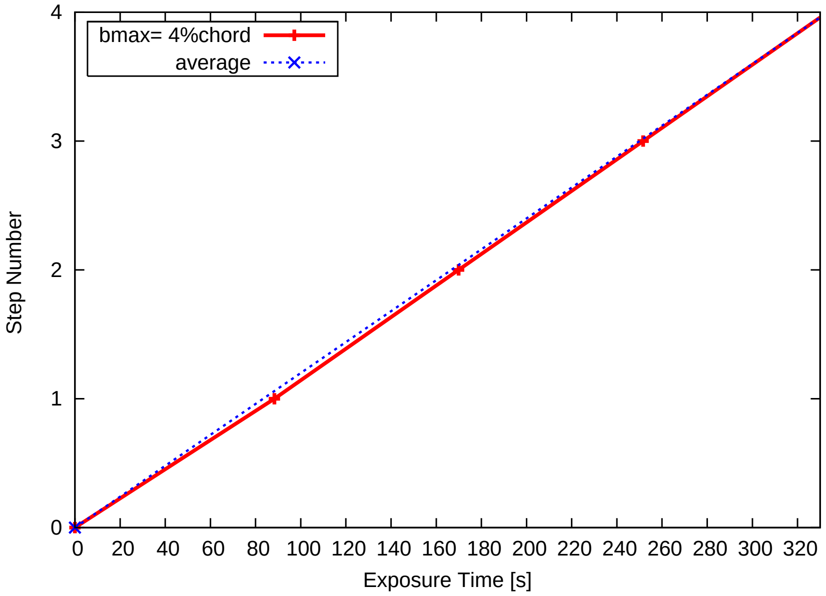

Figure 5.33: *Updates for the computation on a cylinder with the ice height criterion* $b_{max} = 4\%c$. *Large droplets. Exposure time: 5min 30s.* $T_\infty \simeq -3^oC$.

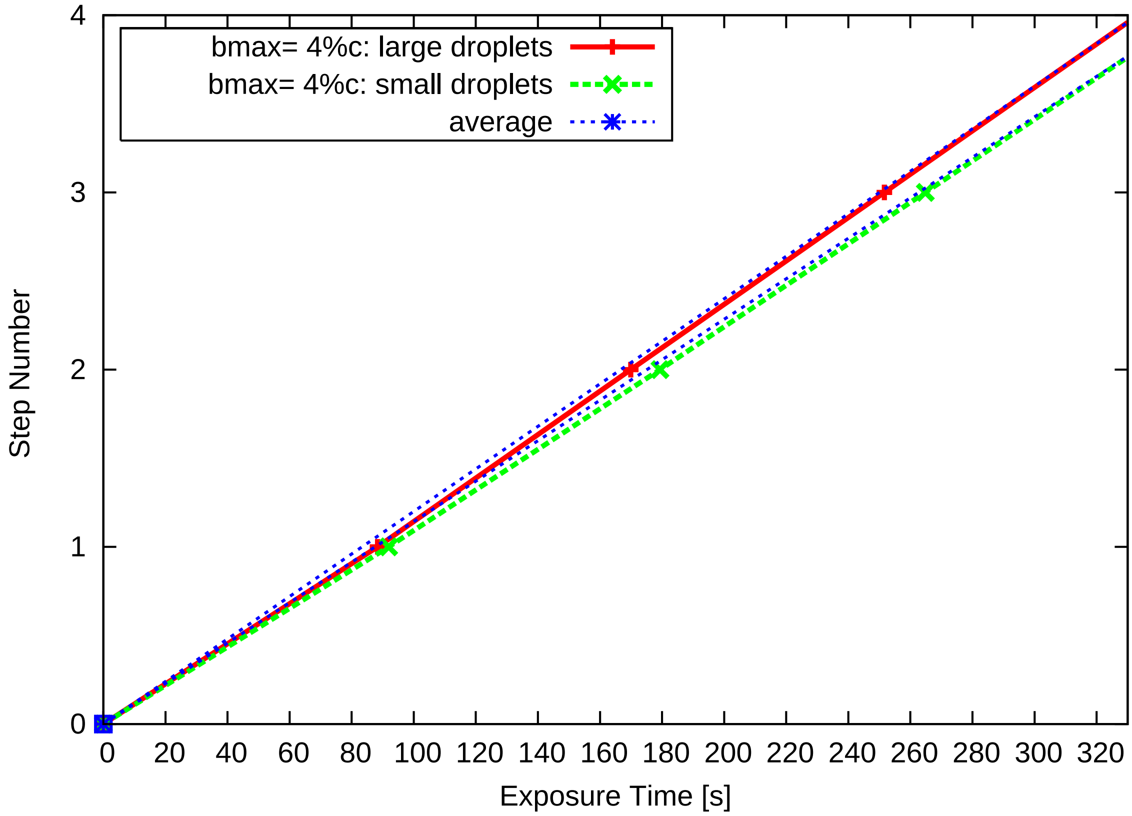

Figure 5.34: *Updates for the computation on a cylinder with the ice height criterion* $b_{max} = 4\%c$*. Small and large droplets. Exposure time: 5min 30s.* $T_\infty \simeq -3^oC$.

Comparison with the time-based result:

The ice shape obtained with the ice triggering criterion will now be compared to those generated with the time triggering criterion described in Section 5.3.1. For the time-based algorithm, convergence was reached in 7 steps, corresponding to the average estimated ice height per step: $X = 2.09\%$c. For the ice height criterion, convergence is reached for $b_{max} = 4\%$c in a 4-step algorithm. Simulated results are plotted together as may be seen in Figures 5.35 and 5.36. Both results are very similar and almost identical, except at the bottom part of the ice layer and for a small part of the top surface. When looking at the overall ice shape, the ice-based result seems closer to experiments. While this criterion requires 4 flow solutions, 7 were necessary for the standard multi-step procedure, which is equivalent to a gain of time around 43%. The ice based algorithm is once again the fastest procedure. A criterion value of $b_{max} = 4\%$c is therefore recommended for ice predictions on a cylinder in glaze ice conditions.

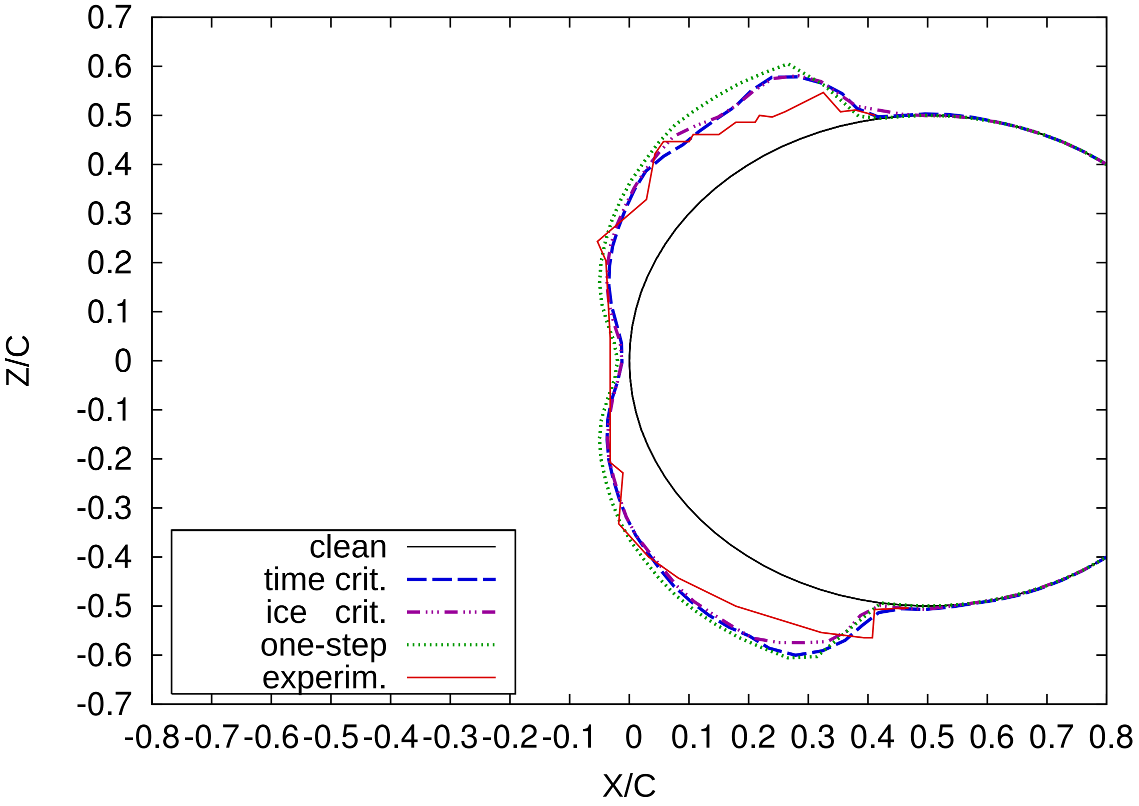

Figure 5.35: *Criteria comparison. Ice shapes obtained on a cylinder in glaze ice conditions. Large droplets. Exposure time: 5min 30s.* $T_\infty \simeq -3^oC$.

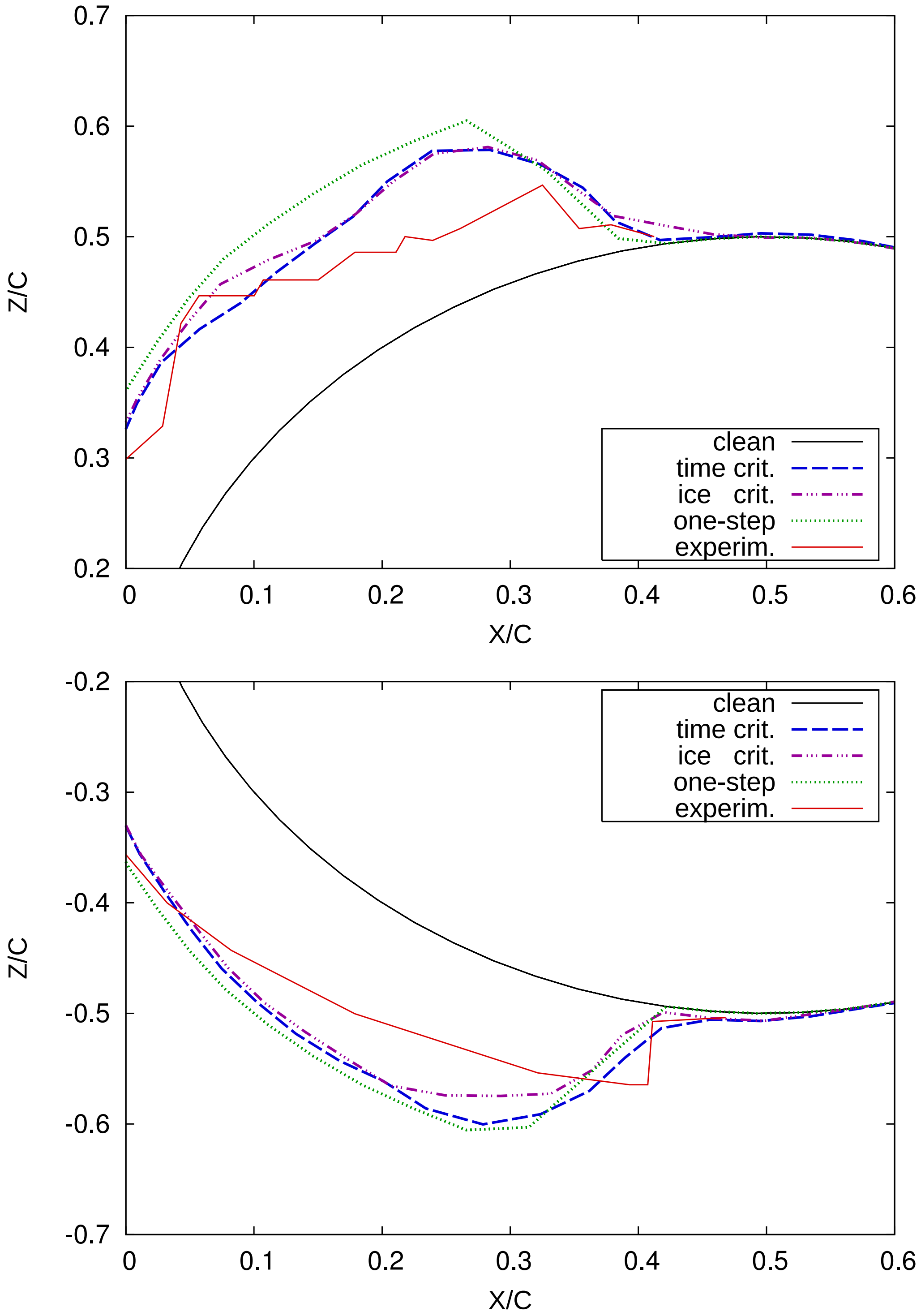

Figure 5.36: *Criteria comparison. Ice shapes obtained on a cylinder in glaze ice conditions. Large droplets. Exposure time: 5min 30s.* $T_\infty \simeq -3^oC$.

The ice-based algorithm being the most efficient of the two methods, the simulated ice shape using $b_{max} = 4\%$c will be compared to those generated with standard icing codes for the NATO/RTO exercise held in December 2000 [120].

Comparison with standard icing codes:

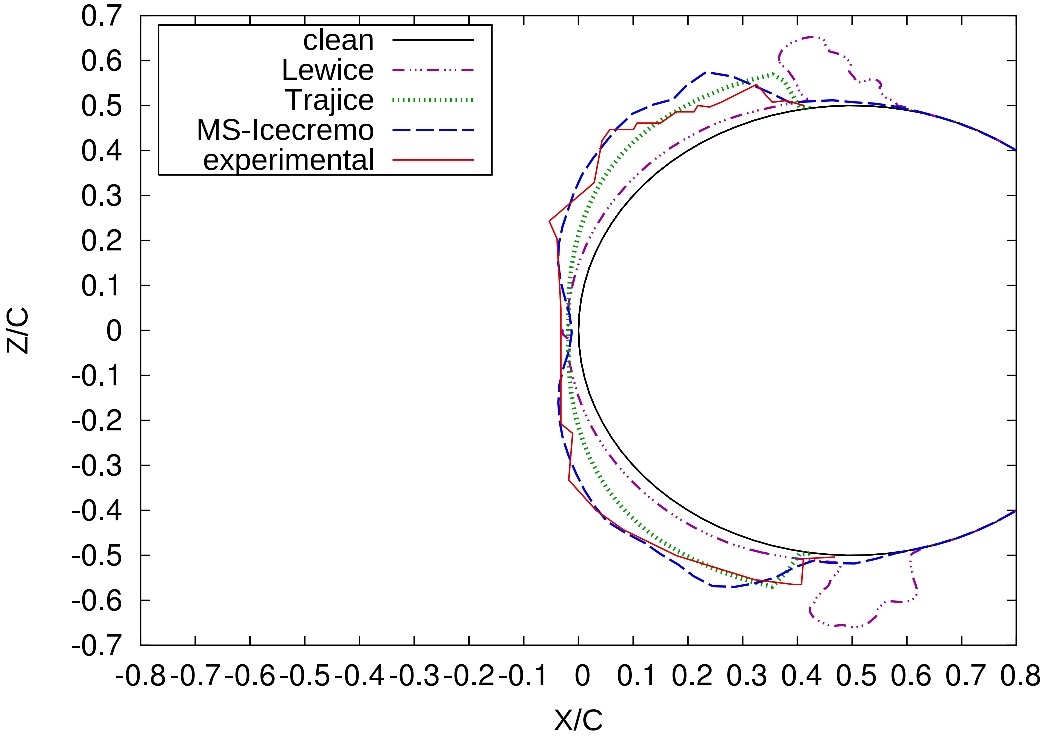

Figure 5.37: *Comparison of the multi-step with standard icing codes [120] for the impingement of large droplets in glaze ice conditions at* $T_\infty = -3^oC$*. Exposure time: 5min 30s.*

Ice shape predictions for the impingement of the large droplets on the cylinder surface may be seen from Figures 5.37 to 5.39. For this particular case, simulation data from the ONERA2000 icing code are not included for comparison as user-interaction produced erroneous results, as specified in [120].

The ice prediction generated by LEWICE is quite surprising: a horn appears at the ice limits of the cylinder upper and lower surfaces. A peak of ice is also noticeable at the stagnation line and the overall ice shape is under-estimated.

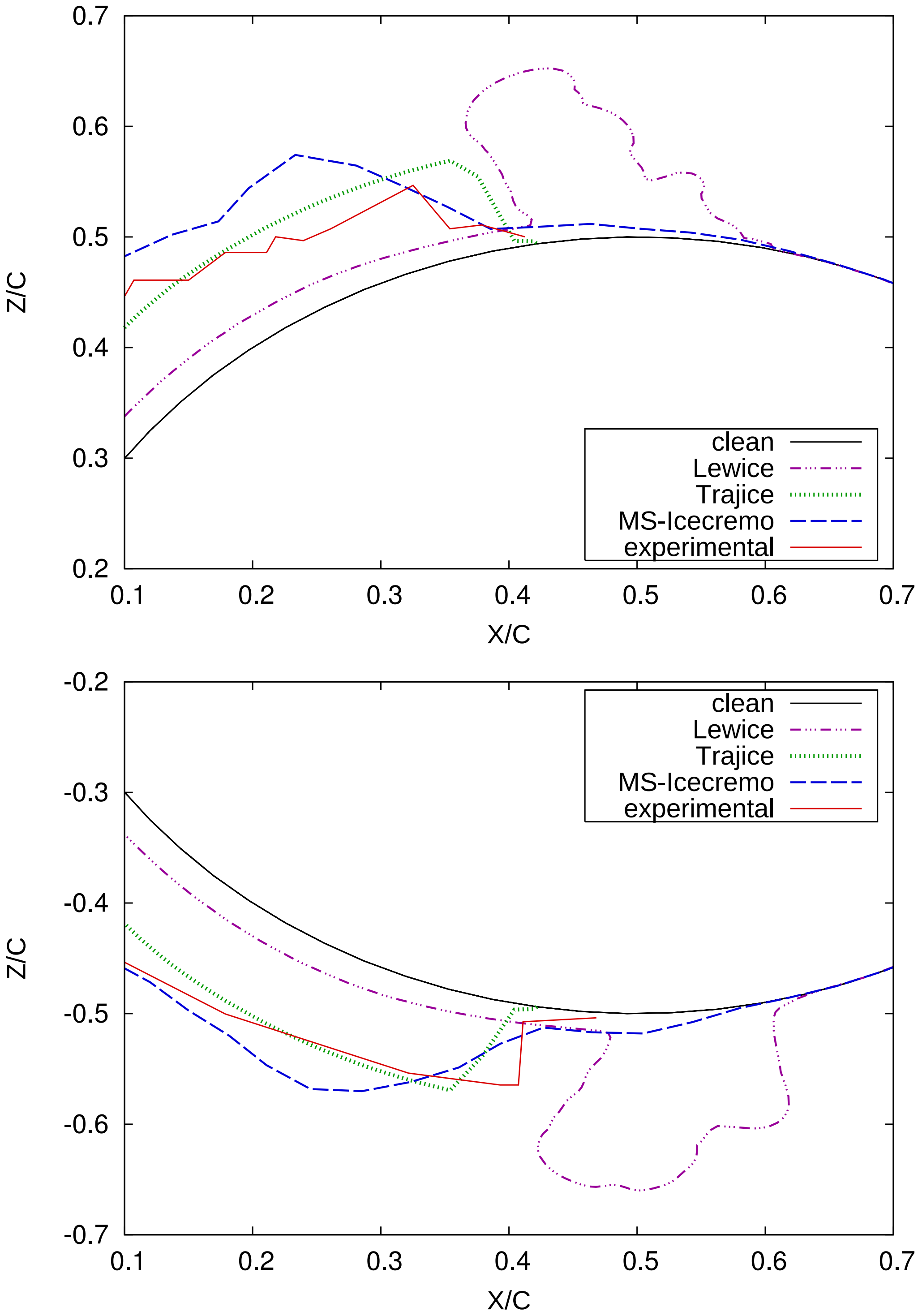

Figure 5.38: *Comparison of the multi-step with standard icing codes [120] for the impingement of large droplets in glaze ice conditions at* $T_\infty = -3^oC$*. Exposure time: 5min 30s. Exposure time: 5min 30s. Upper and lower regions.*

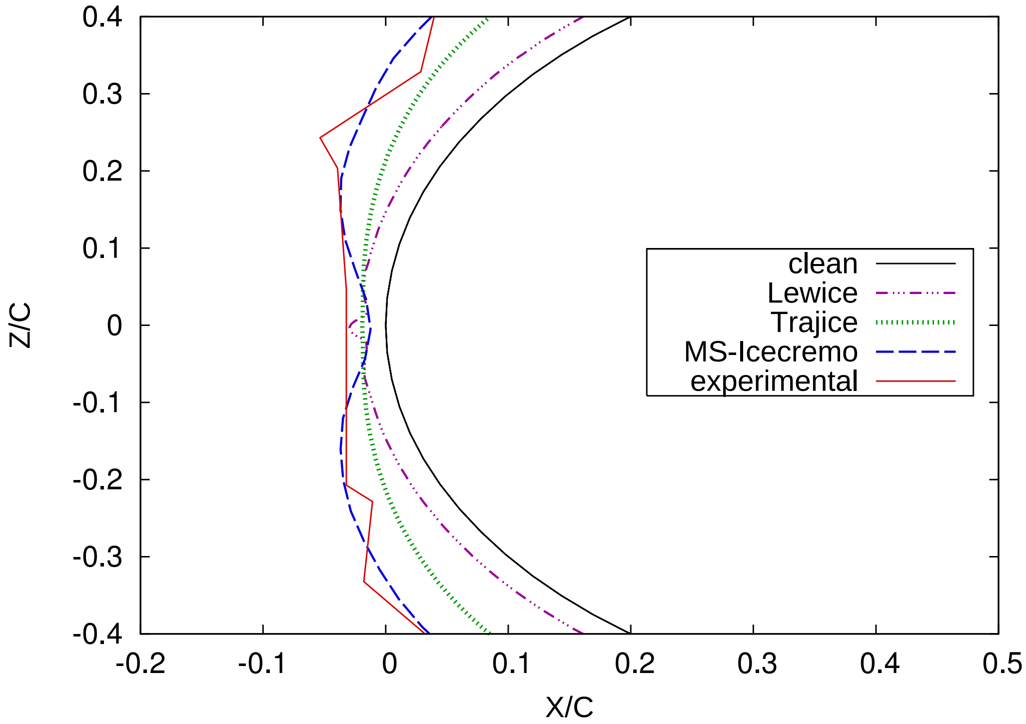

Figure 5.39: *Comparison of the multi-step with standard icing codes [120] for the impingement of large droplets in glaze ice conditions at* $T_\infty = -3^oC$. *Exposure time: 5min 30s. Stagnation region.*

Among all Messinger-based codes, the ice estimation from TRAJICE is closer to experiments. However, when looking at the whole ice structure, the result from this code is under-predicted. This is particularly noticeable along the forward faces of the cylinder.

Basically, the overall simulated ice shape obtained with the multi-time step algorithm implemented in ICECREMO2 matches better the experimentally measured shape in all regions and appears much more accurate than all simulated ice shapes obtained with the standard Messinger-based icing codes. The step-by-step algorithm based on the ice-height criterion appears efficient and reliable for predictions in glaze ice conditions on cylinders.

5.3.3 Summary

This section has outlined the advantages of a step-by-step algorithm over the standard one-step calculation. The influence of the update of the water film in such a procedure has been demonstrated, showing noticeable differences at the boundaries of the ice layer for simulations performed with and without this update. Two criteria have been investigated and tested in rime and glaze ice conditions. A summary of these results is written in Table 5.5.

case	**type**	**time crit**			**ice height crit**			**t_{exp}**	**c**
		t_{step} [s]	**n_{step}**	**%c**	**b_{max} [mm]**	**%c**	**n_{step}**	**[s]**	**[mm]**
O1	rime	55	6	2.16	2.54	4	3	330	63.5
O1	glaze	55	6	2.36	2.54	4	4	330	63.5
O2	glaze	47.14	7	2.09	2.54	4	4	330	63.5

Table 5.5: *Summary: criteria study on a cylinder under rime and glaze ice conditions.*

- In rime ice conditions, convergence was reached in 6 multi-time steps for the time-triggering algorithm. Three flow solutions and a maximum ice height per step equal to $b_{max} = 4\%$c was necessary for the ice-triggering procedure.
- The size of the droplets did not seem to influence significantly the number of steps required in glaze ice conditions. Six or seven flow solutions were necessary for the simulation based on the time criterion while only four were required for the ice-triggering algorithm. In the latter case, an ice height allowed per step of $b_{max} = 4\%$c was best to reach convergence.

Two or three additional flow calculations were necessary for the time-based algorithm to reach convergence. The ice-based criterion was established as the best criterion due to consequent time savings around 50% in rime ice conditions, 33% and 43% in glaze ice conditions, without loss of accuracy. A maximum ice height value of $b_{max} = 4\%$c in an ice-based multi-step algorithm is therefore recommended for ice predictions on cylinders.

Ice prediction will now be studied on a NACA0012 wing configuration. The purpose of the next section is to define whether or not the structure and size of the body will influence the multi-step algorithms.

5.4 Ice Predictions on Airfoils

A multi-step approach applied to cylinders evaluates the ice accretion more accurately than a single-step procedure. The purpose of this section is to examine the ice accretion on airfoils under various icing conditions and determine the criterion that delivers the most accurate results. The conclusions drawn from the cylinder study may not be applicable to a different geometry and different atmospheric conditions. This will now be investigated.

5.4.1 Problem Configurations

Two configurations are studied, first at low temperature: $T_\infty \simeq -26^oC$ and secondly at mild temperature: $T_\infty \simeq -7^oC$. These temperatures are typical of rime and glaze ice conditions, respectively. The airflow velocity is $V_\infty = 67$ m/s and the wing inclination (angle of attack) equal to $\alpha = 4^o$ in rime ice conditions and $\alpha = 3^o$ in glaze ice conditions. Droplet size from 20 μm to 25 μm, which is standard in icing conditions, will impinge on a NACA0012 wing. Exposure time is 6 and 20 min respectively. Atmospheric and icing conditions applied to the airfoil study are listed in Table 5.6.

ice type	**T_∞** **[°C]**	**V_∞** **[m/s]**	**d_d** **[μm]**	**t_{exp}** **[min]**	**α** **[°]**	**chord** **[m]**
rime	-26	67	20	6	4	0.534
glaze	-7	67	25	20	3	0.914

Table 5.6: *Airflow and icing conditions applied to a NACA0012 wing [17, 120].*

5.4.2 Time Criterion

The time-based criterion is the first criterion tested on the NACA0012 wing configuration for the different atmospheric conditions listed in Table 5.6. Predicted shapes in rime ice conditions are first discussed.

Rime Ice Prediction

Simulations were carried out at $T_\infty = -26^oC$ for a 6 min exposure time to icing. Figure 5.40 shows the results determined with several multi-time steps and the experimental data. As usual, only the most relevant ice shapes are plotted. However, simulated results for different multi-time steps may be seen in Appendix E.

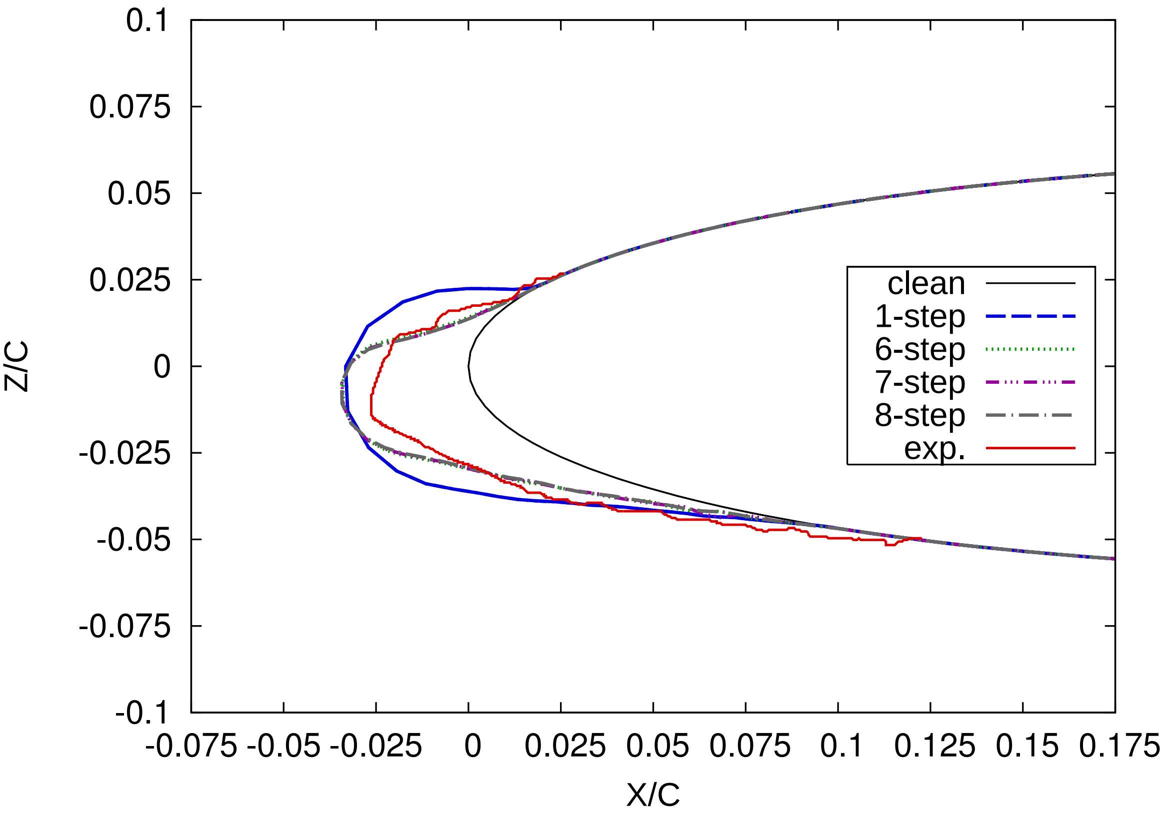

Figure 5.40: *Rime ice shapes obtained on a NACA0012 wing with a step-by-step calculation based on the time-criterion. Exposure time: 6 min.* $T_\infty \simeq -26^oC$.

The ice shapes obtained in 6, 7 and 8 steps are plotted together with the single-step result and compared to experiments from Shin and Bond [17]. As previously noticed, the ice height is over predicted and here again, the step-by-step algorithm reduces the error significantly. A perfect convergence is achieved with the 7-step procedure. The total ice height being $b = 18.69$mm, the average ice height per step can be determined as the percentage of chord length $X = 0.5\%$c, with $c = 0.534m$.

The current approach applied to the wing should not be compared directly to the one used on a cylinder without further simulations. For the cylinder study at the same temperature, convergence was reached for $X = 2.16\%$ of the diameter

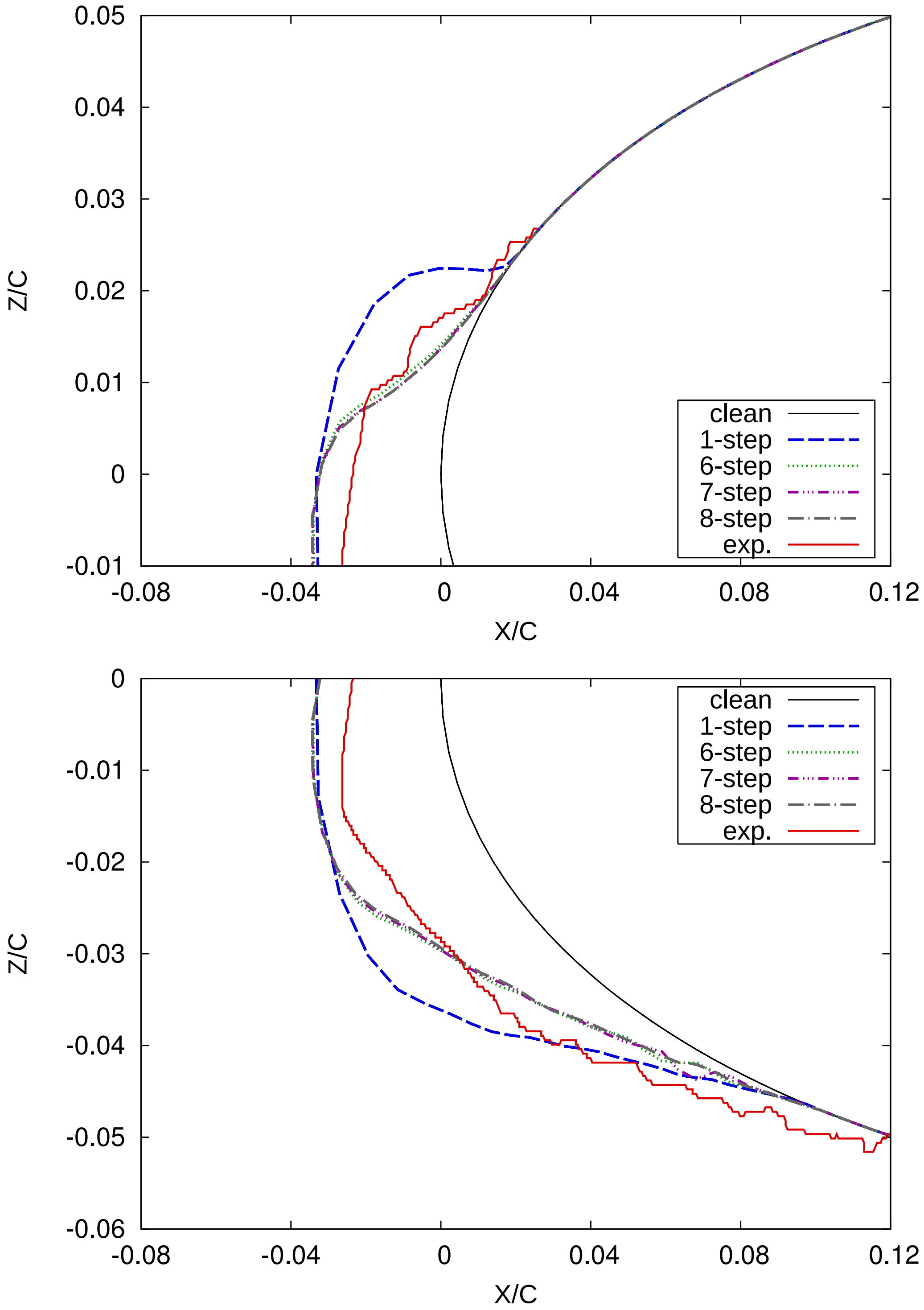

Figure 5.41: *Rime ice shapes obtained on a NACA0012 wing with a step-by-step calculation based on the time-criterion. Exposure time: 6 min.* $T_\infty \simeq -26^oC$.

length. A high number of simulations under similar conditions would be necessary to establish an accurate proportional factor between the results obtained on the cylinder and on the wing. However, this value of 0.5% is consistent with the statement of the LEWICE manual [119]: "*the maximum amount of ice accreted in any time step should be no greater than* 1% *of the chord*". This value is used in LEWICE as the default setting for multi-step calculations on airfoils, but is not adapted to smaller geometries: "*for very small chord geometries (<6 inch) such as cylinders, the number of time steps recommended by the code may be considered prohibitive by the user. It may be possible (and even necessary) to decrease the number of time steps for these cases*". When using the formula from Wright et al [118], the estimated proportion of chord per step is $X = 0.74\%$. This value, determined for seven steps in Equation 5.2.1 is slightly higher than the value $X = 0.5\%$ obtained in the current work with the time-based algorithm.

For the rime ice study on the cylinder, 6 steps were required to reach convergence, which is almost identical for the wing case since one more multi-time step is necessary.

Convergence of the ice shapes will now be investigated in glaze ice conditions.

Glaze Ice Prediction

The time-based criterion is applied to the NACA0012 wing in glaze ice conditions at $T_\infty = -7^o C$ for the impingement of droplets of size $d_d = 25\mu m$ with the conditions specified in Table 5.6. For the present test case, the chord length is $c = 0.914$m and the exposure time to icing is $t_{exp} = 20$min. The corresponding relevant final ice shapes may be seen in Figure 5.42 and Figure 5.43, where they are plotted together with the experimental ice shape. The results obtained with steps ranging from 11 to 14 are considered to determine the ice shape convergence. Additional simulated ice shapes generated with a lower number of steps may be seen in Appendix F.

The measured ice shape is classical for glaze ice conditions with two main peaks located either side of the leading edge. This ice shape is slightly inclined towards the negative values of z, this is due to the angle of attack $\alpha = 3^o$. Not surprisingly, this type of ice structure is very difficult to reproduce numerically due to large ice surface deformations that disturb the airfoil surrounding air flow significantly. Such surface deformations may lead to re-meshing and convergence problems with the mesh generator and with the flow solver, respectively.

Ice shape predictions are quite different from experiments, particularly when obtained with the single-step algorithm which does not estimate the double horn structure and appears very smooth.

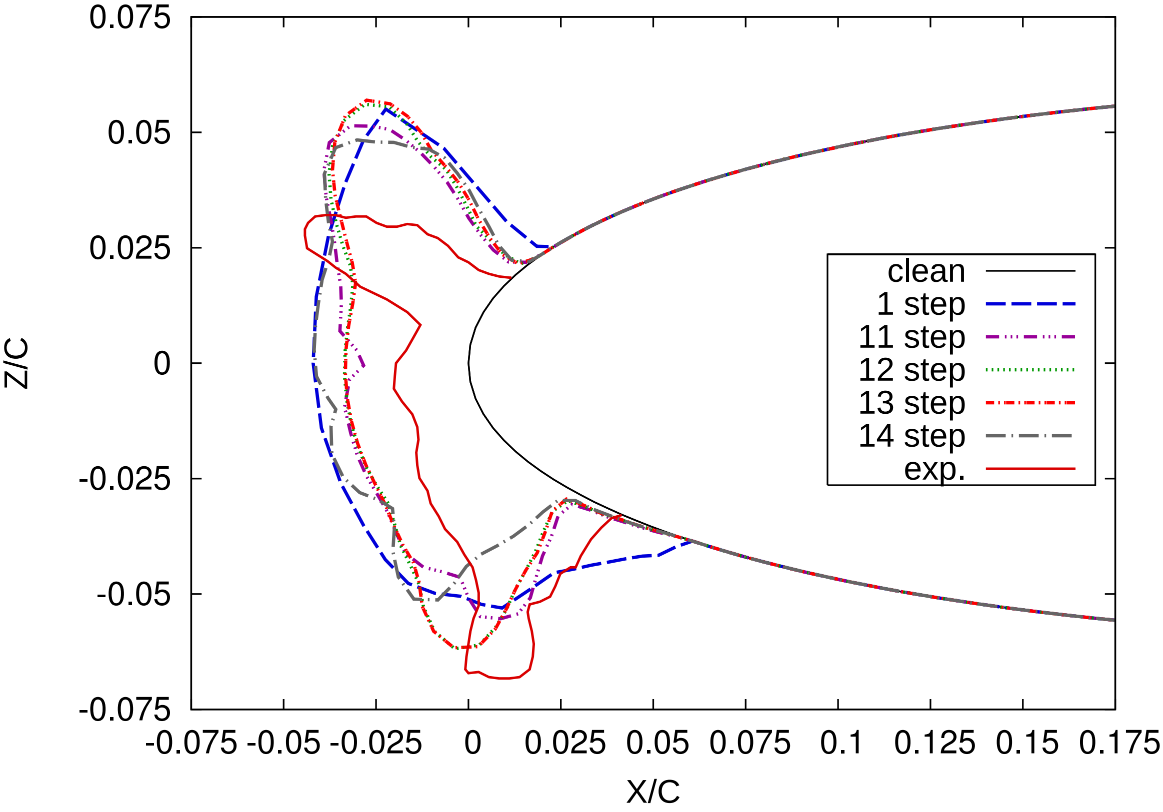

Figure 5.42: *Glaze ice shapes obtained on a a NACA0012 wing with a step-by-step calculation based on the time criterion. Exposure time: 20 min.* $T_\infty \simeq -7^oC$.

- The upper ice extent is almost similar for all simulations and appears larger than experiments. The upper ice horn is predicted using both single and multi-step algorithms. However, the direction of this horn is wrong and the ice mass over-predicted.

- The depression measured in the stagnation region is not predicted by the single-step algorithm, which contradicts experimental observations. As may be noticed, a multi-time step algorithm enhances the quality of the results, even if predictions remain far from being similar to the experimental data.

- The lower ice horn is predicted using either the one-step algorithm or the multi-step calculation but the direction does not agree with experiments and the ice structure is globally under-estimated. Despite being in most cases too close from the nose region, the lower horn is better predicted with all multi-step algorithms.

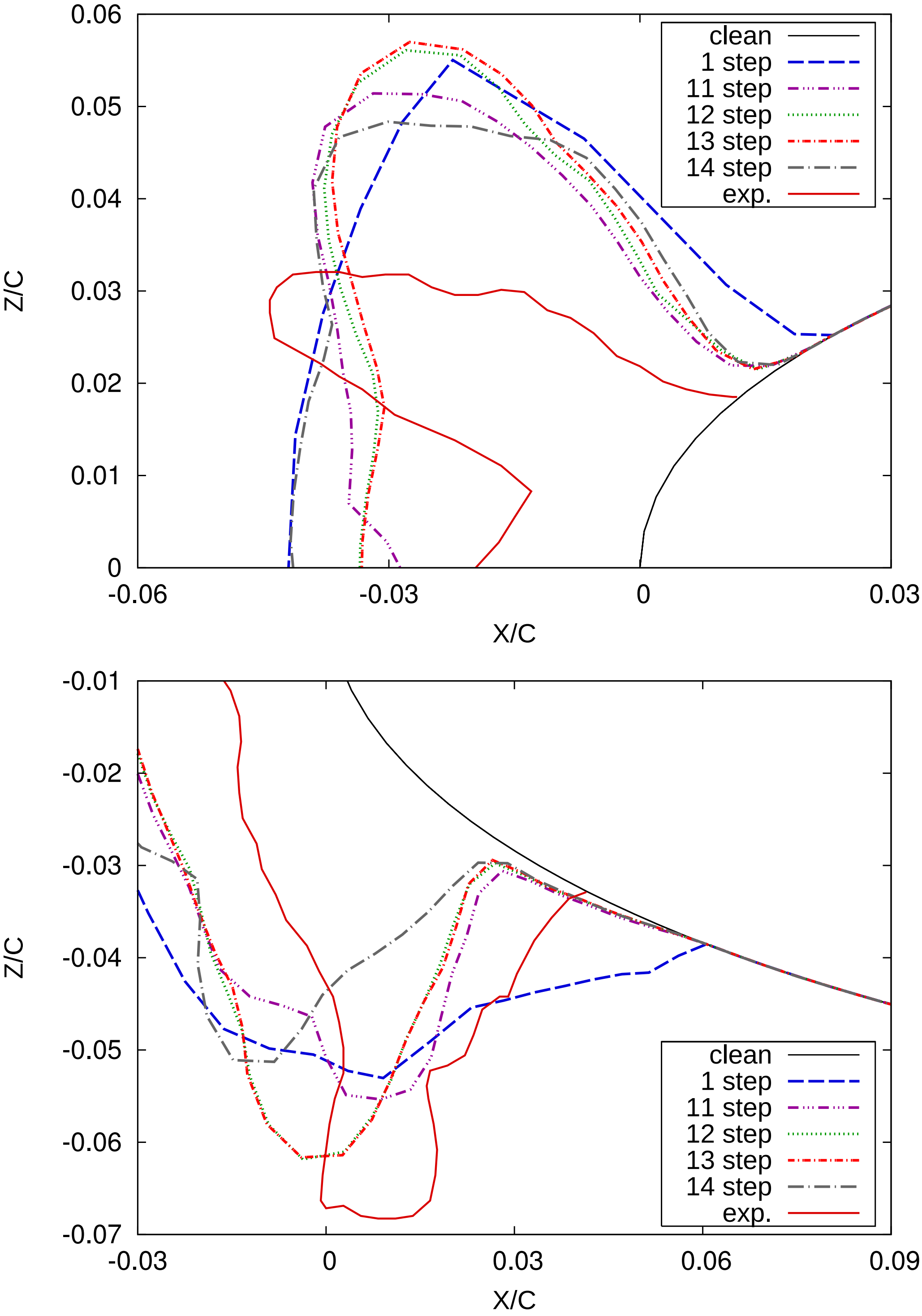

Figure 5.43: *Glaze ice shapes obtained on a a NACA0012 wing with a step-by-step calculation based on the time criterion. Exposure time: 20 min.* $T_\infty \simeq -7^oC$.

Convergence is achieved for step 12 and only minor differences appear betwen the simulated results generated in 12 and 13 steps. This result is astonishing considering the high complexity of the ice shape under these conditions (glaze ice, large exposure time, high number of flow solutions). When the simulation is run with a number of steps lower than 12 or higher than 13, the final ice estimation agrees much less with experiments. This underlines once again the requirement for an accurate number of steps in a multi-step algorithm. Although being relatively far from experiments, the 12-step algorithm clearly demonstrates the advantage of a multi-stepping procedure compared to a single-step calculation: the upper and lower horns are more pronounced and a better agreement with experiments is obtained between the double horn regions. Each of the characteristics of the measured ice shape is retrieved, however in a slightly different proportion.

As for the previous cases based on the time criterion, the average ice height estimated per step may be written in terms of chord length. For the 12-step algorithm, this corresponds to $X \simeq 0.46\%c$ per step. This proportion of chord is below the value $X = 0.8\%$ calculated using the formula from Wright et al. (5.2.1) for 12 steps.

The update of the water film appeared as an important parameter for icing studies on a cylinder. It has been demonstrated for the cylinder cases that this update insured a better accuracy of the multi-step predictions. The influence of the water film update for a larger exposure time, a different geometry and a different temperature is now discussed briefly.

Influence of the water film update:

Figures 5.44 and 5.45 show the final ice estimation with and without the update of the water film. The ice shape simulated without the update of the height and temperature of the water film required a new algorithm similar to the one used in ICECREMO1 and detailed in the previous chapter. As on the cylinder geometry, the effects of the water layer appear clearly.

- Both ice shapes are strictly identical in the first step only. Immediately after this first step, the influence of the water update is clearly noticeable.

- For the ice shape generated with the update of the water film, more ice is present on top of both the upper and the lower horns and the ice layer extends more in the lower region. This is more apparent on the closer view, see Figure 5.45.

- For the test run without the water update, the ice layer is slightly higher on the upper horn when the ice shape reattaches to the clean surface. As shown

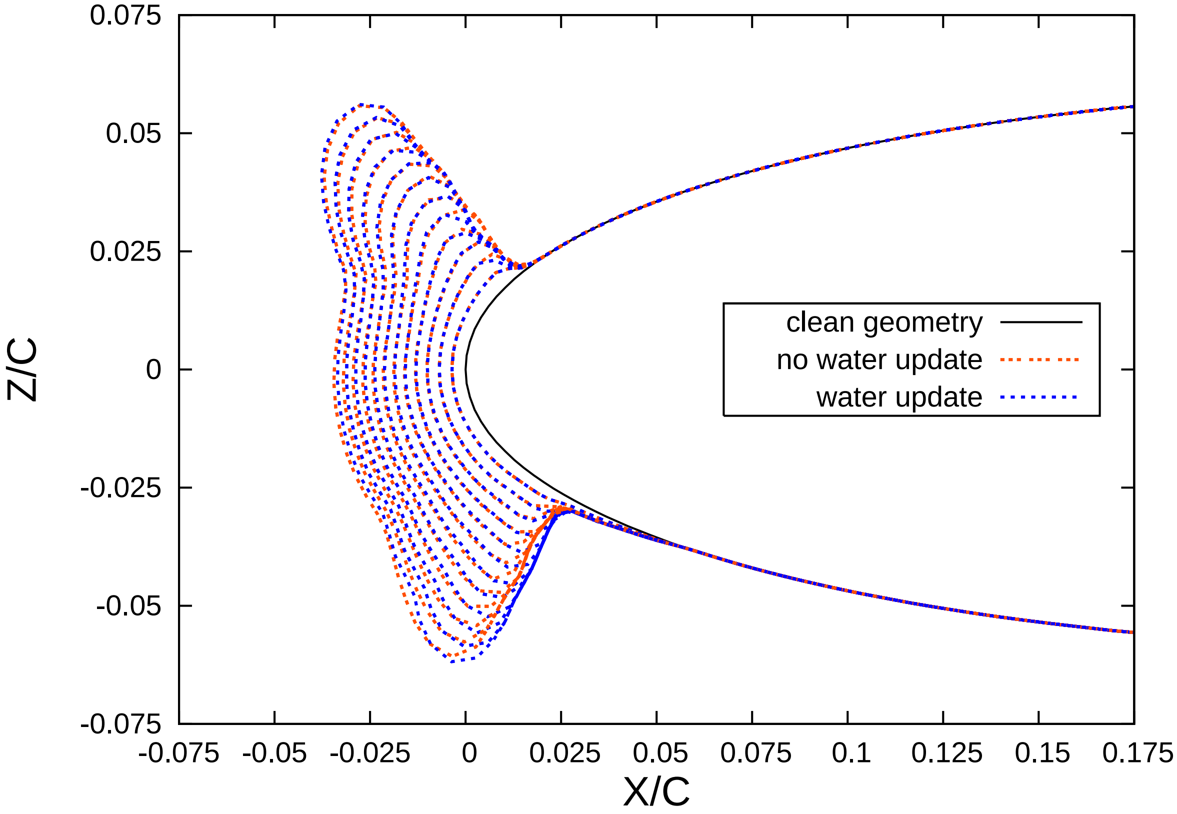

Figure 5.44: *Influence of the water update on a NACA0012 wing for the step-by-step calculation based on the time criterion. Exposure time: 20 min.* $T_\infty \simeq -7^oC$.

in Figure 5.46, the ice layer appears clearly higher between the double horn shape when the update is not performed.

Globally, the update of the water film increases the ice height of both the upper and lower horns and allows the ice shape to extend more in the lower region. As in the cylinder case, the presence of a pre-existing fluid film allows more water to flow up to the top of the upper and lower horns and the ice layer is reduced in the stagnation region since there is less liquid likely to freeze. Although slightly noticeable at this temperature, the influence of the water film update will be even more important for temperatures close to freezing. For instance, the study performed on the cylinder at the temperature $T_\infty = -3^o$C and described in Section 5.3.1 showed a significant difference on the upper and lower aft due to the water film and temperature history preserved from one step to the next.

As performed for ice growth study on the cylinder, the multi-step algorithm based on the ice height criterion will now be investigated for the NACA0012 wing geometry.

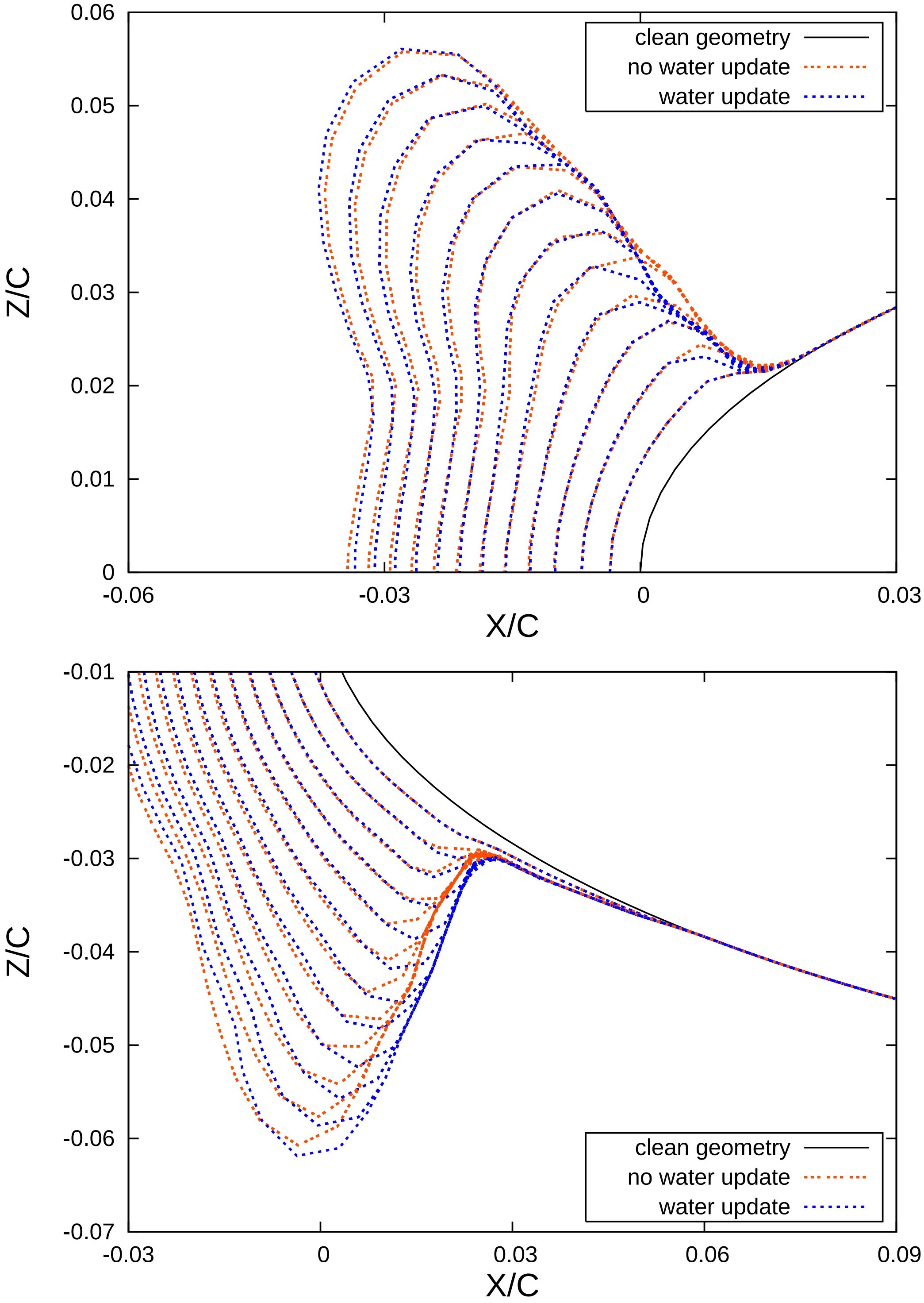

Figure 5.45: *Influence of the water update on a NACA0012 wing for the step-by-step calculation based on the time criterion. Exposure time: 20 min.* $T_\infty \simeq -7^o C$.

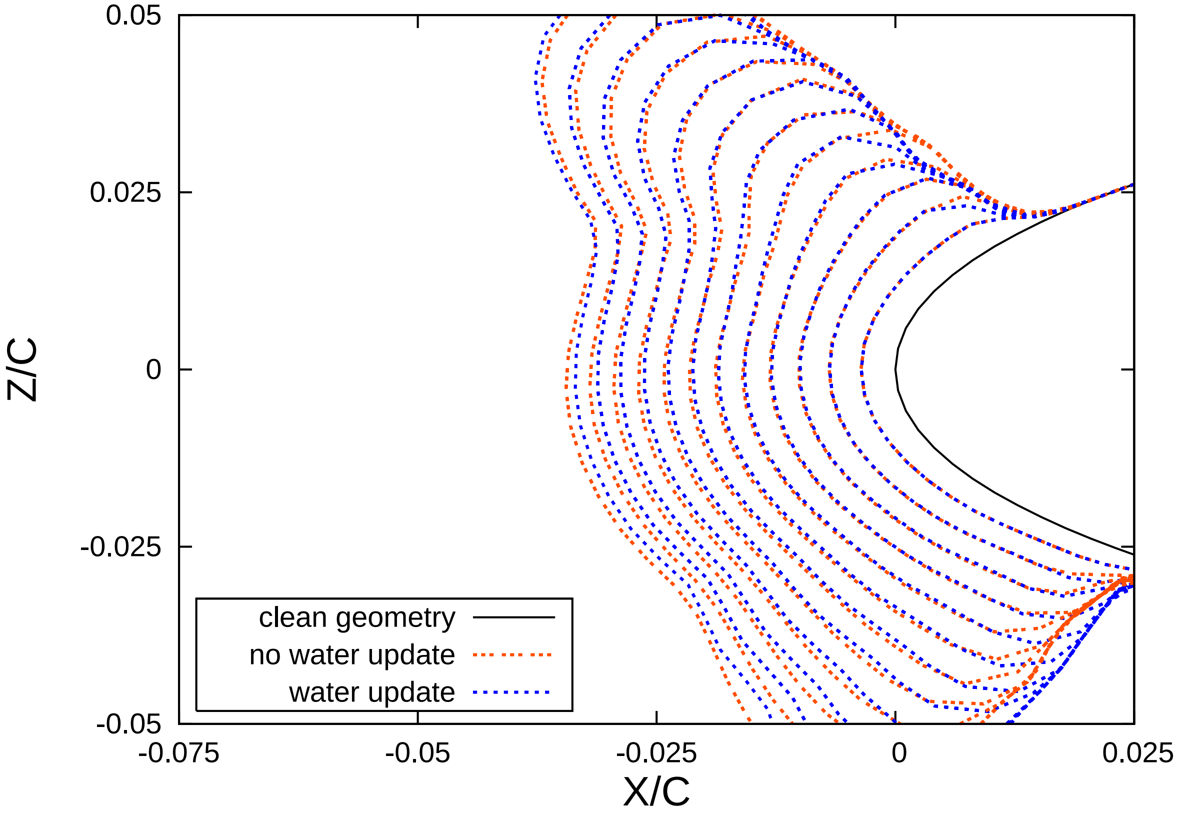

Figure 5.46: *Influence of the water update on a NACA0012 wing for the step-by-step calculation based on the time criterion. Exposure time: 20 min.* $T_\infty \simeq -7^oC$.

5.4.3 Ice Height Criterion

As discussed earlier in Section 5.3, the ice height criterion has proved efficient. The objective of this section is to determine the convergence on a different geometry and establish the number of steps necessary to insure the accuracy of the predictions. A NACA0012 wing structure will be investigated for the same two chord lengths used for the time-based algorithm: $c = 0.534$m and $c = 0.914$m for simulations performed in rime and glaze ice conditions, respectively. Airflow and icing conditions applied to the wing remain the same and are those defined in the previous section.

Rime Ice Prediction

The ice-height criterion defined as a percentage of the chord length $c = 0.534$m is first tested in rime ice conditions, at the temperature $T_\infty = -26^oC$. The most important

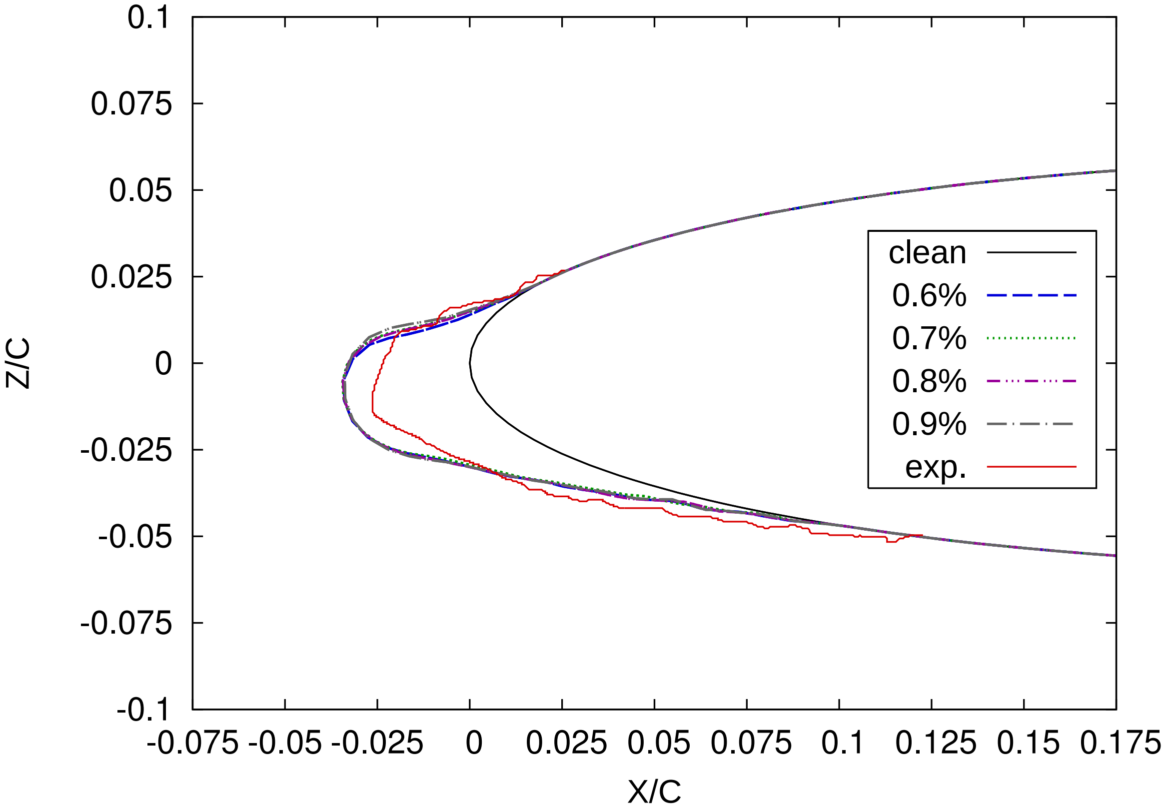

Figure 5.47: *Rime ice shapes obtained on a NACA0012 wing with a step-by-step calculation based on the ice height criterion. Exposure time: 6 min.* $T_\infty \simeq -26^o C$.

simulated results are represented in Figure 5.47, but the full set of predicted ice shapes obtained under these conditions may be seen in Appendix E.

Simulation results are globally satisfactory, despite the ice height being overestimated in the nose region. As may be seen on Figure 5.48, convergence is reached for the value of criterion $b_{max} = 0.8\%c$ ($\simeq$ 4.2mm). Five flow solutions and flow-related parameters calculations have been necessary for this simulation.

Results obtained with this criterion are in perfect agreement with the previous observations on the cylinder geometry or when using the time-criterion in rime ice conditions: the ice accretion follows the evolution of the collection efficiency and this accretion is linearly proportional to the exposure time. Such procedure based on the ice height criterion in rime ice conditions is therefore very similar to a procedure based on the time criterion as the time per step is almost constant throughout the computation, as may be seen in Figure 5.49. This picture describes the ice height generated in each step for simulations run with the time-based criterion generated in 7 steps and with the ice-based criterion for $b_{max} = 0.8\%$c. As may be noticed in

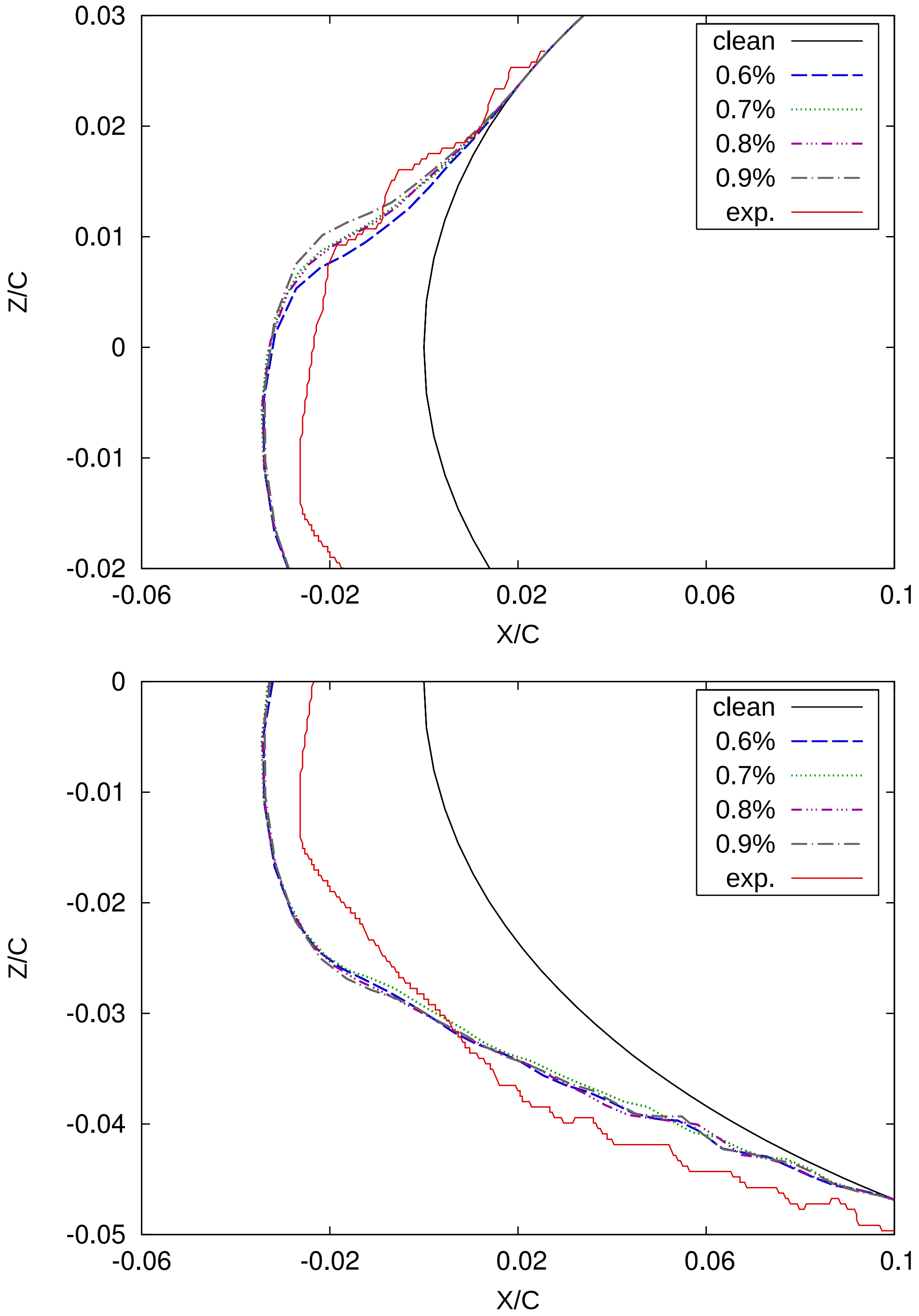

Figure 5.48: *Rime ice shapes obtained on a NACA0012 wing with a step-by-step calculation based on the ice height criterion. Exposure time: 6 min.* $T_\infty \simeq -26^o C$.

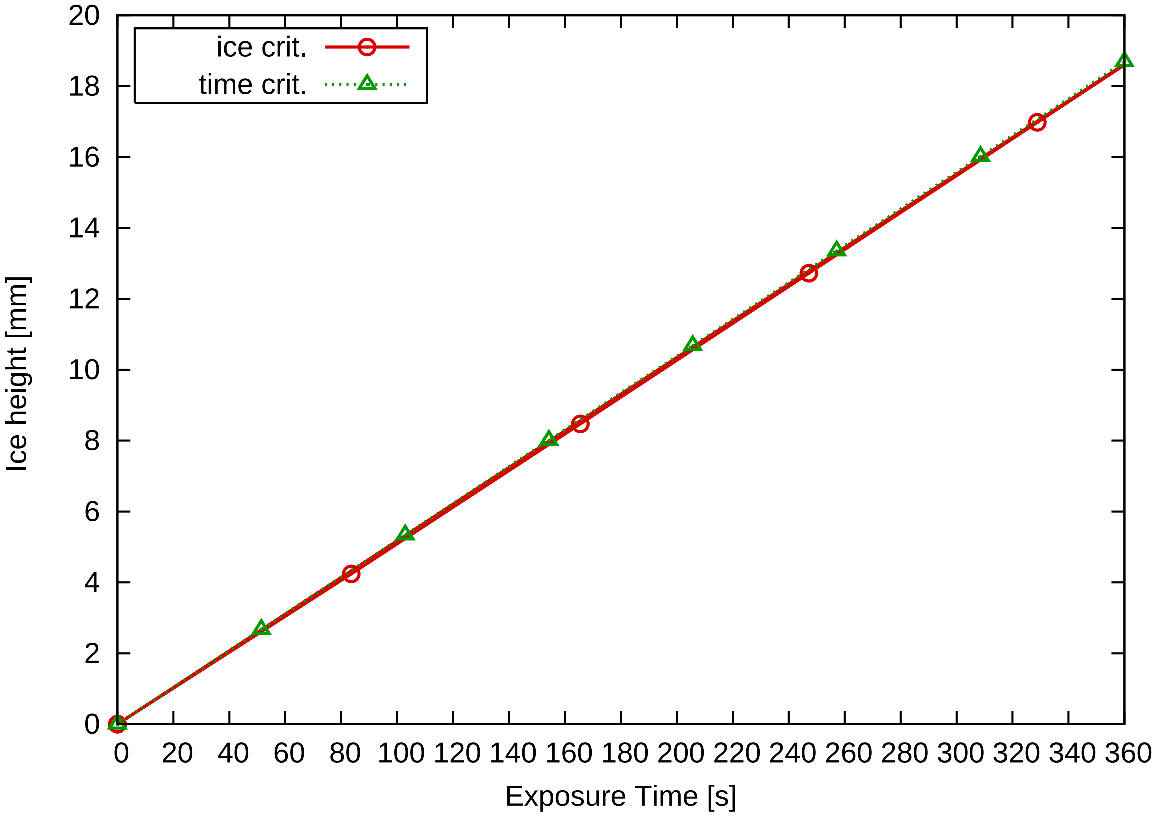

Figure 5.49: *Ice height comparison in each step for both criteria. Exposure time: 6 min.* $T_\infty \simeq -26^oC$.

this figure, the time per step is constant in each algorithm, but the time per step is greater for the ice-based algorithm. This shows once again the advantages of using the ice criterion: the overall computation time is reduced as there is no need for a new flow update before $t = 83.4$s. When using the time-criterion, the first update is performed a the time $t = 51.4$s, i.e. 32 seconds before the first update in the ice-based simulation.

As for the time-based model, the results obtained on the wing with the ice criterion can not be compared directly to those obtained on the cylinder. For the cylinder study at the same temperature, convergence was reached for an ice height criterion equal to $b_{max} = 3\%$c. For the simulation performed on this wing, convergence is achieved with $b_{max} = 0.8\%$c. This value is however in agreement with the statement of the LEWICE manual [119]: a maximum amount of ice per step should not be greater than 1% of the chord length.

Comparison with the time-based result:

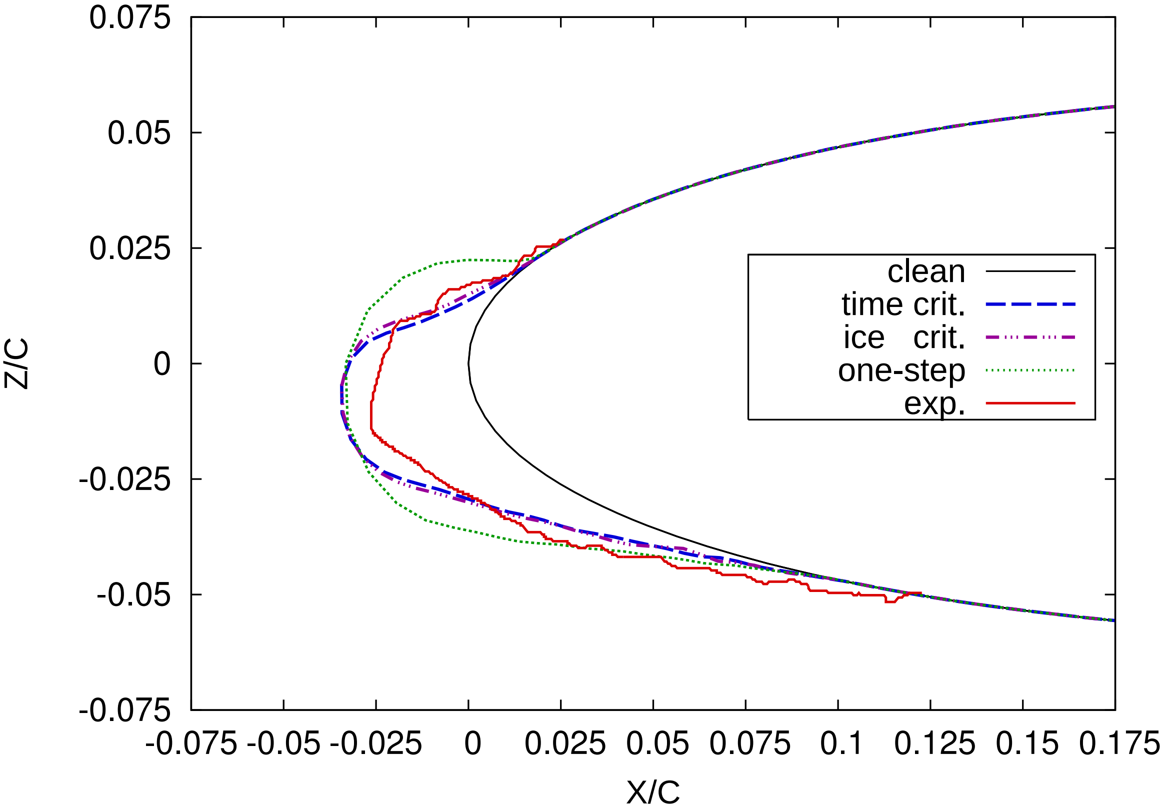

Figure 5.50: *Criteria comparison. Ice shapes obtained on a NACA0012 in rime ice conditions.* $T_\infty = -26^oC$. *Exposure time: 6 min.*

To conclude this section concerning rime ice growth, final ice prediction with both criteria may be seen in Figure 5.50. They are almost identical. The result obtained for the simulation based on the ice-height criterion is slightly closer to experiments in the upper part of the airfoil. Predictions are however identical in the nose and lower regions. Although relatively close to each other, the simulated result based on the ice-height criterion predicts a final ice shape which matches better the experimentally measured results. In addition, as previously stated, the whole computing time is largely reduced with this procedure. This is in agreement with the conclusions drawn from the ice study on a cylinder in rime ice conditions. Consequently, the ice criterion $b_{max} = 0.8\%$c can be retained as the best ice shape estimator under these specific icing conditions.

Glaze Ice Prediction

In this section, the NACA0012 wing is subject to the impingement of small droplets, $d_d = 25\mu$m, at the temperature $T_\infty = -7^o C$. Different values of ice criterion are tested for a 20 min exposure time to icing. Each criterion is written as a proportion of the chord length $c = 0.914$m.

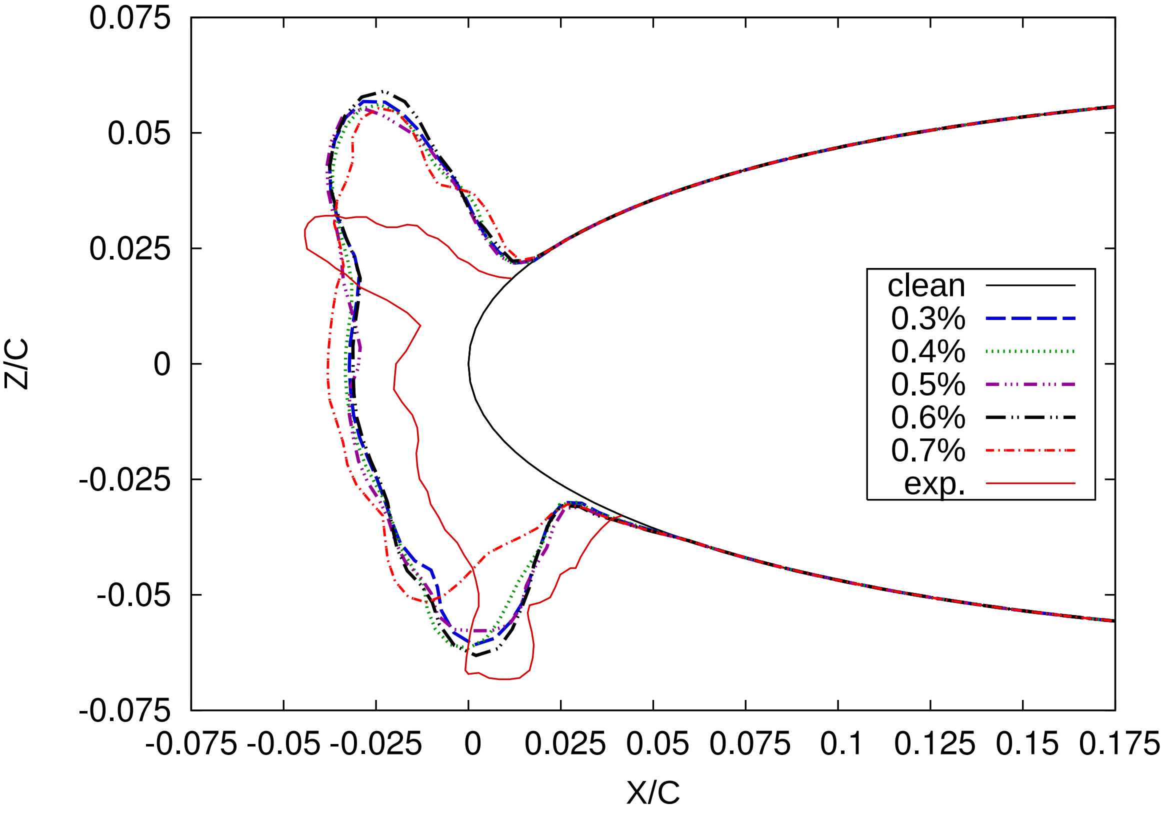

Figure 5.51: *Study of the convergence of the glaze ice shapes obtained on a NACA0012 wing with a step-by-step calculation based on the ice height criterion. Exposure time: 20 min.* $T_\infty = -7^o C$.

Simulated results are plotted in Figures 5.51 and 5.52. Some sort of convergence is achieved for the maximum ice height allowed per step $b_{max} = 0.6\%$c ($\simeq$ 5.5mm). For this case, 10 flow calculations have been necessary. The ice estimation is far from being perfect for an ice height criterion greater than $b_{max} = 0.6\%$c as the convergence is not achieved yet. This outlines one more time the requirement for a correct number of steps to insure some accuracy in the results.

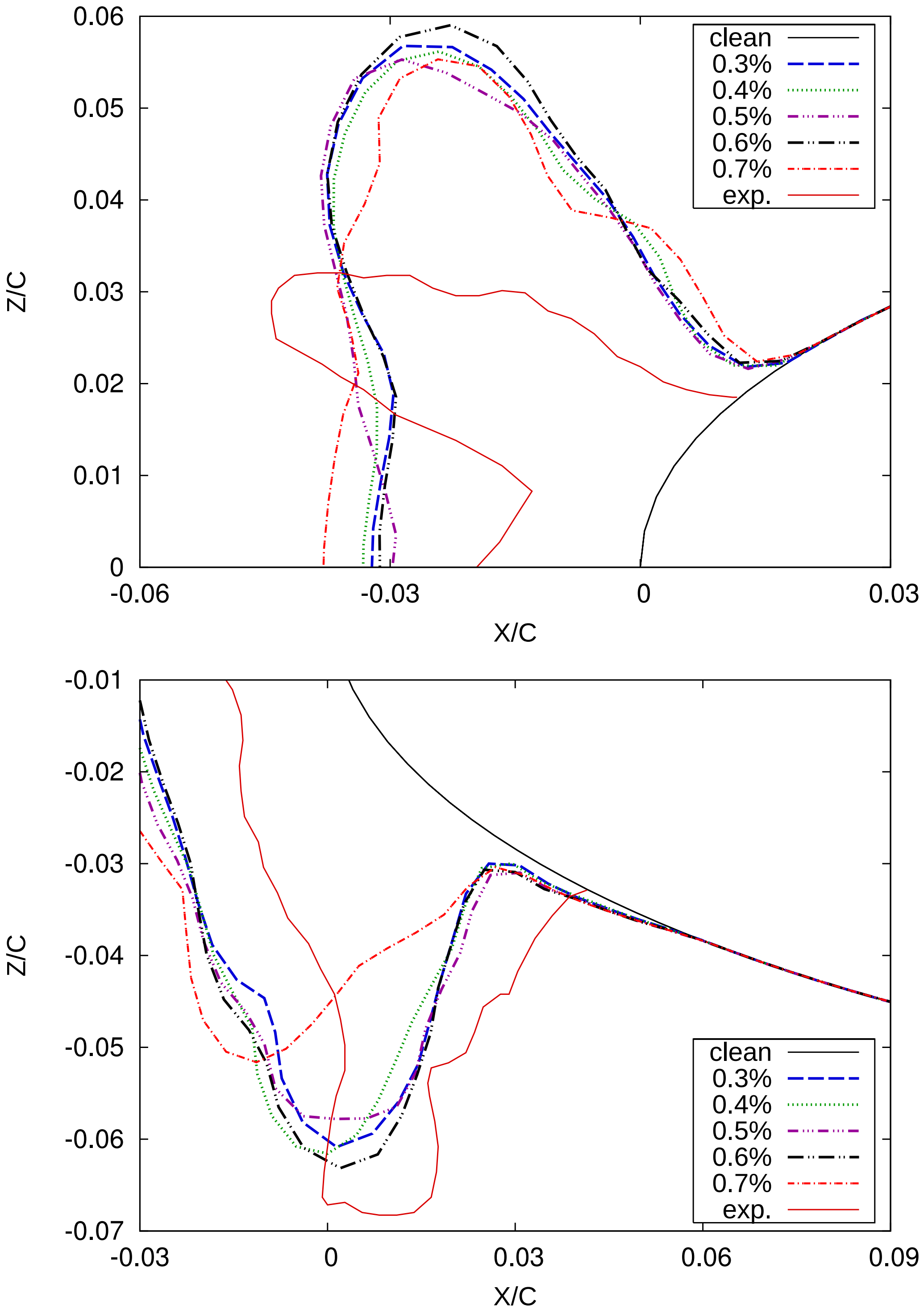

Figure 5.52: *Closer view of the glaze ice shapes obtained on a NACA0012 wing with a step-by-step calculation based on the ice height criterion. Convergence study. Exposure time: 20min.* $T_\infty = -7^oC$.

The converged ice shape obtained for $b_{max} = 0.6\%$c will now be compared to the time-based result.

Comparison with the time-based result:

The converged ice shape for the ice-based criterion may be compared with the time based result. While the convergence is obtained in 10 steps with $b_{max} = 5.48$mm equivalent to $b_{max} \simeq 0.6\%$c in the ice-based case, two more steps were necessary for the time-based algorithm. In the latter case, the average ice growth value per step was $b = 0.46\%$c. The ice shapes obtained with both algorithms may be seen in Figure 5.53 and a closer view of the wing top and bottom regions is shown in Figure 5.54.

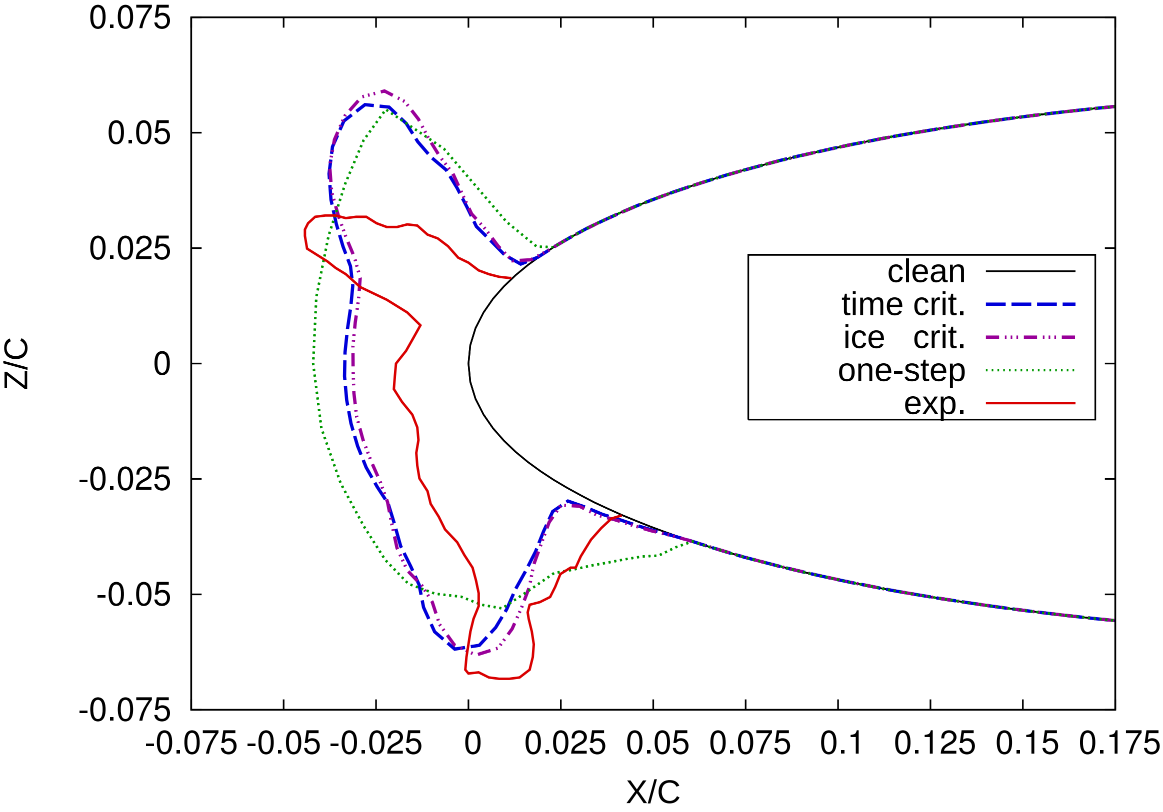

Figure 5.53: *Criteria comparison. Ice shapes obtained on a NACA0012 in glaze ice conditions.* $T_\infty = -7^oC$. *Exposure time: 20 min.*

Simulated ice shapes are relatively close to each other, this shows some kind of consistency in the results and in the reliability of the algorithms developed in this thesis. A bit more ice is nevertheless estimated for the upper and lower horn regions

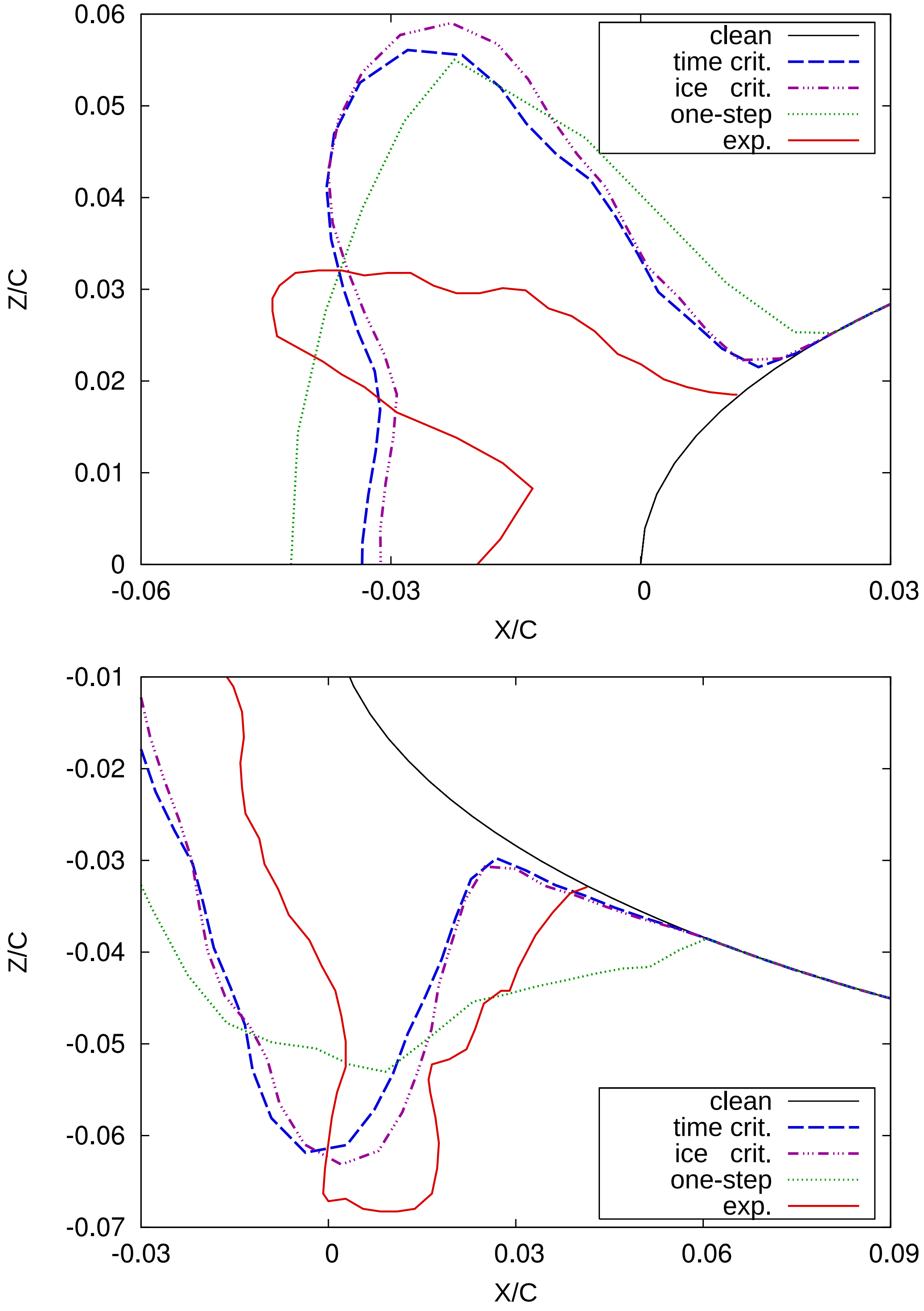

Figure 5.54: *Criteria comparison. Ice shapes obtained on a NACA0012 in glaze ice conditions.* $T_\infty = -7^oC$*. Exposure time: 20 min.*

with the ice height criterion; this ice shape is closer to experiments in the lower region and farther in the upper region. Less ice is predicted in the stagnation region when using this criterion, which is again closer to experiments.

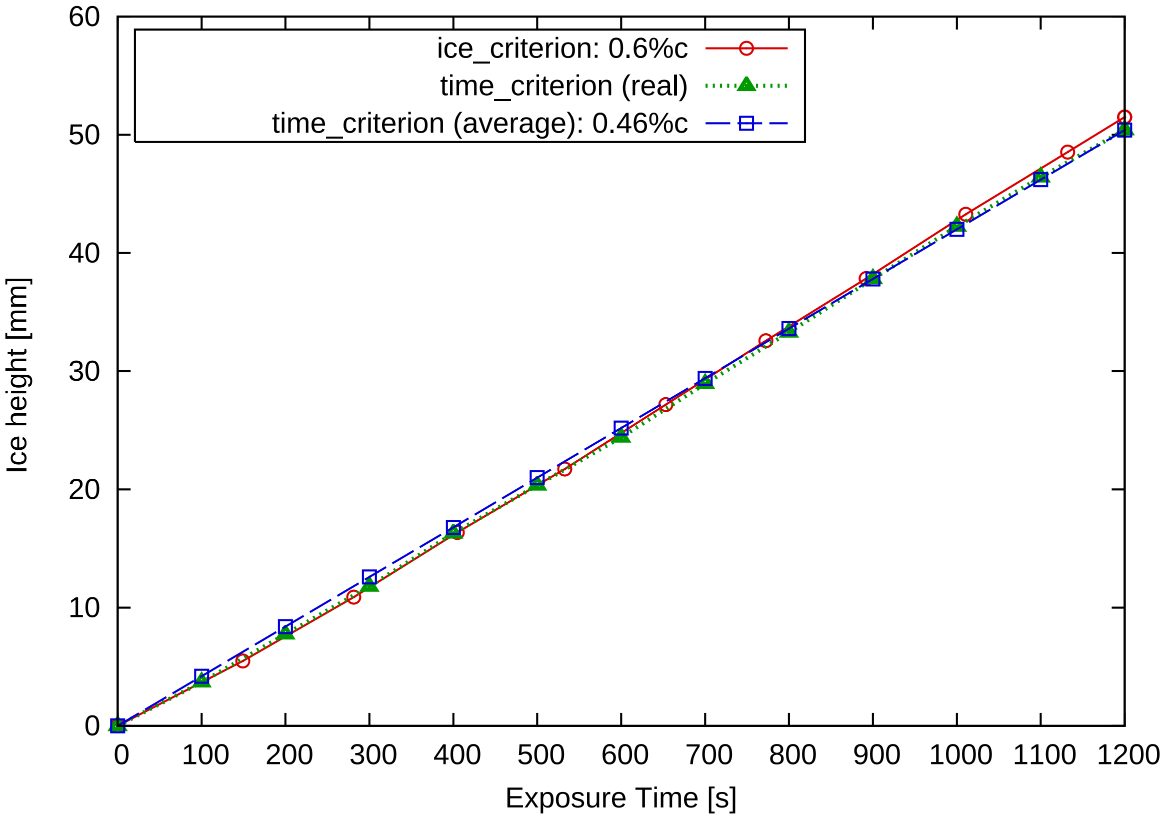

Figure 5.55: *Comparison of the ice height obtained in each step for both criteria. Exposure time: 20 min.* $T_\infty \simeq -7^oC$.

All the characteristics of the experimentally measured ice shape may be retrieved with the multi-stepping calculations, however, in a slightly different proportion. The overall ice height is better estimated with the ice-based criterion and the whole computation time is reduced with 10 flow solutions required against 12 for the standard multi-step algorithm. This agrees with the conclusions drawn from the ice study on the cylinder for a standard size of droplets in glaze ice conditions: the ice-based algorithm was faster and the number of flow solutions was reduced by two for the ice criterion.

To study more thoroughly the differences between the two multi-step results, the evolution of the ice growth has been plotted for both algorithms, see Figure 5.55. The third evolution shown in this picture describes the average ice height per step, equal to the total ice height obtained in the time-based simulation divided by the number of steps. When comparing both evolutions, the accreted ice appears almost identical after an exposure time of 15min (900s). The ice height increases slightly more afterwards for the ice-based algorithm.

In terms of accreted ice, it appears clearly that both algorithms are rather equivalent, but the ice-based algorithm is the fastest procedure with a gain of time around 17%. An ice height criterion of 0.6% of the chord length should be recommended for the ice prediction on a wing, in glaze ice conditions.

The ice triggering method being the most efficient of both algorithms, the results obtained with this model will now be compared with standard icing code results. As previously stated, since codes evolve constantly and are always being improved, the shapes obtained with Messinger-based icing codes may be different if they were simulated again today. However, for lack of more recent data, the results of the NATO/RTO exercise held in December 2000 [120] will be used as references.

Comparison with standard icing codes:

The ice shape calculated with the ice criterion implemented in ICECREMO2 is compared with the results obtained with the three standard Messinger icing codes: LEWICE, TRAJICE2 and ONERA2000, see Figure 6.34. The sort of expected ice shape under these conditions is rather difficult to reproduce numerically and none of the ice prediction codes could obtain a result that perfectly matches experiments.

- The upper horn region is better estimated by TRAJICE: the simulated ice shape has the right direction, but not the right shape, as may be seen more precisely in Figure 6.35. As for all codes, TRAJICE over-estimates the ice thickness in this region. The better estimated ice thickness seems to be obtained by LEWICE but the horn shows a wrong direction. The predicted ice shape obtained with the step-by-step algorithm in ICECREMO2 is also larger than experiments and points out in a wrong direction.
- The ice shape in the stagnation region is over-estimated by ICECREMO and the ONERA code, and under-estimated by LEWICE. This region is best estimated by TRAJICE.
- The lower horn region is largely under-estimated by all Messinger-based codes, while the best match is obtained with ICECREMO.

When looking at the overall ice shape, two code results are closer to experiments: the one generated by TRAJICE and the one from ICECREMO. The upper horn and stagnation region are best with TRAJICE, while the lower horn is better estimated with ICECREMO.

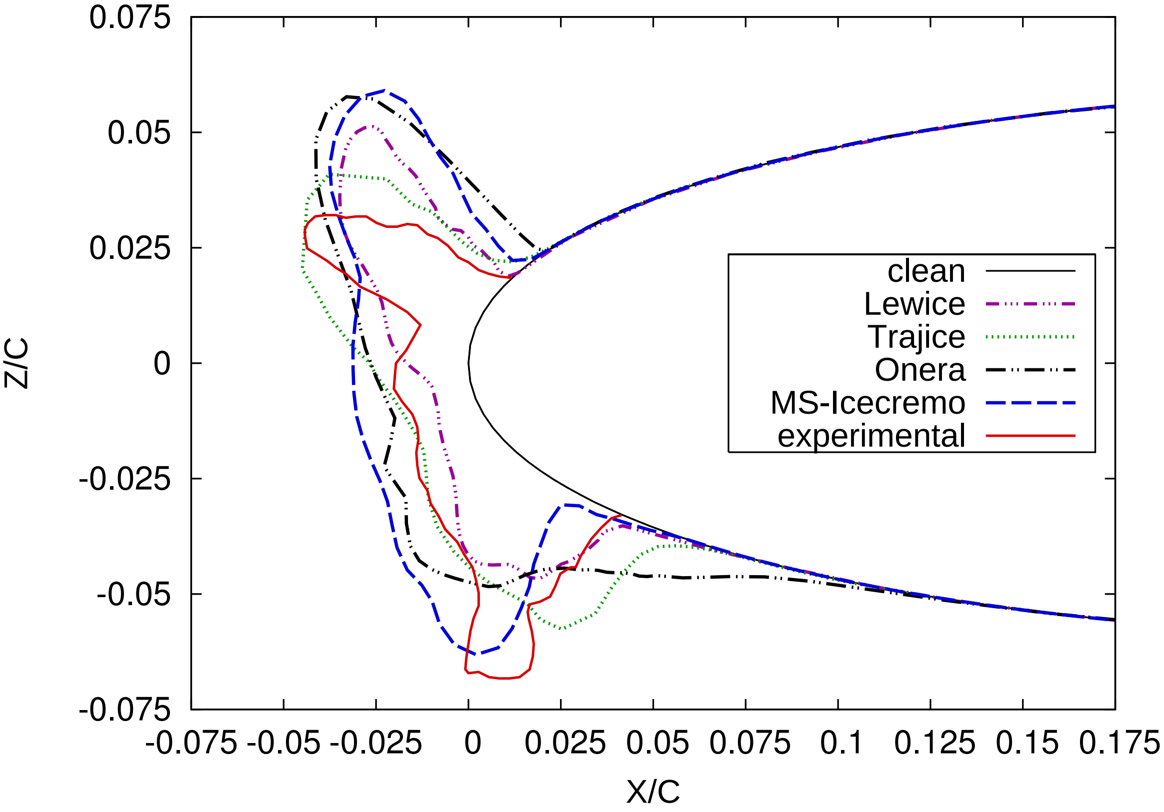

Figure 5.56: *Comparison of the multi-step result with standard ice predictions codes results [120] on the NACA0012 wing in glaze ice conditions at* $T_\infty = -7^oC$. *Exposure time: 20 min.*

To conclude, results generated on the airfoil using a step-by-step algorithm based on the ice criterion are very encouraging. The predicted ice shapes obtained with this procedure compare well with standard Messinger-based results and compare well with experiments. The main difference between simulated and measured ice heights is noticed in the stagnation region. As already mentioned, a release of droplets too close from the airfoil may explain this phenomenon, the collection efficiency being most probably too high. However, no experimental data were available to check this parameter. Despite being most probably improvable, the predicted ice shape presented here and obtained with $b_{max} = 0.6\%$c in a 10-step algorithm is the best so far.

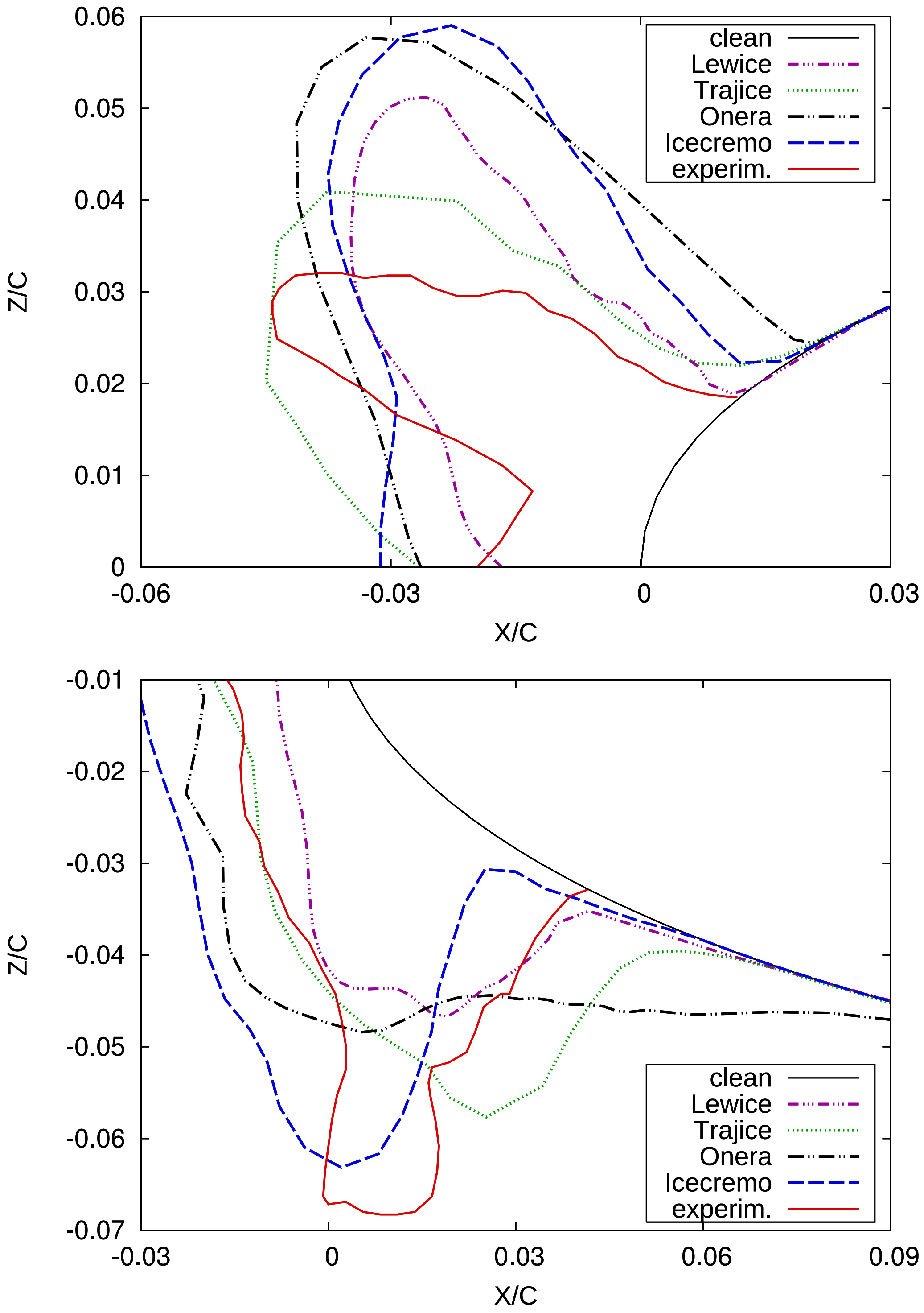

Figure 5.57: *Comparison of the multi-step result with standard ice predictions codes results [120] on the NACA0012 wing in glaze ice conditions at* $T_\infty = -7^oC$. *Exposure time: 20 min.*

5.4.4 Summary

The ice accretion on a NACA0012 wing geometry has been studied in this section. The time and ice based algorithms have been investigated and convergence has been established for each case. Results are listed in Table 5.7. The ice height allowed per step and the corresponding number of steps are written for the ice-height criterion, while the number of steps and the average ice height generated per step are determined for the time-based criterion. Ice heights are written as a percentage of the chord length equal to $c = 0.534$m in rime ice conditions and $c = 0.914$m in glaze ice conditions. Concluding remarks may be written for the study performed on the wing:

$\mathbf{T_\infty}$ [^{o}C]	**drop size** [μm]	**time crit**			**ice height crit**			$\mathbf{t_{exp}}$ [s]
		$\mathbf{t_{step}}$ [s]	$\mathbf{n_{step}}$	**%c**	$\mathbf{b_{max}}$ [mm]	**%c**	$\mathbf{n_{step}}$	
−26	20	51.4	7	0.8	4.24	0.8	5	360
−7	25	100	12	0.46	5.48	0.6	10	1200

Table 5.7: *Summary of the criteria study on a wing under rime and glaze ice conditions.*

- Rime ice conditions:
  In rime ice conditions, the final estimated ice shapes were found almost identical for both the time and the ice-based algorithms and the results based on the ice criterion appeared very slightly closer to experiments. In this case, five flow calculations were necessary to reach convergence against seven for the time triggering algorithm. The procedure based on the ice criterion $b_{max} = 0.8\%$c is therefore the fastest of both methods with a gain of time around 28% and should be recommended for future studies on a NACA0012 wing geometry in rime ice conditions.

- Glaze ice conditions:
  For the conditions investigated, it has been found that the update of the water film had a noticeable influence on the final ice shape. Simulated ice shapes obtained with both algorithms had about the same profile, the ice triggering criterion producing an ice shape slightly closer to experiments. As for rime ice conditions, the main difference is the number of flow solutions, twelve for the time-based algorithm, down to ten for the ice height based method which

corresponds to a gain of time around 17%. The ice criterion is therefore also recommended in a multi-step algorithm in glaze ice conditions.

Results obtained with the ice triggering procedure have also been compared to those generated by standard Messinger-based icing codes. The ICECREMO2 code used with the step-by-step algorithm developed in this thesis appeared as one of the best ice estimator. The ice criterion is therefore recommended for future work.

5.5 Conclusion

Ice predictions based on a fully automated multi-stepping approach have been widely studied in this chapter.

- A step-by-step algorithm largely enhances the quality of the predicted ice shapes. However, a correct number of steps is required to insure its accuracy.
- The water height update between the different steps of the procedure has an influence on final ice shapes, particularly for temperatures close to freezing. However, this influence remains relatively small.
- In all the test cases investigated in this chapter, no significant shape differences could be noticed between the time-based criterion results and the ice-based criterion results. However, the simulation was time saving when based on the ice criterion since the number of flow solutions required to get convergence was reduced by two or three compared to the standard multi-step procedure based on time. Due to a more physically realistic approach of the ice layer evolution and significant time saving, the ice-height criterion has been established as the best ice estimator for a step-by-step simulation. Table 5.8 presents the conclusion drawn from the ice study on the cylinder and on the wing. The last two columns represent the values of ice criterion and the number of steps determined by the code to reach convergence. These values of ice criterion are recommended for future work on this kind of geometries.
- The ice shapes obtained with the ice-height criterion have been compared to those generated with standard Messinger-based icing codes. In most of the cases, the results obtained with the multi-step algorithm have shown a better agreement with experiments.

The step-by-step algorithms have been studied in this chapter, they largely enhance the accuracy of the results compared to the standard one-step calculation. Another multi-stepping procedure, called predictor-corrector, is used in several 2D

	ice type	**T_∞ [°C]**	**V_∞ [m/s]**	**d_d [μm]**	**t_{exp} [s]**	**c [mm]**	**%c**	**n_{step}**
cylinder	rime	-26	77.2	18	330	63.5	4	3
	glaze	-3	77.2	18	330	63.5	4	4
	glaze	-3	77.2	100	330	63.5	4	4
airfoil	rime	-26	67	20	360	534	0.8	5
	glaze	-7	67	25	1200	914	0.6	10

Table 5.8: *Ice-height criterion for the ice accretion study on cylinder and wing type geometries under typical icing conditions.*

icing codes [25, 75, 100]. To date, this approach has only been tested in Messinger-based models. The aim of the next chapter will be to study the predictor-corrector algorithm in the Stefan-based ice prediction code ICECREMO2.

Chapter 6

Predictor-Corrector Approach

6.1 Introduction

Multi-stepping may be a lengthy procedure. Repeated grid generations and flow calculations are extremely time consuming. Being able to limit the number of flow computations in long procedures and still get some sort of time dependence for the flow parameters would be a great advantage. When using the step-by-step approach, the flow parameters are only updated periodically, when in real life, their variation is continuous. The objective of this section is to study an alternative to the step-by-step approach where the flow parameters evolve continuously with time. This is known as predictor-corrector. This procedure is inspired from the predictor-corrector numerical method, see [126] and [127] for instance. It aims to reproduce the variations of the quantities involved in aircraft icing [25, 35, 75, 100].

Two icing calculations are performed during a predictor corrector icing algorithm, the first icing calculation, called predictor, uses constant flow parameters estimated on the clean airfoil. The flow parameters are then re-evaluated on the wing covered with this first ice shape and the second icing calculation uses an interpolation of the values on the clean airfoil and the values at the end of the predictor. There are only two conditions on interpolation functions: the values of the flow parameters at the start of the calculation should be the predictor values, the values at the end of the calculation should be the corrector values. Any function verifying these two conditions could be used. As in the previous chapter, the interpolations could be either based on time, ice height or both. For the sake of simplicity, a time based linear interpolation is adopted for the simulations carried out in this chapter: for any flow parameter, the interpolated value A_i between the predictor value A_p and the corrector value A_c may be written:

$$A_i = A_p \left(1 - \frac{t}{t_{exp}}\right) + A_c \left(\frac{t}{t_{exp}}\right) \ , \tag{6.1.1}$$

where t denotes the current simulation time and t_{exp} is the total exposure time.

In the following, the predictor-corrector approach will be fully detailed and analysed. Simulations will be carried out in both rime ice and glaze ice conditions for a cylinder and a NACA0012 airfoil in Sections 6.2 and 6.3 respectively. The convergence of the algorithm is studied and when possible the results are compared with experimental measurements.

6.2 Ice Predictions on Cylinders

The predictor-corrector algorithm is applied to the cylinder geometry using the conditions specified in Table 5.1 of Chapter 5. As in the previous chapter, icing is studied in rime conditions in Section 6.2.1 for the temperature $T_\infty = -26^oC$ and in glaze ice conditions in Section 6.2.2 for $T_\infty = -3^oC$. In all cases, the cylinder is subject to ice accretion for an exposure time of $t_{exp} = 5$min 30s.

A standard predictor-corrector will be performed first. An interpolation must be performed for several parameters: the collection efficiency, the shear stress and the heat transfer coefficient, at each time step Δt of the simulation, which means this procedure may be repeated several hundred times for each minute of the simulation. The process may become time consuming, particularly when a fine grid is used and there are a great number of nodes. For the various cases investigated in this chapter, the value of the time step is $\Delta t \simeq 0.1$s.

The convergence of the algorithm is here again the key element and this aspect will be given full attention. The number of successive predictor-corrector calculations necessary to achieve a converged solution is investigated.

6.2.1 Rime Ice Conditions

Standard Procedure

Figure 6.1 depicts the two ice shapes produced at each stage of the predictor-corrector algorithm: the predicted shape, equivalent to the one-step calculation and the corrected shape. In the vicinity of the stagnation line, the two ice layers are nearly the same, with the corrected shape very slightly thicker than the predicted one. Away from $z = 0$, the corrected ice shape becomes thinner than the predicted ice layer. This is consistent with the evolution of the collection efficiency shown on Figure 6.2 and detailed in the previous chapters.

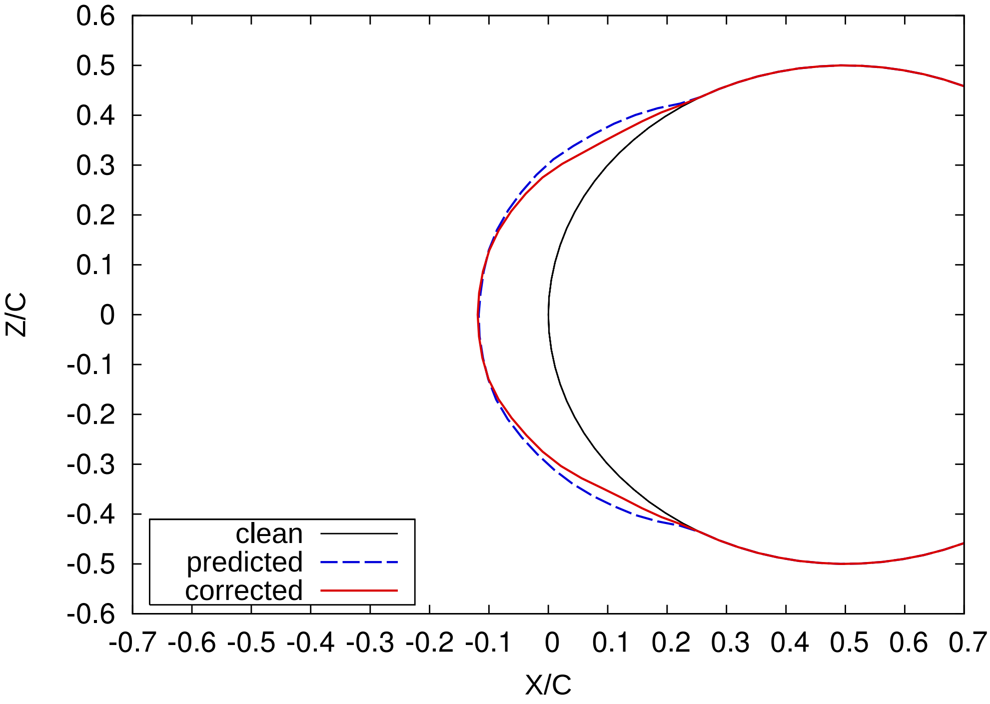

Figure 6.1: *Study of the predictor-corrector algorithm applied to a cylinder in rime ice conditions. Exposure time: 5min 30s.*

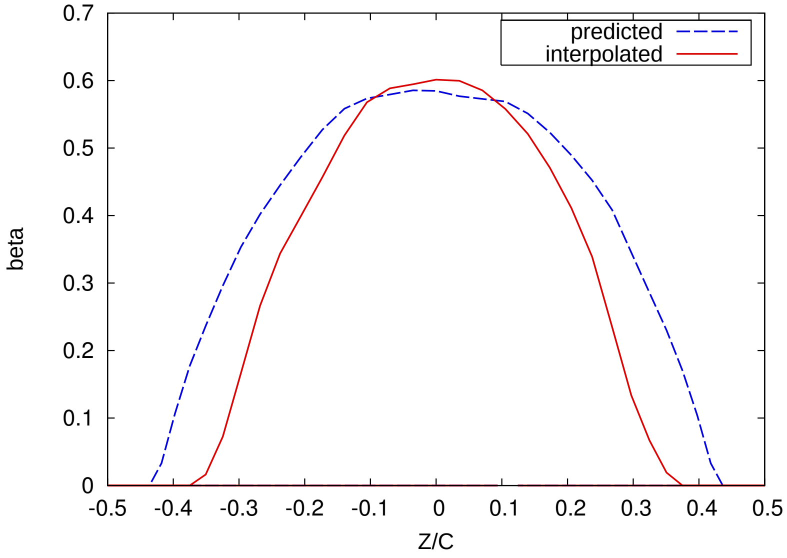

Figure 6.2: *Collection efficiency. Predictor-corrector algorithm applied to a cylinder in rime ice conditions. Exposure time: 330s*

However, there is no guarantee that the algorithm has converged and this will now be detailed.

Convergence Study

The purpose of this study is to determine the number of times the predictor-corrector algorithm should be applied to obtain an ice shape that remains unchanged with an additional iteration of the algorithm. The procedure may be summarised as:

1. Single-step procedure to determine the predictor.
   => predictor values, => predicted ice shape
2. New flow and flow-related parameters determined for the ice covered geometry.
   => corrector values 1
3. New ice calculation using the interpolated values between the predictor and the corrector 1.
   => interpolated values 1, => corrected ice shape 1
4. New flow and icing parameters determined for the new interpolated iced geometry.
   => corrector values 2
5. New ice calculation using the interpolated values between the predictor and the corrector 2.
   => interpolated values 2, => corrected ice shape 2
6. Repeat stages 4. and 5. as many times as necessary.

Note that the predictor values determined on the clean surface remain identical thoughout the calculation while the corrector values are updated each time a new flow solution is obtained.

The convergence is studied for the cylinder test-case presented in this section. The corresponding results are plotted in Figures 6.3 and 6.4. As may be seen, the convergence is achieved very quickly, for the first corrected ice shape corresponding to the results from the standard predictor-corrector algorithm. Only this first corrected result produces significant changes. There are minor corrections operated afterwards on the cylinder upper and lower regions, which do not modify the overall ice shape significantly. To understand more thoroughly the evolution of the simulated ice accretion on the cylinder, the final ice heights calculated on the clean geometry are plotted on the unfolded surface, starting from the one-step result up to the second corrected ice height, see Figure 6.5. The differences between the corrected curve 1

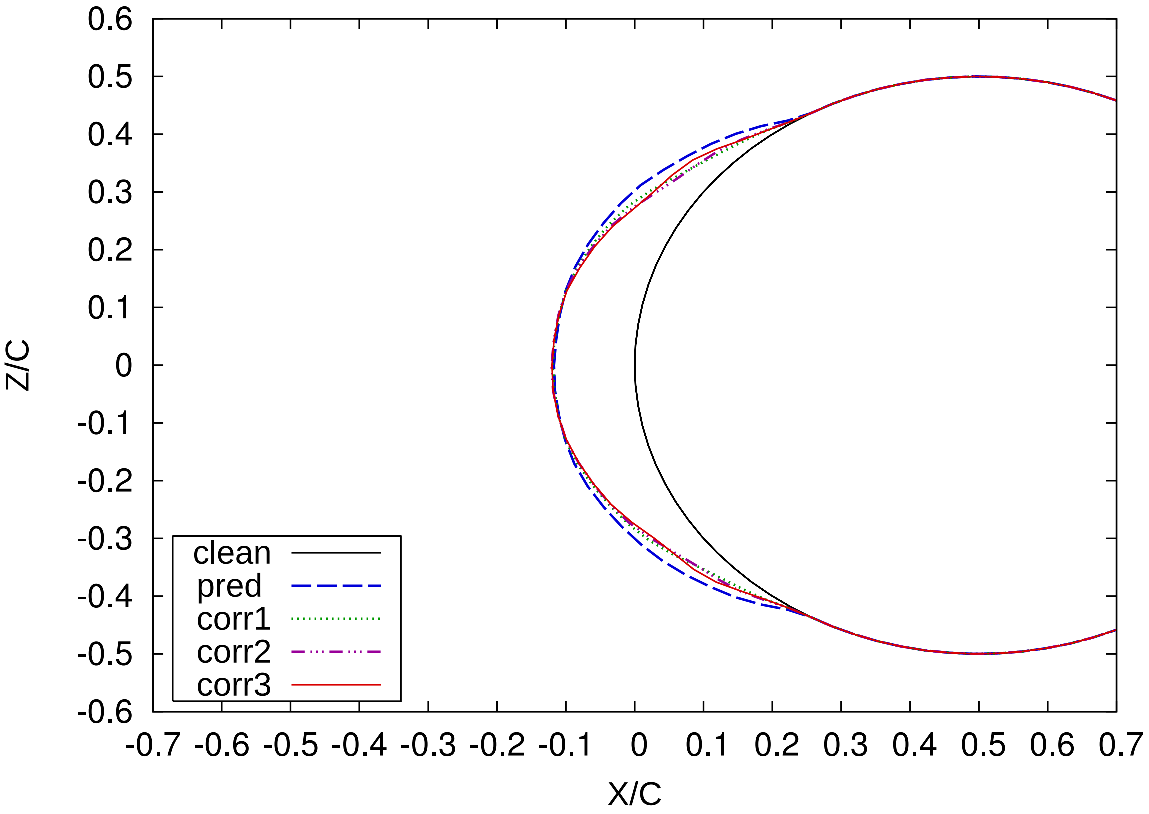

Figure 6.3: *Study of the convergence for the predictor-corrector algorithm applied to a cylinder in rime ice conditions. Exposure time: 5min 30s.*

corresponding to the first corrector and the corrected curve 2 corresponding to the updated values of the corrector, are more apparent in this picture. These differences are unavoidable when dealing with this kind of numerical interpolation for a set of complex parameters. However, these discrepancies are relatively minor, the largest difference being observed between the ice heights estimated in the first two steps.

In the present case, the standard predictor-corrector procedure is sufficient to obtain an acceptable ice prediction. This result will be used for comparison with the simulated ice shape obtained with the step-by-step approach studied in the previous chapter.

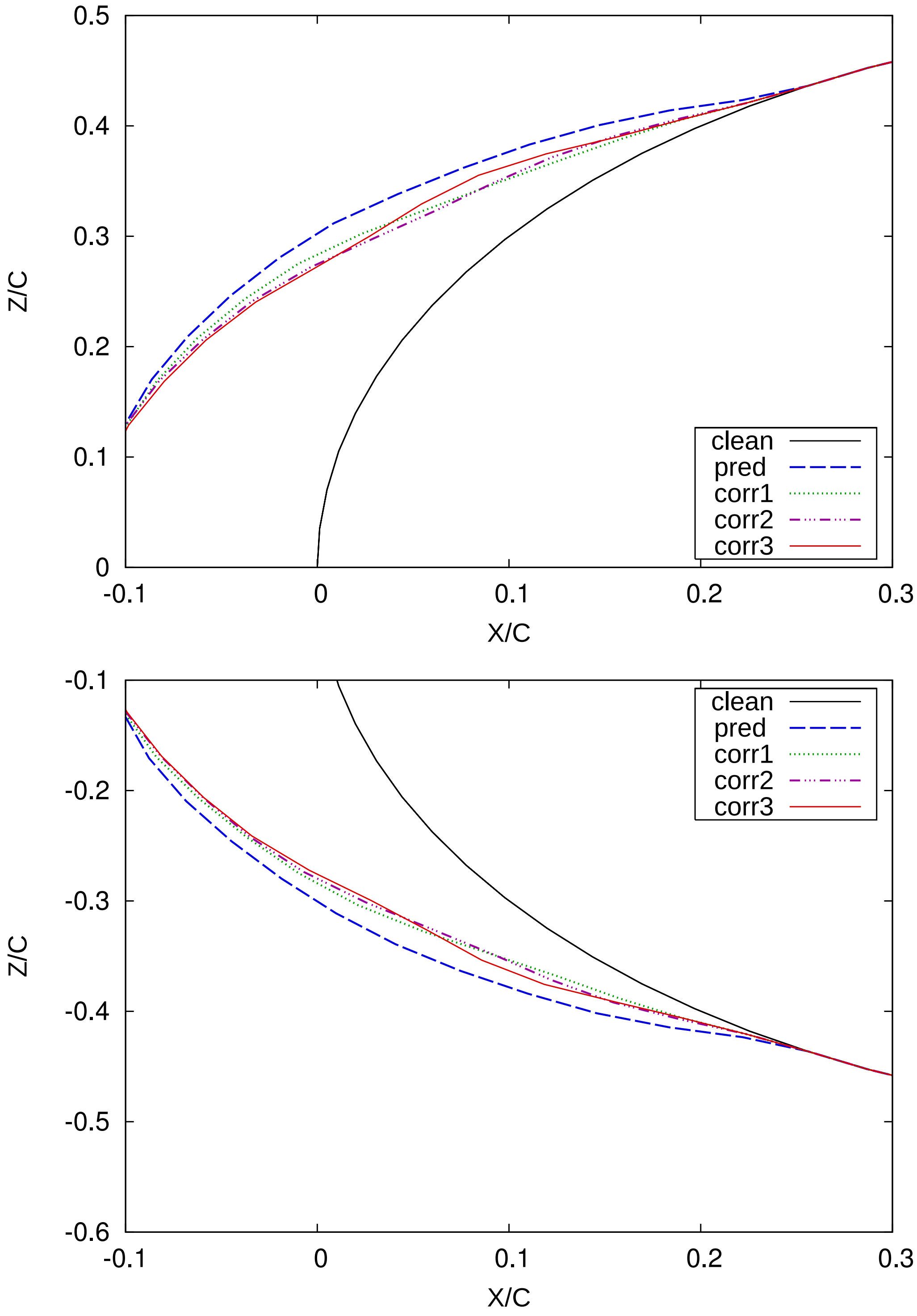

Figure 6.4: *Study of the convergence for the predictor-corrector algorithm applied to a cylinder in rime ice conditions. Exposure time: 5min 30s.*

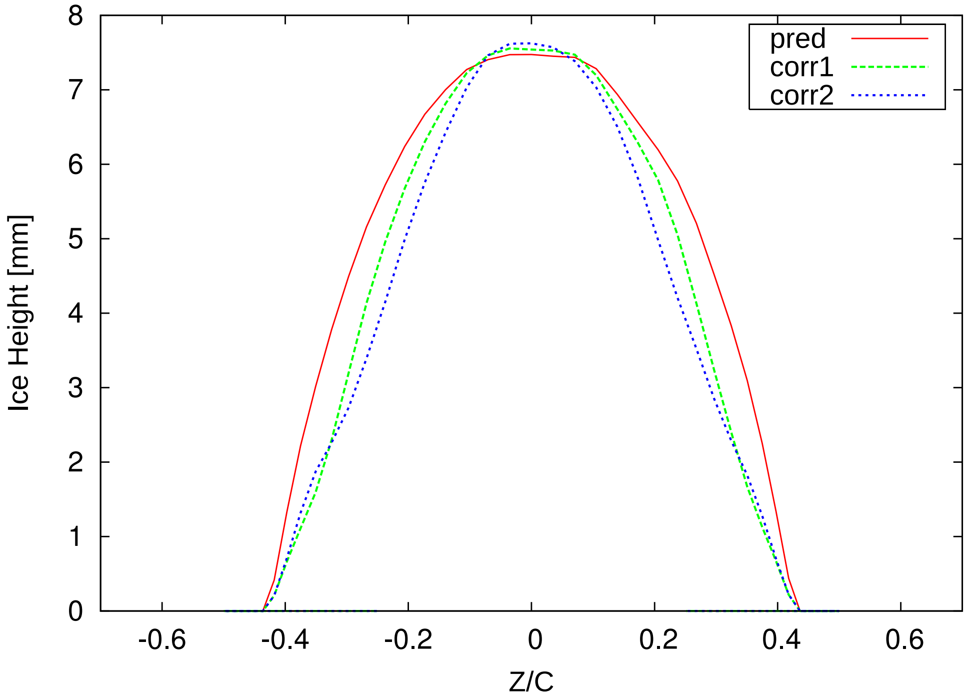

Figure 6.5: *Predictor-corrector. Comparison of ice heights on a cylinder in rime ice conditions.*

Comparison with the step-by-step result

The predicted ice shape obtained with the step-by-step algorithm studied in Section 5.3 of Chapter 5 was best estimated for the ice criterion $b_{max} = 0.3\%$c, with c the diameter length. The ice-based simulation required three flow solutions, while only two are necessary with the predictor-corrector algorithm. The corresponding simulated ice shapes may be seen in Figures 6.6 and 6.7. At this stage, the lack of experimental data does not allow to draw any conclusion concerning the final ice shape. However, in both cases, the simulated ice growth is almost identical with either algorithm. This agrees with the statement from Mingione et al. [25] who did not find any appreciable differences between the predictor-corrector and the step-by-step results in rime ice conditions.

The standard predictor-corrector algorithm requires only two flow calculations against three required for the step-by-step procedure based on the ice criterion. The predictor-corrector algorithm should therefore be favoured for time-saving reasons since the time necessary for the update of the collection efficiency in the icing solver is likely to be less than the time required for a new re-meshing and a new flow calculation.

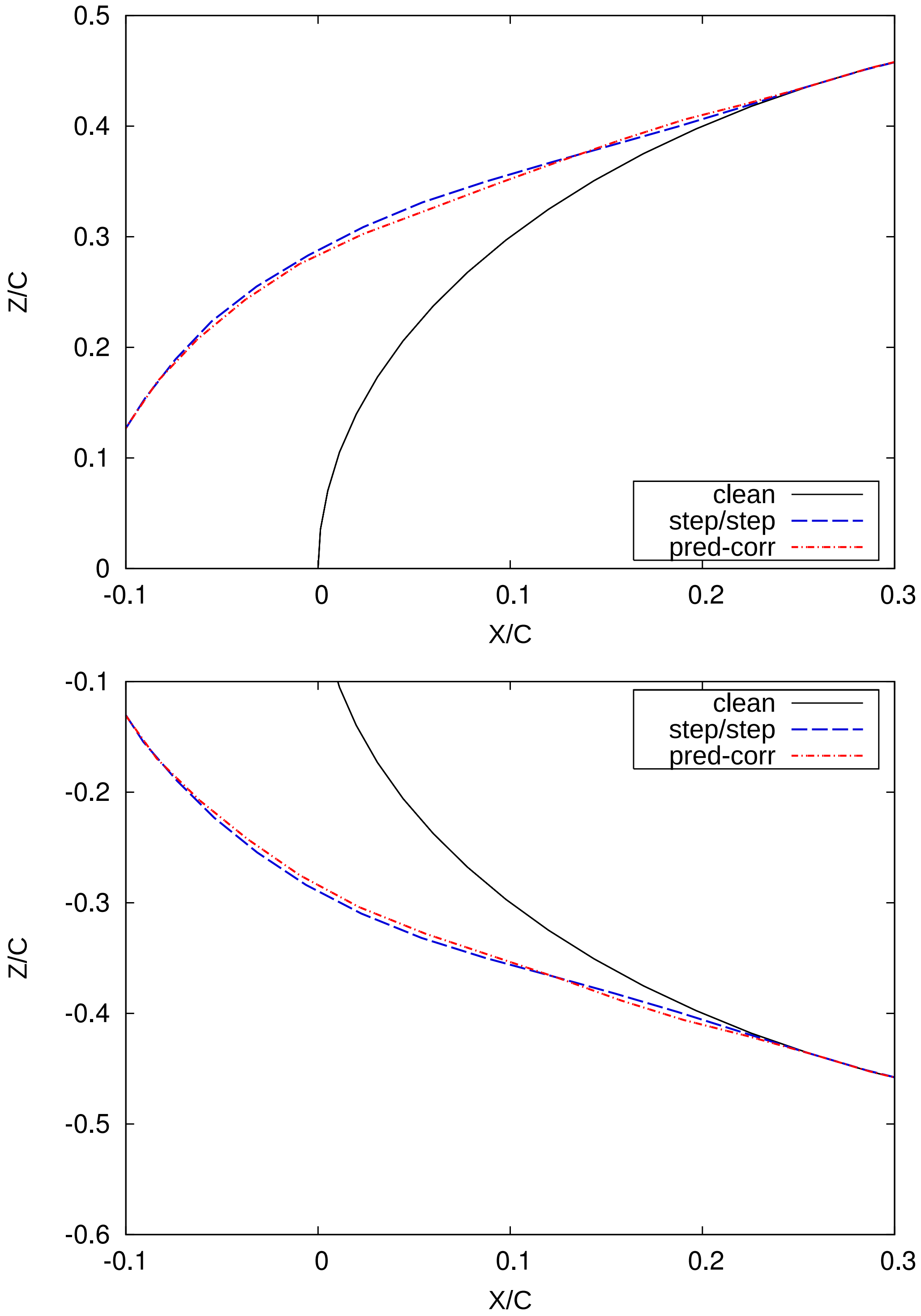

Figure 6.6: *Comparison step-by-step versus predictor-corrector for a cylinder in rime ice conditions. Exposure time: 5min 30s.*

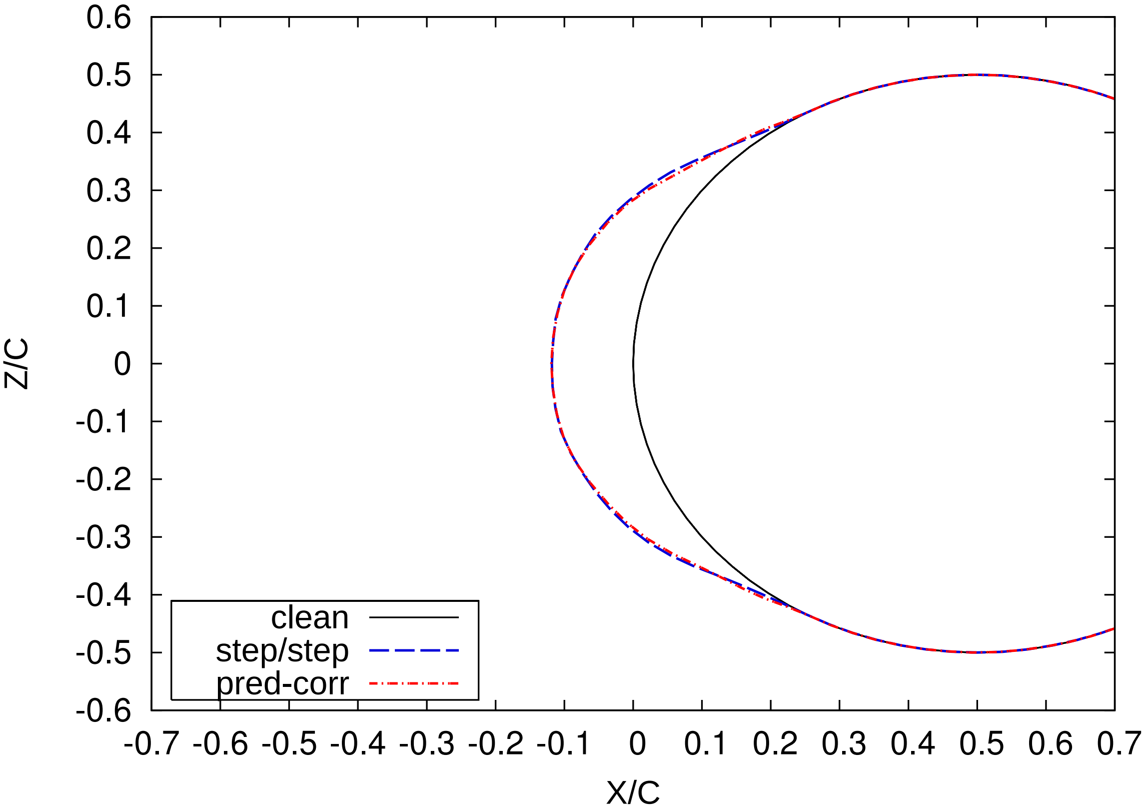

Figure 6.7: *Comparison step-by-step versus predictor-corrector for a cylinder in rime ice conditions. Exposure time: 5min 30s*

The same study may now be performed on the cylinder in glaze ice conditions with small and large impinging droplets.

6.2.2 Glaze Ice Conditions

The predictor-corrector algorithm is now studied on a cylinder in glaze ice conditions. As in the previous example, the standard predictor-corrector is first investigated, followed by the study of the convergence. Ice conditions remain those specified in Table 5.1 for the cylinders $O1$ and $O2$. The main difference between these two cases is the size of droplets. Since the final ice shape is quite different, they will be studied separately.

Impingement of Small Droplets

- **Standard procedure**

  The ice shapes obtained in the first step and at the end of the predictor-corrector calculation may be seen in Figure 6.8. The result from the standard predictor-corrector algorithm does not appear closer to experiments. The ice layer is under-estimated in all regions of the cylinder surface. For this case, the result generated in a single step agrees better to the experimentally measured ice shape. Nevertheless, the corrected ice shape is consistent with the previous conclusions drawn for a multi-step algorithm: the update of the flow solution and flow-related parameters globally reduce the ice layer.

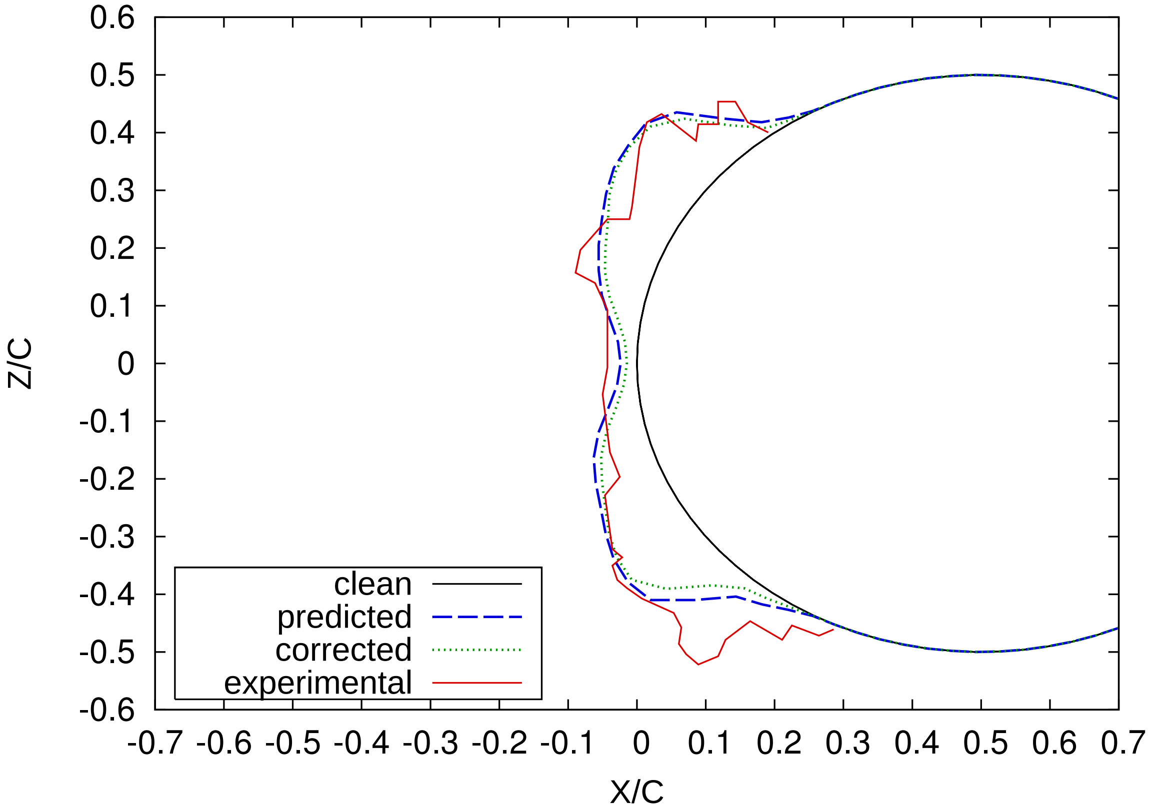

Figure 6.8: *Study of the predictor-corrector algorithm applied to a cylinder in glaze ice conditions. Small droplets. Exposure time: 5min 30s.*

- **Convergence study**

  Figure 6.9 shows the ice shapes obtained with the computation based on updated values of the corrector. Only the first three simulated results are shown in this figure since convergence is reached very quickly. As in the rime ice

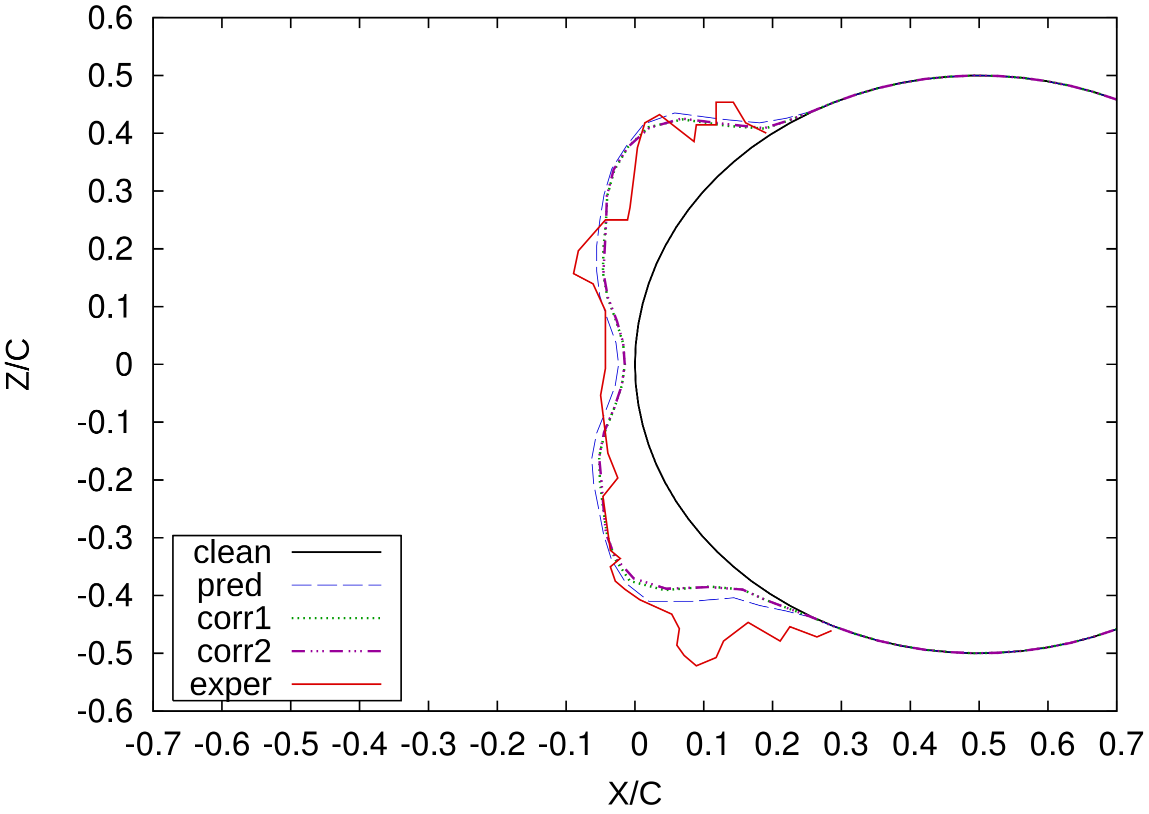

Figure 6.9: *Study of the convergence for the predictor-corrector algorithm applied to a cylinder in glaze ice conditions. Small droplets. Exposure time: 5min 30s.*

case, one correction is enough to reach convergence and there is no benefit in calculating several additional corrected ice shapes. Minor differences are nevertheless noticeable between the corrected results, which are once again unavoidable with complex parameters. Only one small difference may be noticeable on the top part of the lower horn, as may be seen more precisely in Figure 6.10 and on the unfolded surface shown in Figure 6.11. This slight discrepancy is however not significant. The corrected ice profiles are virtually identical. The two-step standard predictor-corrector approach may therefore be used for further studies and may be considered as the best ice estimator for this algorithm.

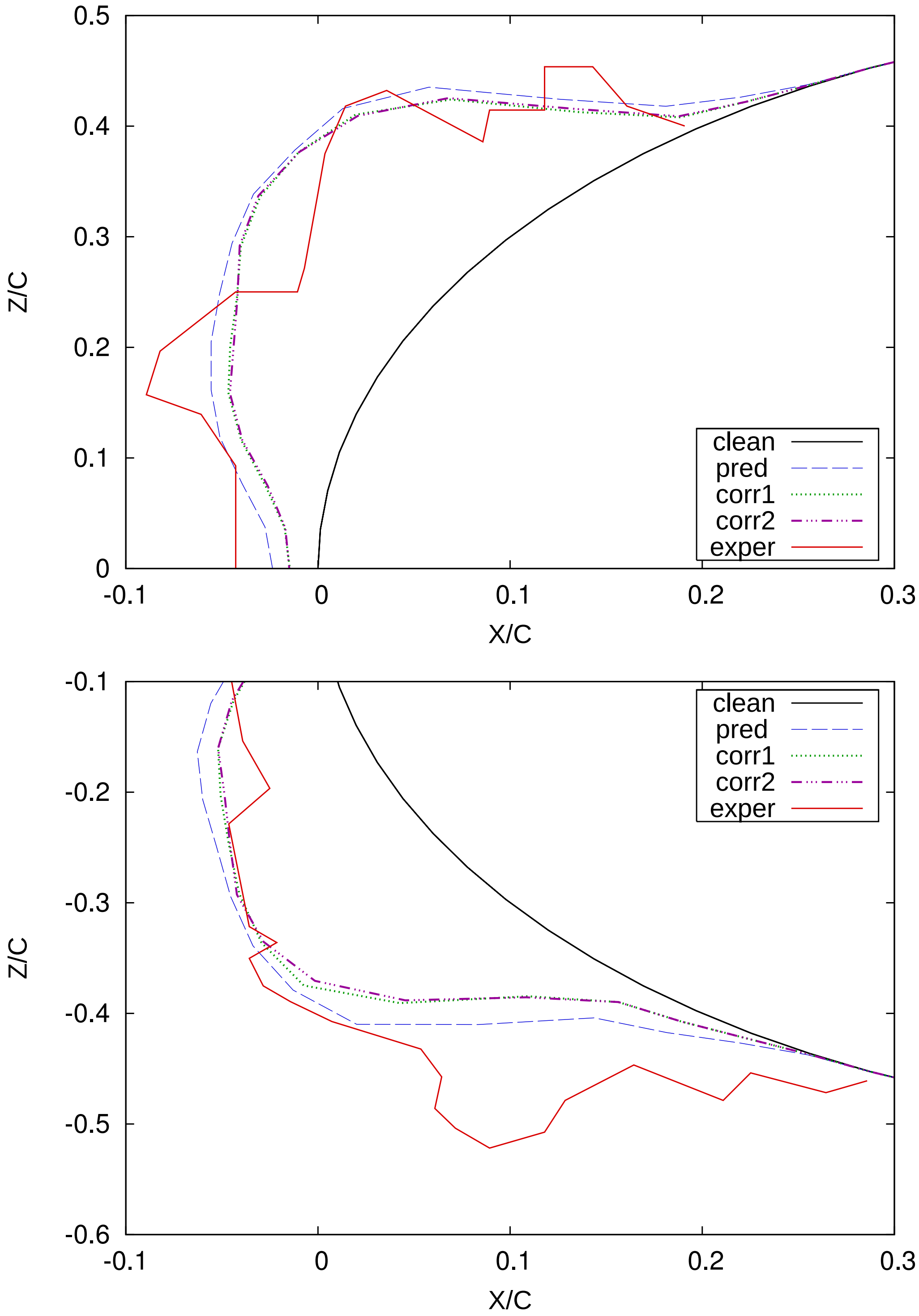

Figure 6.10: *Study of the convergence for the predictor-corrector algorithm applied to a cylinder in glaze ice conditions. Small droplets. Exposure time: 330s*

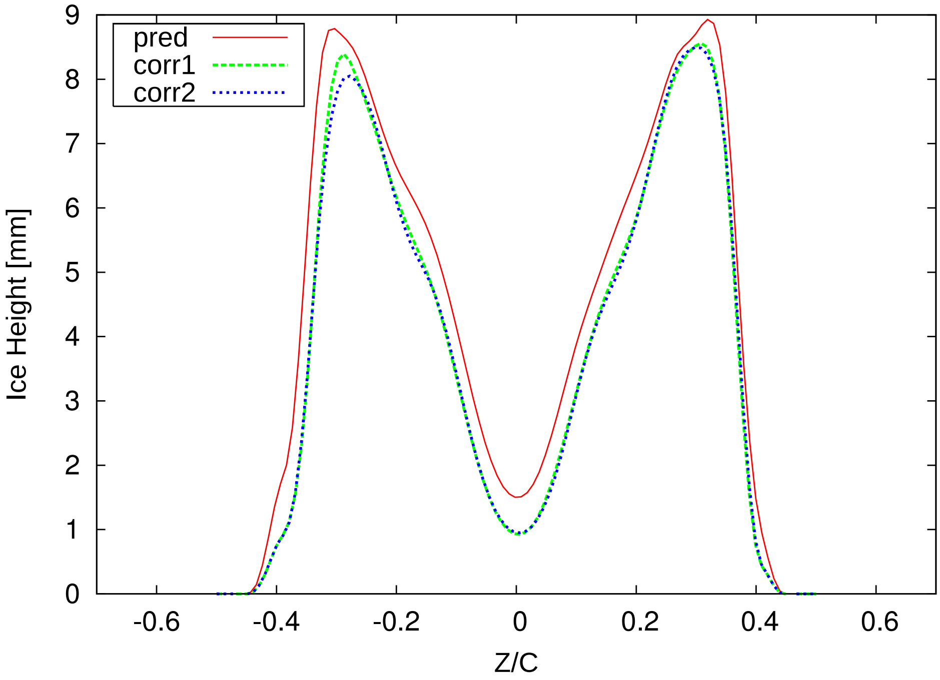

Figure 6.11: *Predictor-corrector. Comparison of ice heights.*

The differences between the predicted and the corrected ice shapes being rather important, the interpolation of the flow dependent parameters appears as a key-element in the process since it modifies the ice shape significantly. The evolution of these flow related parameters will now be discussed briefly.

Evolution of flow dependent parameters

The key icing parameters, i.e. the collection efficiency, shear stress and heat transfer coefficient values are plotted in Figures 6.12, 6.13 and 6.14 for each step of the algorithm, starting from the values of predictor determined on the clean geometry ($t_{exp} = 0s$) and those of corrector determined on the ice covered surface. The interpolated values evolve continuously as time increases. However, for the sake of clarity, two profiles only are represented on these pictures, the first one at ($t_{exp} = 110s$) and the second one at ($t_{exp} = 220s$). As expected the interpolated curves are comprised between the predictor and the corrector. This is in agreement with the interpolation function (6.1) written in Section 6.1 of this chapter. When the icing exposure time is reached $t_{exp} = 330s$, the interpolated value is therefore equal to the value of corrector. The noticeable minor discrepancies that appear on these pictures for $z/c > 0.45$ correspond to the downstream ice region where the flow starts reattach-

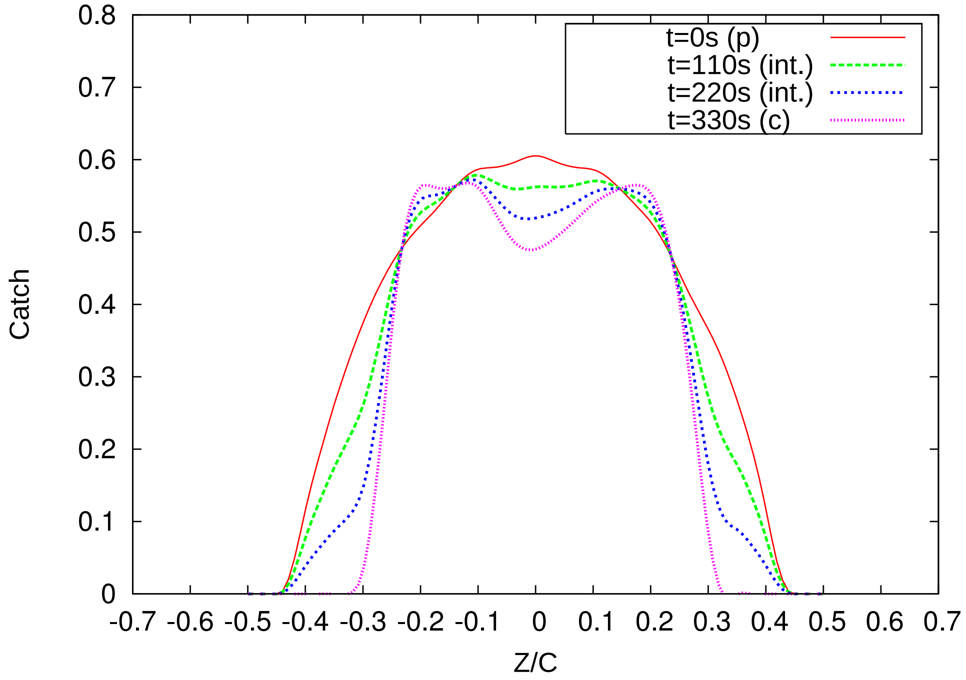

Figure 6.12: *Predictor-corrector. Evolution of the collection efficiency.*

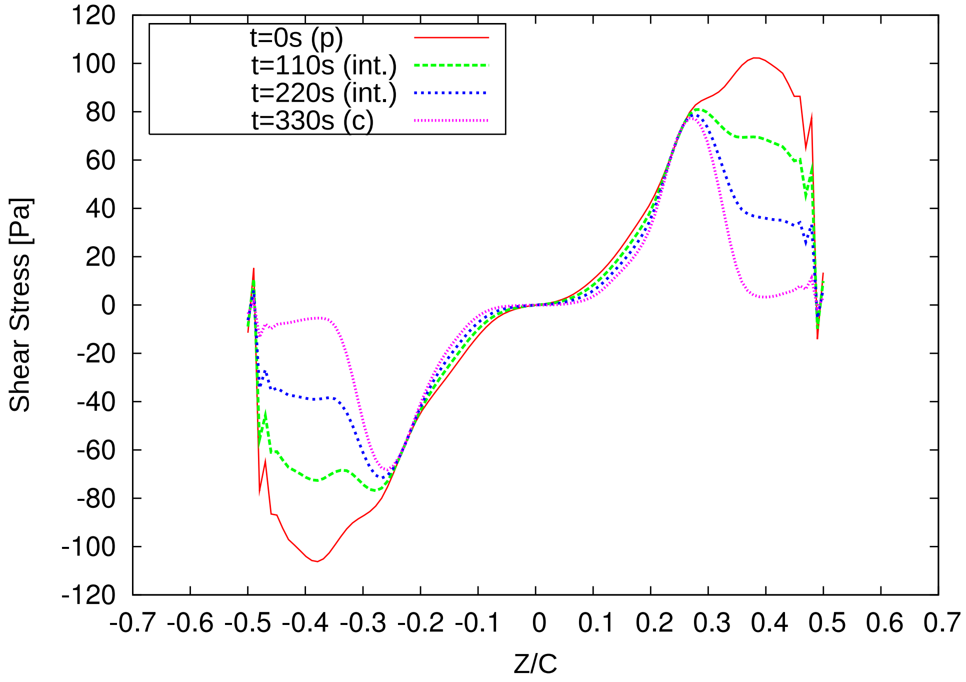

Figure 6.13: *Predictor-corrector. Evolution of the shear stress.*

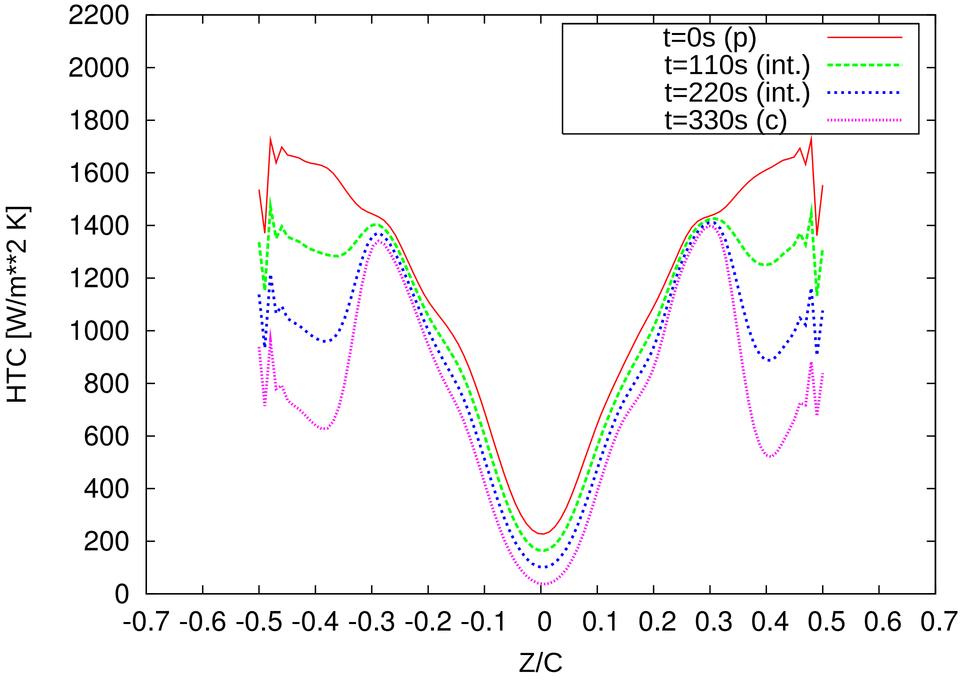

Figure 6.14: *Predictor-corrector. Evolution of the heat transfer coefficient.*

ing to the clean geometry. While the flow is highly perturbed in this region, these discrepancies are enhanced due to a spline-based scheme used for plotting.

Note that the curves represented from Figure 6.12 to 6.14 correspond to the ice height obtained with the corrector 1 of Figure 6.11. To study the convergence of the algorithm and generate the ice height corresponding to the corrector 2, the flow has to be recalculated around the new iced surface and new values of corrector, corrector2, have to be determined. The second time the icing model is run, again for the total icing exposure time, the new interpolated curves are generated using an interpolation between the same predictor values and the corrector2 values.

There are huge differences between the different values of predictor and those of corrector. This clearly demonstrates that a permanent update of the flow related parameters is required in a multi-step algorithm. All icing parameter values are higher when determined on the clean geometry than when calculated using the interpolation function. This explains the higher and larger ice layer obtained with the single step procedure.

The evolution of the flow related parameters is consistent with the results from the step-by-step on the cylinder: the heat transfer coefficient and the shear stress values were also higher when determined on the clean geometry.

This evolution of flow-related parameters is however very different from the results obtained with ICECREMO1: it was found in Chapter 4 that the icing parameters did not vary significantly from one step to the next. However, the multi-step procedure developed for ICECREMO1 was also very different as the water update was not performed and the thermal history was not preserved from one step to the next. In either cases, the multi-step results obtained with the initial code version were arguable but the multi-step algorithm now developed for ICECREMO2 is far more reliable and accurate.

The corrected ice shape obtained in this section will now be compared to simulation results from the standard ice accretion codes LEWICE, TRAJICE and ONERA.

Comparison with standard icing codes:

As in the previous chapter, the results of the predictor-corrector algorithm will now be compared with results obtained with standard Messinger-based icing codes. Figure 6.15 shows the corresponding ice shapes. Although under-estimated in most

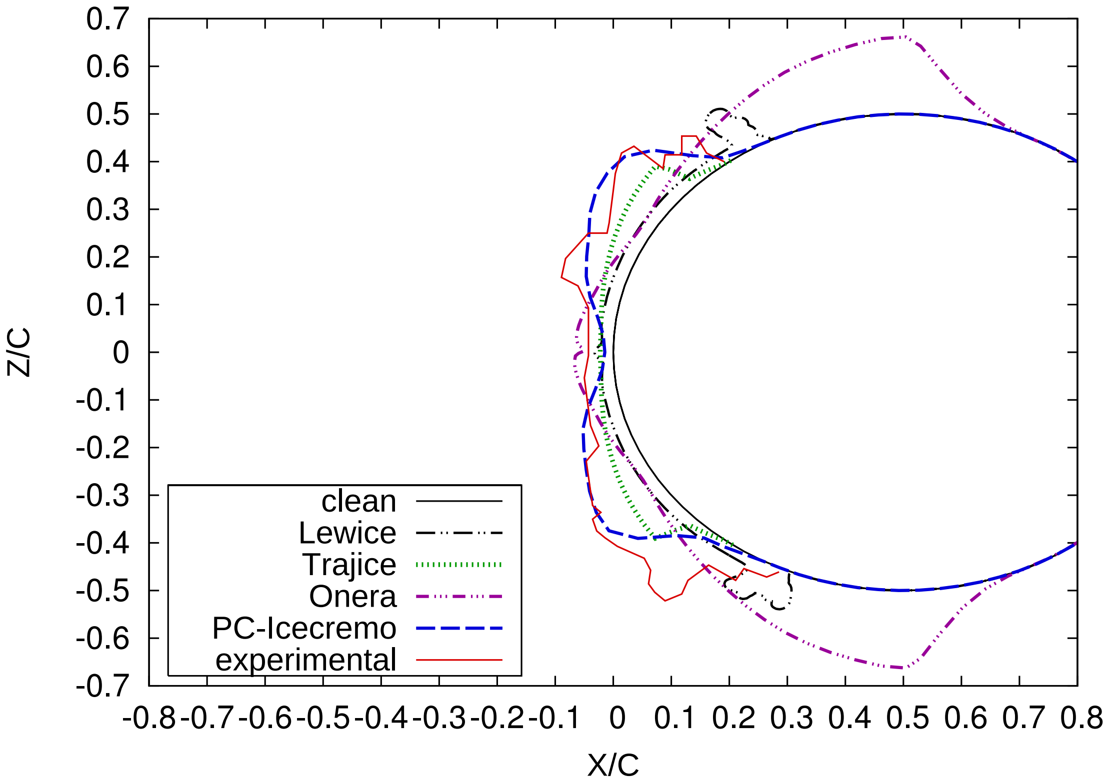

Figure 6.15: *Comparison of the predictor-corrector result with standard ice prediction codes results [120] on a cylinder for small droplets in glaze ice conditions at* $T_\infty = -3^oC$.

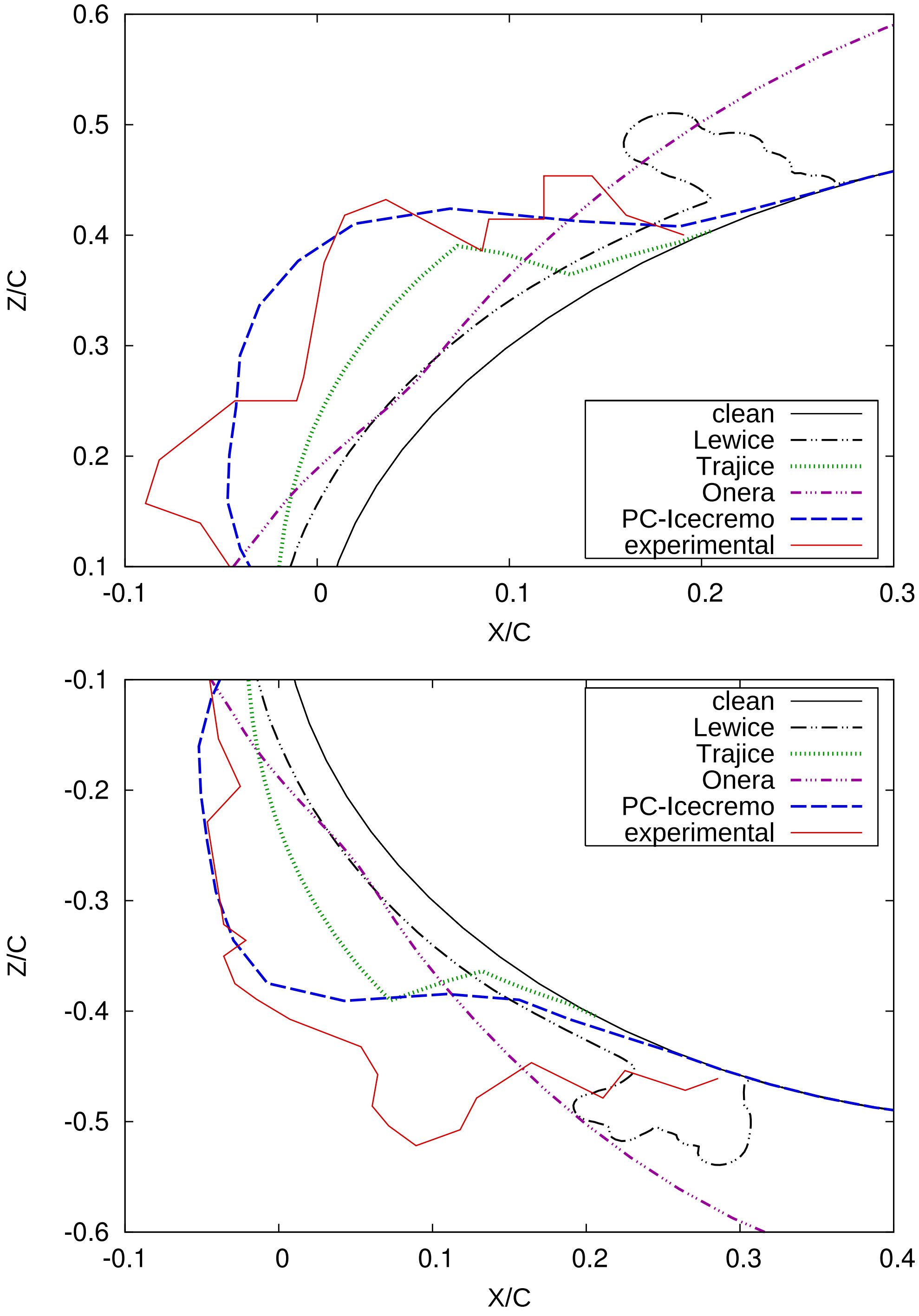

Figure 6.16: *Comparison of the predictor-corrector result with standard ice prediction codes results [120] on a cylinder for small droplets in glaze ice conditions at* $T_\infty = -3^o C$*. Exposure time: 5min 30s. Upper and lower regions.*

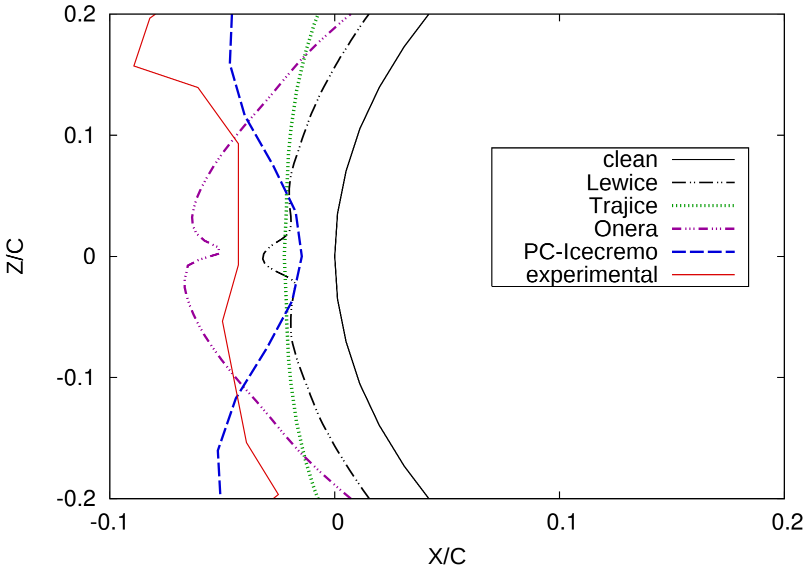

Figure 6.17: *Comparison of the predictor-corrector result with standard ice prediction codes results [120] on a cylinder for small droplets in glaze ice conditions at* $T_\infty = -3^oC$*. Exposure time: 5min 30s. Stagnation region.*

regions, the result from the standard predictor-corrector fairly agrees with the measured ice shape. The corrected ice shape also shows a better agreement with experiments than those generated with the Messinger model, as may be seen in details in Figure 6.16.

The ice height is under-predicted in the stagnation region, see Figure 6.17. As discussed in the previous chapter, this phenomenon is due to the temperature on the cylinder surface which remains constant during the whole computation. This is also due to the value of heat transfer coefficient that appeared very low in this region when calculated on the iced surface. These values of heat transfer coefficient previously shown in Figure 6.14 were lower on the iced geometry in the upper and lower horn regions and the profile was less extended than on the clean surface. This may explain the large difference between the predictor-corrector algorithm and the experimentally measured ice shape in these regions.

To conclude the predictor-corrector study on the cylinder case $O1$ for the impingement of small droplets, the corrected ice shape is now compared with the step-by-step result.

Comparison with the step-by-step result:

The converged solution obtained with the step-by-step algorithm and the ice shape determined via the predictor-corrector may be seen on Figure 6.18. The difference is quite important at the bottom and top part of the ice shape and the step-by-step result shows a better agreement with experiments. These differences between both curves is a sign that more than two flow solutions may be required to determine a more accurate ice prediction. The predictor-corrector therefore does not appear as the best algorithm for icing studies in glaze ice conditions. This is not a real surprise as a multi-time step procedure is known to provide a more favourable agreement than the predictor-corrector technique in glaze ice conditions [128]. This is particularly true for temperatures close to freezing, where accurate results are the most difficult to obtain.

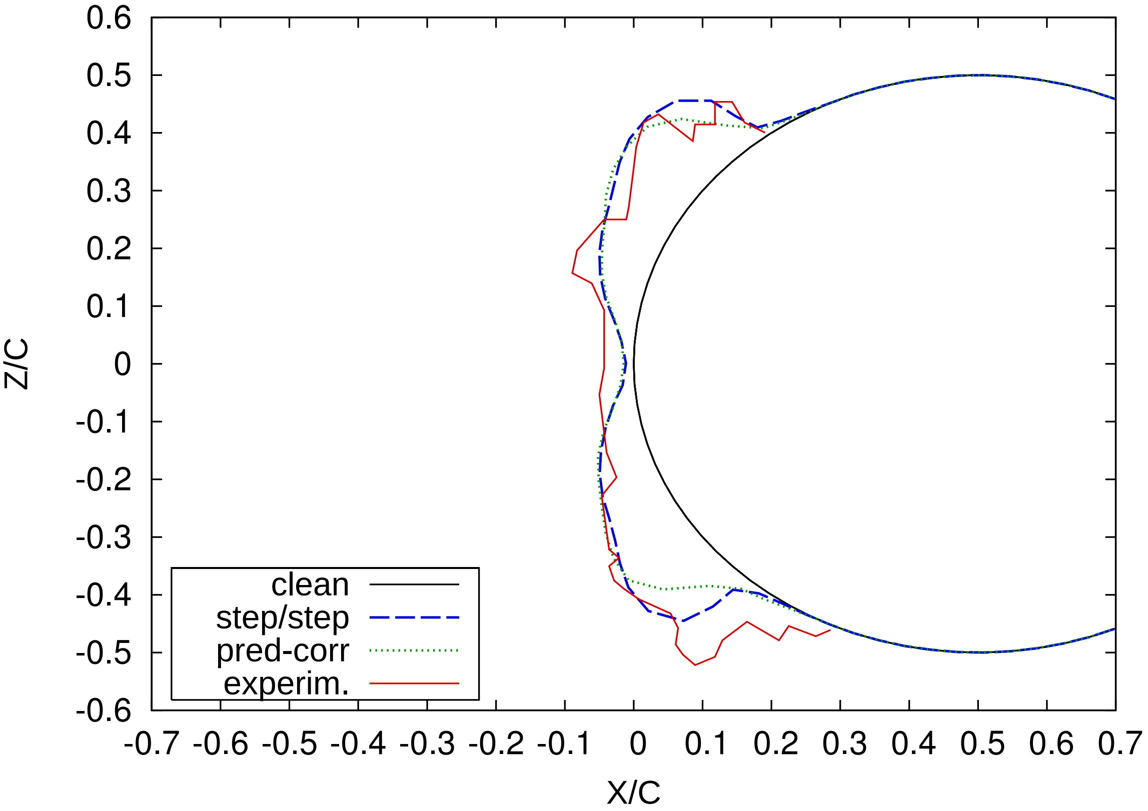

Figure 6.18: *Comparison between the step-by-step and the standard predictor-corrector results obtained for a cylinder in glaze ice conditions. Exposure time: 5min 30s.*

The same study will now be performed for larger droplets. Except for the size of droplets, conditions remain identical than for the impingement of the small droplets.

Impingement of Large Droplets

- **Standard procedure**

  Figure 6.19 represents the results generated on a cylinder subject to the impingement of large droplets $d_d = 100\mu$m with the standard predictor-corrector algorithm. A massive difference is noticeable between the different simulated results. The corrected ice shape extends less in the upper and lower regions of the cylinder and the ice layer is globally thinner. The standard predictor-corrector may not be the perfect algorithm for icing simulations when large droplets impinge on a cylinder. However, this simulated result compares fairly well to experiments and it appears more accurate than the single step result: the thickness of the ice layer is closer to measurements while it is largely over predicted with the single-step procedure.

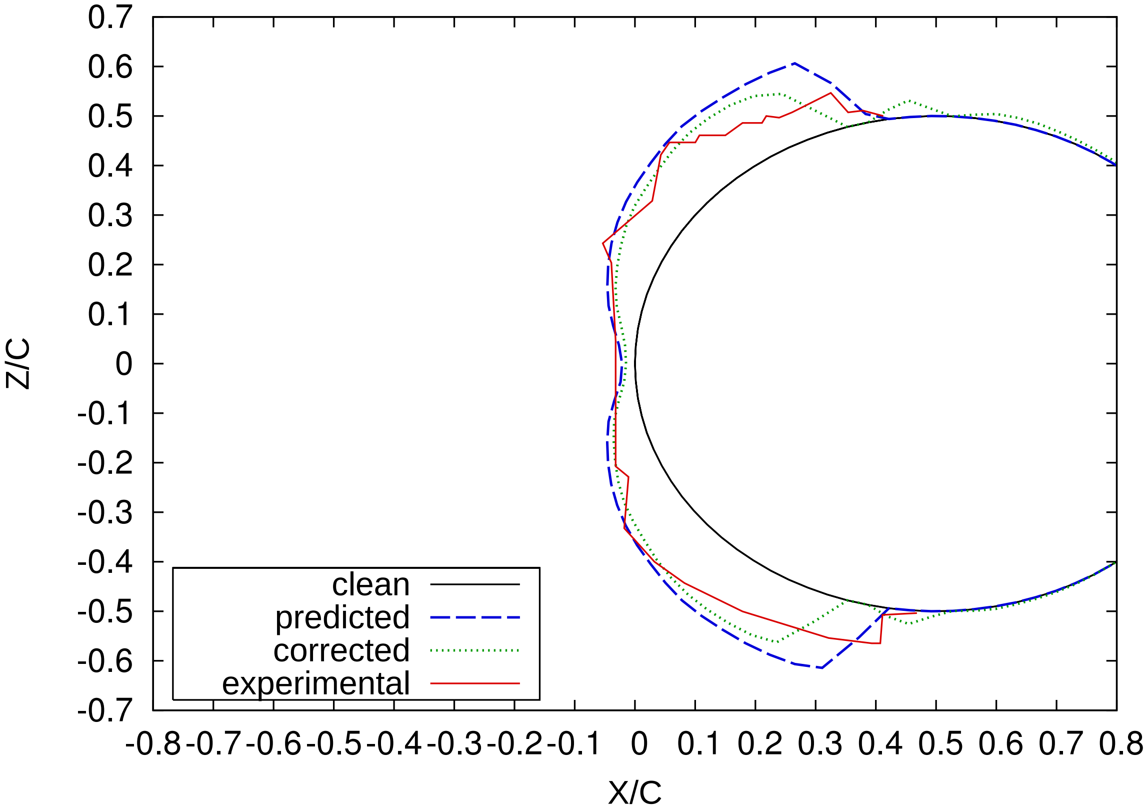

Figure 6.19: *Study of the predictor-corrector algorithm applied to a cylinder in glaze ice conditions. Large droplets. Exposure time: 5min 30s.*

- **Convergence study**

As for the cylinder case $O1$, convergence is reached quickly. Only the first correction is necessary, this corresponds once again to the standard predictor-corrector result. Minor differences are noticeable for the second corrected ice shape. However, they do not modify the estimated ice shape significantly, as may be seen in Figures 6.20 and 6.21.

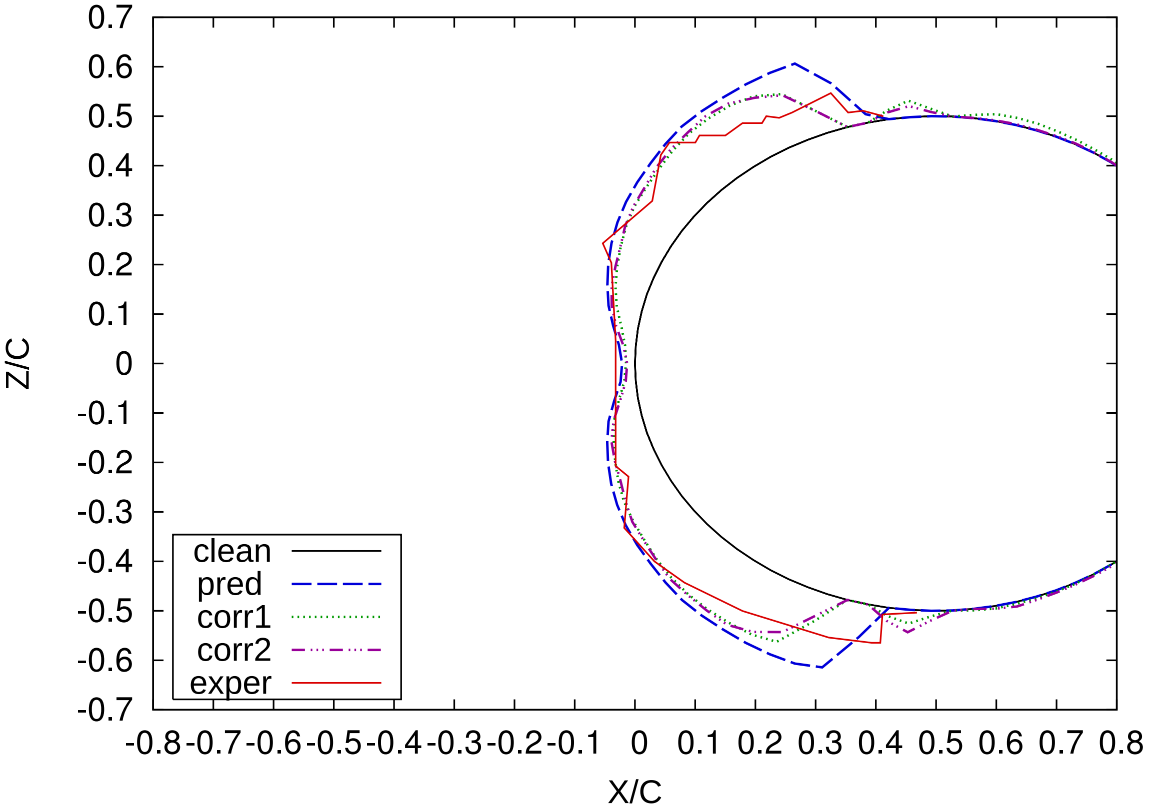

Figure 6.20: *Study of the convergence for the predictor-corrector algorithm applied to a cylinder in glaze ice conditions. Large droplets. Exposure time: 5min 30s.*

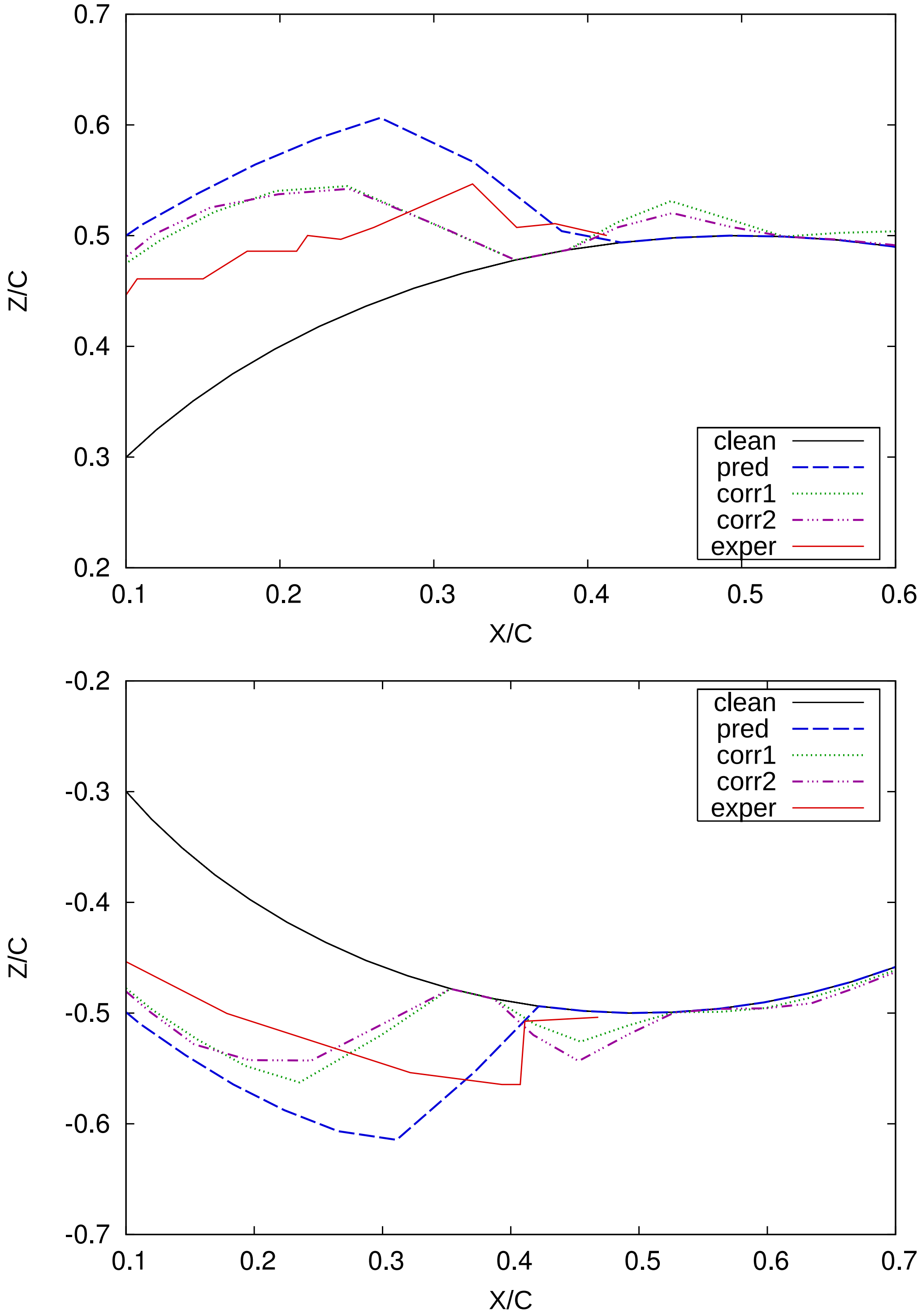

Figure 6.21: *Study of the convergence for the predictor-corrector algorithm applied to a cylinder in glaze ice conditions. Large droplets. Exposure time: 5min 30s*

To evaluate a bit more thoroughly whether or not the predictor-corrector may be suitable for icing studies in glaze ice conditions when large droplets impinge on a cylinder, the standard predictor-corrector result will now be compared to ice shapes from standard Messinger-based ice accretion codes.

Comparison with standard icing codes:

Simulated ice shapes obtained with the standard Messinger codes are plotted together with the predictor-corrector result generated with ICECREMO2, as may be seen in Figure 6.22. While not perfect, the corrected ice shape agrees fairly well to experiments compared to simulated results generated by the Mesinger-based ice accretion codes LEWICE and TRAJICE. The TRAJICE code is the best ice shape estimator at the boundaries limits on the top and bottom regions, but the overall ice shape is under-estimated as may be seen more precisely in Figure 6.23. The

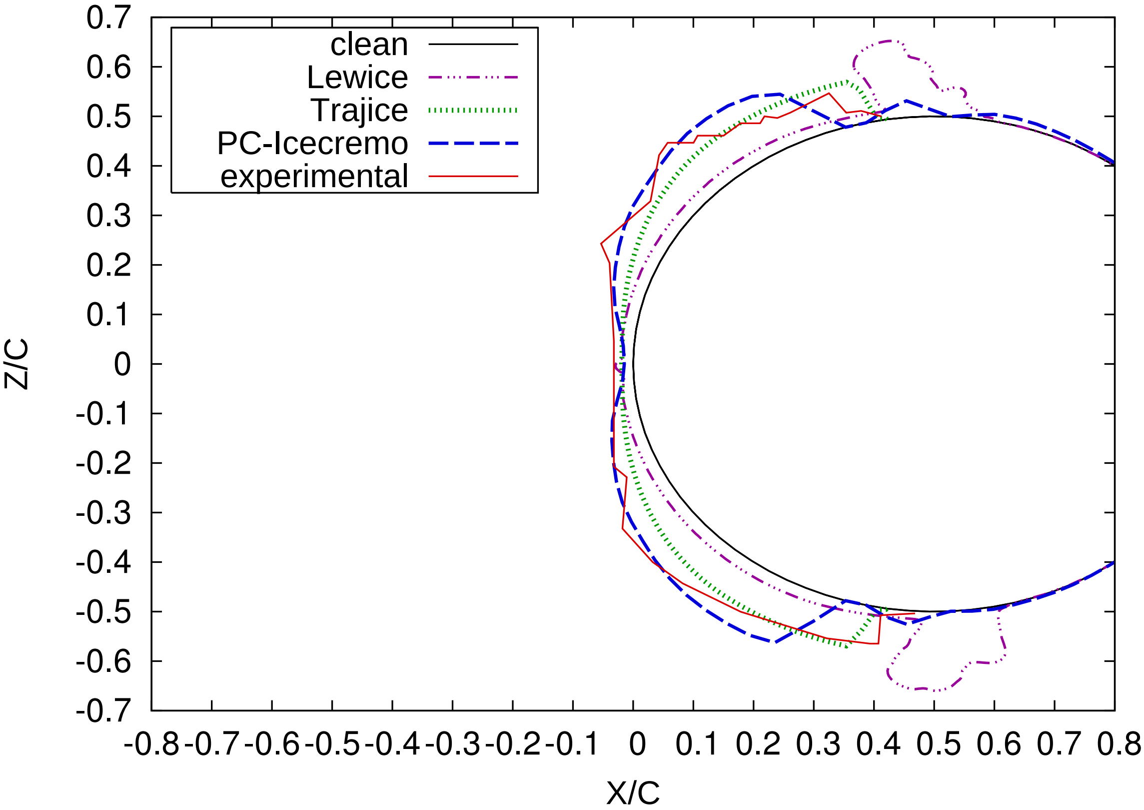

Figure 6.22: *Comparison of the predictor-corrector result with standard ice prediction code results [120] on a cylinder for large droplets, in glaze ice conditions, $T_\infty = -3^oC$. Exposure time: 5min 30s.*

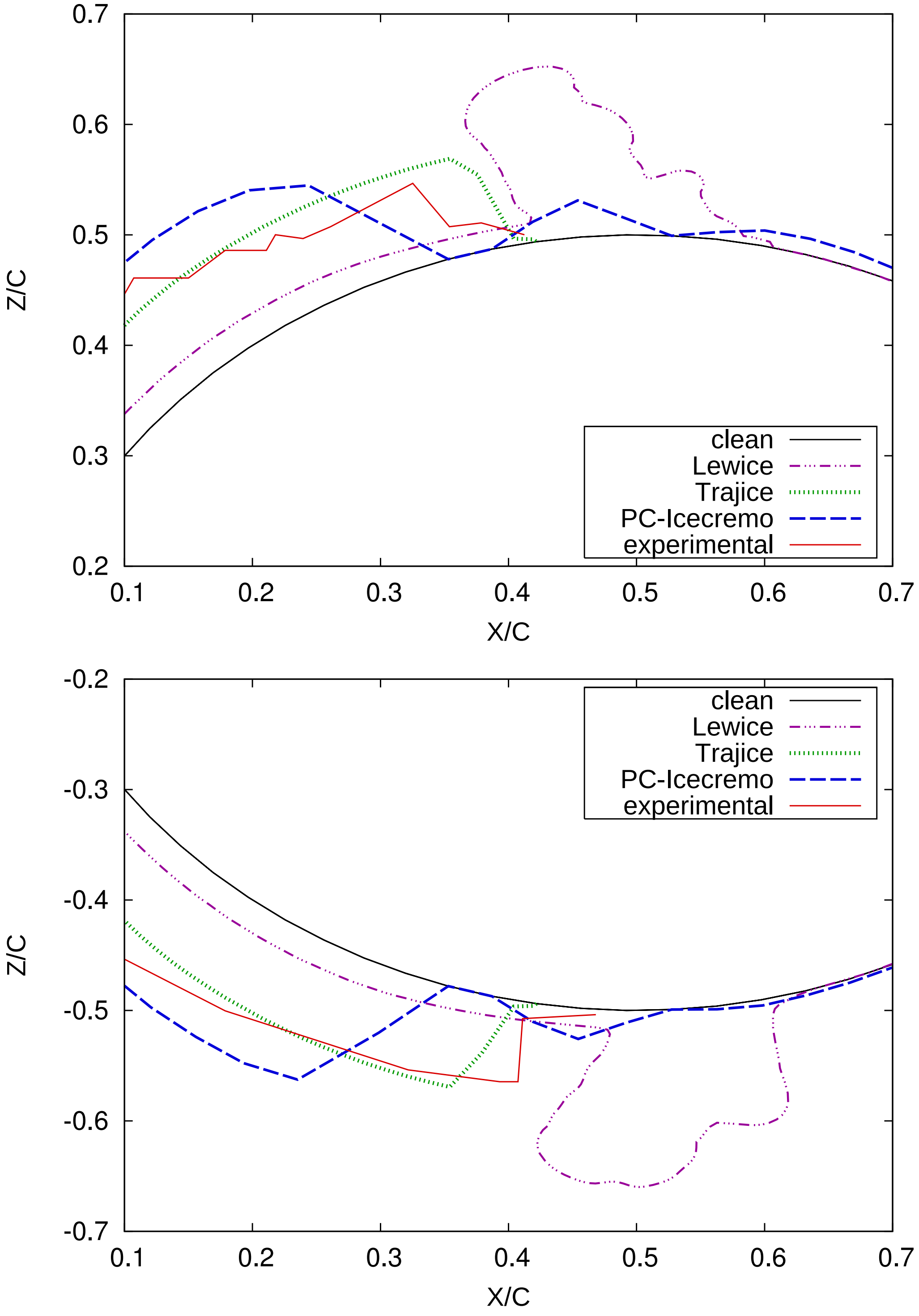

Figure 6.23: *Comparison of the predictor-corrector result with standard ice prediction code results [120] on a cylinder for large droplets,* $T_\infty = -3^oC$. *Exposure time: 5min 30s. Upper and lower regions.*

ice shape simulated with ICECREMO appears closer to experiments in the forward region, but the overall ice shape is over-predicted. It is rather difficult to estimate which of these two codes produces the most accurate result. However, in the previous chapter, it appeared clearly that the step-by-step result agreed better to experiments and that the ice shape determined with ICECREMO was more accurate than the prediction from TRAJICE. A comparison between step-by-step and predictor-corrector is therefore necessary. This is performed in the following section.

Comparison with the step-by-step result:

The simulated ice shape determined with the step-by-step algorithm was best when using the ice criterion. The ice shape studied in Section 5.3 and the standard predictor-corrector result are plotted together in Figure 6.24.

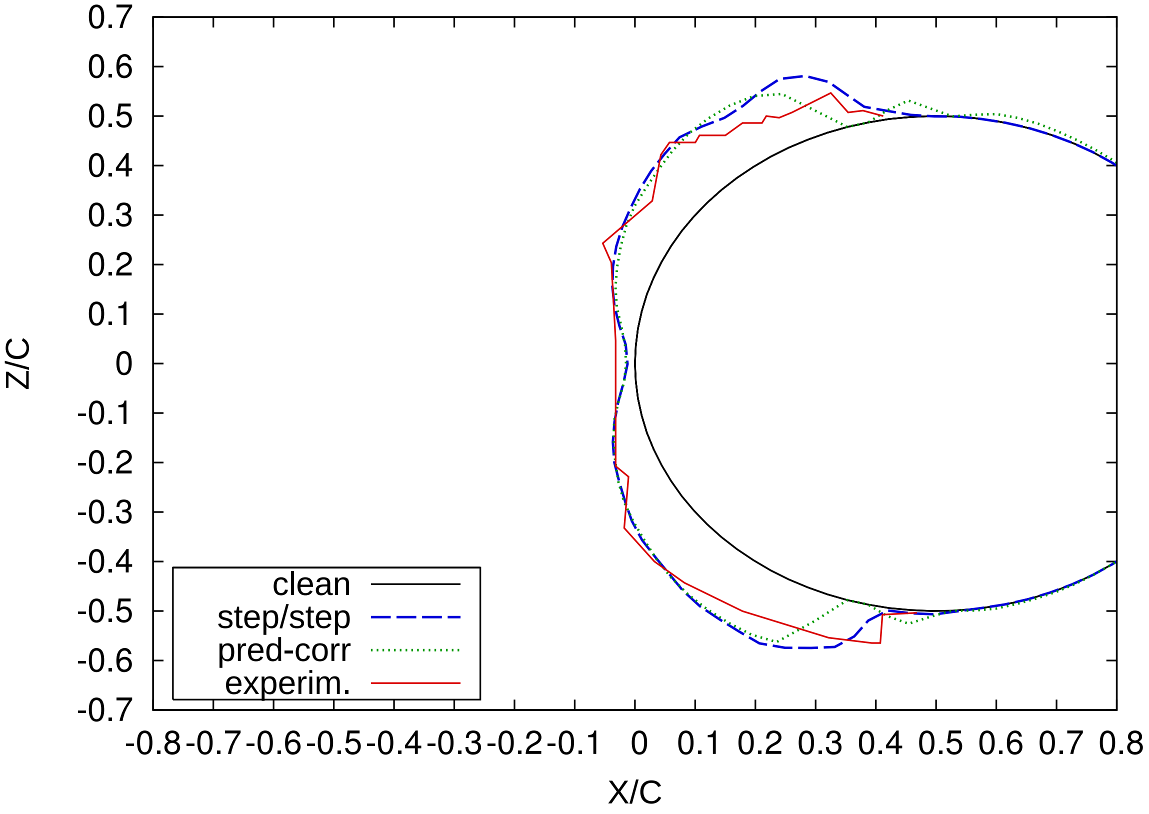

Figure 6.24: Comparison between the step-by-step and the standard predictor-corrector results obtained for a cylinder in glaze ice conditions. Exposure time: 5min 30s.

Obviously, the ice shape obtained with the predictor-corrector algorithm does not compare perfectly well with the step-by-step result and not either with the experimental data. This is particularly noticeable for the ice limits in the top and bottom regions of the body. For the impingement of large droplets, it appears that more than two flow solutions improve the ice shape predictions significantly. The step-by-step procedure is once again the best estimator for the impingement of large droplets in glaze ice conditions.

6.2.3 Summary

The predictor-corrector algorithm was studied on cylinders in this section, in rime and glaze conditions.

- Convergence was reached after the first corrected ice shape. A standard predictor-corrector is therefore sufficient to determine the ice accretion on a cylinder in both rime and glaze ice conditions.

- The predictor-corrector approach is rather accurate in rime ice conditions. Results are very similar to those generated with the step-by-step algorithm. However, the interpolation-based procedure should be favoured for time saving reasons since only two flow solutions are required against three for the step-by-step approach based on the ice criterion.

- In glaze ice conditions, the corrected ice shapes did not show the same accuracy than the step-by-step approach. Results were nevertheless acceptable. They compared reasonably well with experiments and sometimes agreed better with experiments than the standard Messinger-based ice prediction codes. Nevertheless, the step-by-step algorithm based on the ice height criterion is the recommended approach as it has proved efficient and more reliable in glaze ice conditions.

The predictor-corrector algorithm will now be investigated on a wing geometry.

6.3 Ice Predictions on Airfoils

The study of the predictor-corrector algorithm is now extended to a wing under rime and glaze ice conditions. The icing and atmospheric conditions for all simulations are here again those previously applied to the NACA0012 wing geometry specified in Table 5.6 of Chapter 5.

6.3.1 Rime Ice Conditions

Standard Procedure

Ice shapes are determined on the NACA0012 wing in rime ice conditions at the temperature $T_\infty \simeq -26^o C$ using the predictor-corrector algorithm. The final results may be seen in Figure 6.25. For conditions similar to the cylinder case $O1$, the simulated ice shape seems slightly more affected by the interpolation between the values of predictor and those of corrector. As a reminder, for the cylinder case, the ice shape appeared thinner on either side of the nose region. The shape obtained on the wing is quite similar, but the differences are more pronounced between the predicted and corrected results. This due to the larger geometry and to the angle of attack $\alpha = 4^o$ which affects the collection efficiency and subsequently the corrected ice shape in the bottom part of the wing.

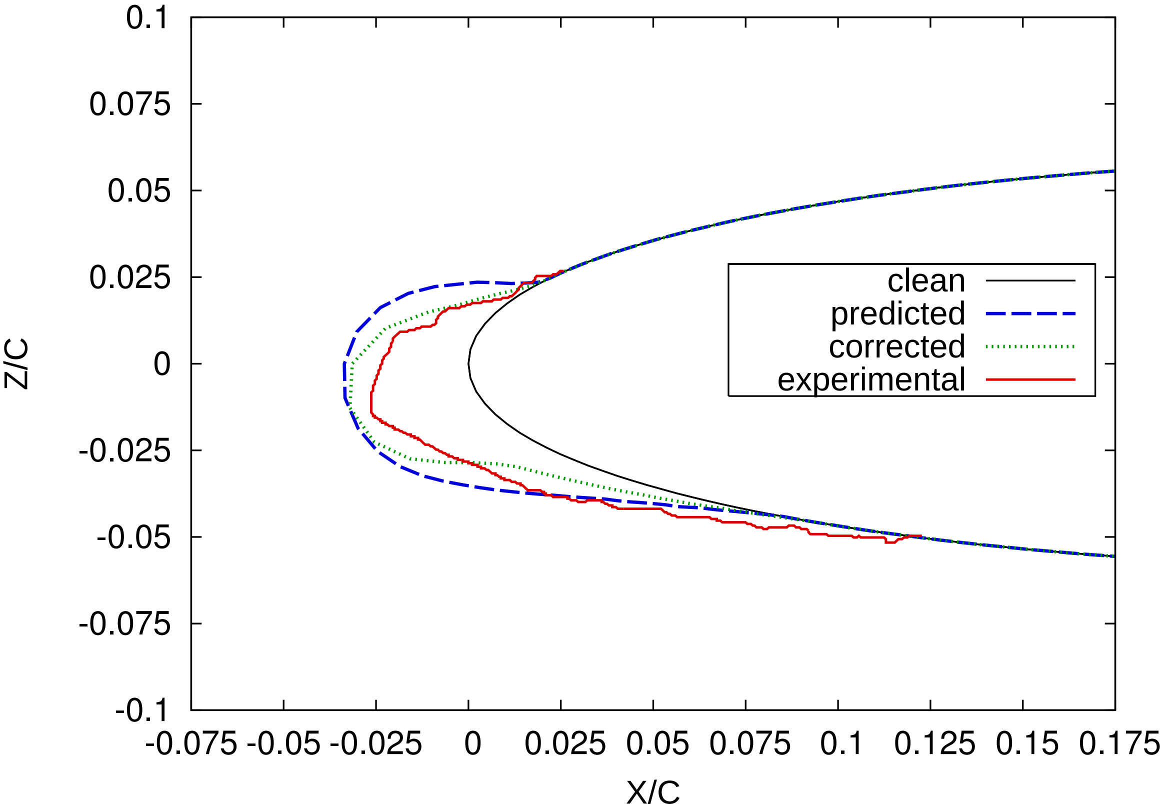

Figure 6.25: *Study of the predictor-corrector algorithm applied to a wing in rime ice conditions. Exposure time: 360s*

The standard predictor-corrector algorithm does improve the accuracy of the prediction in the wing upper and nose regions. However, the single-step result agrees better with the measured ice shape in the lower region. The convergence of the algorithm will now be investigated.

Convergence Study

Figure 6.26 depicts the corrected ice shapes corresponding to the new updates of the corrector. The convergence of the algorithm is more difficult to obtain on the wing geometry than on the cylinder structure. Some sort of convergence is reached after the second correction, more clearly visible in Figure 6.27. Past this second correction, the ice shape looses its accuracy and discrepancies appear due to instabilities in the model which were expected for a high number of iterations on a large geometry. This is clearly apparent on the lower part of the wing where the roughness of the ice

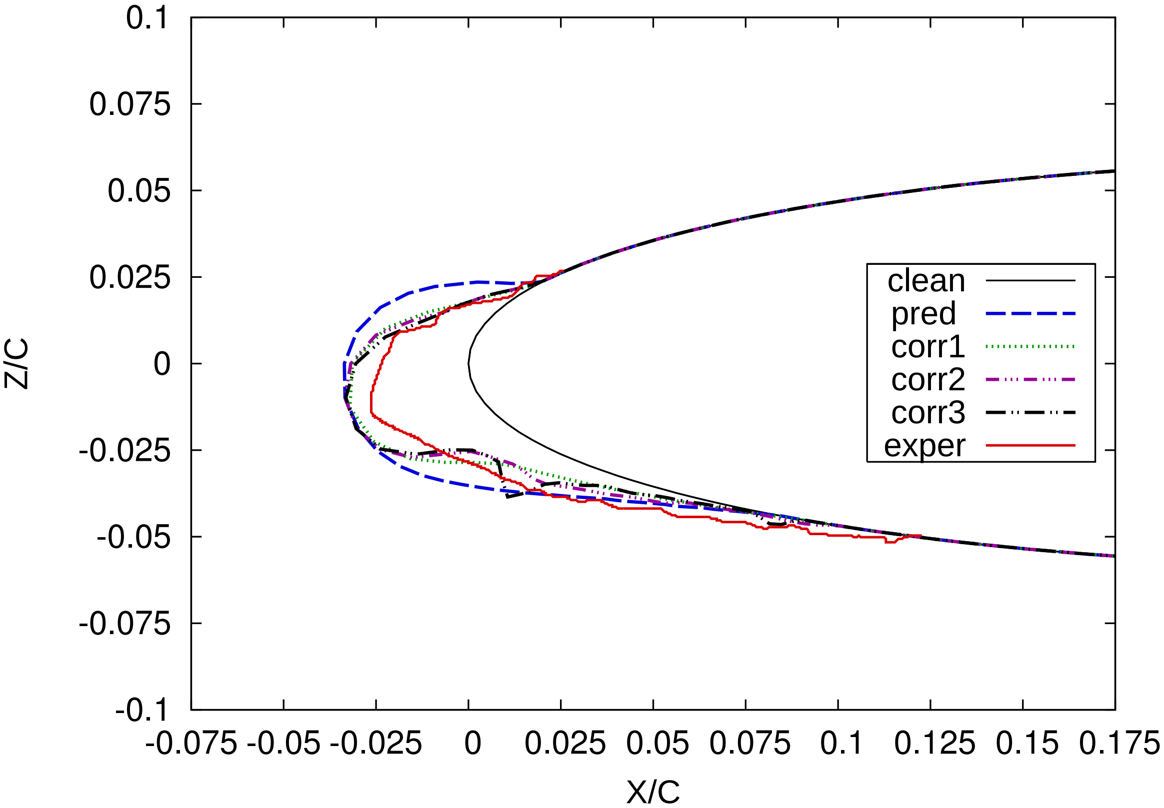

Figure 6.26: *Study of the convergence of the predictor-corrector algorithm applied to a wing in rime ice conditions. Exposure time: 6 min.*

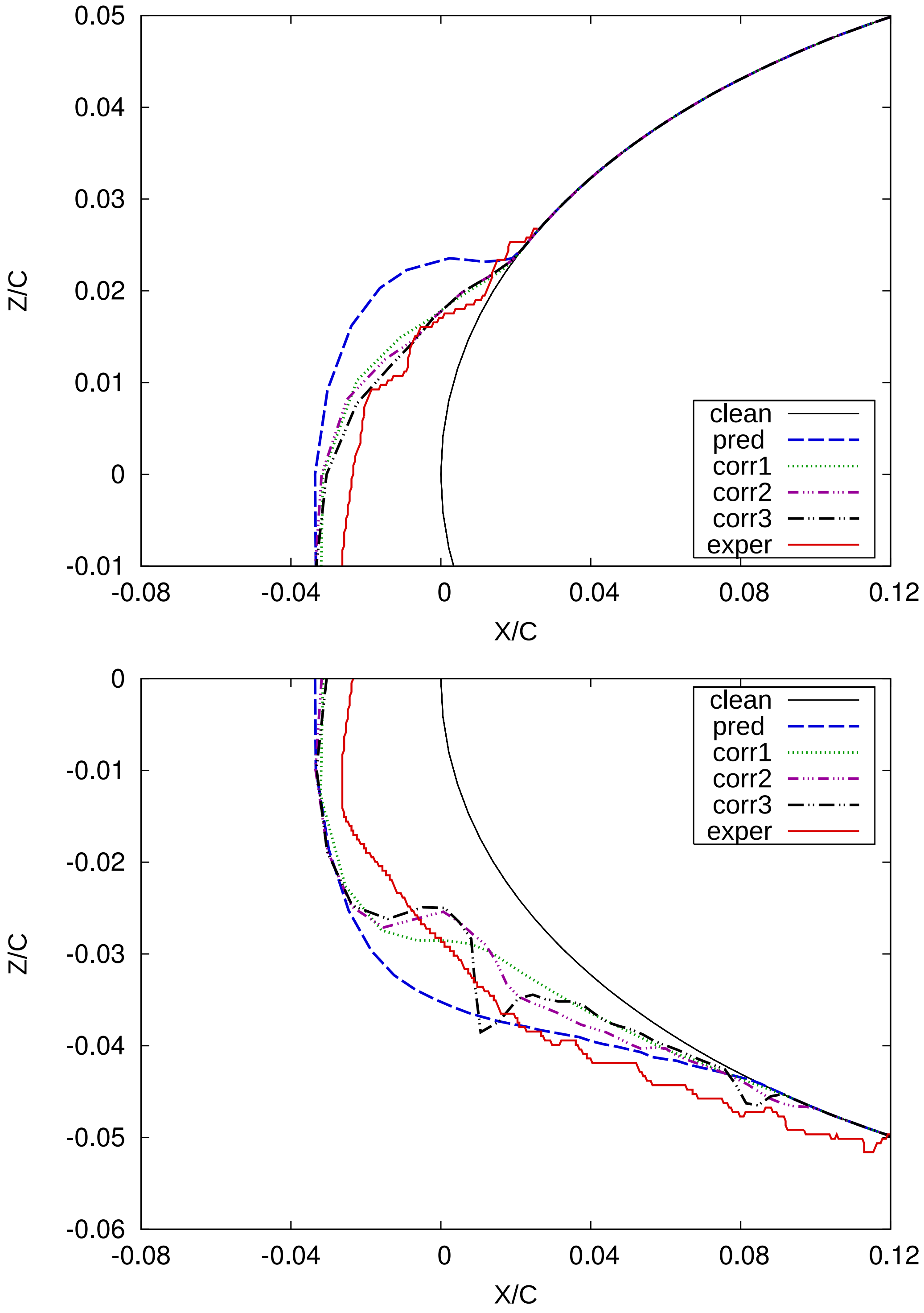

Figure 6.27: *Study of the convergence of the predictor-corrector algorithm applied to a wing in rime ice conditions. Exposure time: 6 min.*

layer is the most important. The rough nature of the accreted ice is also noticeable for the experimentally measured ice shape.

Convergence is established for the second correction. However, the first corrected ice shape being rather close to convergence, the standard predictor-corrector approach may be considered as suitable for rime ice calculations on a wing. This procedure is favoured for time saving reasons. Nevertheless, it may be a safer solution to calculate a second corrector to insure a perfect convergence of the predictor-corrector algorithm on this kind of geometry.

Note that the accuracy of the simulated ice shape obtained with the predictor-corrector algorithm is strongly dependent on the values of predictor. As already discussed for the cylinder case, if the single-step result is of poor quality, the corrected ice shape will not show a high improvement and even worse, can induce a wrong ice profile. The poor flow solution in the first step of the algorithm can jeopardize the accuracy of the predictor-corrector method due to a chain reaction phenomenon.

The step-by-step algorithm based on the ice height criterion turned out to be an appropriate approach in rime ice conditions. The simulated result obtained in the previous chapter and based on the ice height criterion will now be compared to the standard predictor-corrector approach.

Comparison with the step-by-step result

Figure 6.28 shows the simulated results for the two multi-step algorithms: the step-by-step studied in Section 5.4 of the previous chapter and the standard predictor-corrector obtained in a two-step process. As may be observed, the final ice shape obtained with each procedure is very similar. The ice layer is slightly higher in the upper region for the predictor-corrector result, while the ice layer is slightly higher in the lower and nose regions for the step-by-step algorithm. However, these small differences do not modify the overall ice shape very significantly. This is in agreement with the results obtained on the cylinder geometry and also in agreement with the statement from Mingione et al. [25] for simulations run with the icing code ICE developed by the Italian Aerospace Reseach Center (CIRA).

A standard predictor-corrector algorithm should therefore be the favoured multi-step algorithm in rime ice conditions for time saving reasons, two flow solutions being required against five for the step-by-step procedure based on the ice height criterion.

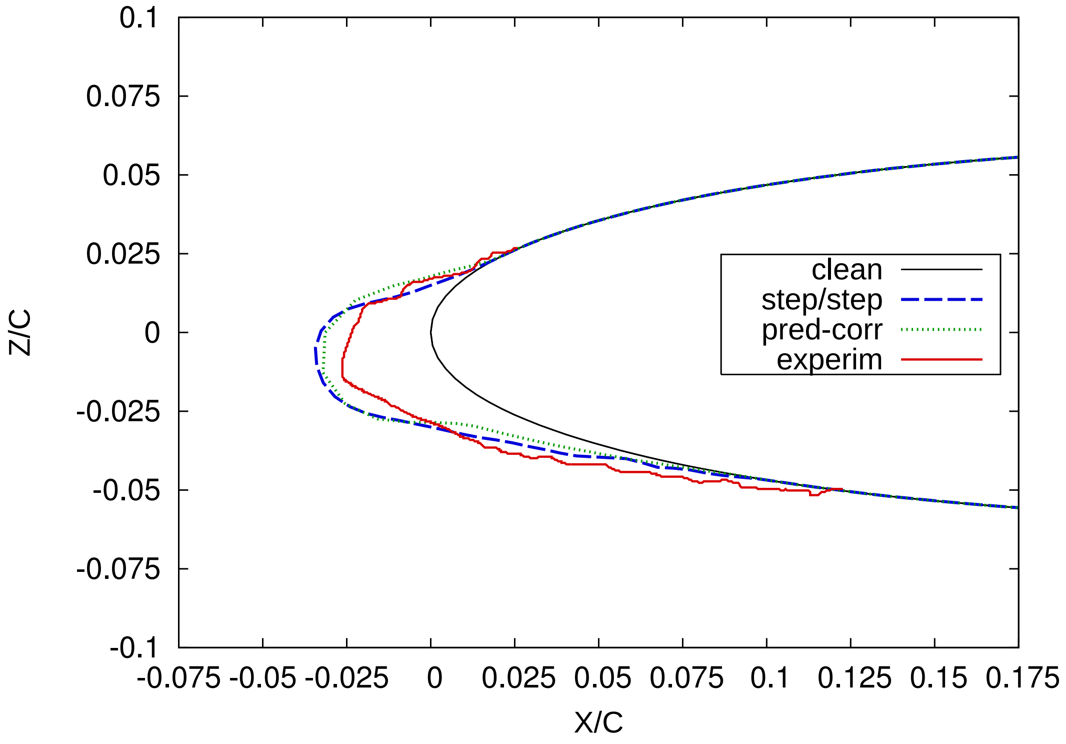

Figure 6.28: *Comparison step-by-step versus predictor-corrector for a wing in rime ice conditions.* $T_\infty = -26^oC$. *Exposure time: 6 min.*

The same analysis is now performed for the ice accretion on the NACA0012 wing in glaze ice conditions.

6.3.2 Glaze Ice Conditions

Standard Procedure

The final ice shape obtained with the standard predictor-corrector approach after an icing exposure time of $t_{exp} = 20$min at the temperature $T_\infty = -7^oC$ is presented in Figure 6.29. Large differences appear between the results obtained with the interpolation based approach and with the one-step procedure.

- As for each multi-stepping case investigated in this thesis, the predictor-corrector approach globally predicts less ice in comparison to the single step algorithm and the ice extents in the upper and lower regions are identical for both simulations.

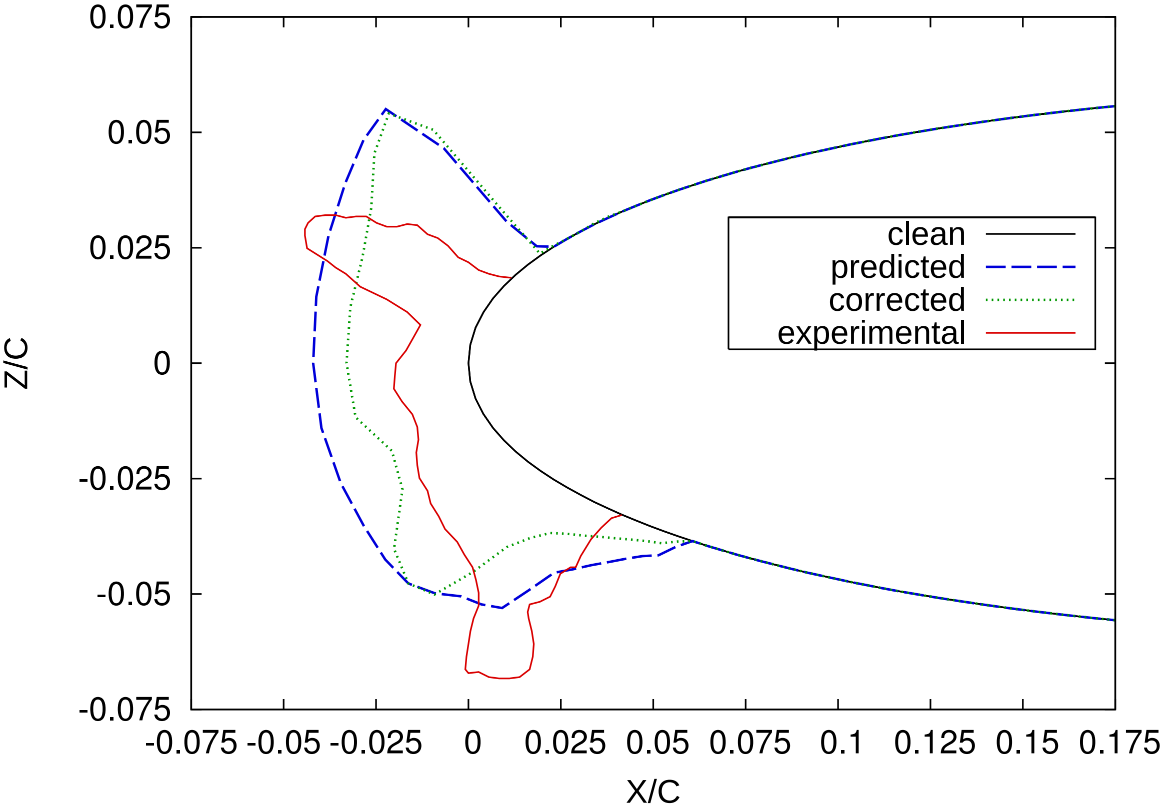

Figure 6.29: *Study of the predictor-corrector algorithm applied to a wing in glaze ice conditions.* $T_\infty = -7^oC$*. Exposure time: 20 min.*

- In the contrary of the single-step approach, the predictor corrector algorithm captures the double-horn ice structure. All the characteristics of the measured ice shape may be retrieved in the predictor-corrector result, however in a different proportion:
  - The upper horn is over-estimated and shows a wrong direction,
  - The stagnation region is over-predicted,
  - The lower horn is too close of the nose region and is under-predicted.

When analysing Figure 6.29, the predictor-corrector algorithm undeniably matches experiments better than the single-step procedure. However, the agreement is not as good as with rime ice and the corrected ice shape remains far from the experimental data. The ice shape obtained with the predictor-corrector is however a great improvement for the sort of expected ice shape under these specific conditions.

The lack of accuracy of the predictor-corrector algorithm was somehow expected in glaze ice conditions. As specified in [128], this approach is best for rime icing rather than glaze ice type accretions. The reason for this is that rime ice accretion is proportional in time to the collection efficiency. The number of parameters influencing glaze ice accretion being greater, the interpolation between the predictor and the corrector is prone to piling up errors. Furthermore, the flow solution is a key-element in a predictor-corrector algorithm:

1. A poor quality of flow field data will generate poor values of predictor leading to a lack of accuracy in the first estimated ice shape,
2. The flow around this first estimated ice shape will also be of poor quality and the corrector values inaccurate,
3. The interpolation errors between inaccurate values of predictor and corrector are likely to increase with the exposure time. This may be an issue for a large exposure time to icing and for a small time-step in the icing solver.

To further analyse the predictor-corrector approach applied to the ice prediction shape on an NACA0012 wing in glaze ice conditions, a study of the convergence will now be performed.

Convergence Study

For the cylinder configuration in glaze ice conditions, convergence was reached almost instantaneously. The computing time was minimum as only two flow solutions and one interpolation were necessary. The standard procedure was therefore sufficient on this small geometry. However, several difficulties were encountered with the convergence of the flow solution around the iced body. Not surprisingly, the convergence of the flow solution is even more difficult to reach on a larger geometry such as a wing, associated with a larger surface deformation due to icing. Obtaining the convergence of the predictor-corrector algorithm in these conditions for a long icing duration is therefore a tremendous and time-consuming task. The corresponding corrected ice shapes obtained with updated values of corrector are presented in Figure 6.30.

As may be seen more precisely in Figure 6.31, results are oscillating. The convergence is not immediate and five new correctors are necessary. The difficulties for the ice shape to reach convergence is most probably due to the values of corrector. Obviously, the ice shape determined with the one-step algorithm is not of sufficient quality, the ice shape being rather far from experiments. The predictor-corrector algorithm tries to improve this first ice estimation: in the first few steps, the results are just readjusting and in the end, the same sort of shape is obtained as if a more accurate first corrector was obtained. To limit the effects due to a

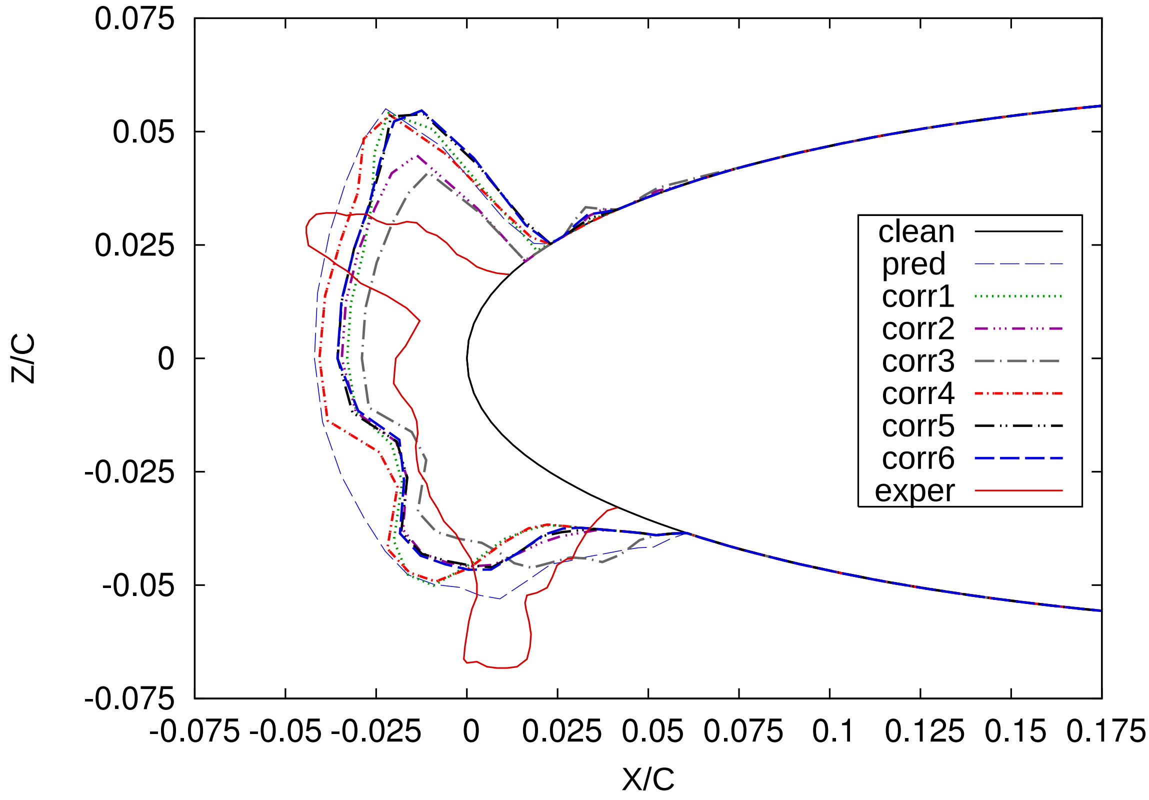

Figure 6.30: *Study of the convergence of the predictor-corrector algorithm applied to a wing in glaze ice conditions.* $T_\infty = -7^o C$. *Exposure time: 20 min.*

potential inaccurate flow calculation around the iced geometry, one solution could be to allow for a periodical update of the flow data during the whole computation. This could be achieved by coupling step-by-step and predictor-corrector algorithms. This procedure will have the advantage to increase the accuracy of the predictions significantly, but will also increase the number of flow solutions and subsequently the total computing time.

When the convergence is reached, the double-horn ice structure is clearly visible and a depression is present in the stagnation region. The final ice prediction obtained with the predictor-corrector matches better the experimentally measured ice shapes than the one-step algorithm does.

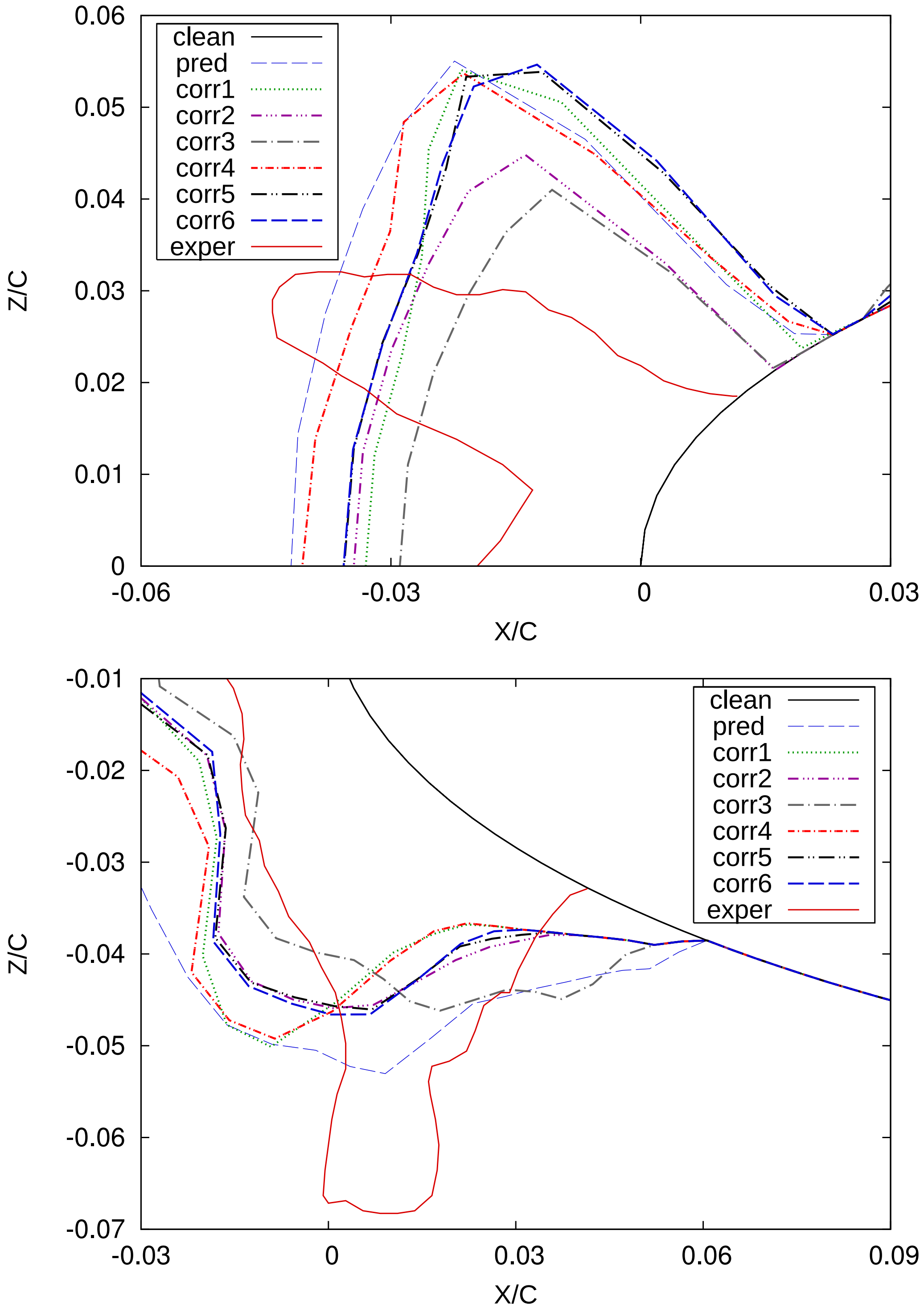

Figure 6.31: *Study of the convergence of the predictor-corrector algorithm applied to a wing in glaze ice conditions.* $T_\infty = -7^oC$. *Exposure time: 20 min.*

The ice shape obtained in five interpolations between the values of predictor and corrector being so far the best ice estimation with this algorithm, it will now be compared with the step-by-step result.

Comparison with the step-by-step result

The ice height criterion was established as the best ice estimator on a wing in glaze ice conditions for the step-by-step study performed in Section 5.4. Ten flow solutions were required for the ice-based algorithm to reach convergence while five only are necessary with the predictor-corrector approach. The corresponding simulated ice shape is plotted against the predictor corrector result, as may be seen in Figures 6.32 and 6.33.

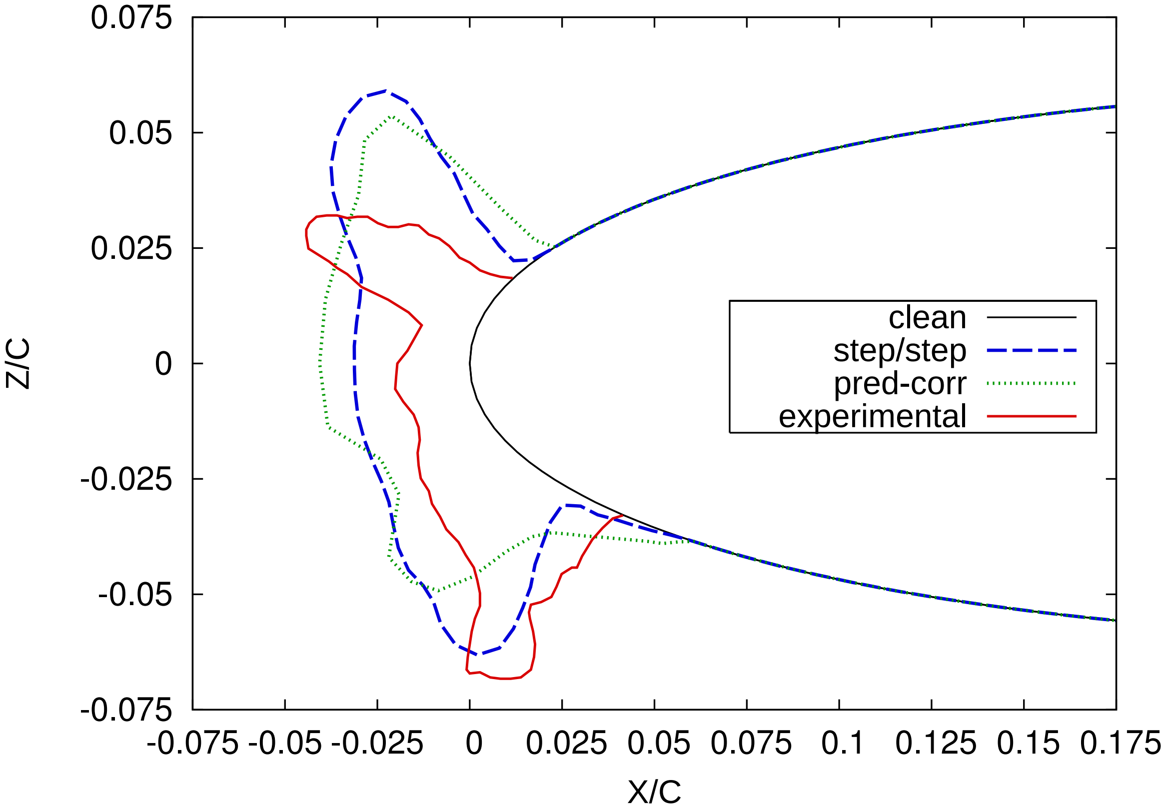

Figure 6.32: *Comparison step-by-step versus predictor-corrector for a wing in glaze ice conditions.* $T_\infty = -7^oC$. *Exposure time: 20 min.*

The step-by-step algorithm provides a better agreement with experiments in all regions of the wing surface. However, the depression observed in the experimentally

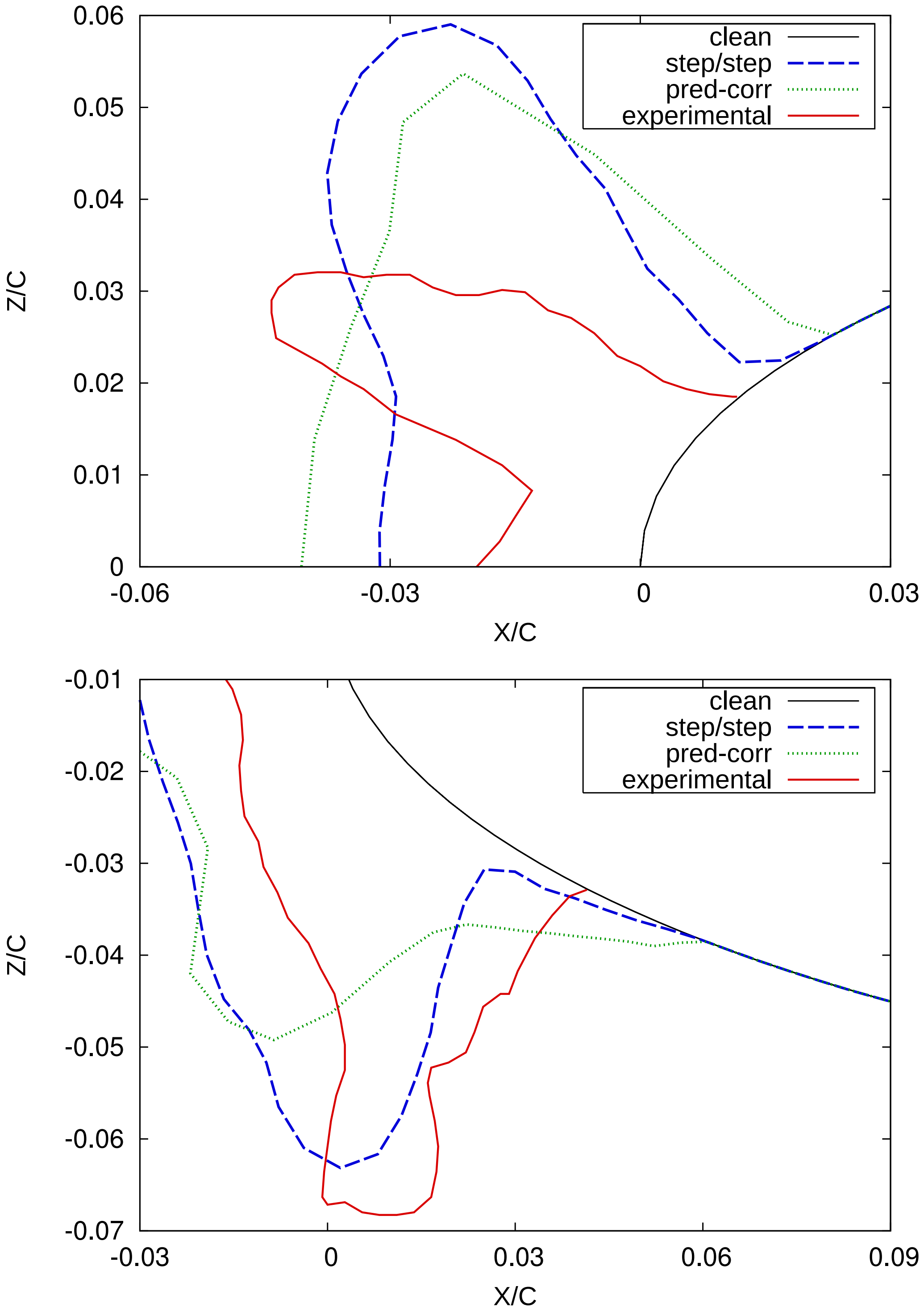

Figure 6.33: *Comparison step-by-step versus predictor-corrector for a wing in glaze ice conditions.* $T_\infty = -7^oC$. *Exposure time: 20 min.*

measured ice shape is only estimated by the corrected result, which is rather encouraging. As previously explained, limitations of the icing model will not allow for the simulated result to agree perfectly with the sort of expected ice shape on a wing in glaze ice conditions. The predicted ice shape obtained here with the predictor-corrector technique is a great achievement already, even if there is still large room for improvement. Such a potential improvement could be achieved using the ice height as an alternative to the time based interpolation. In this case, the ice height will replace the time in the interpolation function given by Equation 6.1. However, as detailed in Chapter 5, the difference of ice shape between the step-by-step results based on the time criterion and on the ice height criterion were relatively minor. Choosing the ice height as a parameter in the predictor-corrector should therefore not show a large difference. The exact consequences are nevertheless unpredictable: this approach could reduce or enhance or be neutral to the influence of the corrector part. This would have to be tested thoroughly and could be proposed for future work on multi-stepping.

The predictor-corrector simulated ice shape obtained with ICECREMO2 will now be compared to the result generated with the ice prediction codes LEWICE, TRAJICE2 and ONERA2000.

Comparison with standard icing codes

Figures 6.34 and 6.35 show the simulated ice shape calculated with the predictor-corrector algorithm implemented in ICECREMO2 and the results from the standard Mesinger based ice predictions codes. The corrected ice shape is rather different from LEWICE and TRAJICE. However, the overall ice shape has some common features with the ONERA code result, also based on a predictor-corrector algorithm. Nevertheless, the corrected ice shape extends less in the lower part of the wing and the ice layer in the stagnation region appears higher than for the ONERA code result.

Either with the step-by-step or with the predictor-corrector approach, the ice layer in the stagnation zone is always over-predicted with ICECREMO in glaze ice conditions. This is most likely due to the flow perturbation around the iced geometry which makes the flow rather turbulent and renders the collection efficiency difficult to calculate. Another reason may be due to a release of the droplets too close from the surface. For the fully automated procedure, the starting point of these droplets remains at the same position, independently of the number of steps or of the icing exposure time. This starting position is established at the beginning of the computation, around $x/c = -2$ for the present case, and usually works fine for a single-step calculation. Such an approach is acceptable when the ice accretion is

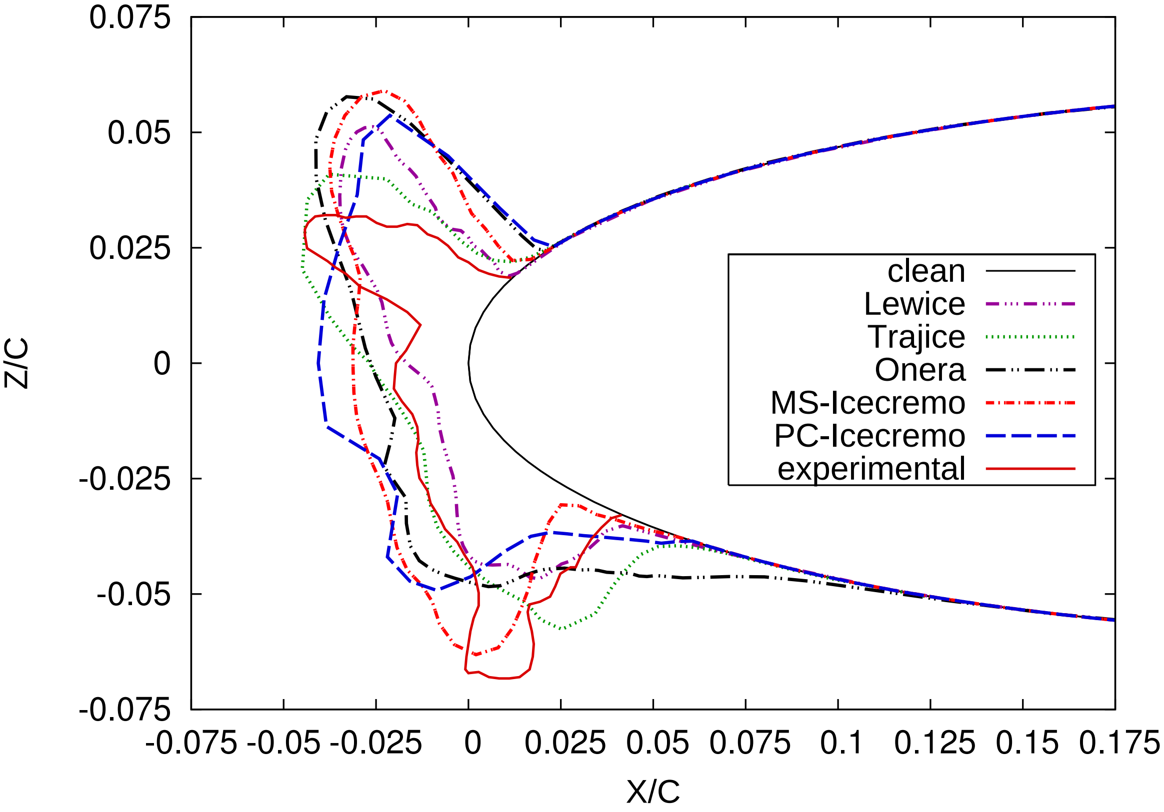

Figure 6.34: *Comparison of the predictor-corrector result and standard ice prediction code results [120] on a NACA0012 wing in glaze ice conditions,* $T_\infty = -7^oC$. *Exposure time: 20 min.*

small. However, for a large ice accretion time, this may be an issue as the collection efficiency may become too high, leading to a large increase of the ice shape between the impingement limits. In the case of the predictor-corrector algorithm, the flow solution must be determined around the final ice shape to determine the values of corrector. A release of droplets too close from the iced surface will produce inaccurate values of corrector. This may explain the over-predicted ice layer in the forward region of the wing surface and the lack of ice in the lower horn region, see Figure 6.34. This points out a limitation in the current automated process. A solution could be to automatically change the starting point of the droplets when the ice layer becomes higher than a defined ice height. Such a limitation and the nature of the icing model in ICECREMO justifies the shape and direction of the corrected result obtained with the predictor-corrector algorithm.

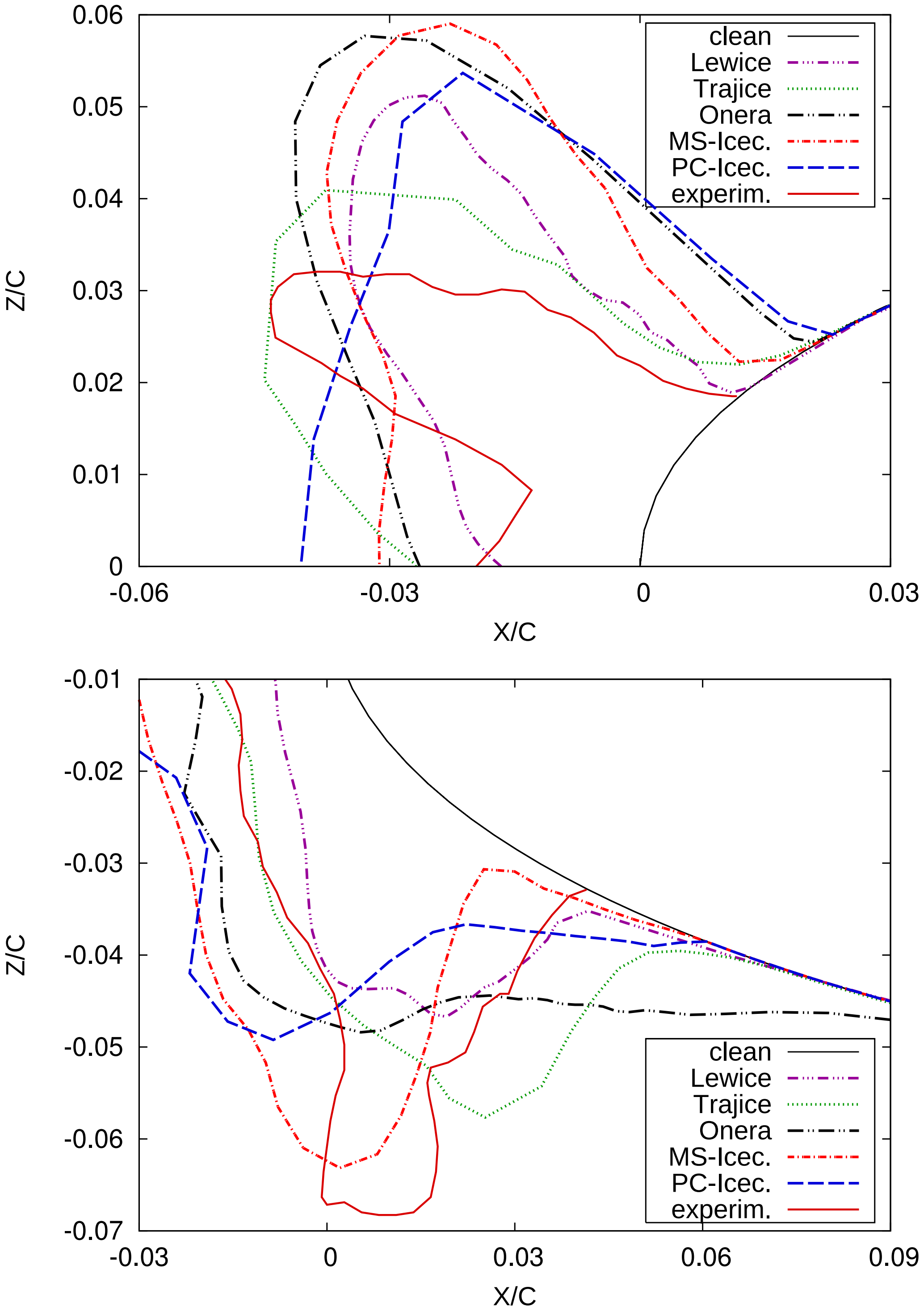

Figure 6.35: *Comparison of the predictor-corrector result and standard ice prediction code results [120] on a NACA0012 wing in glaze ice conditions,* $T_\infty = -7^oC$. *Exposure time: 20 min.*

6.3.3 Summary

A study of the predictor-corrector has been performed on a wing geometry in rime and glaze ice conditions.

- The predictor-corrector algorithm compared favourably to experiments and step-by-step results in rime ice conditions. This approach should be recommended and used for time saving reasons: only two flow solutions are required with the standard predictor-corrector algorithm to reach convergence, against five for the ice based procedure. However, it could be a safer solution to perform one more interpolation to guarantee the accuracy of the final results as this procedure appeared to be affected by the quality of the air flow solution.

- In glaze conditions, the simulation was more tricky and unpredictable. Convergence was nevertheless established after six flow calculations corresponding to five values of corrector. Despite being rather far from experiments, the predictor-corrector result compared fairly well with simulated results from standard ice accretion codes. However, the ice shape obtained with the step-by-step algorithm agreed better with the experimental data. It appeared clearly that the predictor-corrector algorithm was strongly dependent on the accuracy of the air flow solution.

6.4 Conclusion

The study of the predictor-corrector algorithm was carried out in this chapter for different icing scenarios on cylinders and wings.

- The standard predictor-corrector is the algorithm recommended in rime ice conditions since it saves considerable computation time compared to the step-by-step algorithm. However, this approach is strongly dependent on the accuracy of the flow solution. The predictor-corrector is therefore faster but less reliable than the step-by-step procedure based on the ice criterion.

- In glaze ice conditions, the accuracy was best established with the step-by-step algorithm.
  - The standard predictor-corrector can be used on a cylinder structure if the flow solution is of very good quality. The corresponding results showed a better agreement to experiments than most standard ice prediction codes based on the Messinger model. However, the results obtained in this

  chapter remained less accurate than those obtained with the step-by-step in a four-step procedure.
  - Simulated ice shapes were far less satisfactory on a larger geometry such as a wing. In this case, the converged solution reached after five interpolations between the values of predictor and corrector did not agree with measurements and not either with the step-by-step result.

Simulated ice shapes based on the predictor-corrector appeared strongly dependent on the quality of the flow solution. Several alternative solutions may be tested and developed to try to improve the results:

1. Use an alternative method of interpolation based on ice height instead of time. However, there is no guarantee of improvement.
2. Develop a procedure that will combine step-by-step and predictor-corrector algorithms. This will improve the accuracy of the results but will also increase the computing time significantly.

The combined procedure between step-by-step and predictor-corrector algorithm is the most appropriate solution. If the flow solution is not of good quality, its influence will be limited in time. Such a procedure is likely to reduce the large differences observed in this chapter in glaze ice conditions for a long exposure time to icing, between the measured ice shape and the simulated results. A combined approach would have the huge advantage to limit this sort of problem since the flow dependent parameters could be updated regularly and the time of accretion could be divided into an appropriate number of multi-time steps. Such a procedure will be investigated in the next chapter.

CHAPTER 7

COMBINED STEP-BY-STEP AND PREDICTOR-CORRECTOR

7.1 Introduction

Step-by-step and predictor-corrector have been studied in details in the previous chapters. Both methods proved efficient in rime ice conditions and the convergence of the algorithms was reached quickly. The step-by-step method showed a good agreement with experiments and compared favourably with standard ice prediction codes. In all cases previously investigated in this thesis with the step-by-step approach, the fastest algorithm was based on the ice height criterion. The ice shape calculated with a predictor-corrector algorithm was less reliable as it was more strongly dependent on the quality of the flow solution. A combined procedure between the step-by-step and the predictor-corrector will allow for an update of the predictor during the total exposure time to icing and will reduce the risk of inaccuracy inherent to a poor flow solution around the iced geometry. This approach has nevertheless a cost as it requires around twice as more flow solutions than in a step-by-step algorithm. However, combining the ice based step-by-step algorithm and the predictor-corrector approach should improve the accuracy of the results considerably, particularly in glaze ice conditions.

A complete description of the combined algorithm may be find in Appendix G. However, the main stages of the algorithm are described as follows:

1. Flow solution determined around the clean geometry and flow-related parameters calculated.
   => predictor 1 values.

2. Icing model run for the first multi-time step period.
   => predicted ice shape 1.

3. Flow recalculated around the iced geometry and flow-related parameters re-evaluated
   => corrector 1 values.
4. Icing model run again for the same multi-time step period using an interpolation between the predictor 1 and the corrector 1.
   => interpolated 1 values.
   => corrected ice shape 1.
5. Flow recalculated around the first corrected ice shape and flow-related parameters re-evaluated
   => predictor 2 values.
6. Icing model run for the second multi-time step period.
   => predicted ice shape 2.
7. Flow recalculated around the second predicted ice shape and flow-related parameters re-evaluated
   => corrector 2 values.
8. Icing model run again for the second multi-time step period using an interpolation between the predictor 2 and the corrector 2.
   => interpolated 2 values.
   => corrected ice shape 2.
9. Stages 5 to 8 repeated for new increments of predictor and corrector as many times as required until the final ice accretion time is reached.

The combined procedure will be first investigated in Section 7.2 on a cylinder geometry in rime and glaze ice conditions, while the study of the algorithm on a wing configuration will be the scope of Section 7.3. Simulated results will be compared to the previous methods described in Chapter 5 and Chapter 6 and when possible, compared to experimentally measured ice shapes.

7.2 Ice Prediction on Cylinders

7.2.1 Rime Ice Conditions

The cylinder case $O1$ is first studied in rime ice conditions. Icing and atmospheric conditions remain the same and are those defined in Table 5.1. The most suitable step-by-step algorithm was based on the ice criterion and the convergence was achieved for a maximun ice height allowed per step of 4% of the diameter length c, for a number of required flow solution equal to three. The predictor-corrector algorithm has been studied thoroughly in Chapter 6 and the standard procedure has been established as the recommended method for icing studies in rime ice conditions. This combination has therefore been used in the combined algorithm. Six flow solutions were required for the present calculation, three for the step-by-step part of the algorithm and another three for the predictor-corrector part. Figure 7.1 shows the final simulated ice shapes obtained with the combined methodology. A closer view of the top and bottom part of the cylinder is shown in Figure 7.2. As expected, the simulated ice shape determined with the combined procedure is in agreement with the step-by-step and the predictor-corrector results. A slightly lower ice height is estimated with the combined algorithm on the top and bottom part of the ice layer while all results are identical in the nose region. However, these small variations do not modify the ice shape significantly in rime ice conditions.

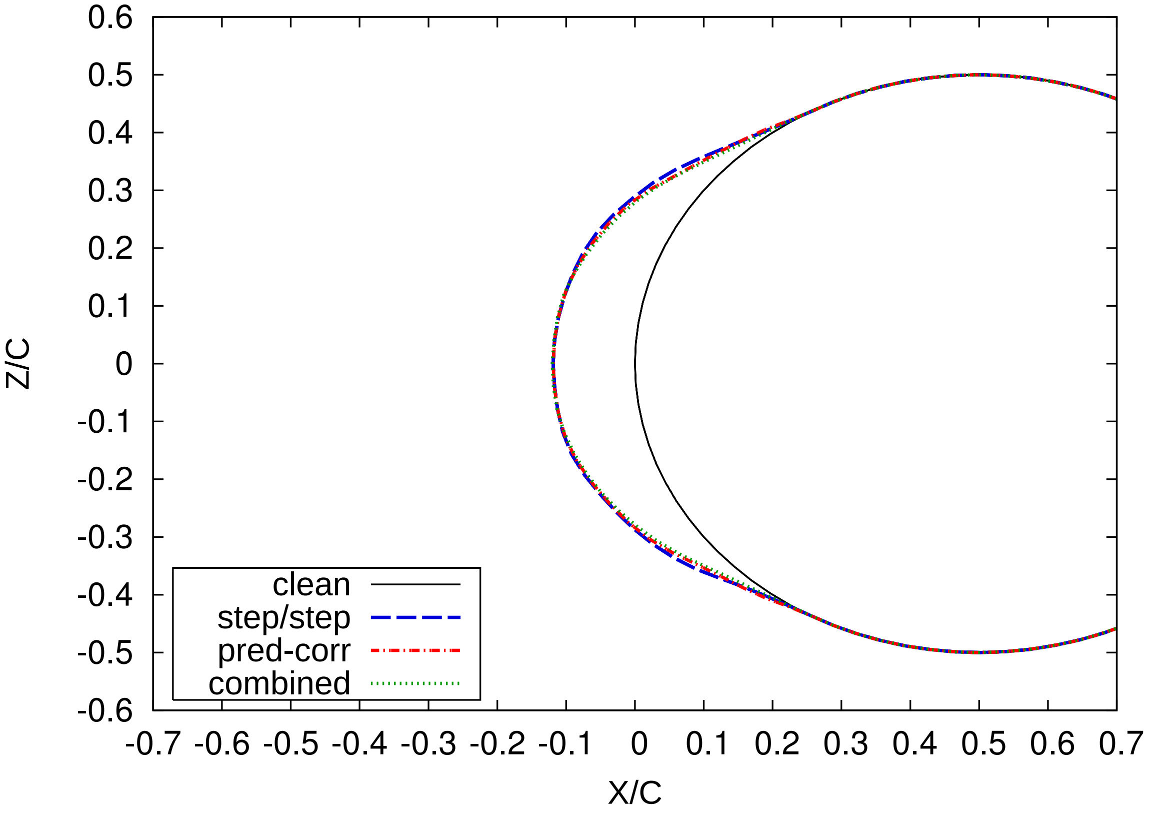

Figure 7.1: *Simulated rime ice on the cylinder using the combination step/step-predictor/corrector. Comparison with step-by-step and predictor-corrector results. Exposure time: 5min 30s.* $T_\infty = -26^oC$.

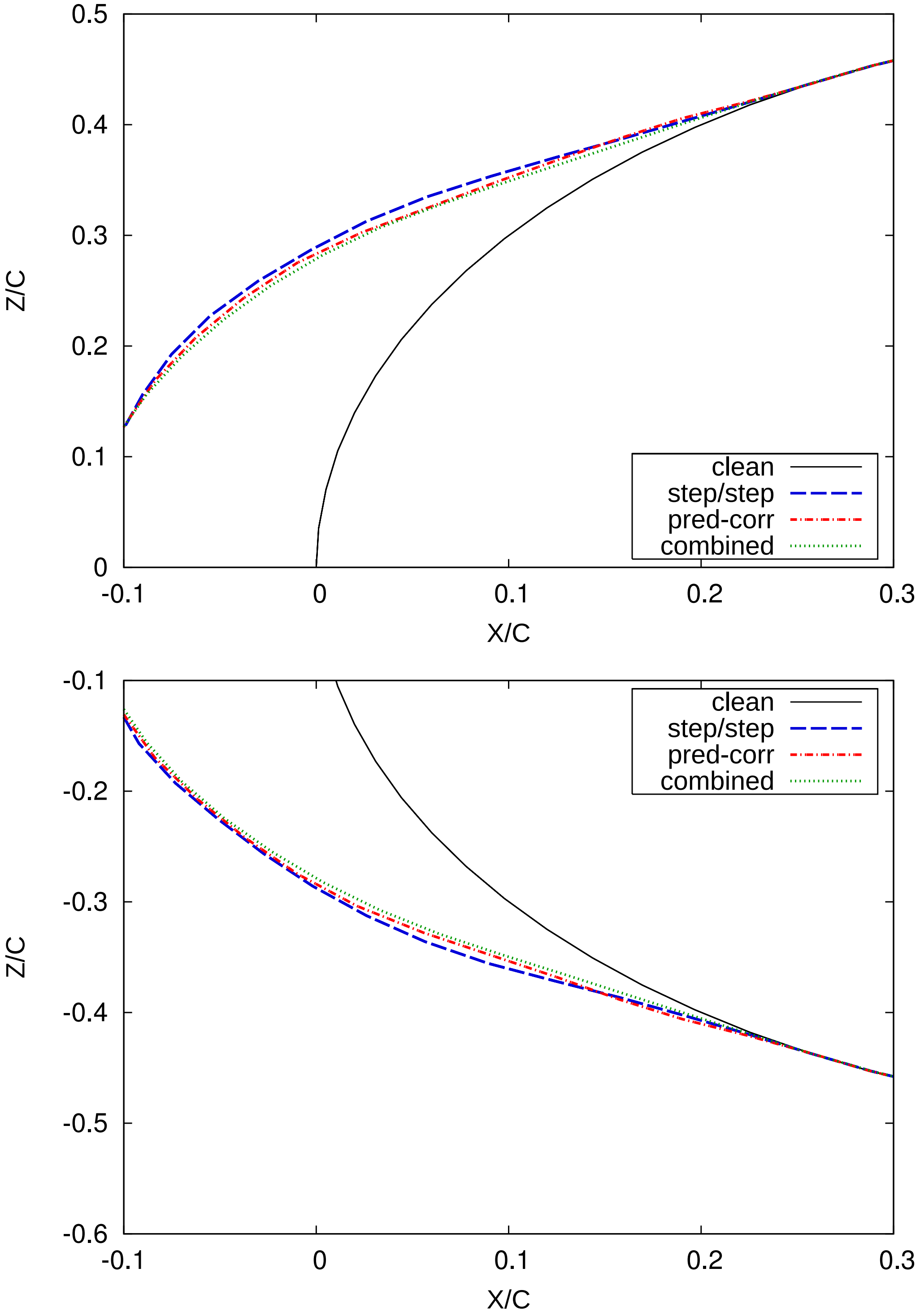

Figure 7.2: *Simulated rime ice on the cylinder using the combination step/step-predictor/corrector. Comparison with step-by-step and predictor-corrector results. Exposure time: 330s.* $T_\infty = -26^o C$.

There is therefore no real benefit in using a combined procedure on a cylinder in rime ice conditions. This adds considerable computing time compared to the fastest method: the standard predictor-corrector. It should nevertheless be noted that the combined result obtained here is closer to the second corrected ice shape determined with the predictor-corrector, as may be seen in Figure 7.3. The only small differences in both ice shapes appear at the ice layer boundaries in the upper and lower regions of the cylinder. As explained in the previous chapter, the standard predictor-corrector is suitable in rime ice studies, but it may be a safer solution to perform one more update of the corrector to insure the accuracy of the results. The most accurate and faster multi-step method is therefore a predictor-corrector approach based on two updates of the corrector. In this case, three flow calculations are necessary.

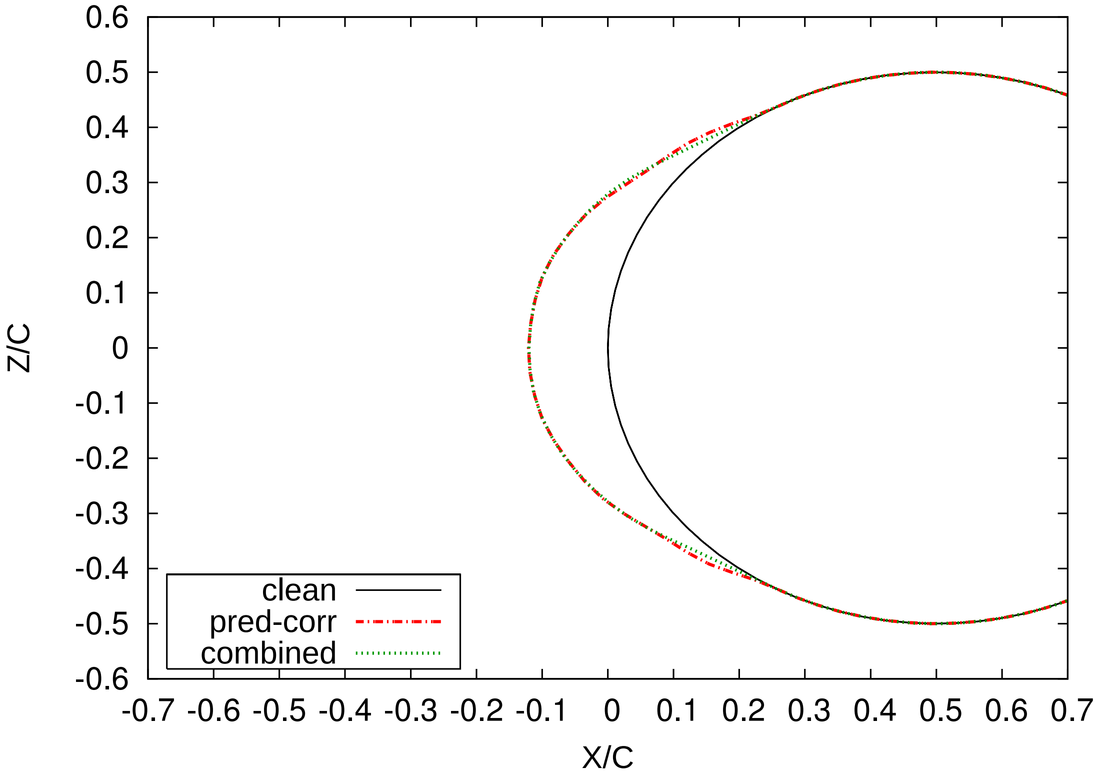

Figure 7.3: *Comparison of simulated ice shapes on a cylinder in rime ice conditions. Combined procedure result and second corrected ice shape from the predictor-corrector algorithm. Exposure time: 5min 30s.* $T_\infty = -26^oC$.

The time-step durations for the combined procedure and for the step-by-step algorithm are summarized in Table 7.1. The first time-duration is identical since the first update of the flow solution occurs when the ice height criterion is satisfied.

The following step durations are also almost identical for both algorithms, the ice growth being proportional to the accretion time.

	combined	**step-by-step**
step	$\mathbf{t_{step}}$ [s]	$\mathbf{t_{step}}$ [s]
1	113.3	113.3
2	109	109.8
3	107.7	106.9

Table 7.1: *Time-step duration for the combined and the step-by-step procedures.*

Results previously obtained were more disparate and subject to discussion in glaze ice conditions. Simulated ice shapes generated with the combined algorithm will now be investigated for the impingement of small and large droplets in glaze ice conditions.

7.2.2 Glaze Ice Conditions

The step-by-step solution was best for the ice height criterion $b_{max} = 4\%c$, as detailed in Chapter 5 and the convergence of the predictor-corrector has been established for the standard procedure, see Chapter 6. These two criteria are combined in the new algorithm. A total number of eight flow calculations was necessary to complete the whole simulation: four required for the step-by-step part and an extra four for the predictor-corrector part of the algorithm. Simulated ice shapes obtained for the impingement of small droplets are first discussed.

Impingement of Small Droplets

Figure 7.4 shows the ice shapes simulated when small droplets impinge on a cylinder in glaze ice conditions. As may be seen more precisely in Figure 7.5, the ice shape generated with the combined algorithm is much more accurate than the one obtained with the standard predictor-corrector approach. The stagnation region between the extremities of the lower and upper horns is similar with all algorithms. The ice layer from the combined method agrees better with experiments in the lower region while results seem more accurate with the step-by-step in the upper region. However, the

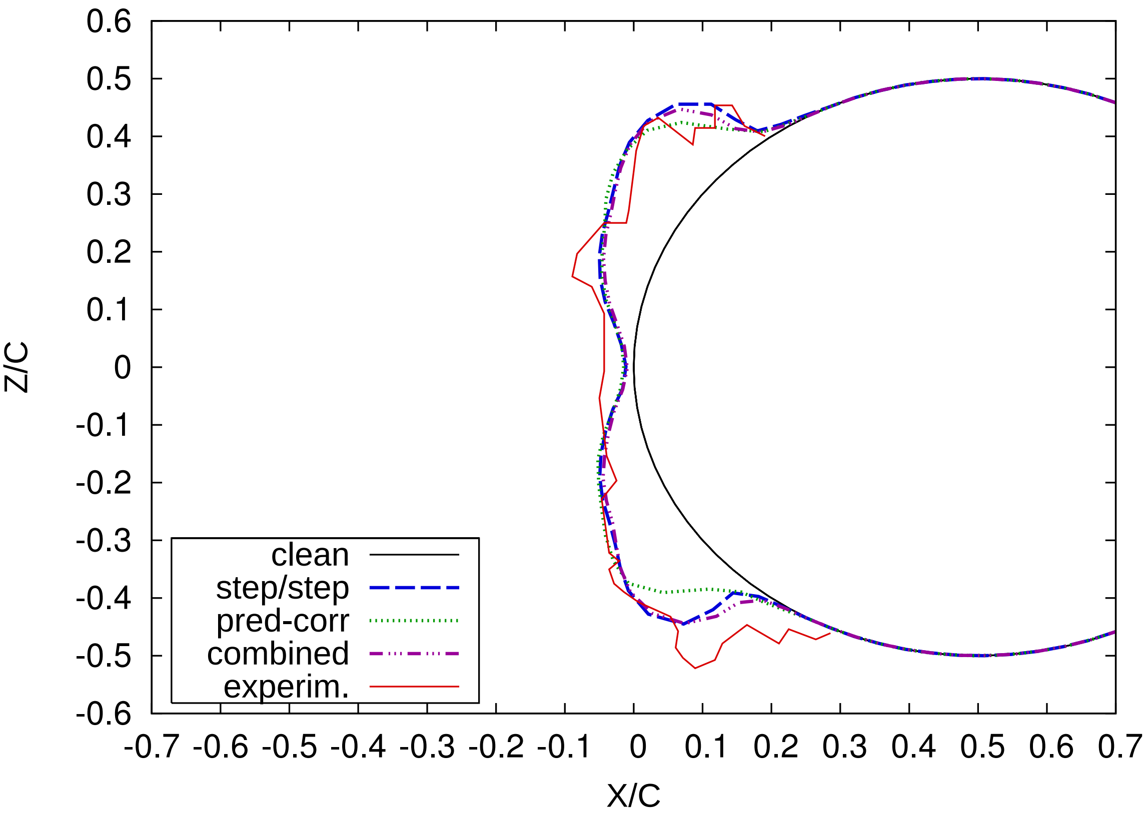

Figure 7.4: Simulated glaze ice on the cylinder using the combination step-by-step and predictor-corrector for the impingement of small droplets. Comparison with step-by-step and predictor-corrector results. Exposure time: 5min 30s. $T_\infty = -3^oC$.

latter method also over-estimates slightly the upper horn. This makes the combined procedure the best ice estimator in these specific icing conditions on a cylinder geometry. Nevertheless, the number of flow calculations is rather prohibitive for such a small difference. It makes such a computation a tedious task to perform without a real benefit on the final ice estimation.

The time duration in each step is summarized in Table 7.2 for the combined and the step-by-step procedures. Once again, the first update of the flow solution occurs at the same time as the ice-height criterion operates in the first step for both methods. The other time-step durations are different for both methods since the interpolation predictor-corrector modifies the form of the accreted ice shape. However, these differences in time-step durations between both algorithm are relatively small. This means that the interpolated ice shape does not modify the ice shape of the predictor significantly and explains that the final estimated ice shapes are very close.

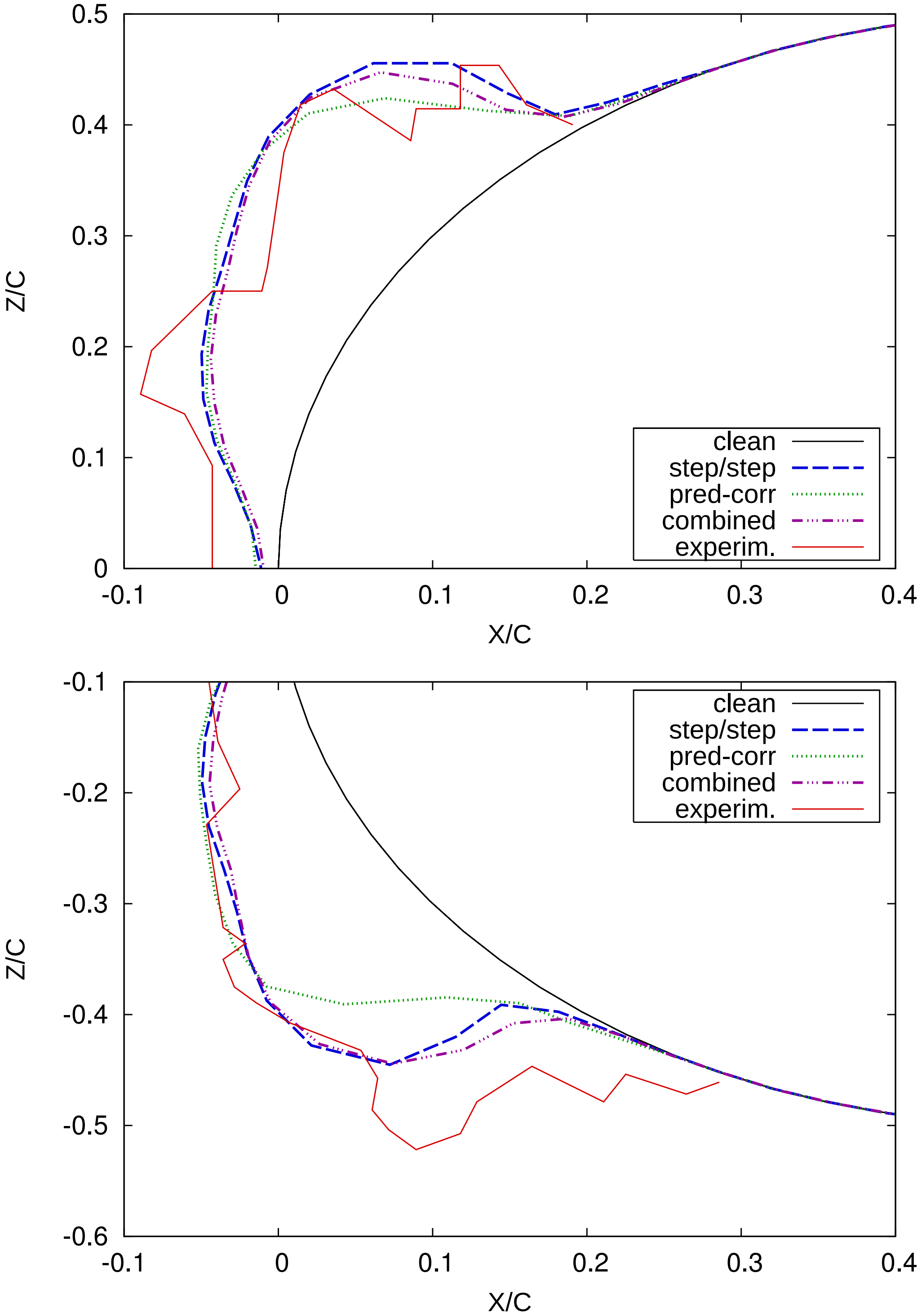

Figure 7.5: *Simulated glaze ice on the cylinder using the combination step-by-step and predictor-corrector for the impingement of small droplets. Comparison with step-by-step and predictor-corrector results. Exposure time: 5min 30s.* $T_\infty = -3^oC$.

	combined	**step-by-step**
step	$\mathbf{t_{step}}$ [s]	$\mathbf{t_{step}}$ [s]
1	91.91	91.91
2	87.54	87.42
3	85.51	85.45
4	65.04	65.22

Table 7.2: *Time-step duration for the combined and step-by-step procedures.*

The same sort of study will now be performed for the impingement of large droplets, on the same geometry.

Impingement of Large Droplets

As in the previous case, eight flow solutions have been necessary to generate the ice shape with the combined procedure. The ice height criterion was $b_{max} = 4\%$ of the diameter length for the step-by-step part. The standard predictor-corrector procedure was combined with the step-by-step algorithm. The final simulated ice shape is plotted with the results from the other multi-step methods and with experiments, as may be seen in Figure 7.6. Despite being more accurate than the predictor-corrector result, the ice shape obtained with the combined algorithm did not show a significant improvement of accuracy. Results are equivalent to those obtained with a step-by-step approach. This algorithm is therefore not recommended for the impingement of large droplets, the overall simulation time being increased without any other benefits on the ice estimation.

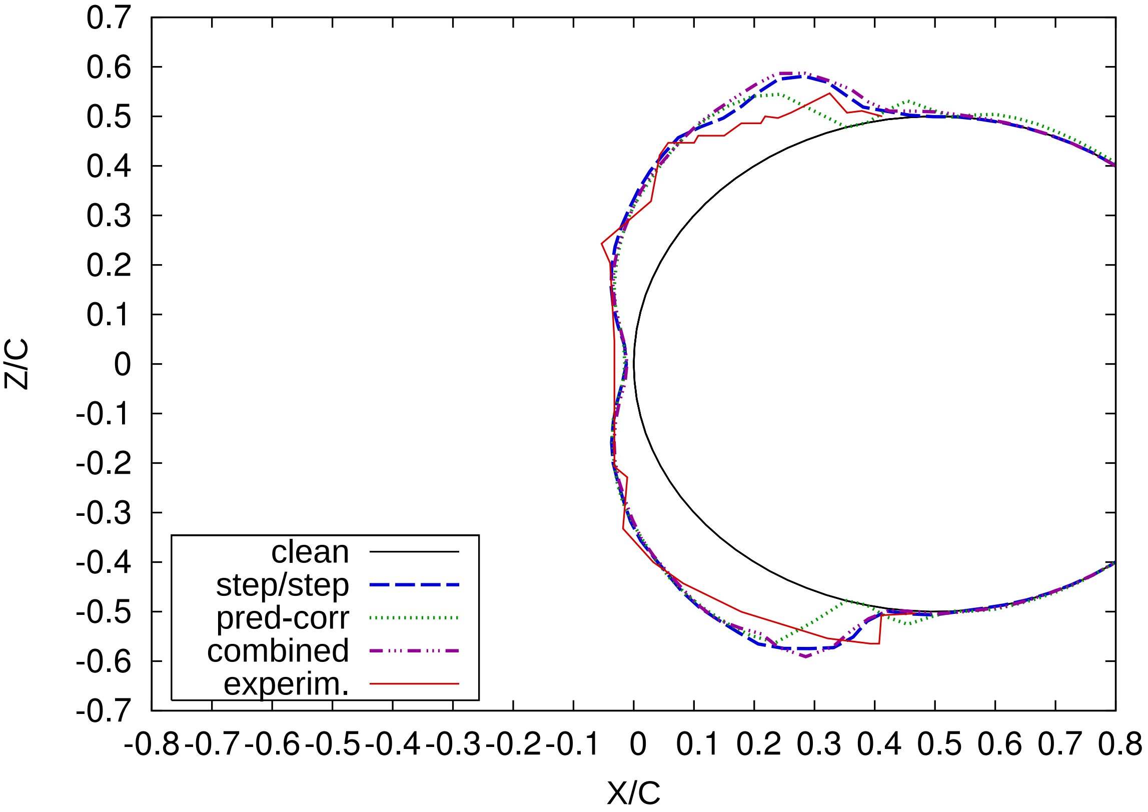

Figure 7.6: *Simulated glaze ice on the cylinder using the combination step-by-step and predictor-corrector for the impingement of large droplets. Comparison with step-by-step and predictor-corrector results. Exposure time: 5min 30s.* $T_\infty = -3^oC$.

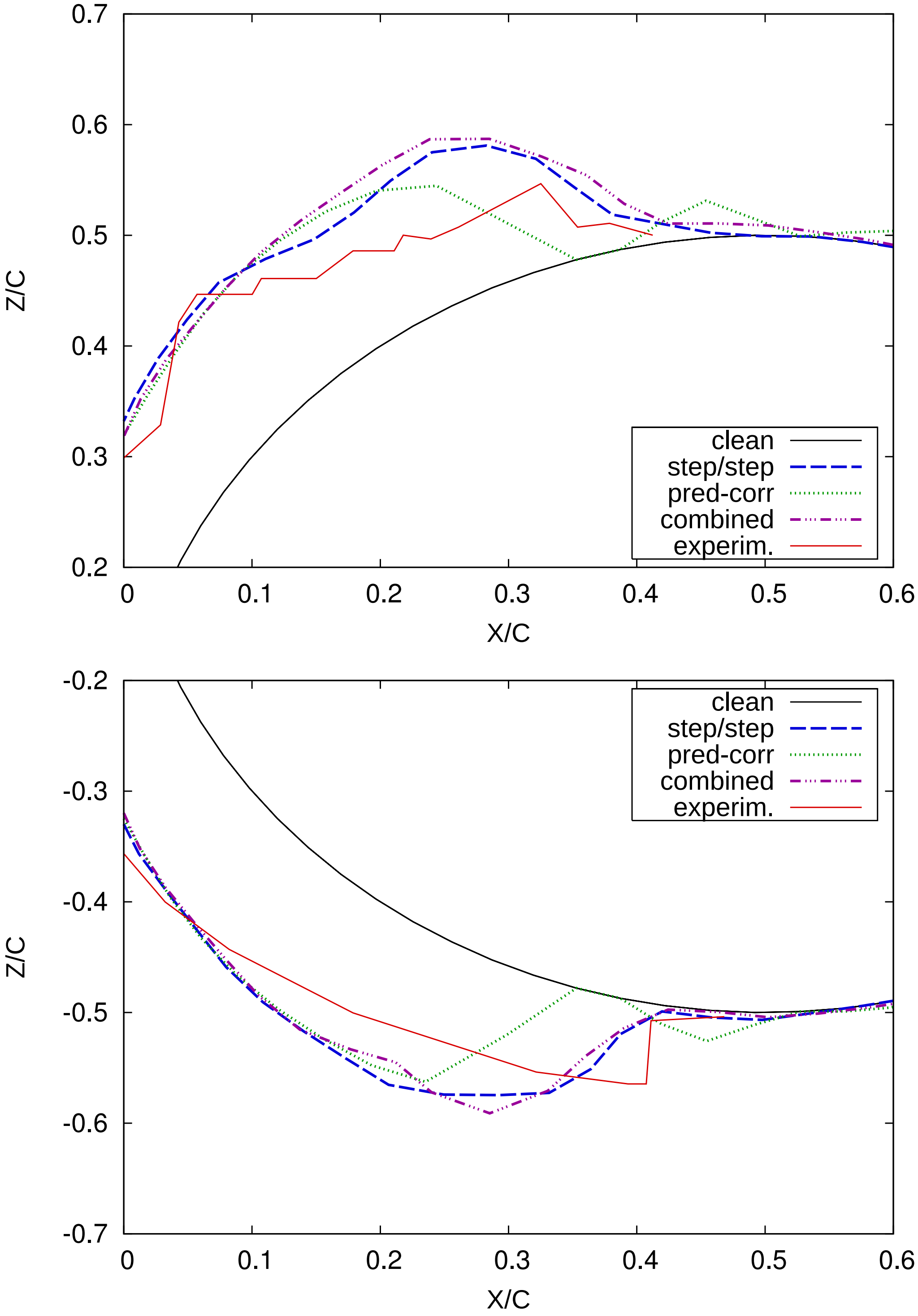

Figure 7.7: *Simulated glaze ice on the cylinder using the combination step-by-step and predictor-corrector for the impingement of large droplets. Comparison with step-by-step and predictor-corrector results. Exposure time: 5min 30s.* $T_\infty = -3^oC$.

7.2.3 Summary

The combined step-by-step and predictor-corrector algorithm did not improve the estimated ice shape significantly on a cylinder geometry in rime ice conditions. The accuracy was slightly better using this algorithm in glaze ice conditions for the impingement of small droplets. However, due to the significant increase of the computing time without a neat benefit on the accuracy, the combined algorithm does not appear as the best methodology on a small geometry. A similar study will now be realised on a wing in rime and glaze ice conditions. The objective of the next section will be to determine whether or not the combined algorithm is more adapted and efficient for ice predictions on larger bodies.

7.3 Ice Prediction on Airfoils

The study of the combined algorithm is now extended to a wing under rime and glaze ice conditions. The icing and atmospheric conditions for all simulations remain those previously applied to the NACA0012 wing geometry and specified in Table 5.6. Simulated results will be discussed for rime ice conditions in Section 7.3.1 and for glaze ice conditions in Section 7.3.2.

7.3.1 Rime Ice Conditions

The ice accretion on the NACA0012 wing is studied for rime ice conditions at the temperature $T_\infty = -26^oC$. As for the cylinder case study, the best ice estimator determined in Chapter 5 was the ice criterion. For rime ice studies on a wing, the maximum ice height allowed in each step was equal to $b_{max} = 0.8\%$ of the chord length, which required five flow calculations. The standard predictor-corrector was also established as a suitable procedure for rime ice simulations on a wing surface. As a reminder, in this case, two flow solutions are required. These two algorithms are therefore combined and the final estimated ice height is presented in Figure 7.8, along with the other two multi-step results and the experimentally measured ice shape. The combined algorithm required ten flow solutions in total to generate the final ice estimation on the wing.

As may be noticed in Figure 7.8, no significant improvement is obtained with the combined procedure in rime ice conditions. This is in agreement with the previous study on the cylinder in rime ice conditions. The final predicted ice shape is almost identical to the one generated with the step-by-step procedure. The best ice estimator in these conditions is therefore the standard predictor-corrector as determined in the previous chapter, which has the great advantage of reducing the number of flow calculations and therefore reduce the overall computing time significantly.

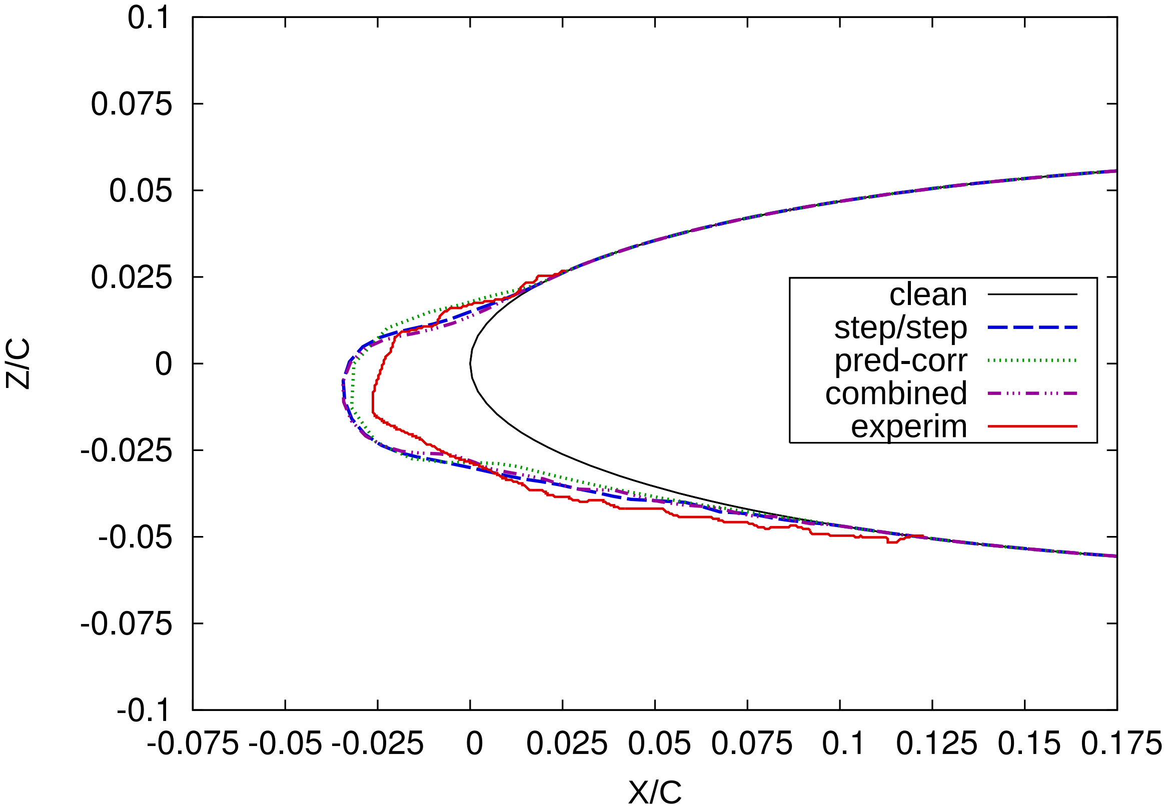

Figure 7.8: *Simulated rime ice on a wing using the combination step-by-step and predictor-corrector. Comparison with step-by-step and predictor-corrector results. Exposure time: 6 min.* $T_\infty = -26^oC$.

The accuracy of the ice shape prediction on the wing geometry studied in this thesis in glaze ice conditions appeared very difficult to obtain due to a large surface deformation and a long icing exposure. This has been discussed in details in the previous chapters. The combined algorithm will now be applied to this geometry in glaze ice conditions.

7.3.2 Glaze Ice Conditions

The convergence of the predictor-corrector algorithm was obtained in five steps in Chapter 6 on the wing geometry in glaze ice conditions. The combined algorithm intends to reduce the influence of the potential poor flow solution around the iced body. In these conditions, the standard predictor-corrector which requires two flow solutions, combined with the step-by-step procedure, should be sufficient to guarantee the accuracy of the estimated ice shape. This methodology seems a sensible approach as too many corrections of the ice shape would make the combined algorithm very difficult to apply and unacceptable, the computing time being an issue.

Simulated results are represented on Figure 7.9. The step-by-step part is based on the ice height criterion for the maximum ice height allowed per step $b_{max} = 0.6\%$c, see Chapter 5. In these conditions, ten flow solutions were required. In the current simulation performed with the combined procedure, a total number of 18 flow solutions and flow-related parameters calculations were necessary to generate the final ice shape shown in Figure 7.9.

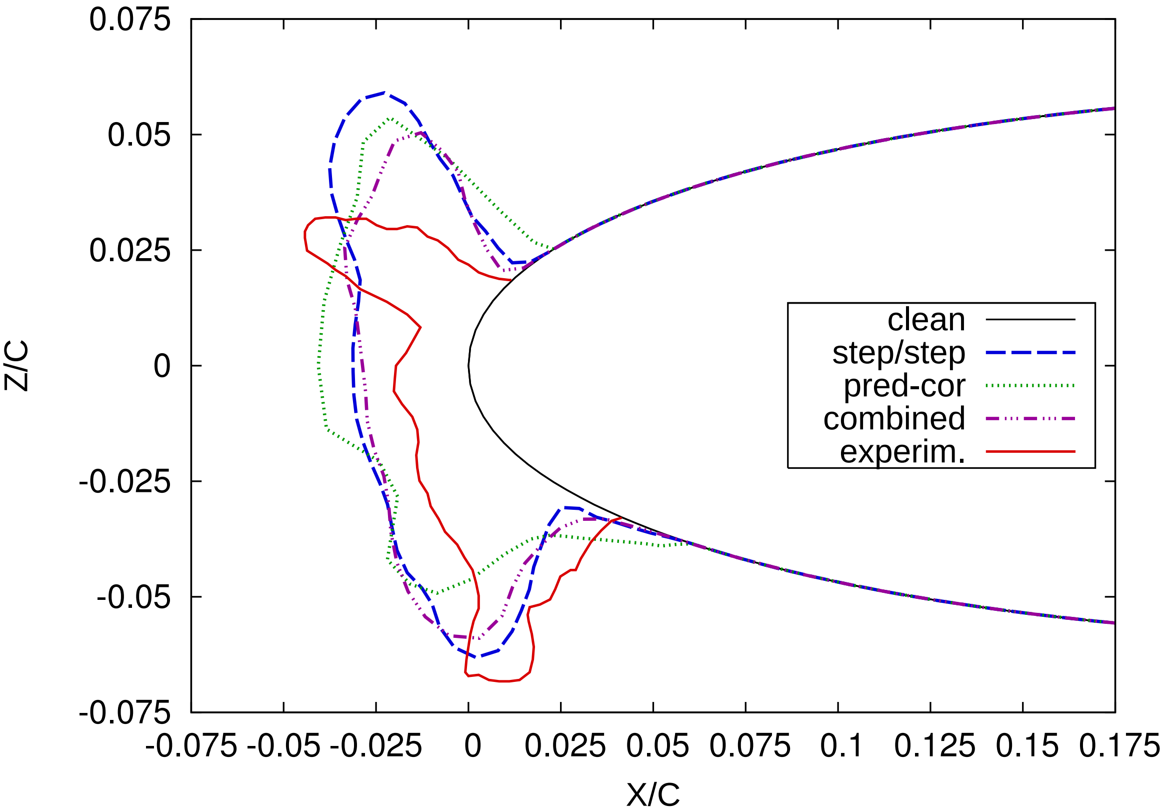

Figure 7.9: *Simulated glaze ice shape on a wing using the combination step-by-step and predictor-corrector. Comparison with step-by-step and predictor-corrector results. Exposure time: 20 min.* $T_\infty = -7^oC$.

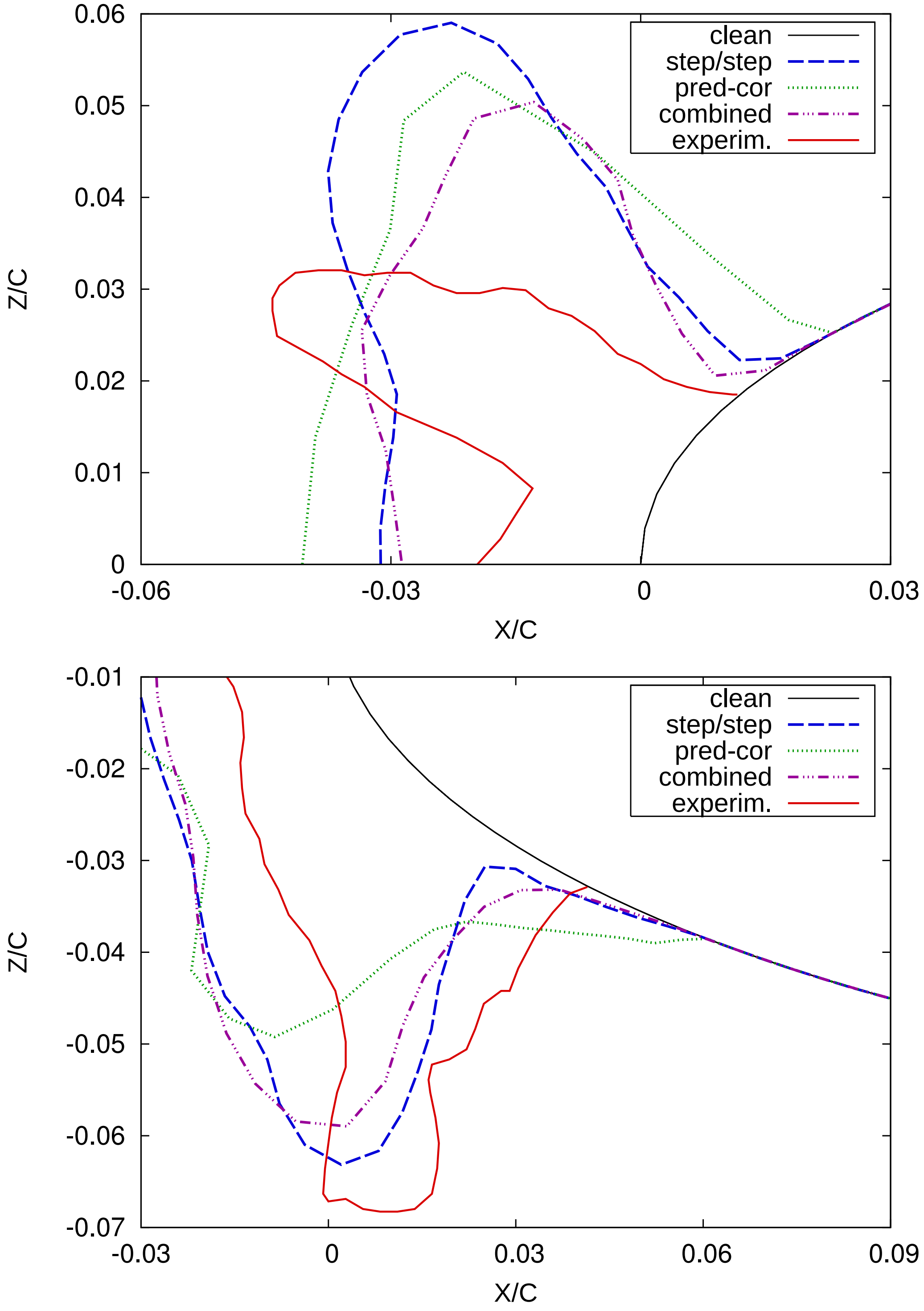

Figure 7.10: *closer view: simulated rime ice shape on a wing using the combination step-by-step and predictor-corrector. Comparison with step-by-step and predictor-corrector results. Exposure time: 20 min.* $T_\infty = -7^oC$.

As may be seen more precisely in Figure 7.10, the simulated ice shapes obtained with the combined algorithm compares fairly well to experiments and shows clearly the advantages of this procedure over the predictor-corrector method and also over the step-by-step procedure:

- the upper horn height matches experiments better than both the step-by-step and the predictor-corrector,
- the stagnation region is also determined slightly more accurately with the new algorithm, the ice height being lower than for the step-by-step and for the predictor-corrector methods,
- the lower horn region is estimated better than with the predictor-corrector algorithm. Despite not being as good as the step-by-step in height, the simulated lower horn fairly agrees with experiments and the extremity of the ice layer is closer to the experimentally measured ice shape in the lower region.

	combined	**step-by-step**
step	t_{step} [s]	t_{step} [s]
1	149.20	149.20
2	145.66	132.12
3	139.16	123.50
4	128.68	128.04
5	128.73	120.43
6	127.11	119.19
7	135.57	119.50
8	129.53	118.56
9	116.30	121.44
10		68.02

Table 7.3: *Time-step duration for the combined and step-by-step procedures.*

These results are in agreement with the study performed on the cylinder in glaze ice conditions. The ice shape simulated on a cylinder subject to the impingement of small droplets appeared slightly more accurate when generated with the combined algorithm than with the step-by-step procedure.

To further analyse this result, the time duration for each step of this procedure has been listed in Table 7.3, along with those from the step-by-step calculation. The number of steps is lower when using the combined algorithm. As already mentioned, when using the predictor-corrector algorithm, the ice shape becomes thinner. A similar effect occurs during each step of the combined algorithm. The update criterion is reached later during the simulation and this reduces slightly the number of flow recalculations necessary.

7.3.3 Summary

The combined step-by-step and predictor-corrector algorithm does not improve the estimated ice shape significantly on the wing geometry in rime ice conditions. The standard predictor-corrector should be favoured in this situation. However, in glaze ice conditions, the combined algorithm improves slightly the accuracy of the simulations. The combined algorithm generally leads to long computing times but this algorithm is the best estimator on a wing geometry in glaze ice conditions.

7.4 Conclusion

The combined step-by-step and predictor-corrector algorithm has been studied in this chapter.

- The algorithm did not improve the accuracy of the ice predictions in rime ice conditions either on the cylinder or on the wing geometry: the other multi-stepping methods previously studied in this thesis were sufficient, faster and should be favoured.
- The algorithm is more efficient in glaze ice conditions. A slight increase of accuracy appeared on the cylinder. The efficiency of this method appeared more clearly on a large geometry such as a wing and for a long exposure time to icing.

The combined procedure is nevertheless rather time consuming. This methodology should therefore only be used to improve the accuracy of the ice predictions in glaze ice conditions.

CHAPTER 8

CONCLUSION AND RECOMMENDATIONS

8.1 Conclusion

In the course of this thesis, fully automated multi-step procedures applied to aircraft ice predictions have been investigated. A multi-step approach aims to estimate the evolution in time of flow related parameters encountered in icing studies. This research work forms the first attempt to generate such an automated process with the temperature history preserved from one step to the next and a full update of the ice and water heights in a Stefan-based ice prediction code. The main objectives were:

- To develop and study algorithms that further enhance the accuracy of the current ice predictions, usually based on a single-step procedure,
- To define the number of times the flow field needs to be recomputed to insure the accuracy of the ice predictions without increasing the overall computing time prohibitively.
- To generate accurate ice shapes without any sort of external interaction.

A review of the standard icing models has been carried out in Chapter 2 and their limitations have been pointed out. The multi-step procedure has first been developed to account for the lack of time dependence of the Messinger model, which is the base of most of the current ice prediction codes. In the present study, the effects of a multi-step approach have been studied for a more realistic time dependent model based on a Stefan condition at the interface between the ice and the water layers. Several flow related parameters strongly influence the ice accretion and require a periodical update during a multi-stepping calculation. These parameters have been identified as being the collection efficiency, the shear stress and the heat transfer coefficient.

A flow field is required to calculate the icing parameters. The Computational Fluid Dynamic code settings have been discussed in detail in Chapter 3. The commercial mesh generator GAMBIT and the flow solver FLUENT constitute an appropriate solution for the development of an automated multi-step procedure as they include a capability to perform automated tasks. Specific boundary conditions and models applied to aerodynamic applications have been rigorously selected, they are nevertheless easily modifiable for future applications.

When the flow related parameters are evaluated, the ice accretion and the water film can be calculated. Two algorithms may be used for a multi-step ice prediction: the step-by-step and the predictor-corrector.

- The step-by-step allows for a regular update of the flow related parameters during the ice accretion. A step-by-step procedure requires several flow calculations to guarantee the accuracy of the predicted ice shapes.
- The predictor-corrector allows for the update of the flow-related parameters in “real time” and is based on an interpolation between the values of parameter determined on the clean geometry and those calculated on the ice covered body. Only two flow solutions are necessary in a predictor-corrector algorithm.

A basic step-by-step procedure has been studied in Chapter 4 for typical flight scenarios in icing conditions and results have been compared to experimentally measured ice shapes. This algorithm did not account for the update of the water film and the thermal history was not preserved from one multi-time step to the next. Despite these limitations, the step-by-step approach has proved to enhance the accuracy of the predictions significantly compared to the standard one-step procedure due to the periodical update of the flow related parameters.

Based on the initial step-by-step implementation in the ice prediction code ICECREMO1, a more advanced algorithm that allows for the update of the ice, water and surface temperature, has been developed and explained in detail in Chapter 5. This approach has been successfully implemented and tested in a more recent icing code: ICECREMO2. Two different ice triggering criteria have been investigated. The first one is based on time and is usually present in standard ice prediction codes. It consists in the systematic update of the flow solution at defined periods of the ice accretion time. In this case, the time-step is constant and the number of multi-time steps is specified at the beginning of the simulation. The second one is more physically realistic and is based on the evolution of the ice layer. The flow solution is systematically re-computed at appropriate times of the computation, when a specified ice height increment is reached. In this case, the time-step varies and the flow field is re-computed only when necessary.

The main objective of the step-by-step algorithm study was to determine which criterion predicts the highest accuracy with a reduced number of flow calculations. For each criterion based method, the convergence of the algorithm has been studied and a suitable value of criterion has been established. Predicted ice shapes did not show significant differences with either algorithm. In each case, the simulated results compared well with experiments and compared favourably with standard ice accretion codes. However, the number of necessary updates being lower than for the time-based criterion, the ice height criterion is the favoured flow triggering criterion due to significant gains of time:

- Around 50% on a cylinder in rime ice conditions, 33% and 43% in glaze ice conditions for the impingement of small and large supercooled droplets.
- Around 28% on the wing geometry in rime ice conditions and 17% in glaze ice conditions.

In the different test cases investigated in this thesis, the best ice height ice estimator was obtained for a maximum ice height allowed in each step of:

- 4% of the diameter length for the cylinder case in rime conditions which required three updates of the flow solution and four updates in glaze ice conditions.
- 0.8% of the chord length for the wing case which required five updates in rime ice conditions.
- 0.6% of the chord length for the wing case where ten updates were necessary in glaze ice conditions.

The influence of the water update on the final simulated ice shape has also been demonstated in this thesis. The water film modifies the predicted ice shape, mainly at temperatures close to freezing.

In order to reduce the computing time and potentially increase the accuracy of the ice predictions, a predictor-corrector algorithm has been studied, as detailed in Chapter 6. This approach is based on a linear interpolation between the values of icing parameters determined on the clean geometry and those calculated on the final ice covered body. The convergence of the algorithm has been studied on various geometries in rime and glaze ice conditions and the results have been compared with the step-by-step approach. No significant difference with the step-by-step results were noticeable in rime ice conditions: the standard predictor-corrector is therefore recommended for time saving reasons since it requires two flow calculations only. In glaze ice conditions, the simulated ice shapes agreed with experiments better with the step-by-step algorithm than with the predictor-corrector approach. In the latter case, interpolation errors are piling-up, they are unavoidable when dealing with a set of complex icing parameters.

The flow solution affects strongly the results of the predictor-corrector and this can jeopardize the simulation if the flow field is not of good quality. To limit the effects of a potential inaccuracy of this flow solution, a procedure based on a combination between the predictor-corrector and the step-by-step algorithms has been developed and discussed in Chapter 7. To date, such a combination had never been studied for ice shape predictions. This procedure has the features and advantages of both the step-by-step and the predictor-corrector: the flow related parameters are re-evaluated periodically during the simulation and these parameters vary in time with the ice accretion. The predictor-corrector coupled with a step-by-step algorithm based on the ice criterion allows for the update of the flow solution at adequate periods of the ice accretion. If the flow solution is not of good quality, its influence will therefore be limited in time. This approach has nevertheless a cost as it increases the number of required flow solutions significantly. The final estimated ice shape did not show any significant accuracy improvement which could justify the increased number of flow computations in rime ice conditions. A faster method such as the standard predictor-corrector should therefore be preferred. However, the combined algorithm was more efficient in glaze ice conditions where ice predictions showed a better agreement with experiments and an overall accuracy improvement.

8.2 Recommendations for Future Work

The different multi-step algorithms studied in this thesis improve icing calculations significantly. However, several aspects could be further investigated:

- The entire multi-stepping process can be very long. The time for gridding and flow calculation may probably be greatly reduced by appropriate modifications within the Computational Fluid Dynamic code. The use of moving boundaries would prevent from general re-gridding. The flow calculation would then be started from the previous converged solution and the results could be achieved quickly.

- Significant accuracy improvement of the ice prediction can be attained if an automated adaptation procedure is used in the icing solver. This approach would allow for a better definition of the ice and water heights [129] by refining/de-refining the mesh when necessary. Coupled with a multi-stepping procedure, this would magnify the precision of the final ice and water predictions. This solution is currently being investigated and will be the object of a future publication.

- The predictor-corrector approach is based on a linear interpolation between the values of predictor and corrector. This interpolation is currently based on time. An alternative solution could be to use the ice height instead. There is no guarantee of improvement, but it could be tested thoroughly.
- The icing model implemented in ICECREMO2 showed limitations for ice shapes predictions in glaze ice conditions, the temperature on the surface remaining constant throughout the whole computation for predictor-corrector computations and constant in each multi-time step for step-by-step simulations. A more sensible approach would be to include a thermal study of the substrate over which the ice is growing. Such an approach should reduce the problems observed near the leading edge.
- The release of the droplets too close of the ice covered surface may lead to an over estimation of the collection efficiency. There is no simple solution for this problem. If the droplets are released too far away from the surface, the mesh will be very coarse at the start of the droplet trajectories and accuracy will be lost. Forcing a fine mesh in the entire domain would increase computational time very significantly. An alternative would be to adapt the initial velocity of the droplets when they are released, but estimating the collection efficiency would then become extremely difficult. A more systematic study should be performed.
- For each case investigated in this research work, one size of supercooled droplet has been used: 20μm or 100μm on cylinders and 20μm or 25μm on wing configurations. The use of a droplet spectrum rather than a mono droplet diameter would have an influence on the collection efficiency and therefore on the final ice shape predictions. In addition, droplets splash when they impinge on the surface. This effect which is particularly important for large droplets has not been taken into account in this work. Splash effects along with the use of a droplet spectrum could be included in multi-stepping simulations.
- Finally, further tests are recommended on a wider database to check the robustness of the multi-step algorithms developed and studied in this thesis. Different icing conditions and different wing geometries should be studied thoroughly. Such testing could be based on the LEWICE validation work described in Reference [119] for simulations performed on cylinder and airfoil configurations.

APPENDIX A

THE ICECREMO PROJECT

A.1 Introduction

Despite considerable work, icing codes are still unable to accurately predict an ice shape. ICECREMO is a three dimensional code aiming to improve the accuracy of ice simulations on various geometries over a wide range of environmental conditions. This project is born from the collaboration between several partners among the aeronautical community in the United Kingdom. The development of this computer code occurred in two phases named ICECREMO1 and ICECREMO2. This appendix describes their development.

A.2 Project Icecremo1

The work program ICECREMO1 [32] is a four-year collaborative project involving BAe Systems, DERA (formerly the Defence Research Agency, now QinetiQ), Rolls-Royce and Westland Helicopters. Cranfield University [130] acted as the main subcontractor and supplied consultancy and development on various numerical issues. This partly Department of Trade and Industry (DTI) funded project started in 1996 with the development of the icing model. This model, developed by Myers et al. [29, 48, 94] can predict both rime and glaze ice type accretions on two and three-dimensional bodies. For rime ice accretions, the predicted ice height is solely function of the incoming water mass flux. A mass balance is therefore sufficient to determine the ice growth ratio. However, when glaze ice accretes, the accretion is coupled with an analysis of the runback water movement. The water layer is considered as a thin film and is modeled using lubrication theory [35]. In this situation, the ice accretion rate is obtained using a Stefan phase change model [33] applied at the water/ice interface.

ICECREMO1, in its final release in 2000, was a single-step procedure written in FORTRAN77 and could only be run under a UNIX based computing system. The flow around the geometry was determined on the clean body along with the physical parameters required for ice calculation. These parameters, as stated in Chapter 2, are mainly the heat transfer coefficient, the shear-stress and the collection efficiency. Flow data and parameters remained constant during the simulation, regardless of the total icing exposure time.

Initially, ICECREMO1 could be run either in a graphic mode using the CFD package GRAFFITI developed by Rolls-Royce or in a non-graphic mode via input formatted files [32]. The CFD suite was, however, not widely distributed. Each company involved in the project had therefore to adapt its own CFD solver to be able to generate a flow solution, written for a structured mesh in a specific binary format.

The CFD solution, which includes the position, velocity components, pressure and temperature of the surrounding airflow needs to be produced and stored for each node of the grid. Droplet trajectories are calculated with a particle tracking routine that reads in the flow solution, leading to the evaluation of the collection efficiency and impingement limits [32]. Information about the size and starting position/velocity of the particles along with the number of droplets to inject in the domain are specified in the input file. ICECREMO1 has a capability to calculate the heat transfer coefficient and the shear stress using an internal process. Heat transfer coefficient and shear stress input files can also be specified and read-in directly from the working directory or being provided by the flow solver.

When the main physical parameters are determined, an icing exposure time is specified before running the icing model. The output file generated by ICECREMO contains information on the calculation, including the 3D clean body coordinates, ice and water heights, collection efficiency, heat transfer coefficient, shear stress, temperature, pressure and density. These data are specified for each node constituting the airfoil surface.

A.2.1 Code Limitations

Limitations in the code may be divided into three groups: new modelling capabilities, technical enhancements in the code and computer issues.

1. New capabilities were required by aircraft designers, such as a multi-stepping procedure to obtain a better accuracy of the predicted ice shape. Anti-icing and de-icing numerical tools were also necessary in order to model ice protection devices, most of the time installed in the structure of the aircraft.

2. Generating a CFD structured grid around an iced airfoil is rather difficult. Consequently, problems arise when calculating the ice accretion via a multi-step procedure. Such a limitation generates considerable difficulties when analyzing complex shapes such as a complete aircraft for which unstructured CFD methods are normally employed.

3. Managing droplet trajectories, calculating heat transfer coefficient or shear stress values may be a tedious and difficult task. If not performed with care, the evaluation of parameters may jeopardise the accuracy of the final result.

4. The ice prediction code was originally designed to operate solely on a UNIX based computing system. However, current manufacturers prefer a code that can be run under a free UNIX like operating system such as Linux.

5. The source code is written in FORTRAN77, which is less adaptable and versatile than an object-oriented language such as the C++.

To tackle these difficulties, a new project called ICECREMO2 started in February 2002.

A.3 Project Icecremo2

The work program ICECREMO2 is a partly funded DTI contract that involved an effective partnership of BAe Systems, Airbus UK, Rolls-Royce, Dunlop Aerospace, Westland Helicopters and QinetiQ. As during the ICECREMO1 project, Cranfield University was the main sub-contractor and supplied consultancy and development on various numerical issues. Figure A.1 depicts the three main modules that constitute the new version:

1. **CORNETTO** aims to determine the trajectories of the supercooled droplets and the resulting collection efficiency,

2. **RIPPLE** calculates the heat transfer coefficient on the surface and values for the shear stress,

3. **MAGNUM** evaluates the ice growth rate and the quantity of water that flows on the surface.

The capabilities of the structured version have been extended to include the modeling of multi-stepping [95, 96, 113], anti-icing and de-icing systems [131, 132, 133], error

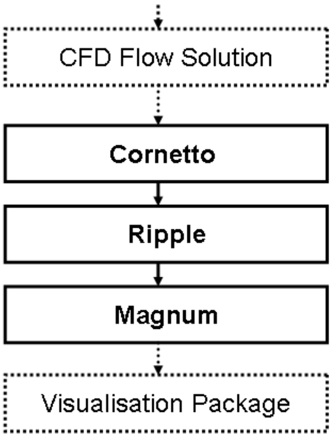

Figure A.1: *Modules constituting the ice prediction and water flow code ICECREMO2. "Cornetto" evaluates the droplet trajectories and the catch, "Ripple" calculates the heat transfer coefficient and shear stress and "Magnum" determines the ice and water heights.*

control and adaptivity [129, 134]. Most of the work for the implementation of these capabilities has been performed in the latter module.

ICECREMO2 is written in the object-oriented language C++, that allows the code to be more versatile and adaptable to future developments. This new version can be executed on a Linux operating system and works with both structured and unstructured grids. The flow solution can be generated by several compatible CFD packages, including the industry standard FLUENT suite.

The particle tracking routine has been considerably improved, particularly with the development of a new particle start location refinement routine. The icing model implemented in ICECREMO1 has also been adapted to ICECREMO2. This three-dimensional water film/freezing model operates on an unstructured surface mesh with a discretisation of quads and/or triangles.

Multi-stepping calculations are necessary to evaluate large ice accretion with accuracy. Such procedures require the use of intermediate flow calculations during the ice growth simulation. The use of unstructured grids allow to describe more easily the geometry patterns that occur during long ice simulations. The updated CFD flow solution around the iced surface is obtained in an iterative loop with icing calculations, without any user interaction [95, 96, 113].

Finally, results are written in a variety of formats for visualization including commercial packages such as TECPLOT and FIELDVIEW.

Appendix B

Convergence study - Rime ice shape on a cylinder - Case O1

The convergence of the step by step method on the cylinder $O1$ in rime ice conditions was studied in Section 5.3. This study showed that convergence was achieved for 6 steps when using the time criterion and a height of 2.54mm per step (corresponding to a chord length of 4%) for the height criterion. In Section 5.3, only the curves corresponding to the relevant number of multi-time steps were considered. More results were calculated to confirm this conclusion. They are presented in this appendix for the time criterion first and then for the ice criterion.

- **Time Criterion**

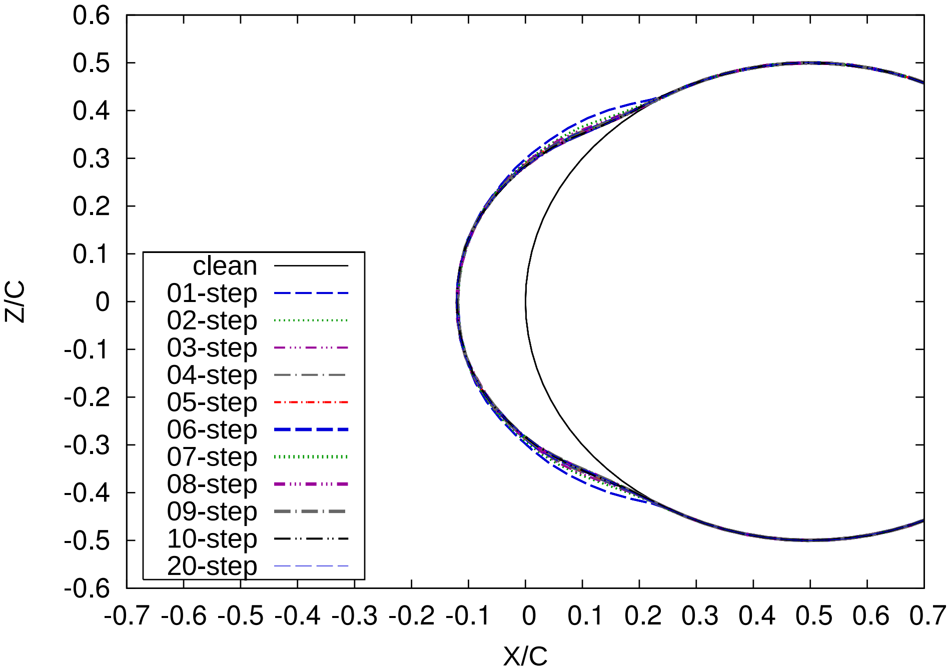

Figure B.1: *rime ice shapes obtained on a cylinder with a step-by-step calculation based on the time-criterion. Small droplets. Exposure time: 5min 30s.* $T_\infty \simeq -26^oC$.

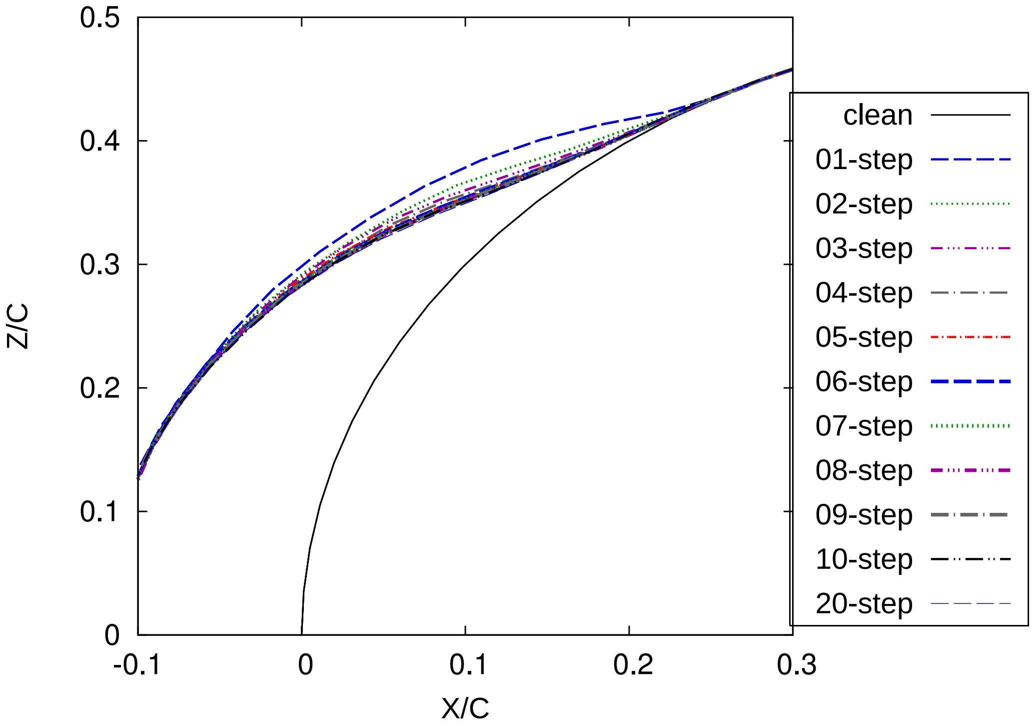

Figure B.2: *Upper Surface*

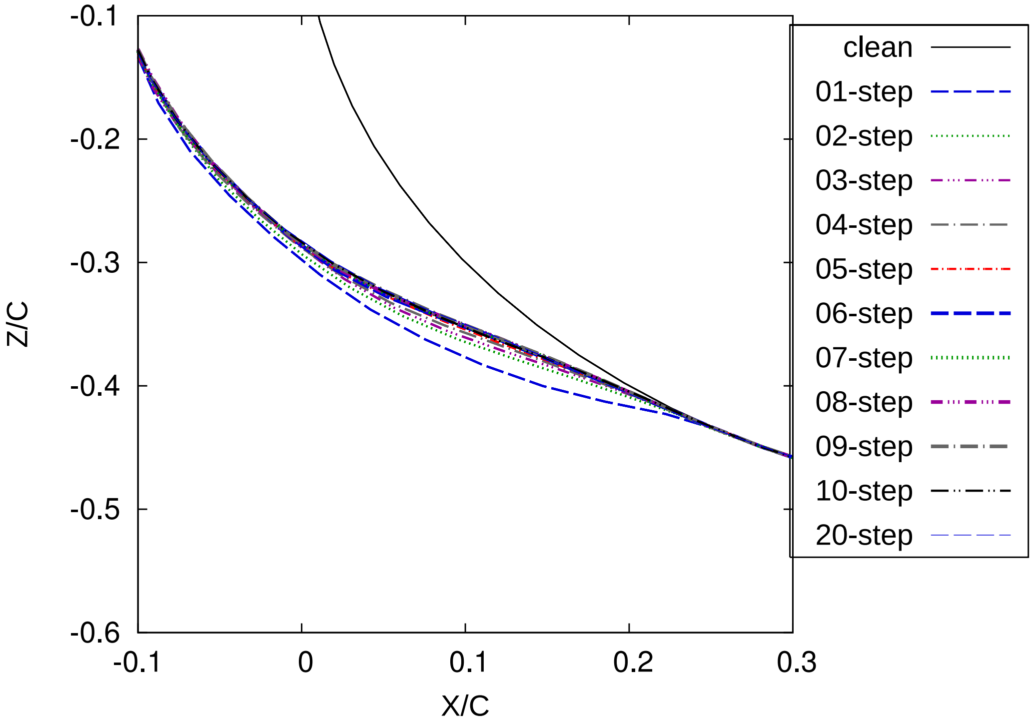

Figure B.3: *Lower Surface*

- **Ice Height Criterion**

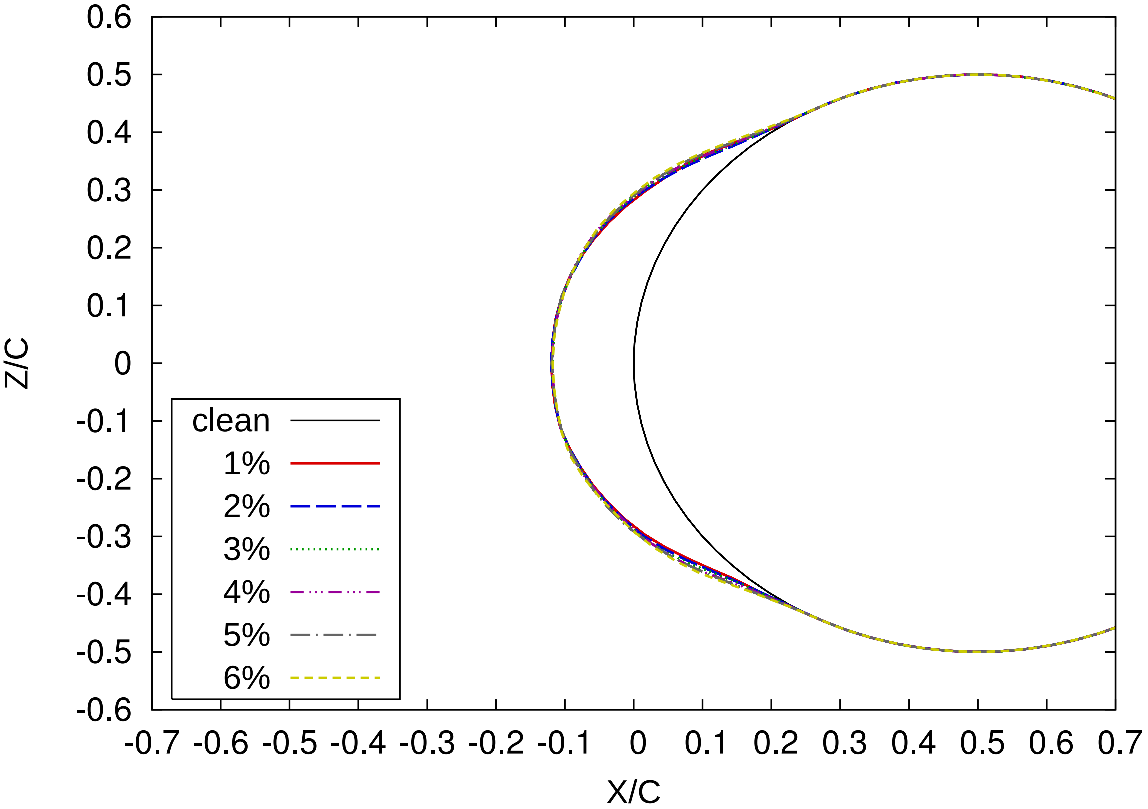

Figure B.4: *rime ice shapes obtained on a cylinder with a step-by-step calculation based on the ice height criterion. Small droplets. Exposure time: 5min 30s.* $T_\infty \simeq -26^oC$.

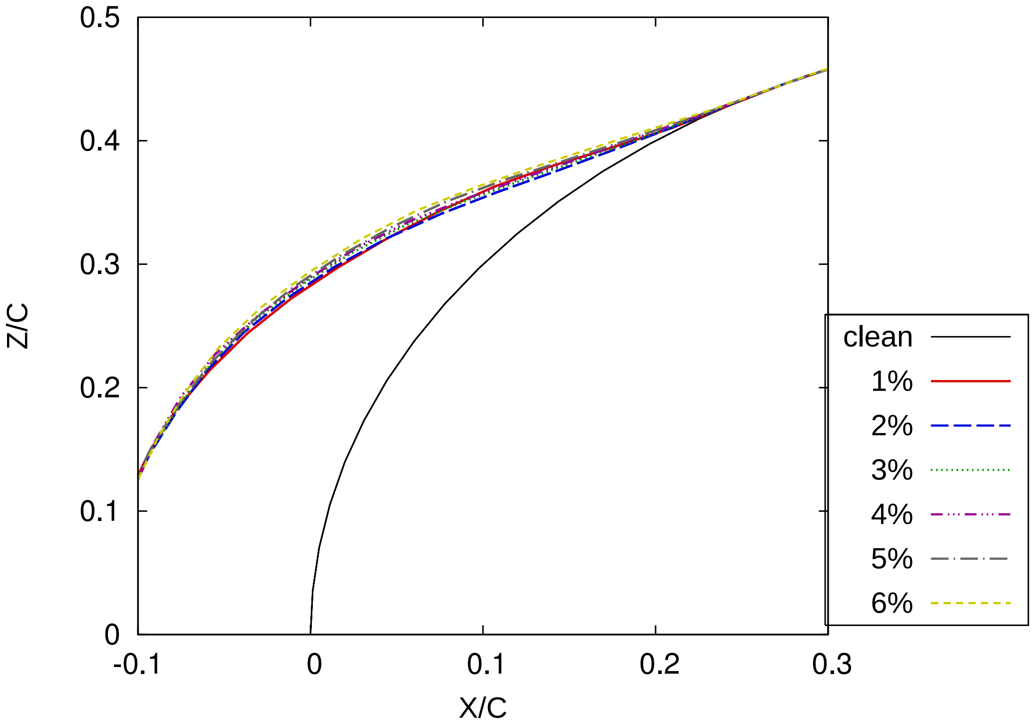

Figure B.5: *Upper Surface*

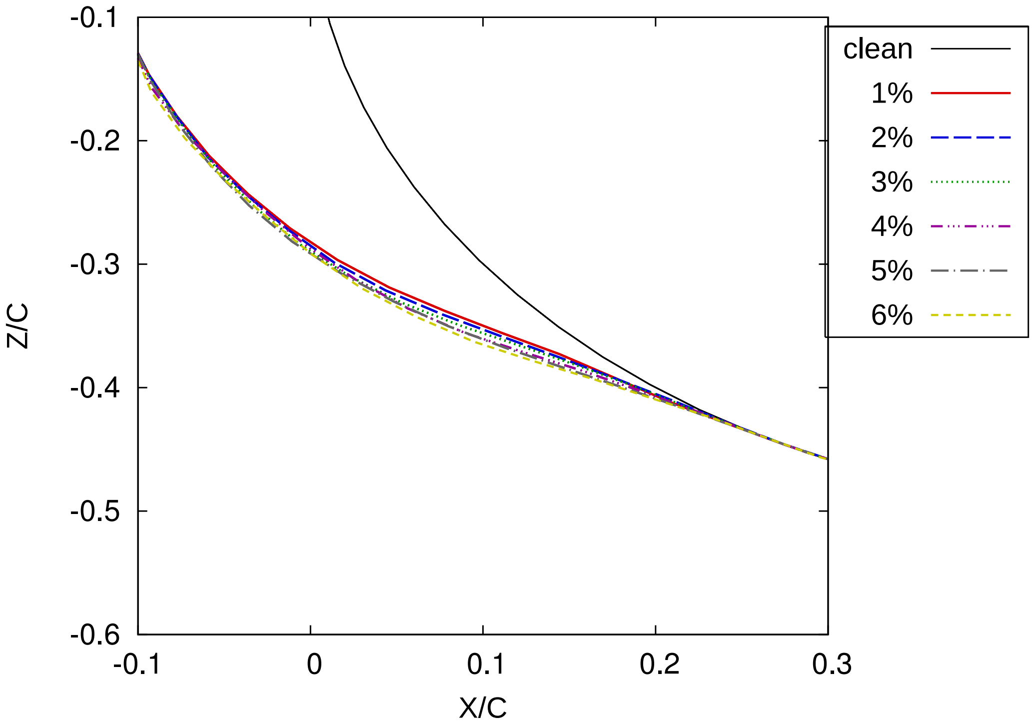

Figure B.6: *Lower Surface*

APPENDIX C

Convergence study - Glaze ice shape on a cylinder - Case O1

This appendix presents additional results calculated during the convergence study of the step-by-step method on the cylinder $O1$ in glaze ice conditions. The results of this study are detailed in Section 5.3.

- **Time Criterion**

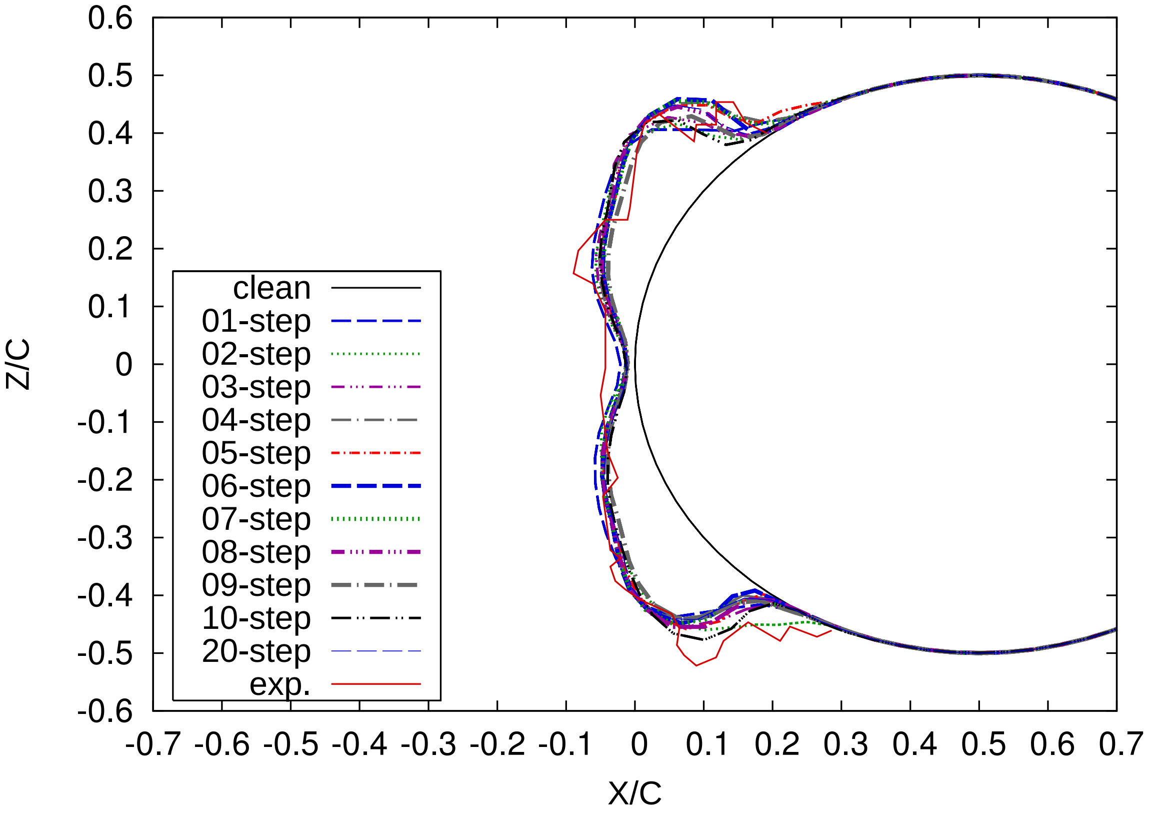

Figure C.1: *Glaze ice shapes obtained on a cylinder with a step-by-step calculation based on the time-criterion. Small droplets. Exposure time: 5min 30s.* $T_\infty \simeq -3^oC$.

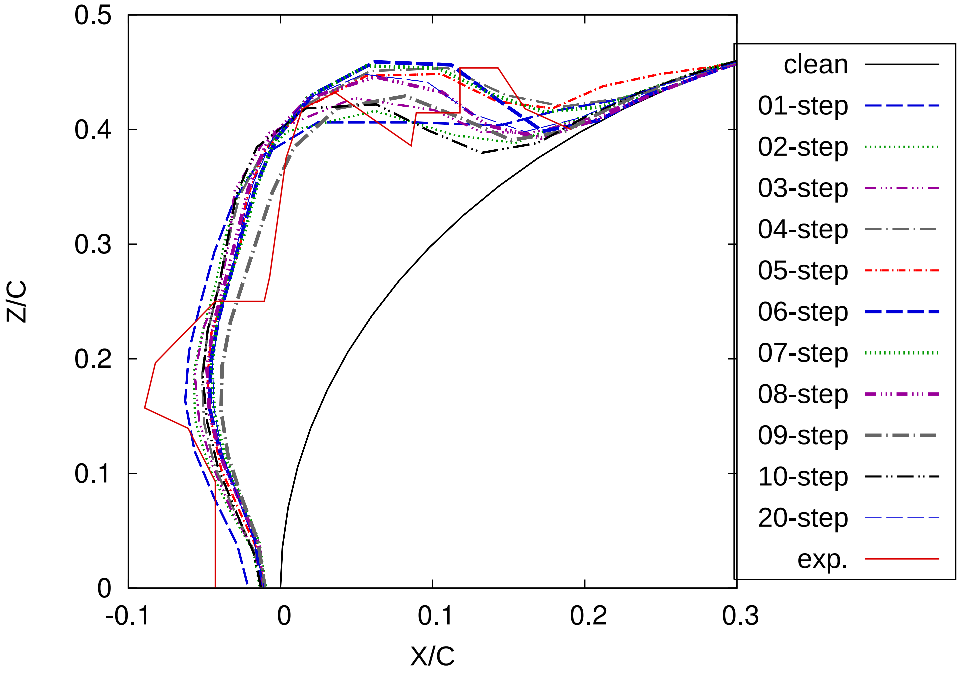

Figure C.2: Upper Surface

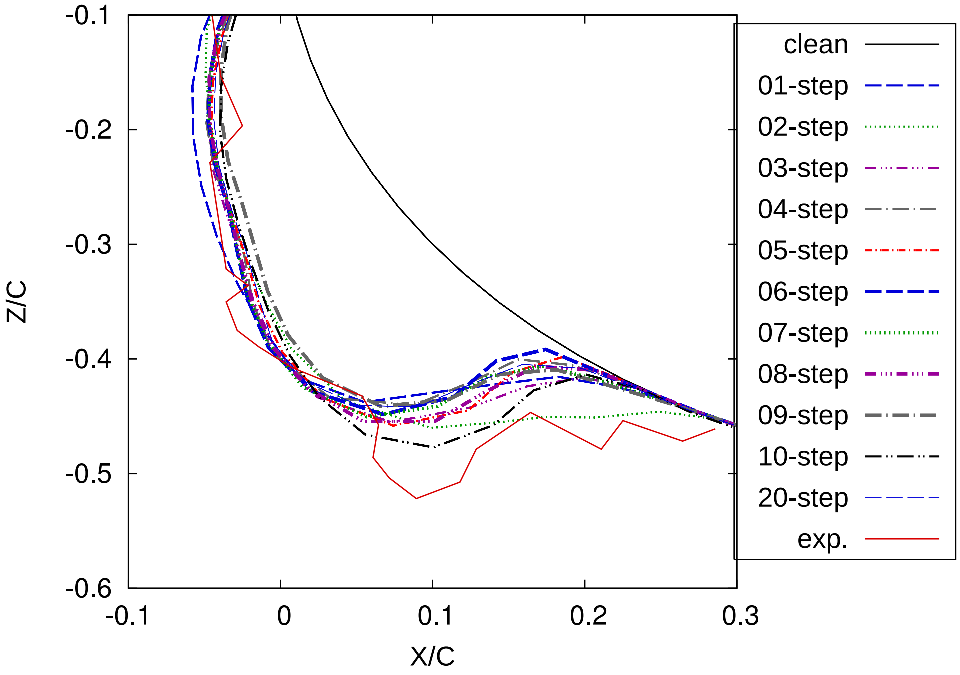

Figure C.3: Lower Surface

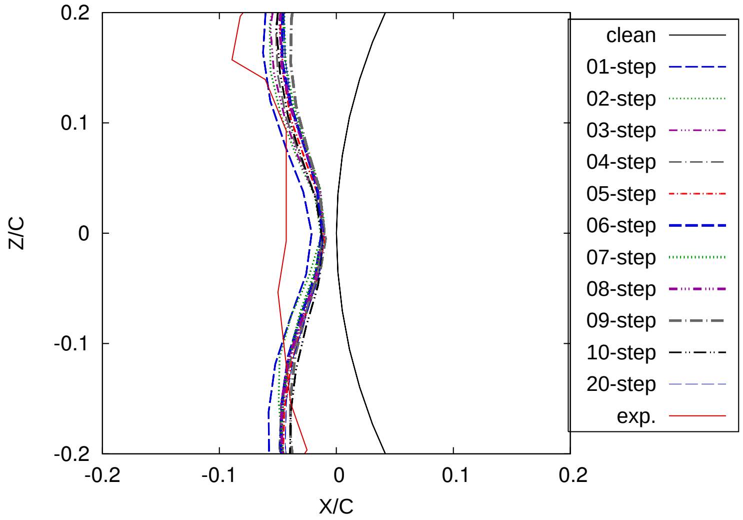

Figure C.4: *Stagnation Region*

- **Ice Height Criterion**

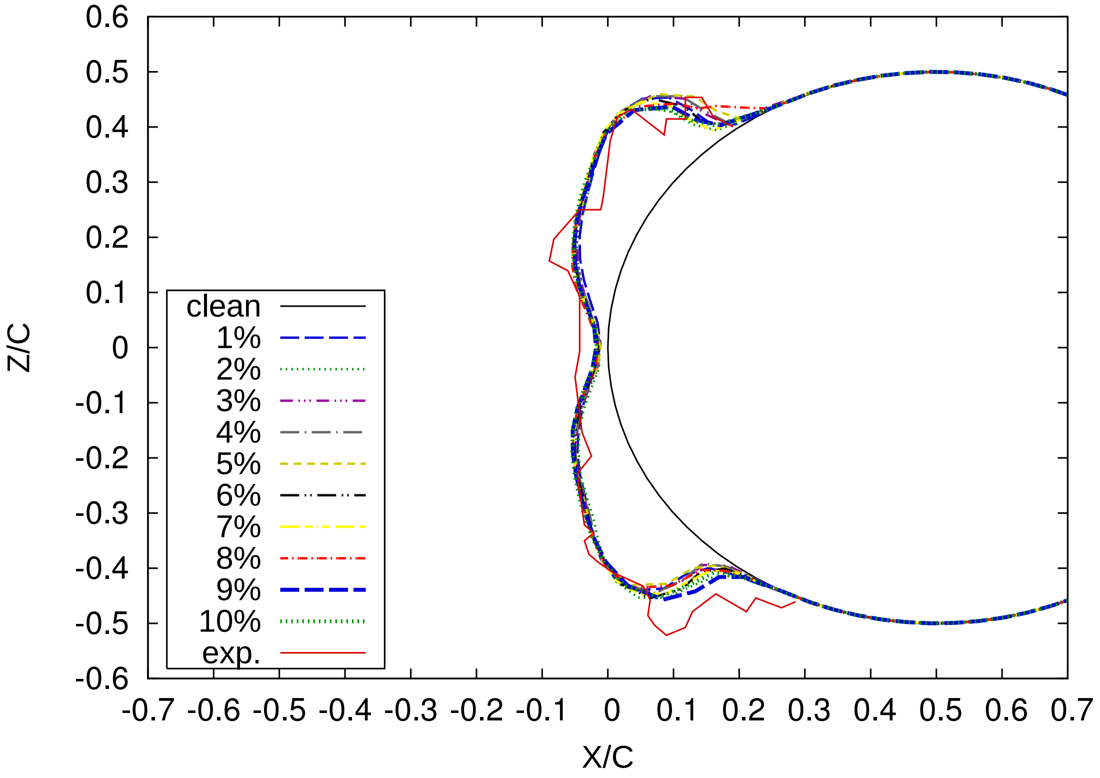

Figure C.5: *Convergence study. Glaze ice shapes obtained with the ice height-criterion. Small droplets. Exposure time: 5min 30s.* $T_\infty \simeq -3^oC$.

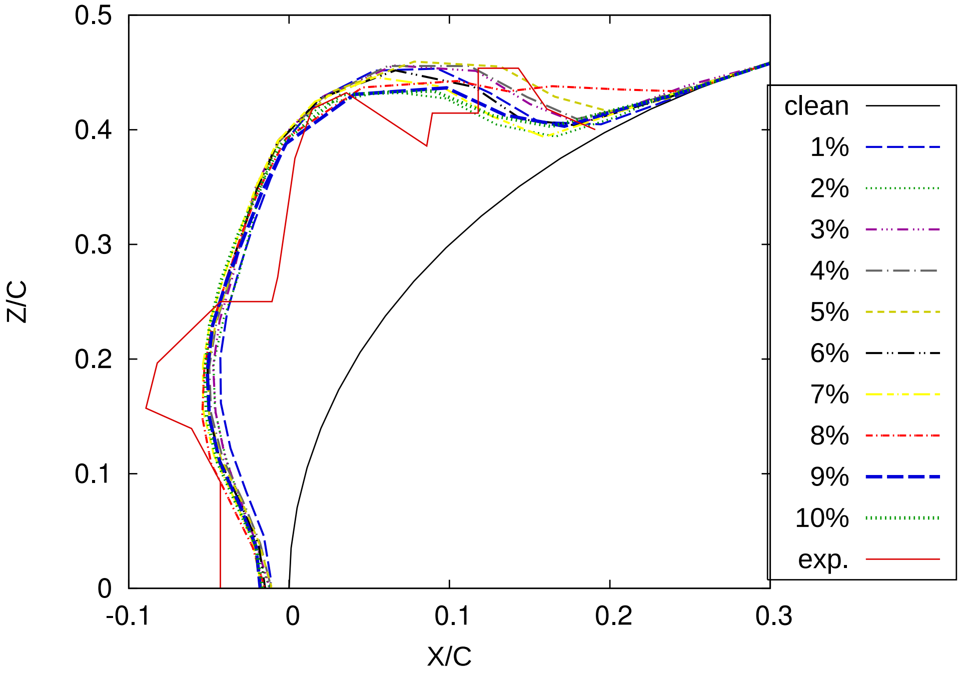

Figure C.6: *Upper Surface*

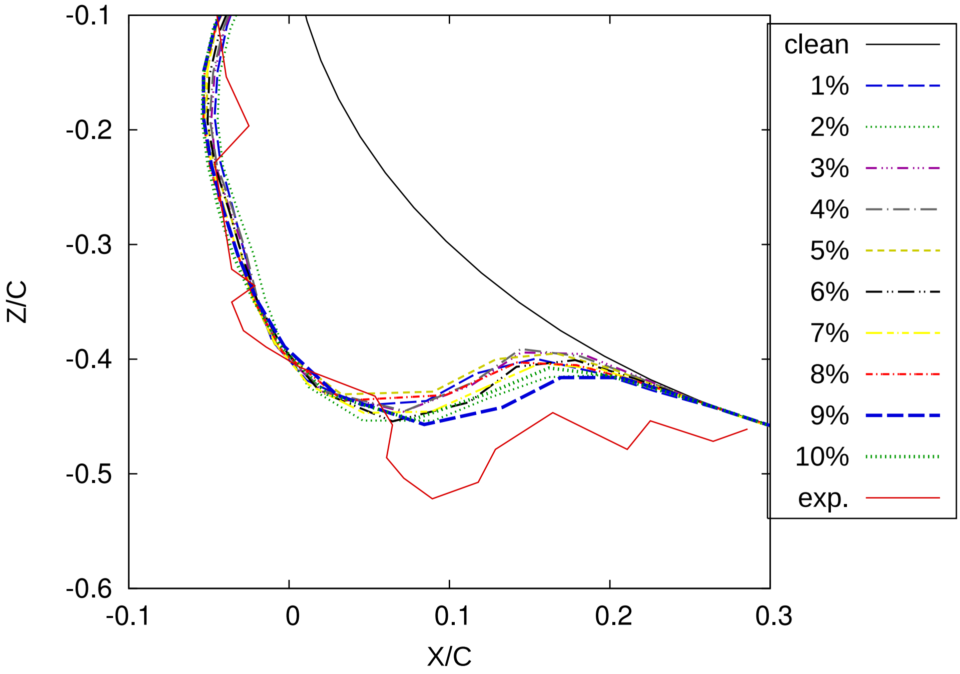

Figure C.7: *Lower Surface*

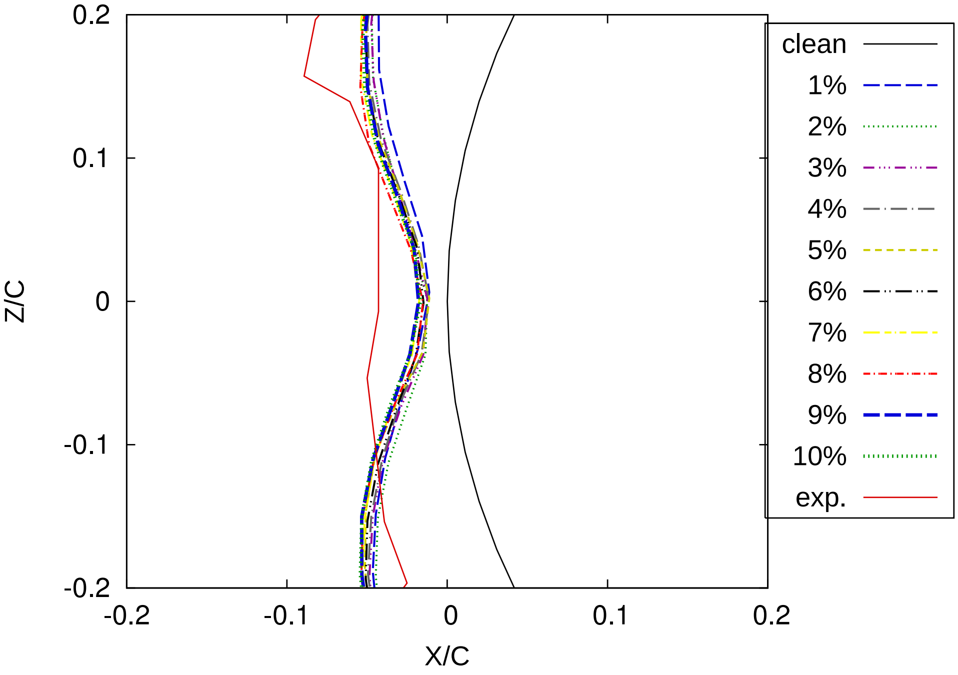

Figure C.8: *Stagnation Region*

APPENDIX D

Convergence study - Glaze ice shape on a cylinder - Case O2

This appendix presents additional results calculated during the convergence study of the step-by-step method on cylinder $O1$ in glaze ice conditions. The results of this study are detailed in Section 5.3.

- **Time Criterion**

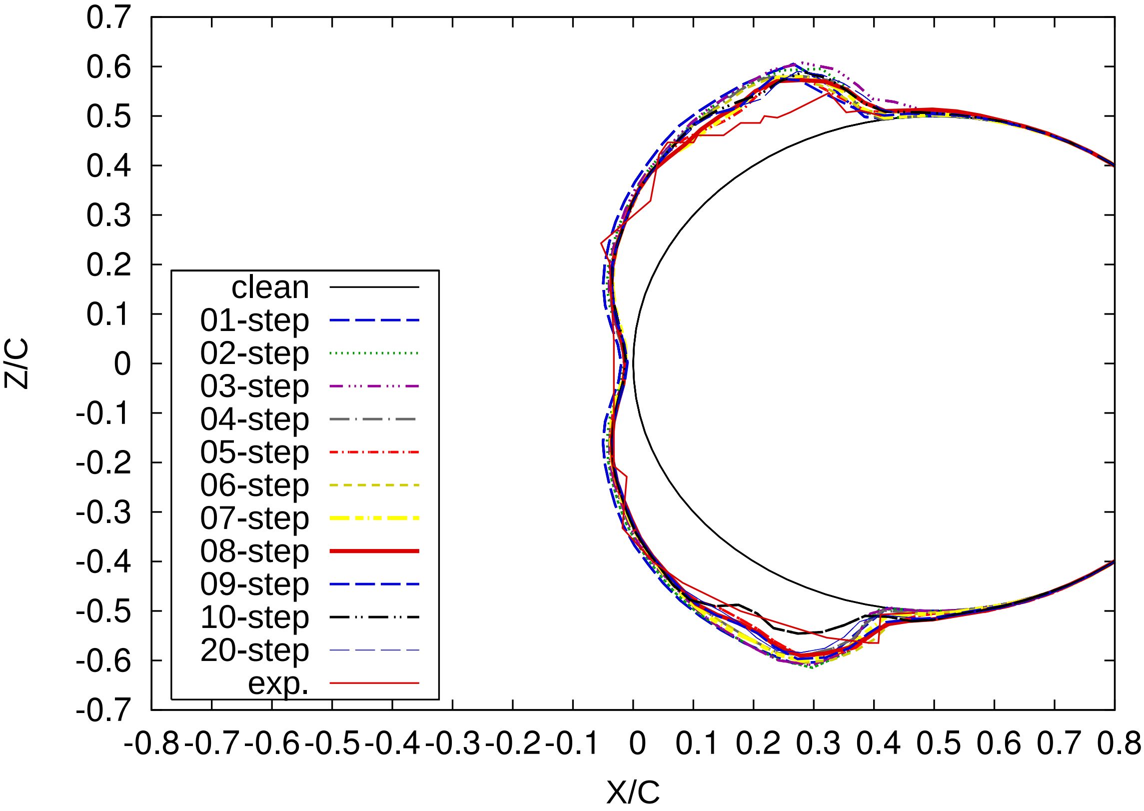

Figure D.1: *Glaze ice shapes obtained on a cylinder with a step-by-step calculation based on the time-criterion. Large droplets. Exposure time: 5min 30s.* $T_\infty \simeq -3^oC$.

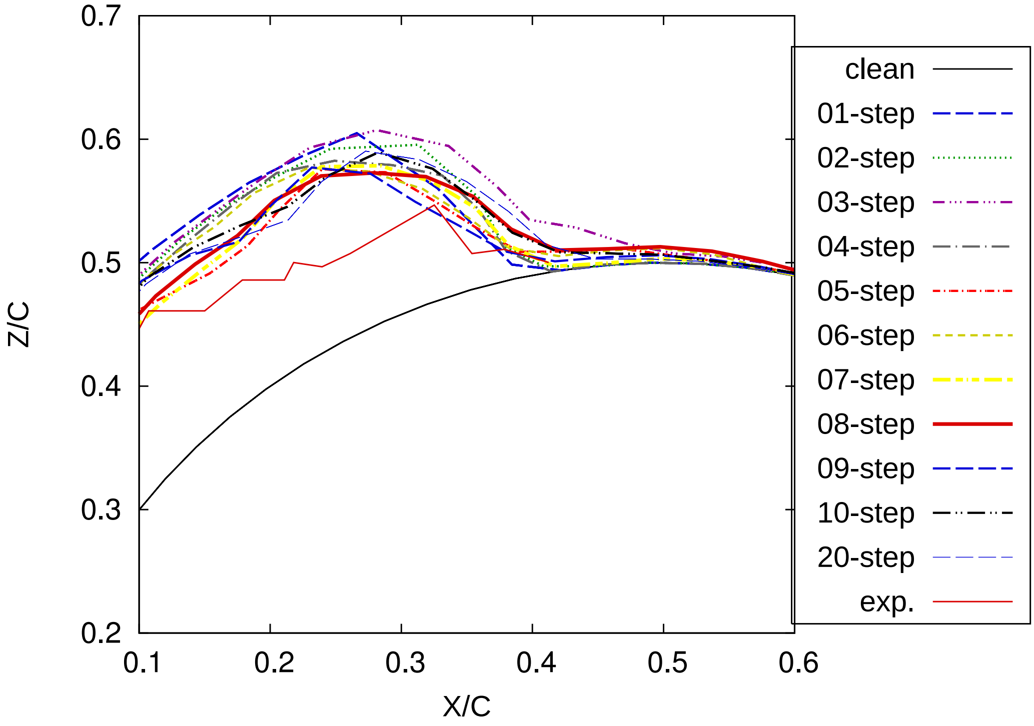

Figure D.2: Upper Surface

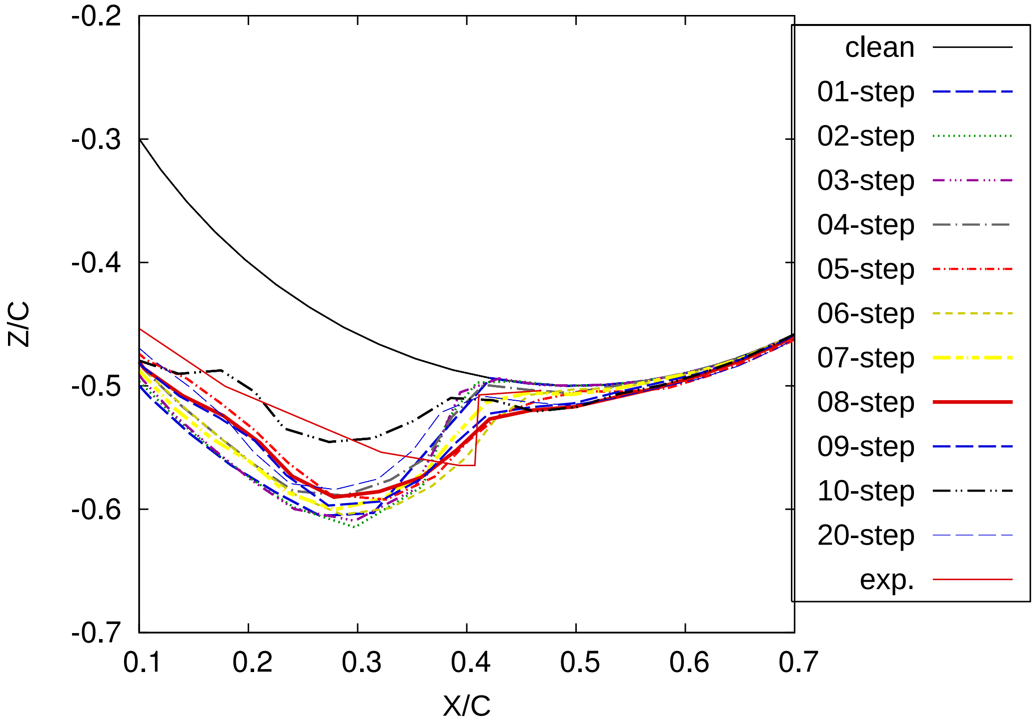

Figure D.3: Lower Surface

- **Ice Height Criterion**

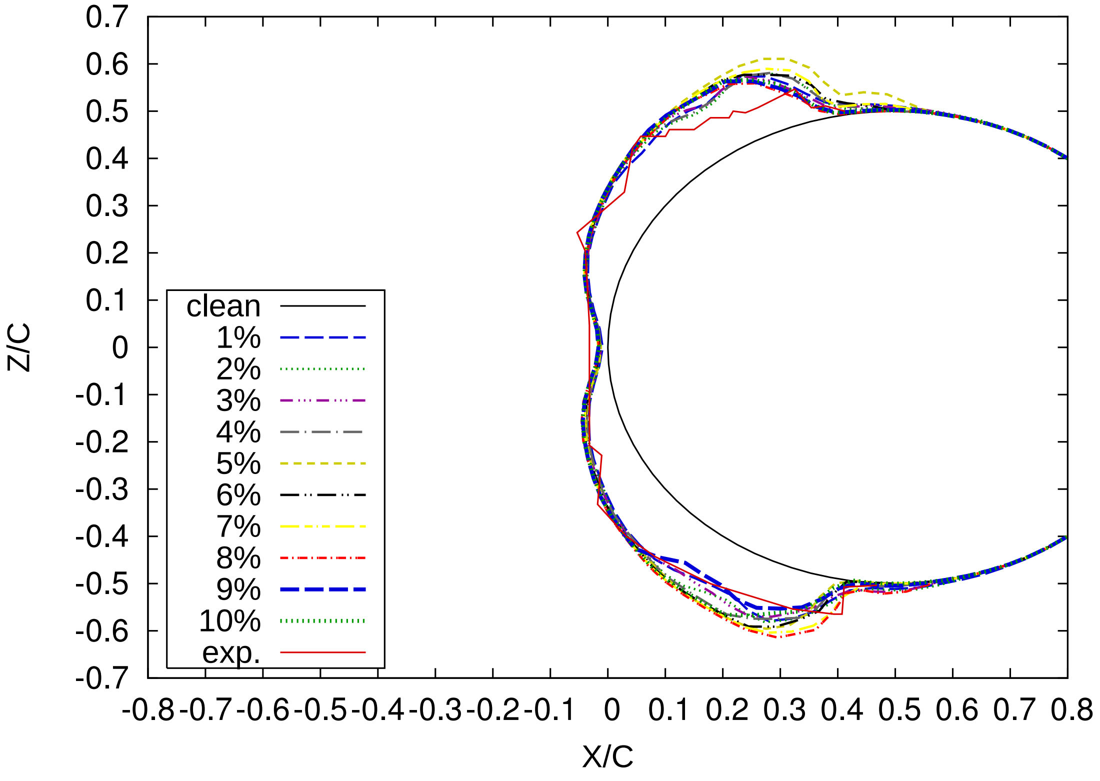

Figure D.4: *Convergence study. Glaze ice shapes obtained with the ice height-criterion (as a percentage of the cylinder). Large droplets. Exposure time: 5min 30s.* $T_\infty \simeq -3^oC$.

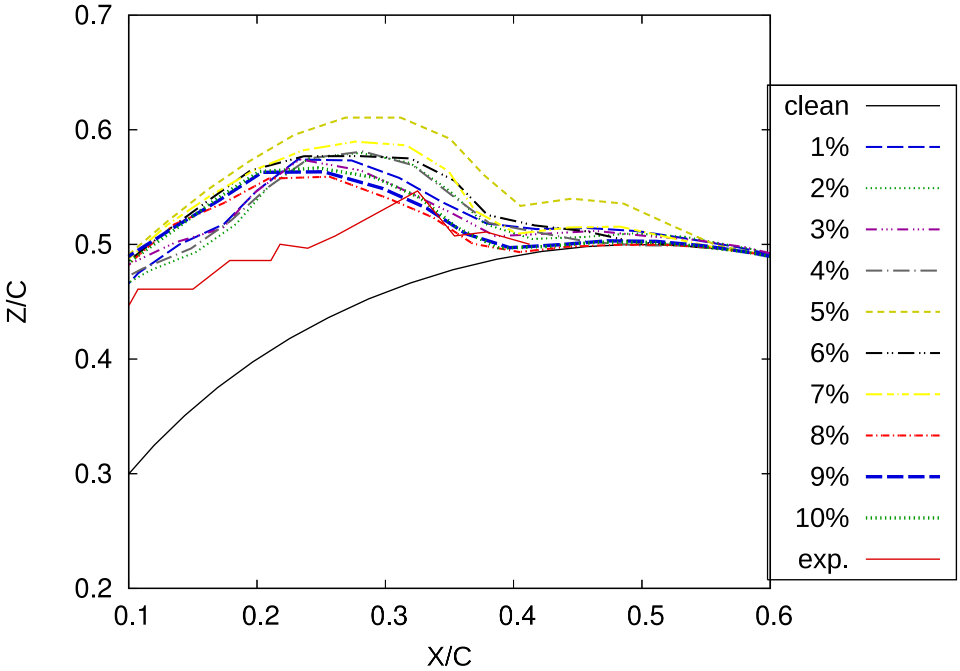

Figure D.5: *Upper Surface*

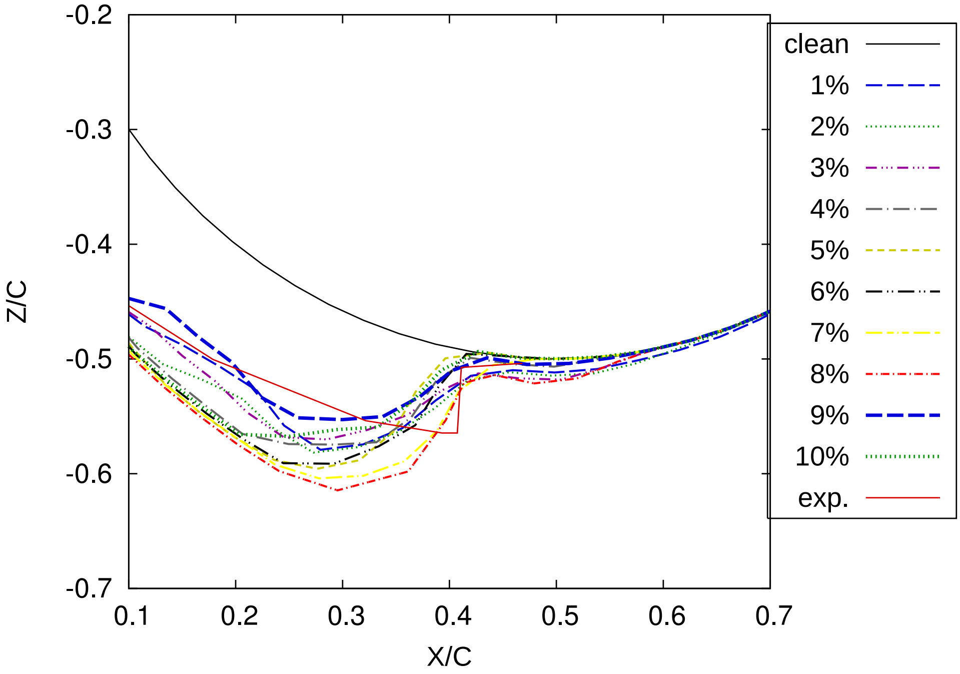

Figure D.6: *Lower Surface*

Appendix E

Convergence Study - Rime ice shape on a wing

Additional results are now presented for a NACA0012 wing in rime ice conditions. As in the previous appendices, the convergence is studied using the time and the ice height criterion. These complete the results detailed in Section 5.4.

- **Time Criterion**

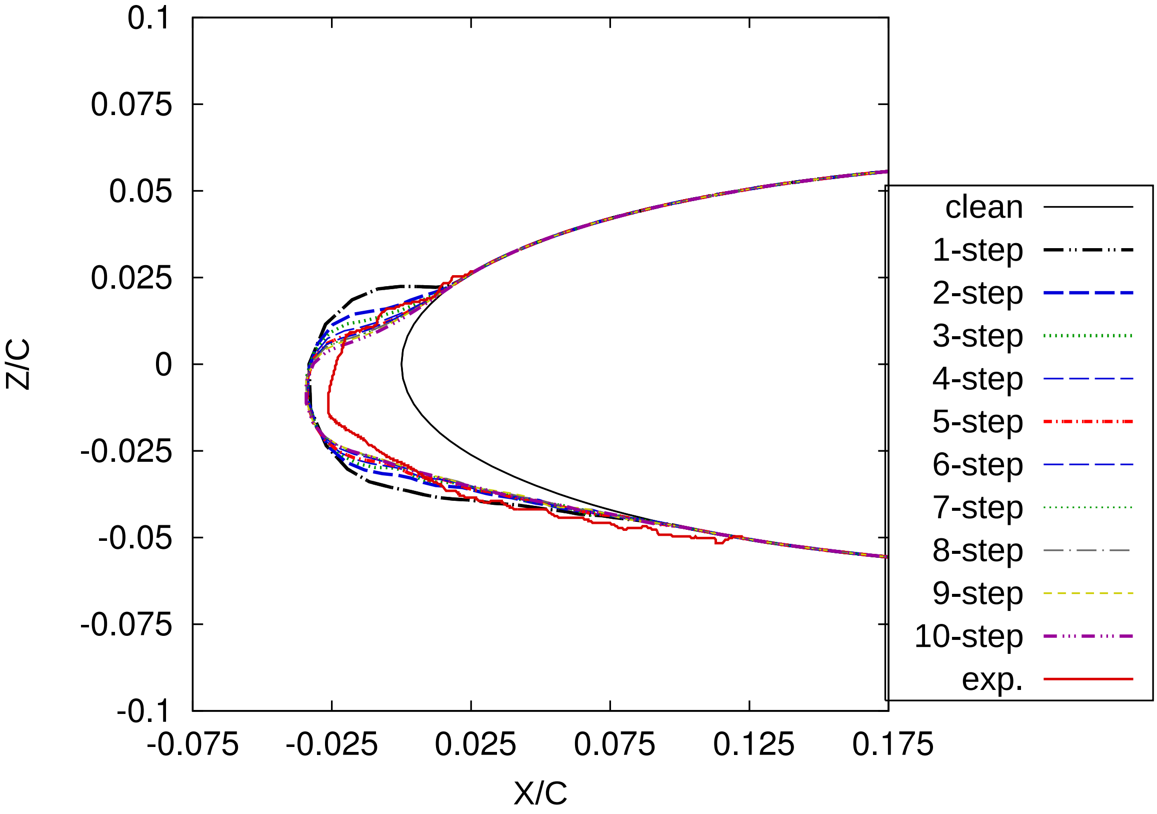

Figure E.1: *rime ice shapes obtained on a wing with a step-by-step calculation based on the time criterion. Small droplets. Exposure time: 6min.* $T_\infty \simeq -26^oC$.

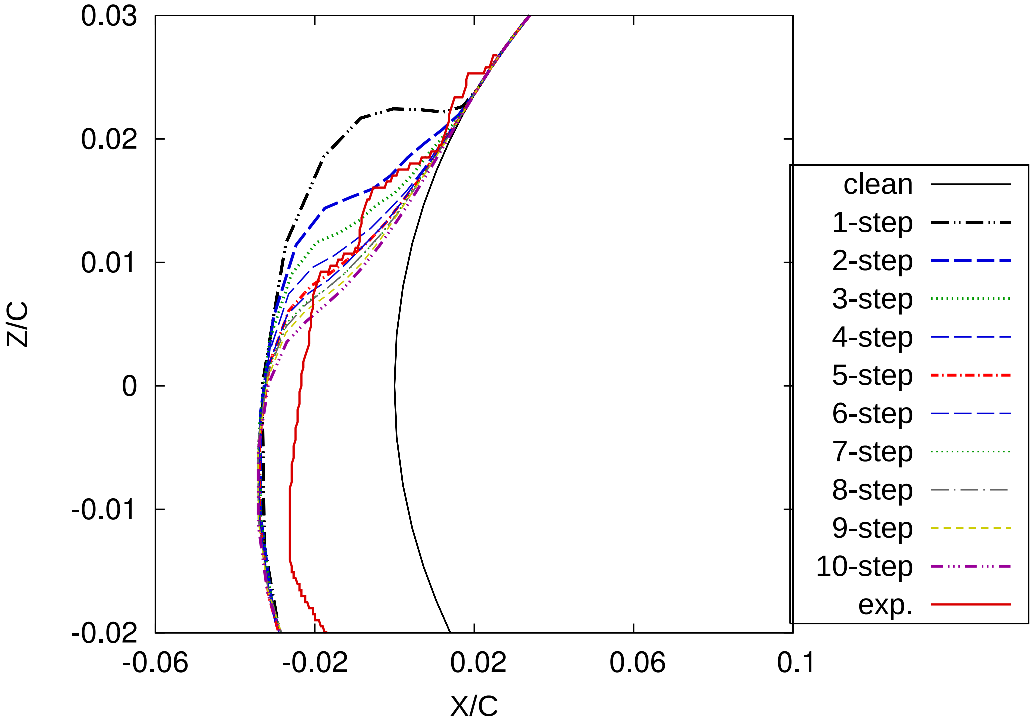

Figure E.2: *Upper Surface*

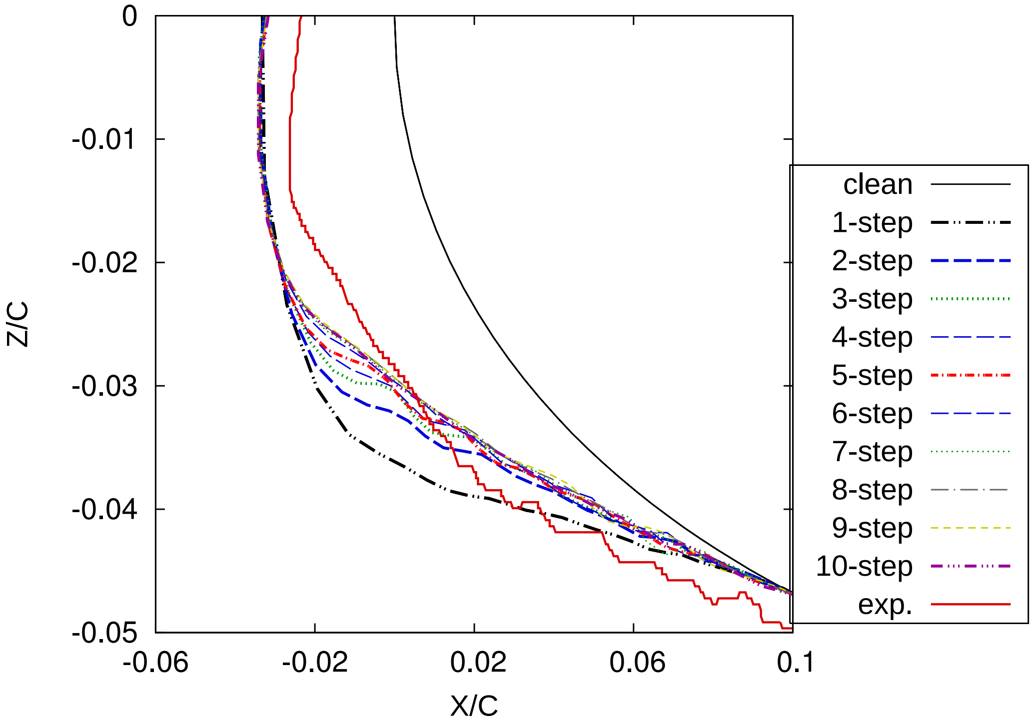

Figure E.3: *Lower Surface*

- **Ice Height Criterion**

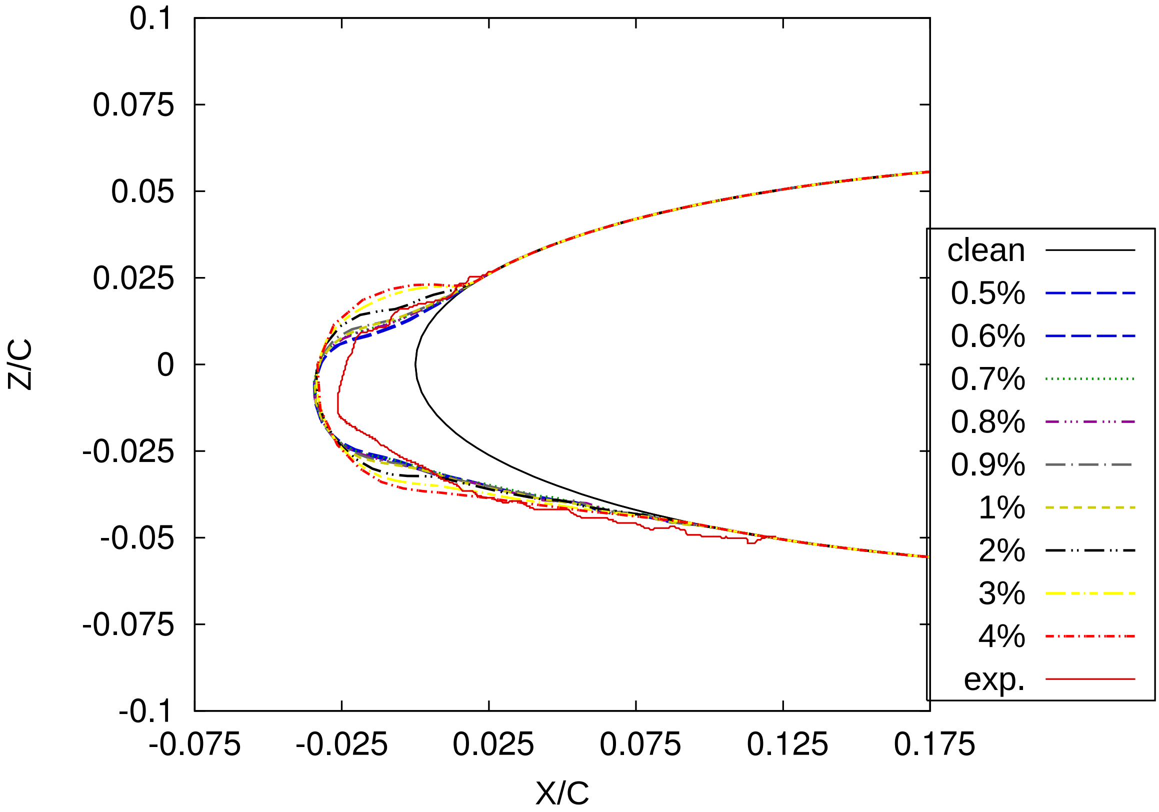

Figure E.4: *rime ice shapes obtained on a wing with a step-by-step calculation based on the ice height criterion. Small droplets. Exposure time: 6min.* $T_\infty \simeq -26^oC$.

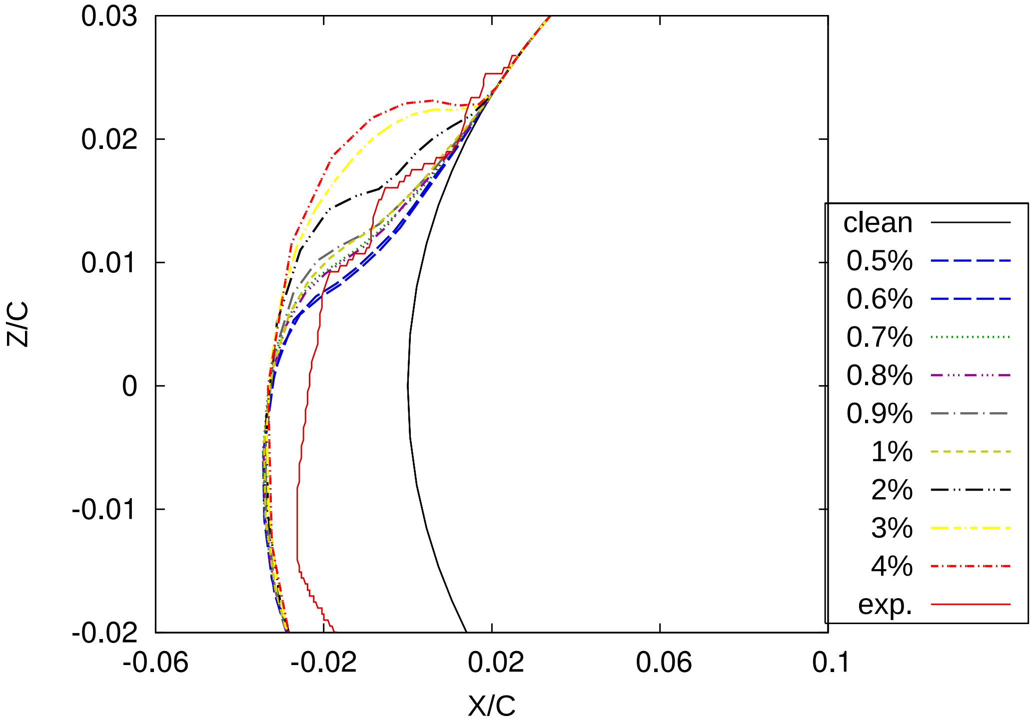

Figure E.5: *Upper Surface*

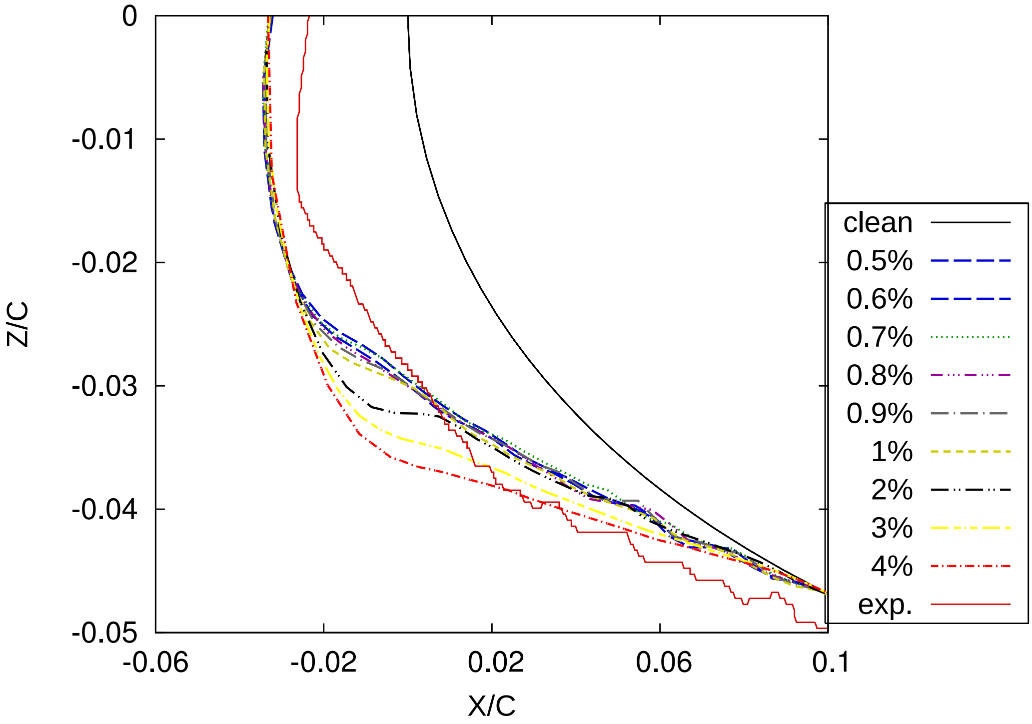

Figure E.6: *Lower Surface*

Appendix F

Convergence study - Glaze ice shape on a wing

Finally, additional convergence results are presented for a NACA0012 wing in glaze ice conditions for the time criterion. No further tests were performed for the ice criterion as an approximative right number of steps could be determined by deduction from the previous analysis on the cylinder and from the study on the wing with the time criterion.

- **Time Criterion**

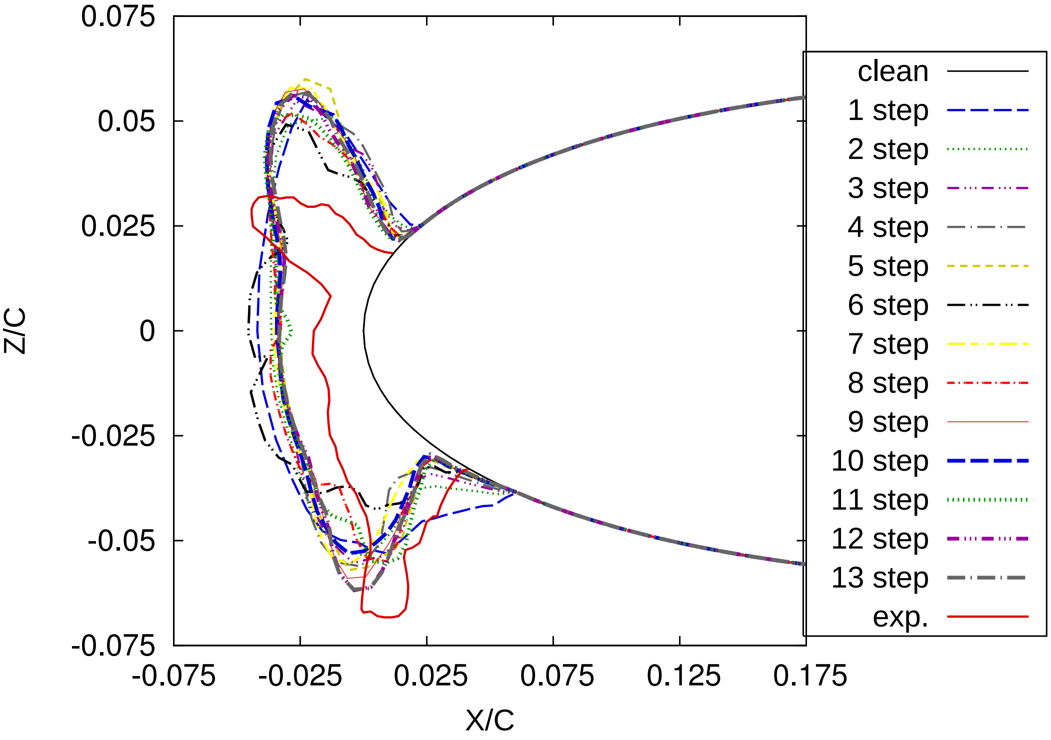

Figure F.1: *glaze ice shapes obtained on a wing with a step-by-step calculation based on the time criterion. Small droplets. Exposure time: 20min.* $T_\infty \simeq -7^oC$.

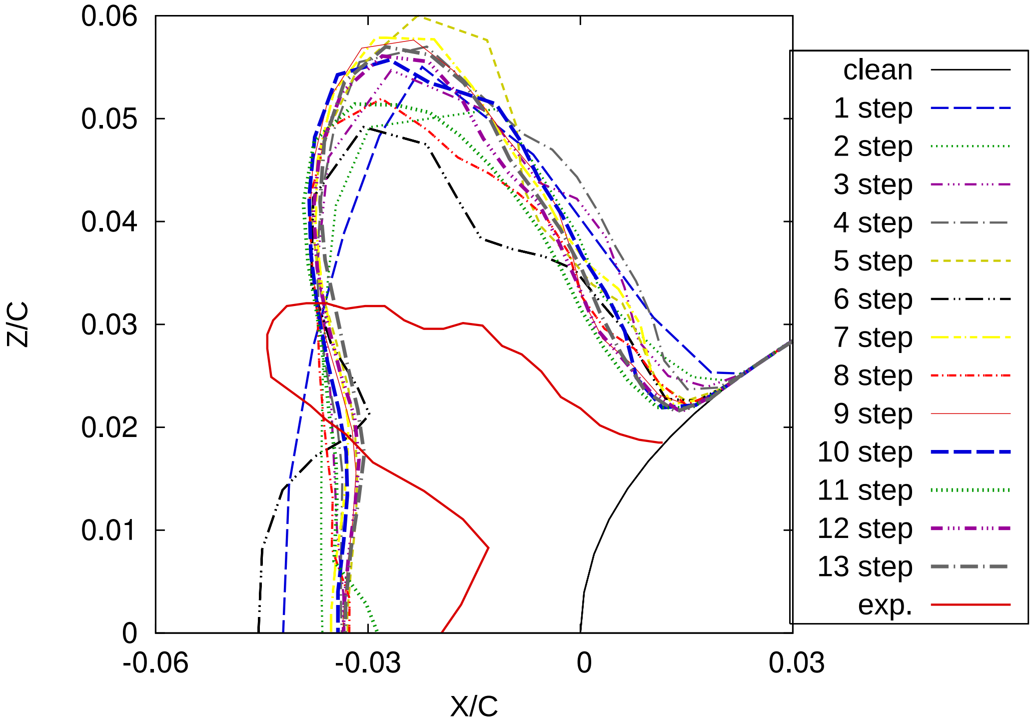

Figure F.2: *Upper Surface*

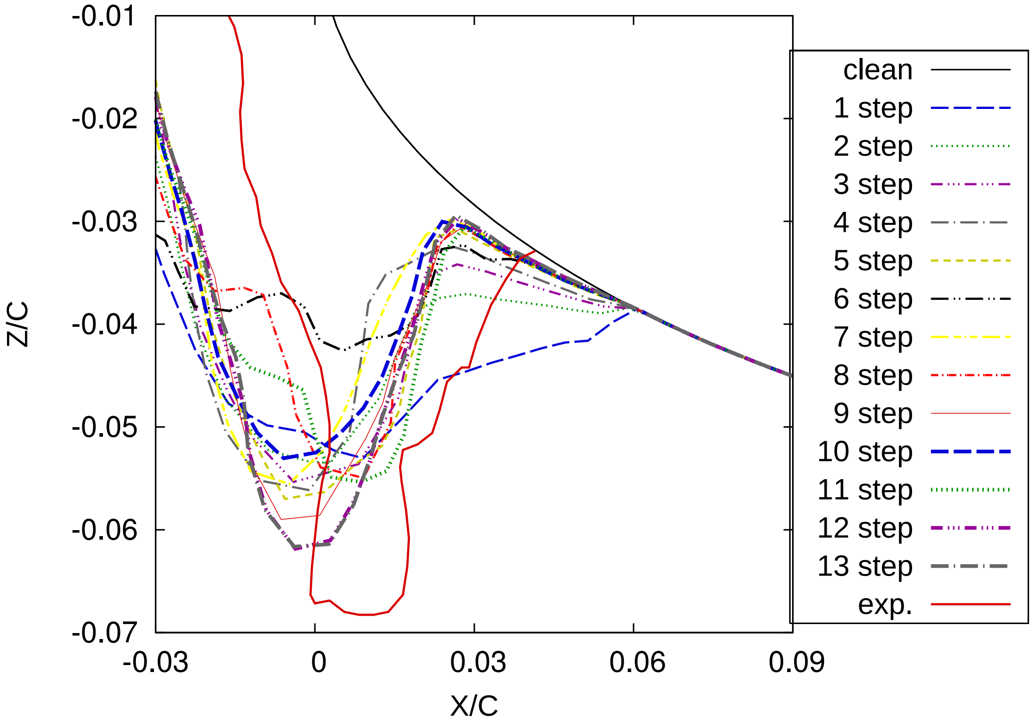

Figure F.3: *Lower Surface*

Appendix G

Combined Algorithm Description

The combined algorithm has been described briefly in Chapter 7. Such a procedure has the features and advantages of both the step-by-step and the predictor-corrector: the flow related parameters are re-evaluated periodically during the simulation and these parameters are updated regularly with the ice accretion. The predictor-corrector coupled with a step-by-step algorithm based on the ice criterion will allow for the update of the flow solution at appropriate periods of the ice accretion. The objective of this appendix is to describe this algorithm more thoroughly.

The time per step, also called multi-time step t_{step}, is defined as the total exposure time divided by a specified number of multi-time steps. For the time criterion, this multi-time step remains constant for each step of the procedure. However, as previously detailed in Chapter 5, this multi-time step is likely to be different for an ice based algorithm as a new flow solution is started as soon as a specified ice height is reached. For the sake of simplicity in this description, the criterion used in the step-by-step part of the algorithm is the time. However, for all simulations performed in Chapter 7, the ice criterion was used instead as it has proved to be more reliable and faster than a computation based on the time triggering criterion.

The combined algorithm is illustrated in Figure G.1. In this picture, A is an icing parameter, where: $A_{p,1} \cdots A_{p,n}$ are the predicted values starting from step$_1$ to step$_n$, $A_{c,1} \cdots A_{c,n}$ are the corrected values, $A_{i,1} \cdots A_{i,n}$ stand for the interpolated values between predictor and corrector. The exposure times for each step are $t_{step_1} \cdots t_{step_n}$.

As already mentioned, when the ice height criterion is used, the time-step duration is likely to vary in glaze ice conditions since the ice growth is not proportional to the accretion time. This means that an error will occur in the ice calculation for the coupling predictor-corrector and ice height criterion:

> In the step-by-step part of the algorithm, the duration of multi-time step t_{step} is obtained when the ice criterion b_{max} is reached. This multi-time step duration is required for the interpolation function in the predictor-corrector

> model. However, the ice-height criterion still operates when the ice growth is calculated using the interpolation function. This means that the ice criterion can be satisfied at a time lower or higher than the multi-time step t_{step}, leading to inaccuracies in the predictions. Such a problem is of course not present for the time-criterion since the duration of the multi-time step always remains constant. This is not either a problem in rime ice conditions as the interpolated ice shape will not modify the ice height significantly and the icing duration per step is likely to be almost identical. However, the problem appears in glaze ice conditions when the time per step is large and this may generate poor and wrong ice shape predictions.

A solution to this problem is to switch the ice height criterion off as soon as the icing model is run using the interpolation function. This will avoid innaccuracies in the predictor-corrector calculation. However, this may not allow for the update of the flow solution at the right time if the interpolated ice shape is very different from the one estimated with the predictor. This version of the algorithm is nevertheless used to generate the results presented in Chapter 7 as it appears the safer solution.

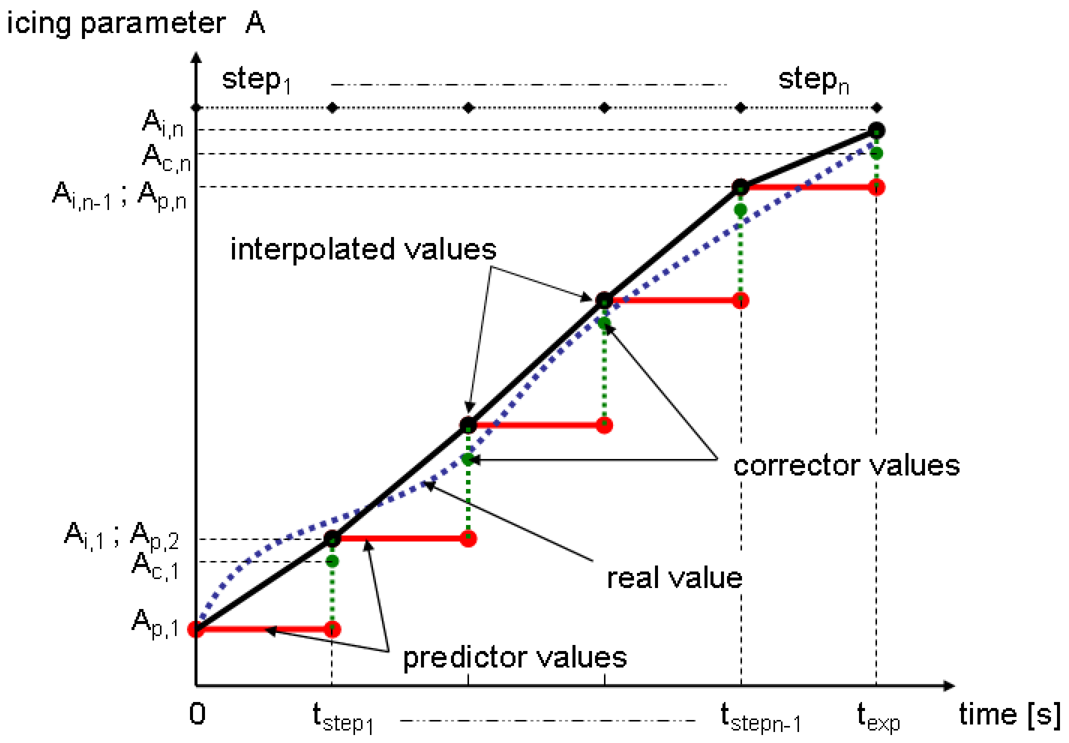

Figure G.1: *Combined procedure between predictor-corrector and step-by-step methods.*

APPENDIX H

DETAILS ON SIMULATIONS

All simulations presented in this thesis from Chapter 5 to 7 are described briefly in this appendix for both cylinder and wing configurations. The grid around the clean and ice covered geometries were generated with the mesh generator GAMBIT 2.2 or 2.4 and the flow solution obtained with FLUENT 6.2 or 6.3. The version used for the computation had no influence on the final results. The ice prediction code ICECREMO version3 (release, July 2005) was used for the icing parameters and ice growth calculations.

H.1 Calculation on the Cylinder Geometry

Details on simulations performed on the cylinder geometry are written in the following.

- **Geometry and mesh**
    - Outer cylinder domain: 8 diameter lengths away from the body
    - Number of nodes on geometry edges: 90
    - Number of nodes on outer edges of domain: 60
    - Mesh type: structured on geometry, hybrid in the rest of the domain
    - Mesh size: 127858 cells Span length: 20 cm
- **CFD**

  Information about the boundary conditions and models used to generate the flow solutions were described in Chapter 3.

  Boundary conditions

    - Pressure-far-field: for the outer domain
    - Wall: on the body surface

  - Symmetry: perpendicularly to the span direction

Models

  - Solver: segregated
  - Turbulence: Spalart-Allmaras one equation model
  - Residual: default convergence criterion: 10^{-3}

- **Ice Calculation**

  Two main input files *Multistep.inp* and *Fluent.inp* are used to perform a simulation. These files are shown in the following for a multi-step algorithm based on the ice height criterion. In this example, droplets of 18μm impinge on the cylinder surface in glaze ice conditions. Atmospheric and icing conditions are those used during the NATO/RTO exercise held in December 2000 [120].

  - *Multistep.inp*

    The multi-step input file is shown below. A maximum number of 200 steps is specified in *line 2*. This maximum number is never reached for a calculation based on the ice-criterion while the number of steps has to be specified by the user when running the time-based algorithm. The gravity term is not accounted for in the computation, as shown in *line 3*.

```
 1 0.  0.02
 2 0 200
 3 0.  270.2  99800.  0.23
 4 0.  0.0635  0.00044
 5 1 60
 6 cylinder
 7 1  330.
 8 0
 9 line1 :span length (initial, final)
10 line2 :nmult,nstep
11 line3 :gravity,tamb,pamb,Mach
12 line4 :AoA,chord,LWC
13 line5 :nrows,nnodes (mesh external shape)
14 line6 :profile(cylinder or airfoil)
15 line7 :ice criterion (time=0,ice=1),exposure time
16 line8 :algorithm (step-by-step=0,predcorr=1)
```

  - *Fluent.inp*

    The input file for ICECREMO corresponding to the previous *Multistep.inp* input file is shown in the following. Further details about the keywords may be found in References [135] and [136]. Small droplets (*line 71*) impinge on the cylinder surface, they are introduced around $x/c = 3.5$, ahead of the body (*line 68*). The initial number of droplets is 4000. However, this number increases due to a refinement method [135, 136] along the z-axis, see lines *81* to *90*. Notice that the z-axis of this input file corresponds to the y-axis in the pictures plotted in this thesis. The ice height criterion value is $b_{max} = 0.00254$m which corresponds to $b_{max} = 4\%$c, see *line 47*.

```
 1 #----------- Film Flow/icing Calculation Data ---------
 2 Gravity_X = 0.0
 3 Gravity_Y = 0.0
 4 Gravity_Z = 0.0
 5 FreeStreamVelocity = 77.2
 6 LiquidWaterContent = 0.00044
 7 AmbientPressure = 99800.
 8 AmbientTemperature = 270.2
 9 RelativeHumidity =62.
10 Unsteady = true
11 FlipSurface = true
12 IncludeIceTerms = true
13 NumberDistributions =1
14 MagnificationFactor = 1.0
15 IsentropicPandT = true
16 OutputTimeStepInterval = -1
17
18 CFL                            = 0.5
19 ConvCrit                       = 0.000001
20 Unsteady                       = true
21 NumCycles                      = 100000000
22 NumTimeSteps                   = 0
23 GlobalTimeStep                 = true
24 GlobalTimeStepValue            = 0.0
25 TotalNumCycles                 = 1000000
26 #----------- Output Data ------------------------------
27 writeLogFile                   = false
28 NumDumpCycles                  = 200
29 NumHistCycles                  = 10000000
30 NumHistRecords                 = 0
31
```

```
#------------ Multi-Step Data --------------------------
Restart=true
RestartVisu=true
FlowUpdate=true
Nsteps=1
Nsteps2=1
#----------------------
# Time Criterion
#----------------------
#ExposureTime =41.25
#----------------------
# Ice Height Criterion
#----------------------
ExposureTime =330.
IceHeightCriterion=true
IceHeightMax=0.00254

#------------ HTC & Shear Stress Calculation Data -------
HeatTransferFactor = 2.5
HTCAveraging = false
HTCLowerLimit = true
BLCalcStepSize = 0.01
RoughnessHeight = 0.003
StagTestOriginal = true
HTCOutputNone = true
HTCOutputSummary = false

#------------ Catch Efficiency Calculation Data ---------
DomainZmin = -0.2
DomainZmax =  0.2
DomainYmin = 0.0
DomainYmax =  0.02
DomainXmax =  0.07
CornettoTraj = true
jh01 = false
fluent = true
DistributionData = -0.2 -0.2 1 0.0 0.02 2 -0.1 0.1 2000
TrackSegments = 50
StepsInCell = 2
```

```
DropletDiameter = 0.000018
RRTraj = false
DragLaw = 2
CatchCalcOption = METHOD1
XTrajMax = 0.02
PathSolverTolerance = 1E-7
updateGlobalParams = true
preCalculateCellCentres = true
PlotNth = 1
useRevStreamLAndProj = false
Refinemethod = 1
XRefine = false
YRefine = false
ZRefine = true
ReqDelxLim = 0.0
ReqDelyLim = 1.
ReqDelzLim = 0.00001
ReqDelxHit = 0.0
ReqDelyHit = 1.
ReqDelzHit = 0.0001
```

H.2 Calculation on the Wing Geometry

A similar short description of the simulation parameters is provided in the following for the ice calculation on a NACA0012 wing section in rime ice conditions (chord length=0.5334m, $T_\infty = -26^oC$).

- **Geometry and mesh**
  - Outer cylinder domain: 8 chord lengths away from the body
  - Number of nodes on geometry edges: 200
  - Number of nodes on outer edges of domain: 180
  - Mesh type: structured on geometry, hybrid in the rest of the domain
  - Mesh size: 514147 cells
  - Chord length: 0.5334m
  - Span length: 20 cm
- **CFD**

  CFD settings are identical to those described previously for the cylinder cases.

- **Ice Calculation**

  Input files used for the ice prediction on a wing are shown in the following. For this example, droplets of 20μm impinge on the wing surface. The atmospheric and icing conditions are those referenced in [17] for experiments performed by Shin and Bond.

  - *Multistep.inp*

    The *Multistep.inp* input file is shown below, for a step-by-step case based on the ice height criterion, in rime ice conditions.

```
0.  0.02
0 100
0.  247.05  101300.  0.20755
4.  0.5334  0.001
2 180
airfoil
1  360.
0
line1 :span length (initial, final)
line2 :nmult,nstep
line3 :gravity,tamb,pamb,Mach
line4 :AoA,chord,LWC
line5 :nrows,nnodes (mesh external shape)
line6 :profile(cylinder or airfoil)
line7 :ice criterion (time=0,ice=1),exposure time
line8 :algorithm (step-by-step=0,predcorr=1)
```

  - *Fluent.inp*

    The corresponding input file for ICECREMO is shown in the following. Droplets of size 20μm are introduced around $x/c \simeq 3$ ahead of the wing. The initial number of droplets is 1600. However, this number increases once again thanks to the automatic refinement method. The ice height criterion value is $b_{max} = 0.00427$m corresponding to $b_{max} = 0.8\%$c, see *line 47*.

```
1 #----------- Film Flow/icing Calculation Data ---------
2 Gravity_X = 0.0
3 Gravity_Y = 0.0
4 Gravity_Z = 0.0
5 FreeStreamVelocity = 67.1
6 LiquidWaterContent = 0.001
```

```
AmbientPressure = 101300.
AmbientTemperature = 247.05
RelativeHumidity =100.
Unsteady = true
FlipSurface = true
IncludeIceTerms = true
NumberDistributions =1
MagnificationFactor = 1.0
IsentropicPandT = true
OutputTimeStepInterval = -1

CFL                            = 0.5
ConvCrit                       = 0.000001
Unsteady                       = true
NumCycles                      = 100000000
NumTimeSteps                   = 0
GlobalTimeStep                 = true
GlobalTimeStepValue            = 0.0
TotalNumCycles                 = 1000000
#------------ Output Data ------------------------------
writeLogFile                   = false
NumDumpCycles                  = 200
NumHistCycles                  = 10000000
NumHistRecords                 = 0

#------------ Multi-Step Data --------------------------
Restart=true
RestartVisu=true
FlowUpdate=true
Nsteps=1
Nsteps2=1
#----------------------
# Time Criterion
#----------------------
#ExposureTime =41.25
#----------------------
# Ice Height Criterion
#----------------------
ExposureTime =360.
```

```
IceHeightCriterion=true
IceHeightMax=0.00427

#------------ HTC & Shear Stress Calculation Data -------
HeatTransferFactor = 1.5
HTCAveraging = false
HTCLowerLimit = true
BLCalcStepSize = 0.01
RoughnessHeight = -1
StagTestOriginal = true
HTCOutputNone = true
HTCOutputSummary = false

#------------ Catch Efficiency Calculation Data ---------
DomainZmin = -0.4
DomainZmax =  0.4
DomainYmin = 0.0
DomainYmax =  0.02
DomainXmax =  0.54
CornettoTraj = true
jh01 = false
fluent = true
DistributionData = -1.55 -1.55 1 0.0 0.02 2 -0.2 0.1 800
TrackSegments = 50
StepsInCell = 2
DropletDiameter = 0.000020
RRTraj = false
DragLaw = 2
CatchCalcOption = METHOD1
XTrajMax = 0.05
PathSolverTolerance = 1E-7
updateGlobalParams = true
preCalculateCellCentres = true
PlotNth = 1
useRevStreamLAndProj = false
Refinemethod = 1
XRefine = false
YRefine = false
ZRefine = true
```

```
ReqDelxLim = 0.0
ReqDelyLim = 1.
ReqDelzLim = 0.00001
ReqDelxHit = 0.0
ReqDelyHit = 1.
ReqDelzHit = 0.0001
```

BIBLIOGRAPHY

[1] Aircraft Traffic and Control Association (ATCA). http://www.atca.org, Last time accessed: 05/07/2005.

[2] National Transportation Safety Board. http://www.nasdac.faa.gov/internet/fw search.html/, Last time accessed: 02/05/2002.

[3] S.P. Williamson, J.J. Kelly Jr., J. Washington, B.G.F.P. Lewis, G. Smith, J. Skeen, A. Peterlin, and D.R. Carver. National Aviation Weather Initiatives. Technical report, FCM-P34-1999, Washington, D.C., February 1999.

[4] Aircraft Owner and Pilots Association (AOPA). http://www.aopa.org, Last time accessed: 20/09/2005.

[5] M. Pereira. Status of NTSB Aircraft Icing Certification-Related Safety Recommendations Issued as a Result of the 1994 ATR-72 Accident at Roselawn, IN. *AIAA 97-0410*, 1997.

[6] Air Accident Investigation Branch (AAIB). S1/2002 Bombardier Challenger CL600-2B16, N90AG. http://www.aaib.dft.gov.uk/, Last time accessed: 22/07/2005.

[7] M.P. Simpson and P.M. render. Certification and Operation of Helicopters in Icing Environments. *Journal of Aircraft*, Vol.35:pp.936–941, 1998.

[8] Civil Aviation Authority. Aircraft Icing Handbook. http://www.caa.govt.nz, Last time accessed: 03/06/2003.

[9] J. Shin, J. Chung, and K.D. Lee. A Computational Investigation of Ice Geometry on Airfoil Performances. *AIAA 2001-0540*, 2001.

[10] M.B. Bragg, T. Hutchinson, J. Merret, R. Oltman, and D.Pokhariyal. Effect of Ice Accretion on Aircraft Flight Dynamics. *AIAA 2000-0360*, 2000.

[11] Air Transport International L.L.C (ATI). Aircraft Ground De-ice/Anti-ice Manual. Technical report, Winter 2004-2005, revision 9, 1 October 2004.

[12] T.J. Vukits. Overview and Risk Assessment of Icing for Transport Category Aircraft and Components. *AIAA 2002-0811*, 2002.

[13] M.B. Bragg and W.J. Coirier. Aerodynamic Measurements of an Airfoil with Simulated Glaze Ice. *AIAA 86-0484*, 1986.

[14] R. Henry, D. Guffond, S. Aschettino, and G. Duprat. Characterization of Ice Roughness and Influence on Aerodynamic Performance of Simulated Ice Shapes. *AIAA 2001-0092*, 2001.

[15] P. Tran, M.T. Brahimi, I. Paraschivoiu, A. Pueyo, and F. Tezok. Ice Accretion on Aircraft Wings with Thermodynamical Effects. *AIAA 94-0605*, 1994.

[16] R.W. Gent, N.P. Dart, and J.T. Candale. Aircraft Icing. *Philosophical Transactions of the Royal Society of London. A*, Vol.358:pp.2873–2911, 2000.

[17] J. Shin and T.H. Bond. Results of an Icing Test on a NACA 0012 Airfoil in the NASA Lewis Icing Research Tunnel. *AIAA 92-0647*, 1992.

[18] F.T. Lynch and A. Khodadoust. Effects of Ice Accretions on Aircraft Aerodynamics. *Progress in Aerospace Sciences*, Vol.37:pp.669–767, 2001.

[19] Advisory Group for Aerospace Research and Development. Ice Accretion Simulation. Technical report, AGARD-AR-344, December 1997.

[20] S. Thomas, R. Cassoni, and C. MacArthur. Aircraft Anti-Icing and Deicing Techniques and Modeling. *AIAA 96-0390*, 1996.

[21] T.G. Keith, K.J. De Witt, W.B. Wright, and K.C. Masiulaniec. Overview of Numerical Codes Developed for Predicted Electrothermal De-Icing of Aircraft Blades. *AIAA 88-0288*, 1988.

[22] W.B. Wright. Users Manual for the Improved NASA Lewis Ice Accretion Code LEWICE 1.6. Technical report, NASA CR 198355, 1995.

[23] R.W. Gent. TRAJICE2 - A combined Water Droplet Trajectory and Ice Accretion Prediction Program for Aerofoils. Technical report, Royal Aerospace Establishment TR 90054, 1990.

[24] T. Hedde and D. Guffond. Development of a Three-Dimensional Icing Code, Comparison with Experimental Shapes. *AIAA 92-0041*, 1992.

[25] G. Mingione, V. Brandi, and B. Esposito. Ice Accretion Prediction On Multi-Element Airfoil. *AIAA 97-0177*, 1997.

[26] M.T. Brahmini, P. Tran, F. Tezok, and I. Paraschivoiu. Prediction of Ice on Supercritical and Multi-Elements Airfoils. *AIAA 95-0754*, 1995.

[27] Y. Bourgault, W.G. Habashi, and H. Beaugendre. Development of a Shallow Water Icing Model in FENSAP-ICE. *AIAA 99-246*, 1999.

[28] B.L. Messinger. Equilibrium Temperature of an Unheated Icing Surface as a Function of Air Speed. *Journal of the Aeronautical Sciences*, Vol.20, No.1:pp.29–42, January 1953.

[29] T.G. Myers. Extension to the Messinger Model for Aircraft Icing. *AIAA Journal*, Vol.39, No.2:pp.211–218, 2001.

[30] A.P. Rothmayer, B.D. Matheis, and S.N Timoshin. Thin Liquid Films Flowing over External Aerodynamic Surfaces. *Journal of Engineering Mathematics*, Vol.42:pp.341–357, 2002.

[31] W.A. Olsen and E. Walker. Experimental Evidence for Modifying the Current Physical Model for Ice Accretion on Aircraft Surfaces. *NASA TM 87184*, 1986.

[32] A.J. Press and N.P. Dart. ICECREMO User Guide. Technical report, ICECREMO/SPEC/DERA/ND990506/3, March 2000.

[33] B. Sarler. Stefan's Work on Solid-Liquid Phase Changes. *Engineering Analysis with Boundary Elements*, Vol.16:pp.83–92, 1995.

[34] T.G. Myers. Combined Ice Growth and Water Flow Model. Technical report, Cranfield University ICECREMO/TR/CRAN2/TM990915/4, 1999.

[35] J.P.F. Charpin. *Water flow on Accreting Ice surfaces.* PhD Thesis, School of Engineering, Cranfield University, UK, September 2002.

[36] E.P. Lozowski, J.R. Stallabrass, and P.F. Hearty. The Icing of an Unheated, Nonrorating Cylinder. Part I: A Simulation Model. *Journal of Applied Meteorology*, Vol.22, Issue.12:pp.844–850, December 1983.

[37] J. Karim. An Investigation of Aircraft Accidents and Incidents Attributed to Icing and Cold Weather Operations. Msc thesis, Cranfield University, 1995.

[38] Association of European Airlines. Recommendations for De-IcingAnti-Icing of Aircrafts on the Ground. http://www.aea.be, 21^{rst} Edition, September 2006, Last time accessed: 02/01/2007.

[39] M.G. Potapczuk and B.M. Berkowitz. Experimental Investigation of Multi-Element Airfoil Ice Accretion and Resulting Performance Degradation. *NASA TM-101441*, 1989.

[40] S. Lee and M.B. Bragg. Experimental Investigation of Simulated Large-Droplet Ice Shapes on Airfoil Aerodynamics. *Journal of Aircraft*, Vol.36:pp.844–850, 1999.

[41] I. Paraschivoiu and F. Saeed. http://www.meca.polymtl.ca/ion/000-main.pdf, Aircraft Icing, Last time accessed: 13/04/2007.

[42] R. Rasmussen, M. Politovich, J. Marwitz, W. Sand, J. McGinley, J. Smart, R. Pielke, S. Rutledge, D. Wesley, G. Stossmeister, B. Bernstein, K. Elmore, N. Powell, E. Westwater, B.B. Stankov, and D. Burrows. Winter Icing and Storms Project (WISP). *American Meteorological Society Journals*, Vol.73:pp.951–974, July 1992.

[43] M.B. Bragg. Aerodynamics of Supercooled-Large-Droplet Ice Accretions and the Effect on Aircraft Control. *Proceedings of the FAA Int. Conf. on Aircraft Inflight Icing*, Report No. DOT/FAA/AR-96/81,II, Vol.2:pp.387–400, August 1996.

[44] B.C. Bernstein, T.P. Ratvasky, D.R. Miller, and F. McDonough. Freezing Rain as an In-Flight Icing Hazard. Technical report, NASA/TM-2000-210058, June 2000.

[45] R.J. Hansman, K.S. Breuer, D. Hazan, A. Reehorst, and M. Vargas. Close-up Analysis of Aircraft Ice Accretion. *AIAA 93-0029*, 1993.

[46] D.G. Jackson and M.B. Bragg. Aerodynamic Performance of an NLF Airfoils with Simulated Ice. *AIAA 99-0373*, 1999.

[47] D.R. Glover Jr. Dictionary of Technical Terms for Aerospace Use. *NASA Lewis Research Center*, Last time accessed: 06/06/2003. http://roland.lerc.nasa.gov/ dglover/dictionary/content.html.

[48] T.G. Myers and D.W. Hammond. Ice and Water Film Growth from Incoming Supercooled Droplets. *International Journal of Heat and Mass Transfer 42(1999)2233-2242*, 1999.

[49] R.J. Hansman Jr. and S.R. Turnock. Investigation of Surface Water Behavior During Glaze Ice Accretion. *Journal of Aircraft*, Vol.26, No.2:pp.140–147, 1989.

[50] K.M. Al-Khalil, T.G. Keith Jr., and K.J. De Witt. Developement of an Anti-Icing Runback Model. *AIAA 90-0759*, 1990.

[51] R. Purvis, F. Smith, and R. Gent. Droplet Impact on Water Layers. *Alan Tayler Day*, 24 November 2003, St Catherine's College, Oxford.

[52] R.J. Kind, M.G. Potapczuk, A. Feo, C. Golia, and A.D. Shah. Experimental and Computational Simulation of In-flight Icing Phenomena. *Progress in Aerospace Sciences*, Vol.34:pp.257–345, 1998.

[53] G.A. Ruff and B.M. Berkowitz. User's Manual for the NASA Lewis Ice Accretion Prediction Code (LEWICE). *NASA CR 185129*, 1990.

[54] T. Hedde and D. Guffond. Improvement of the ONERA-3D Icing Code, Comparison with 3D Experimental Shapes. *AIAA 93-0169*, 1993.

[55] Newmerical Technologies International. http://www.newmerical.com, Last time accessed: 24/02/2006.

[56] G. Croce, W.G. Habashi, G. Guevremont, and F. Tezok. 3D Thermal Analysis of an Anti-icing Device using FENSAP-ICE. *AIAA 98-0193*, 1998.

[57] S. Eberhardt and H. Ok. Aircraft Icing Predictions Using an Efficient, Incompressible Navier-Stokes Solver. http://www.aa.washington.edu/faculty/ eberhardt/icing.pdf, Last time accessed: 13/12/05.

[58] FLUENT Incorporated. Centerra Resource Park, 10 Cavendish Court, Lebanon NH03766, GAMBIT1 Tutorial Guide, May 1998.

[59] FLUENT Incorporated. Centerra Resource Park, 10 Cavendish Court, Lebanon NH03766, FLUENT5 Tutorial Guide, August 1998.

[60] J. Weissinger. *Development of a Discrete Adaptive Gridless Method for the solution of Elliptic Partial Differential Equation.* PhD Thesis, School of Engineering, Cranfield University, UK, July 2003.

[61] S.C. Caruso. NEARICE: An Unstructured-Mesh Navier-Stokes-based Ice Accretion Prediction Code. *AIAA 94-0606*, 1994.

[62] K. Yamaguchi and R.J. Hansman. Heat Transfer on Accreting Ice Surfaces. *Journal of Aircraft*, Vol.29, No1:pp.108–113, 1992.

[63] L. Makkonen. Models for the Growth of Rime, Glaze, Icicles and Wet Snow on Structures. *Philosophical Transactions of the Royal Society of London. A*, Vol.358, No.1776:pp.2913–2939, 2000.

[64] M.G. Potapczuk. LEWICE/E: An Euler Based Ice Accretion Code. *AIAA 92-0037*, 1992.

[65] G.F. Naterer. Dispersed Multiphase Flow with Air-Driven Runback of a Liquid Layer at a Moving Boundary. *Int. Journal of Multiphase Flow*, Vol.29:pp.1833–1856, 2003.

[66] *13/14 Heat Transfer Analysis. Thermofluid Mechanics and Energy.* The Open University, 1985.

[67] A.J. Bilanin and D.N. Anderson. Ice Accretion with Varying Surface Tension. *AIAA 95-0538*, 1995.

[68] M. Pais and S.N. Singh. Determination of the Local Heat Transfer Coefficients of Three Simulated Smooth Ice Formation Characteristics on a Cylinder . *AIAA 1985-1836*, 1985.

[69] K. Szilder and P. Lozowski. Discrete Modelling of Ice Accretion Shape and Structure Forming on a Cylinder under In-Flight Icing Conditions. *AIAA 2003-1075*, 2003.

[70] S.A. Sherif, N. Pasumarthi, and C.S. Bartlett. A Semi-Empirical Model for Heat Transfer and Ice Accretion on Aircraft Wings in Supercooled Clouds. *Cold Regions Science and Technology*, Vol.26:pp.165–179, 1997.

[71] R.J. Hansman, K. Yamaguchi, B. Berkowitz, and M. Potapczuk. Modeling of Surface Roughness Effects on Glaze Ice Accretion. *AIAA 89-0734*, 1989.

[72] M.B. Bragg, A.P. Broeren, and L.A. Blumenthal. Iced-Airfoil Aerodynamics. *Progress in Aerospace Sciences*, Vol.41:pp.323–362, 2005.

[73] J. Shin and T.H. Bond. Experimental and Computational Ice Shapes and Resulting Drag Increase for a NACA0012 Airfoil. *NASA Technical Manual 105743*, 1992.

[74] P.-C. Havugimana, C. Lutz, I. Paraschivoiu, G.-K. Kerevanian, A. Sidorenko, E. Benard, R.K. Cooper, and R.S. Raghunathan. A Comparison of Skin Friction and Heat Transfer Prediction by Various Roughness Models. *AIAA 2002-3052*, 2002.

[75] W.B. Wright, R.W. Gent, and D. Guffond. DRA/NASA/ONERA Collaboration on Icing Research: Part II - Prediction of Airfoil Ice Accretion. Technical report, NASA CR - 202349, 1997.

[76] P. Klebanoff, W. Cleveland, and K. Tidstrom. On the Evolution of a Turbulent Boundary Layer Induced by a Three-dimensional Roughness Element. *J. Fluid Mech.*, Vol.237:pp.101–187, 1992.

[77] E.B. White and M.J. Oliver. Experiments on Surface Roughness Effects in Ice Accretion. *AIAA 2005-5190*, 2005.

[78] FLUENT5. http://venus.imp.mx/hilario/SuperComputo/Fluent.Inc/manuals/fluent5/index.htm. Last time accessed: 09/04/07.

[79] J.C. Tsao and A.P. Rothmayer. Transient Effects in Prediction Bulk Surface Properties for Aircraft Ice Accretion. *AIAA 01-0677*, 2001.

[80] T. Hedde. *Modelisation Tridimensionnelle des Depots de Givre sur les Voilures d' Aeronefs*. PhD Thesis, Universite Blaise Pascal, Clermond-Ferrand II, France, December 1992.

[81] R.A. Da Silveira and C.R. Maliska. Numerical Simulation of Ice Accretion on the Leading Edge of an Aerodynamic Profile. *Proceeding of the 2nd International Conference on Computational Heat and Mass Transfer COPPE/UFRJ, Brazil*, October 22-26, 2001.

[82] M.G Potapczuk and C.S Bidwell. Swept Wing Ice Accretion Modeling. *AIAA 90-0756*, 1990.

[83] M.G. Potapczuk, K.M. Al-Khalil, and M.T. Velazquez. Ice Accretion and Performance Degradation Calculations with LEWICE/NS. *AIAA 93-0173*, 1993.

[84] M. Fregeau, F. Saeed, and I. Paraschivoiu. Surface Heat Transfer Study for Ice Accretion and Anti-Icing Prediction in Three Dimension. *AIAA 2004-0063*, 2004.

[85] J.T. Cansdale and R.W Gent. Ice Accretion on Aerofoils in Two-Dimensional Compressible Flow - A Theoretical Model. Technical report, TR82128, Royal Aircraft Establishment, January 1983.

[86] H. Schlichting. *Boundary-Layer Theory*. McGraw-Hill, 7th edition, 1979.

[87] F. Morency, M.T Brahimi, F. Tezok, and I .Paraschivoiu. Hot Air Anti-Icing System Modelization in the Ice Prediction Code CANICE. *AIAA 98-0192*, 1998.

[88] R.J. Hansman and S.R. Turnock. Investigation of Surface Water Behavior During Glaze Ice Accretion. *Journal of Aircraft*, Vol.26, No.2:pp.140–147, 1989.

[89] B.D. Matheis and A.P. Rothmayer. Numerical Simulation of Thin Air Driven Films. *AIAA 2002-0525*, 2002.

[90] A. Oron, S.H. Davis, and S.G. Bankoff. Long Scale Evolution of Thin Liquid Films. *Review of Modern Physics*, Vol.69, Issue 3:pp.931–980, July 1997.

[91] H. Ockendon and J.R. Ockendon. *Viscous Flow*. Cambridge University Press, 1995.

[92] T.G. Myers. Thin Films with High Surface Tension. *SIAM Review*, Vol.40:pp.441–462, 1998.

[93] J.C. Tsao and A.P. Rothmayer. A Mechanism for Ice Roughness Formation on an Airfoil Leading Edge, Contributing to Glaze Ice Accretion. *AIAA 98-0485*, 1998.

[94] T.G. Myers, J.P.F. Charpin, and C.P. Thompson. Slowly Accretion Ice due to Supercooled Water Impacting on a Cold Surface. *Physics of Fluids*, Vol.14, No.1, 2002.

[95] P.G. Verdin and C.P. Thompson. Multi-Stepping Validation Report ICECREMO I. Technical report, confidential; Deliverable 3.3.4.1, Cranfield University, School of Engineering, April 2005.

[96] P.G. Verdin. Version 1.1, Automatic Multi-Stepping Procedure - User-Guide ICECREMO II. Technical report, confidential; Cranfield University, School of Engineering, August 2005.

[97] A.J. Press and D. Standingford. ICECREMO2 SOFTWARE DESIGN METHODOLOGY. Technical report, JS15066 - Confidential, August 2003.

[98] T.G. Myers, J.P.F. Charpin, and S.J. Chapman. The Flow and Solidification of a Thin Fluid Film on an Arbitrary Three-Dimensional Surface. *Physics of Fluids*, Vol.14, No.8, 2002.

[99] K. Yamaguchi, R.J. Hansman, and M. Kazmierczak. Deterministic Multi-Zone Ice Accretion Modeling. *AIAA 91-0265*, 1991.

[100] D. Guffond and T. Hedde. Prediction of Ice Accretion: Comparison between the 2D and 3D Codes. *La Recherche Aerospatiale*, No.2:pp.103–115, 1994.

[101] D. Thompson, S. Chalasani, and P. Mogili. ICEWING- A Mesh Generation System for Complex Three-Dimensional Iced Wing Configurations. *Year 2 Effort: Icing Effects Studies for a Three-Dimensional Wing*, NASA Contract NAG3-2562, April 2003.

[102] Fluent Computational Fluid Dynamics (CFD) Software and Services. Last time accessed: 01/03/2007. http://www.fluent.com/.

[103] C.L. Ladson, Jr. C.W. Brooks, A.S. Hill, and D.W. Sproles. Computer Program to Obtain Ordinates for NACA Airfoils. Technical report, NACA TM 4741, December 1996.

[104] S.C. Caruso. Three-Dimensional Unstructured Mesh Procedure for Iced Wing Flowfield and Droplet Trajectory Calculations. *AIAA 94-0486*, 1994.

[105] NURBS. http://en.wikipedia.org/wiki/Nonuniform_rational_B-spline. Last time accessed: 11/04/07.

[106] R. Moser and R. Gent. Experience from Application of a 3D Ice Accretion Code. *SAE Technical Papers, 2003-01-2133*, 2003.

[107] H. Beaugendre, F. Morency, and W.G. Habashi. Development of a Second Generation In-Flight Icing Simulation Code. *Journal of Fluids Engineering*, Vol.128, Issue 2:pp.378–387, 2006.

[108] P.R. Spalart and S.R. Allmaras. A One-equation Turbulence Model for Aerodynamic Flows. *AIAA 92-0439*, 1992.

[109] Inc. AeroSoft. GASP Version 4.2 Reference Guide. http://www.aerosft.com, Last time accessed: 14/01/2006.

[110] J.J. Chung and H.E Addy. A Numerical Evaluation of Icing Effects on a Natural Laminar Flow Airfoil. *AIAA 2000-0096*, 2000.

[111] T.A. Dunn, E. Loth, and M.B. Bragg. Computational Investigation of Simulated Large-Droplet Ice Shapes on Airfoil Aerodynamics. *Journal of Aircraft*, Vol.36, No.5:pp.836–843, 1999.

[112] H.M. Gurbacki and M.B. Bragg. Unsteady Aerodynamic Measurements of an Iced Airfoil. *AIAA 2002-0241*, 2002.

[113] P.G. Verdin and C.P. Thompson. Automatic Multi-Stepping Approach for Ice Predictions. *IASME Transactions*, Issue1, Vol.2, January 2005.

[114] P.G. Verdin and C.P. Thompson. Multi-Stepping ICECREMO I User-Guide. Technical report, confidential; Cranfield University, School of Engineering, August 2004.

[115] W.B. Wright and M.G. Potapczuk. Computational Simulation of Large Droplet Icing. Technical report, NASA/CR, 1998.

[116] D.S. Thompson and B.K. Soni. ICEG2D - A Software Package for Ice Accretion Prediction. Technical report, Prepared under Grant NAG3-2235, June 2002.

[117] W.B. Wright. User Manual for the NASA Glenn Ice Accretion Code LEWICE, Version 2.2.2. Technical report, NASA/CR 2002-211793, 2002.

[118] W.B. Wright and A. Rutkowski. Validation Results for LEWICE 2.0. Technical report, NASA CR 1999-208690, 1999.

[119] W.B. Wright. User Manual for the NASA Glenn Ice Accretion Code LEWICE, Version 2.0. Technical report, NASA/CR 1999-209409, 1999.

[120] RTO Technical Report:TR-038. Ice Accretion Simulation Evaluation Test. Technical report, North Atlantic Treaty Organization, 2001.

[121] M.B. Bragg, S. Lee, and C.M. Henze. Heat-Transfer and Freestream Turbulence Measurements for Improvement of the Ice Accretion Physical Model. *AIAA 97-0053*, 1997.

[122] D.W. Hammond, M. Quero, P. Ivey, D. Miller, R. Purvis, O. McGregor, and J. Tan. Analysis and Experimental Aspects of the Impact of Super-cooled Water Droplets into Thin Water Layers. *AIAA 2005-0077*, 2005.

[123] M. Quero, D.W. Hammond, R. Purvis, and F.T. Smith. Analysis of Super-cooled Water Droplet Impact on a Thin Water Layer and Ice Growth. *AIAA 2006-466*, 2006.

[124] S.C. Tan, M. Papadakis, D. Miller, T. Bencic, P. Tate, and M.C. Laun. Experimental Study of Large Splashing and Breakup. *AIAA 2007-904*, 2007.

[125] R.W. Gent, J.M. Ford, R.J. Moser, and D. Miller. Results from Super-Cooled Large Droplets Mass Loss Tests in the Act Luton Icing Wind Tunnel. *AIAA 2003-389*, 2003.

[126] S.C. Chapra and R.P. Canale. *Numerical Methods for Engineers*. McGraw-Hill, 2002.

[127] D. Rodabaugh and J.R. Wesson. On the efficient use of predictor-corrector methods in the numerical solution of differential equations. Technical report, NASA TN D-2946, August 1965.

[128] G. Mingione and V. Brandi. Ice Accretion Prediction On Multi-Elements Airfoils. *Journal of Aircraft*, Vol.35, No.2:pp.240–246, 1998.

[129] Y. Soufflet. *Improvement of Runback Water Film Calculation and Its Impact on Ice Prediction*. PhD Thesis, School of Engineering, Cranfield University, UK, To be submitted.

[130] Cranfield University. School of Engineering, Applied Mathematics and Computing Group, http://www.cranfield.ac.uk/soe/amac/, Last time accessed: 01/03/2007.

[131] O. Harireche, P. Verdin, C.P. Thompson, and D.W. Hammond. Explicit Finite Volume Modelling of Anti-Icing and De-Icing. *Accepted for publication, Journal of Aircraft*, April 2008.

[132] C.P. Thompson and O. Harireche. ICECREMO II - Extensions of the Ice Growth and Water Film Models: Anti-Icing and De-Icing Capabilities. Technical report, confidential; Deliverable 3.1.1, Cranfield University, School of Engineering, March 2005.

[133] O. Harireche and C.P. Thompson. De-icing and Anti-icing capabilities in ICECREMO II. Technical report, confidential; Deliverable 3.1.2, December 2005.

[134] A. Press, Y. Soufflet, and C.P. Thompson. ICECREMO II - Error Control and Adaptivity Methodology. Technical report, December 2005.

[135] A.J. Press. ICECREMO2 Userguide. Technical report, BAE Systems, Advanced Technology Centre, P.O.Box 5, Filton, Bristol, BS34 7QW, June 2005.

[136] A.J. Press. ICECREMO2 Version 4.0 Userguide. Technical report, BAE Systems, Advanced Technology Centre, P.O.Box 5, Filton, Bristol, BS34 7QW, January 2006.